TECHNISCHE UNIVERSITÄT MÜNCHEN
Fakultät für Informatik

Development of Turbulence Simulations for the Edge & Divertor and Validation against Experiment

Thomas Alfred John Body

Vollständiger Abdruck der von der Fakultät für Informatik der Technischen Universität München zur Erlangung eines

Doktors der Naturwissenschaften

genehmigten Dissertation.

Vorsitzender:		Prof. Dr.-Ing. Nils Thuerey
Prüfer*innen der Dissertation:	1.	Hon. Prof. Dr. Frank Jenko
	2.	Prof. Dr. Peter Manz

Die Dissertation wurde am 18.01.2022 bei der Technischen Universität München eingereicht und durch die Fakultät für Informatik am 12.05.2022 angenommen.

TECHNISCHE UNIVERSITÄT MÜNCHEN

DEPARTMENT OF INFORMATICS

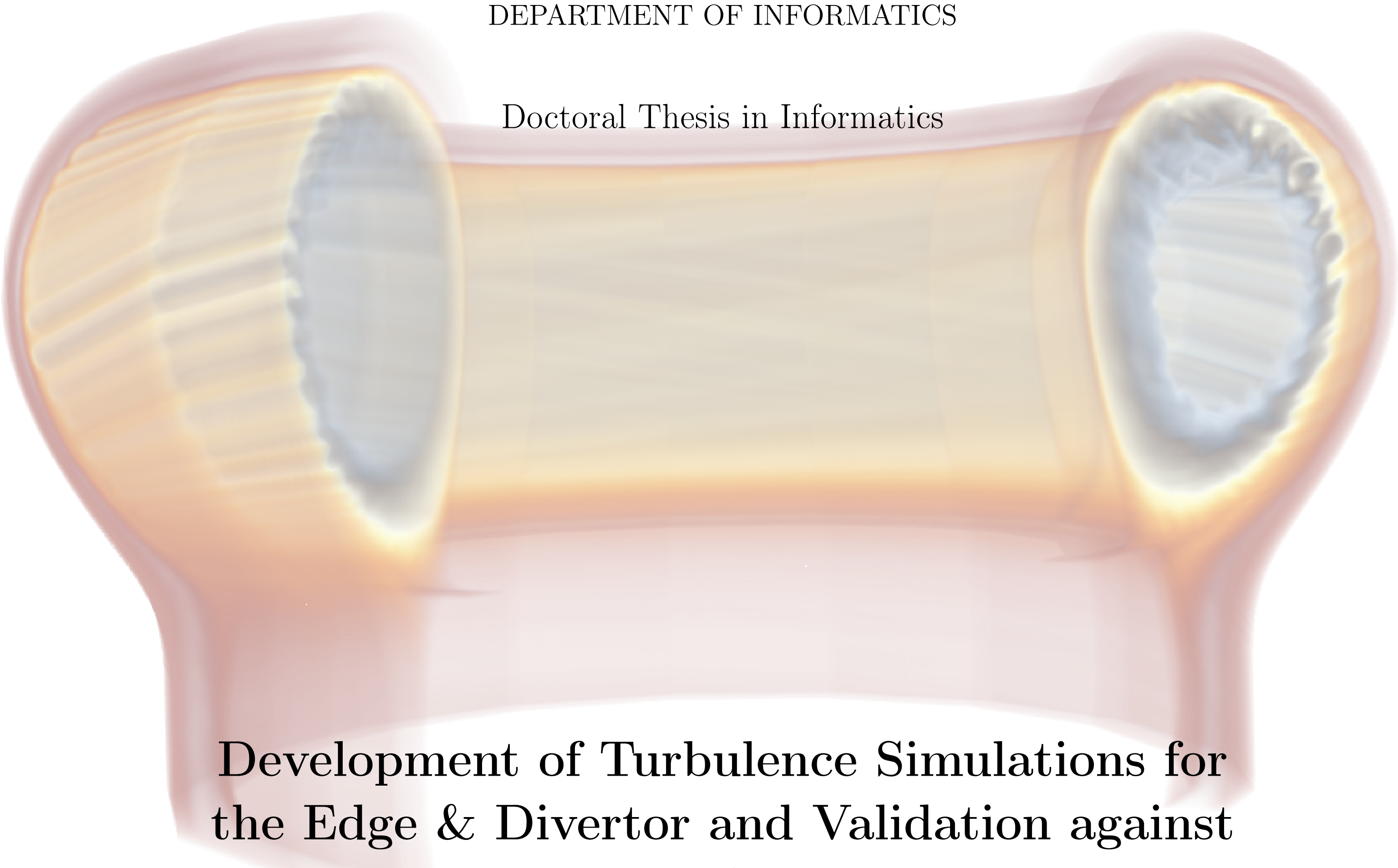

Doctoral Thesis in Informatics

Development of Turbulence Simulations for the Edge & Divertor and Validation against Experiment

Thomas Body

Max-Planck-Institut
für Plasmaphysik

MAX PLANCK
GESELLSCHAFT

TECHNISCHE UNIVERSITÄT MÜNCHEN

DEPARTMENT OF INFORMATICS

Doctoral Thesis in Informatics

Development of Turbulence Simulations for the Edge & Divertor and Validation against Experiment

Author: Thomas Body
Supervisor: Prof. Dr. Frank Jenko
Advisor: Dr. Andreas Stegmeir
Submission Date: 14th January, 2022

IPP Max-Planck-Institut für Plasmaphysik

MAX PLANCK GESELLSCHAFT

I confirm that this doctoral thesis in informatics is my own work and I have documented all sources and material used.

Munich, 14th January, 2022 Thomas Body

Acknowledgements

To Juli, for sharing the adventure

Fusion research is an international collaboration. The work in this thesis was supported by many researchers, both within Germany and internationally. The following is by no means a complete list, but rather a highlight of those without whom this work would not be possible.

First and foremost, my supervisor Andreas Stegmeir deserves a special thanks. He introduced me to the field and to the GRILLIX code, answered questions both sensible and otherwise, helped me to focus and develop the work in this thesis, and backed me up when I needed it most. Wladimir Zholobenko, whose extensive knowledge of plasma physics and numerics helped to separate signal from noise and to run and interpret the simulations, also deserves a special thanks, as does Dominik Michels who gave a new perspective on software engineering and mathematics, helping to improve the quality and performance of our simulations. Frank Jenko helped me to keep an eye on the big picture and encouraged me to take the risks needed to bring this project to fruition, David Coster connected the project to the broader fusion effort, Peter Manz provided a greatly-appreciated introduction to the theory and ideas for several of the numerical diagnostics, Tilman Lunt helped to interpret the results in advanced divertor configurations, and Phillip Ulbl road-tested the `TorX` and TCV-X21 repositories. Outside IPP, the project benefited from several close international collaborations. Fulvio Militello and Christian Theiler supported this project with their respective EUROFusion projects and generously contributed to the development and interpretation of this project. Mana Francisquez and Ben Zhu from the GDB team helped to develop the immersed boundary technique, which permitted open field-line simulations. The ideas in this thesis were developed in discussions with Davide Galassi, Diego Sales de Oliveira, Patrick Tamain, Paolo Ricci, Holger Reimerdes, Matthias Wiesenberger, Frédéric Imbeaux, Fabio Riva, Roberto Ambrosino, John Omotani, Elias Laribi, Guido Ciraolo, and many more.

Abstract

For fusion to become a practical source of energy, we need to understand and control the edge. Current predictions of the edge region of future fusion devices have large uncertainty, and our understanding of currently-observed experimental phenomena is incomplete. Realistic simulations of the edge would help to interpret existing experimental results and predict the performance of new devices and operating scenarios. By improving our understanding and control of the edge, simulations could help us build energy-producing reactors sooner, for less cost and with more robust operating conditions. To simulate the edge, we extend the GRILLIX fluid-turbulence code to perform simulations across the separatrix of existing fusion experiments. We implement a new grid preprocessor and extend the grid generation algorithm to enable simulations in realistic axisymmetric magnetic geometries, including in advanced divertor configurations. We also identify the cause of a numerical issue related to parallel boundary conditions and implement an immersed boundary method to permit simulations with realistic wall geometries and sheath boundary conditions.

We then perform a rigorous validation of the numerical model to determine how realistic the simulations are and to identify how the model can be further improved. We compare against two experimental cases – an ‘X-point’ scenario in the TORPEX basic plasma physics device, and the ‘TCV-X21’ validation case in the TCV tokamak. In TORPEX, the simulations reproduce the experimentally-observed up-down asymmetry and match the density profile. However, the simulations use a heating power 97% less than the experiment and do not match the electron temperature profile due to the omission of neutrals. A significantly better match is found for TCV-X21. At the outboard midplane, the simulations quantitatively match the mean profiles and fluctuations mostly within uncertainty. They also reproduce the non-Gaussian nature of the turbulence in the SOL, correctly predicting that the far-SOL should be dominated by coherent filaments. The drive mechanism for the filaments is identified via a Fourier analysis as drift-wave turbulence in the outer confined-region. Towards the divertor targets, the quality of the match decreases due to an issue in applying drift-corrected boundary at glancing angles of incidence and the use of insulating-sheath boundary conditions for the potential. Despite this, the electron temperature at the targets matches remarkably well in the scrape-off-layer. The validations show that GRILLIX can now perform simulations of real devices, and can qualitatively and often quantitatively match experimental measurements. The validation methodology and cases developed in this thesis are being used to test improved versions of GRILLIX, guiding the development of validated predictive simulations of the edge and divertor.

Kurzfassung

Damit Fusion zu einer praktischen Energiequelle wird, muss der Randbereich verstanden und kontrolliert werden. Aktuelle Vorhersagen des Randbereiches zukünftiger Fusionsanlagen weisen große Unsicherheiten auf und unser Verständnis der derzeit beobachteten experimentellen Phänomene ist unvollständig. Realistische Simulationen des Randbereiches würden helfen, vorhandene experimentelle Ergebnisse zu interpretieren und die Leistung neuer Geräte und Betriebsszenarien vorherzusagen. Simulationen könnten uns durch Verbesserung unseres Verständnisses und durch bessere Kontrolle des Randbereiches helfen, energieerzeugende Reaktoren früher, kostengünstiger und mit robusteren Betriebsbedingungen zu bauen. Zur Simulation des Randbereiches erweitern wir den GRILLIX-Fluid-Turbulence-Code, um Simulationen über die Separatrix bestehender Fusionsexperimente hinweg durchzuführen. Wir implementieren einen neuen Gitter-Präprozessor und erweitern den Gittererzeugungsalgorithmus, um Simulationen in realistischen axialsymmetrischen magnetischen Geometrien, einschließlich fortgeschrittener Divertor-Konfigurationen, zu ermöglichen. Wir identifizieren auch die Ursache eines numerischen Problems im Zusammenhang mit parallelen Randbedingungen und implementieren eine sogenannte Immersed-Boundary Methode, um Simulationen mit realistischen Wandgeometrien und Randbedingungen zu ermöglichen.

Anschließend führen wir eine strenge Validierung des numerischen Modells durch, um festzustellen, wie realistisch die Simulationen sind und zu ermitteln, wie das Modell weiter verbessert werden kann. Wir vergleichen mit zwei experimentellen Fällen – einem "X-Punkt"-Szenario im einfachen TORPEX Experimemt für Plasmaphysik und dem "TCV-X21"-Validierungsfall im TCV-Tokamak. In TORPEX reproduzieren die Simulationen die experimentell beobachtete vertikale Asymmetrie und das Dichteprofil stimmt überein. Allerdings weisen die Simulationen eine um 97% geringere Heizleistung als das Experiment auf und stimmen aufgrund der Vernachlässigung von Neutralgasphysik nicht mit dem Elektronentemperaturprofil überein. Eine deutlich bessere Übereinstimmung wird für TCV-X21 gefunden. An der äußeren Mittelebene stimmen die Simulationen quantitativ mit den mittleren Profilen und Fluktuationen größtenteils innerhalb der Unsicherheit überein. Sie reproduzieren auch die nicht-Gaußsche Natur der Turbulenz in der Abschälschicht und sagen richtig voraus, dass die entfernte Abschälschicht von kohärenten Filamenten dominiert werden sollte. Der Antriebsmechanismus für die Filamente wird über eine Fourier-Analyse als Driftwellenturbulenz im äußeren eingeschlossenen Bereich identifiziert. Zum Divertor hin nimmt die Qualität der Übereinstimmung aufgrund eines Problems bei der Anwendung einer driftkorrigierten Grenze bei flachen Einfallswinkeln und der Verwendung von Randbedingungen für das Potential ab. Trotzdem stimmt die Elektronentemperatur an den Divertorplatten in der Abschälschicht bemerkenswert gut überein. Die Validierungen zeigen, dass GRILLIX nun Simulationen realer Geräte durchführen und experimentelle Messungen qualitativ und oft auch quantitativ reproduzieren kann. Die Validierungsmethodik und die in dieser Arbeit entwickelten Fälle werden verwendet, um verbesserte Versionen von GRILLIX zu testen und die Entwicklung validierter vorhersagekräftiger Simulationen des Randbereiches und des Divertors zu leiten.

Resources

There are several papers and software projects associated with this thesis, which will be referred to throughout the thesis. These include

- `GRILLIX` (`gitlab.mpcdf.mpg.de/tbody/GRILLIX@baa5cadd`, legacy version): a high-performance fluid turbulence code, used for the TORPEX and TCV-X21 validations presented in this thesis. This has since been replaced by a refactored version based on `parallax`.
- `TorX` (`gitlab.mpcdf.mpg.de/phoenix/torx@40964572`): a post-processing library developed for GRILLIX (both legacy and refactored versions) and GENE-X, used to analyse the simulations in this thesis.
- `parallax-equilibrium` (`gitlab.mpcdf.mpg.de/phoenix/parallax_equilibrium@a0c591ae`): a grid preprocessor developed for GRILLIX (both legacy and refactored versions) and GENE-X, used to handle axisymmetric magnetic equilibria in various formats.
- `TCV-X21` (`github.com/SPCData/TCV-X21@784c55a`): a publicly-accessible dataset of edge and SOL measurements from a TCV scenario for validating turbulence simulations, used to validate GRILLIX in chapter 8.
- Body et al., *Treatment of advanced divertor configurations in the flux-coordinate independent turbulence code GRILLIX*, published in Contributions to Plasma Physics, 2020. This paper details the grid processing required to handle arbitrary axisymmetric geometries, discussed in more detail in chapter 5.
- Galassi et al., *Validation of edge turbulence codes in a magnetic X-point scenario in TORPEX*, published in Physics of Plasmas, 2022 [1]. For this paper, I performed and post-processed the GRILLIX simulations, discussed in chapter 7.
- Oliveira & Body et al., *Validation of edge turbulence codes against the TCV-X21 diverted L-mode reference case*, published in Nuclear Fusion, 2022 (co-first authorship) [2]. For this paper, I performed the GRILLIX simulations, wrote the post-processing library, organised the FAIR data repository with the help of Fair4Fusion, and wrote the paper with D.S. Oliveira, D. Galassi, C. Theiler, A. Stegmeir and P. Tamain. The results of this validation are discussed in chapter 8.

We additionally provide the notebooks used to generate the figures and for demonstrations in the thesis. These are available from `doi.org/10.5281/zenodo.5851526`.

Contents

Part I.

Introduction

Prelude: How to build a fusion reactor

> When we look up at night and view the stars, everything we see is shining because of distant nuclear fusion.
>
> *(Carl Sagan)*

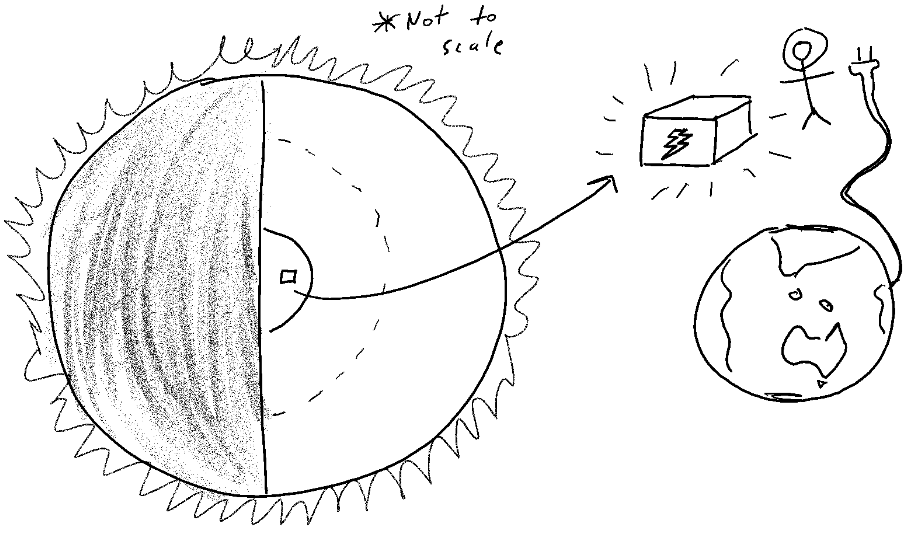

This is a brief introduction to magnetic confinement fusion, intended for readers who do not have a background in plasma physics. If you are already familiar with the topic, it can be safely skipped. Alternatively, if you would like an extended introduction, Ongena et al., 2016 [3] is recommended.

Nuclear fusion is the process that powers the stars. It occurs when the nuclei of light elements (such as Hydrogen) collide and fuse to form heavier elements. When the products of nuclear fusion have a higher nuclear binding energy than the reactants, the excess energy is eventually converted into heat – such as sunlight or the solar wind. Before this can occur, however, the reactants must be extremely hot. Since like charges electrically repel each other, fusion will only occur when the colliding particles have enough energy to overcome the Coulomb barrier. In the core of a star, this isn't an issue: the immense gravity of a star increases the pressure in the core until fusion reactions start to occur. Once fusion starts to release energy, the inwards pressure due to gravity is balanced by an opposing pressure from the higher-temperature core and an equilibrium is reached. In the centre of our sun, stellar fusion occurs around a pressure of 2.6×10^{11} atm, and it produces only about $0.3\mathrm{kW\,m^{-3}}$. To put these numbers in perspective, the kinetic energy-per-unit-volume associated with the pressure is similar to the detonation of a thermonuclear weapon, while the power-per-unit-volume is roughly equivalent to a compost heap[1]. Evidently, without the tremendous pressure and size of the sun, stellar fusion is not a practical energy source.

Thankfully, we can cheat a little. In 1934, an (Australian!) physicist Mark Oliphant reported that firing Deuterium ions into a Deuterium target produced an "enormous effect" – a much higher rate of nuclear reactions than similar tests using normal protons [4]. By changing the fuel, the thermonuclear fusion rate could be boosted enormously, and further still by increasing the temperature beyond the temperature in the Sun. The effect of this is remarkable – in the ITER reactor (under construction), the power density will be $500\,\mathrm{MW}/840\,\mathrm{m}^3 = 600\,\mathrm{kW\,m^{-3}}$ at a core pressure of only $10^{20}\mathrm{m}^{-3} \times 15\,\mathrm{keV} = 2.4\,\mathrm{atm}$ – 2000× more power-per-volume, at a pressure (and energy density) $10^{11}\times$ lower. This is excellent news! Instead of having an energy density similar to a thermonuclear weapon, the ITER plasma has only $360\,\mathrm{kJ\,m^{-3}}$. This is the same as the potential energy density of water at a height of 35 m, which is pretty manageable. Therefore, saying that the goal of fusion research is to "put a star in a bottle" is somewhat misleading. In a fusion reactor, we're putting much less energy into the fuel and getting far more energy out in return.

As well as improving the safety of fusion reactors, the low energy density means that – perhaps surprisingly – heating the plasma isn't the biggest challenge in fusion (not to say that it is trivial, but at least that temperatures in excess of 150 million Kelvin are readily attainable). Instead, the main challenge is *energy confinement* – keeping the energy in the hot plasma for long enough that it can heat more fuel, to achieve a self-sustaining reaction. This is, in a way, similar to lighting a fire on a windy day – the energy available in a match is more than sufficient to light a fire on a calm day. However, if the wind spreads the heat quickly, either you won't burn anything other than matches, or maybe you can burn part of the wood, but it won't catch to the surrounding fuel. As such, when we talk about achieving fusion, we don't really mean burning some D-T fuel[2], but rather gaining energy from the fusion reaction. *Break-even* ($Q = 1$) means that the fusion reaction is producing as much energy as was supplied to it – that we're getting as much heat from the wood as we are from burning matches. *Ignition* ($Q = \infty$) means that the fusion reaction is completely self-heating – that we put away our matchbox, and the fire keeps on going.

We need to keep the heat confined for long enough that the fuel self-heats. In our fire analogy, we need a 'windbreak' – something to reduce how quickly heat is lost from our fuel. The most popular confinement method for fusion is 'magnetic confinement fusion'. Charged particles in a magnetic field are subject to the Lorentz force $F = q\mathbf{v} \times \mathbf{B}$. This leads to free motion along the magnetic field, and circular orbits perpendicular to the magnetic field. If the magnetic

---

[1] There isn't a particularly good reference for this, but a back-of-the-envelope calculation shows that the average power density of the sun's core must be small. As per the power density of a compost heap, the value sounds reasonable (it's not entirely negligible, but not large).

[2] A bench-top device called a 'fusor' can easily achieve D-D fusion. In fact, these devices produce enough fusion neutrons that they can be used as a compact neutron source.

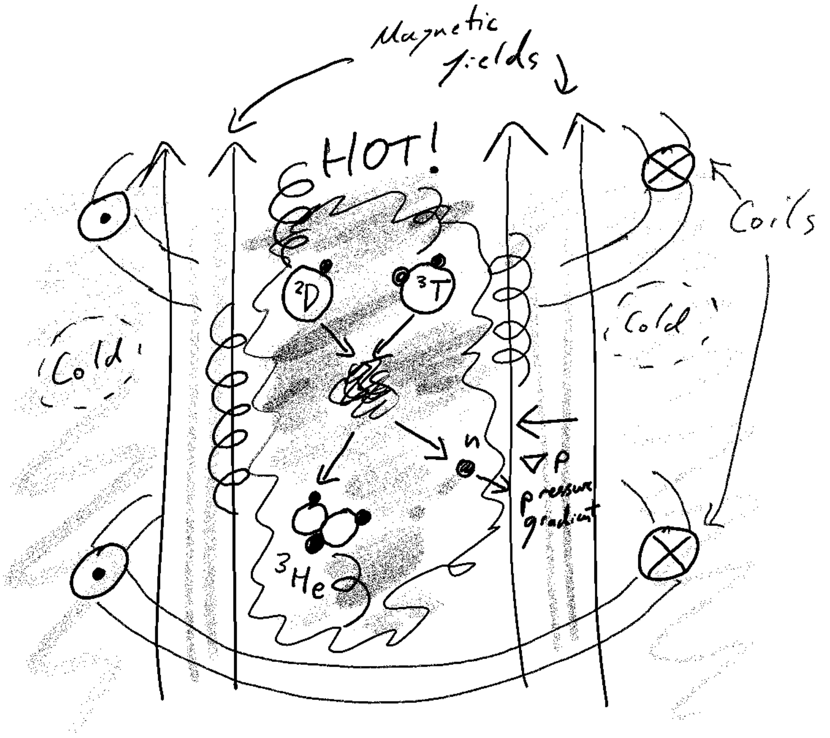

field is strong enough, the Larmor radius $r_L = \frac{mv_\perp}{qB}$ (the radius of the circular orbit) is much smaller than the size of our device. This prevents charged particles from moving across magnetic field-lines. This means that we can support a pressure gradient perpendicular to the magnetic field – we can build a system for confining the fusion plasma, without putting a solid wall anywhere near it. Since the plasma will be significantly hotter than the melting point of all known materials, being able to confine the plasma at a distance is a great advantage.

Since $\nabla \cdot \mathbf{B} = 0$ (no magnetic monopoles), magnetic field-lines are always closed loops. The simplest topology which can be constructed from magnetic field-lines and which is always perpendicular to some volume is a torus, and modern magnetic confinement fusion devices are topologically toroidal. However, a simple toroidal magnetic field is not sufficient to confine the plasma. In an idealised infinitely-long straight solenoid, the magnetic field is homogenous. However, if you bend a solenoid into a ring to make a toroidal field, then the coils are packed more closely towards the axis of rotational symmetry. This leads to a non-homogenous magnetic field – roughly, the toroidal field varies as $B_\phi \simeq B_0 \times R_0/R$. Additionally, since the magnetic field is now curved, particles are subjected to a centripetal force. Both the ∇B and centripetal forces lead to a vertical particle drift. Electrons and ions drift in different directions, which causes a charge separation and an electric field, in turn causing an outwards $E \times B$ drift. As such, a purely toroidal field also cannot confine a plasma. To counteract the charge separation, we can add a poloidal component to the magnetic field, giving a helical magnetic field. This helps to counteract the vertical drifts in two ways. Firstly, the vertical drift mostly cancels over a poloidal orbit – the drift is always in the same direction, but this is either towards or away from

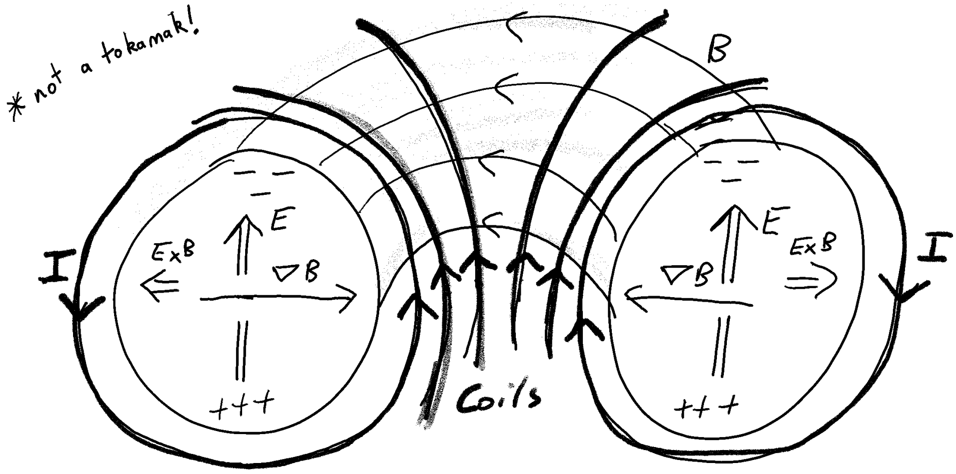

the magnetic surface depending on whether the particle is above or below the magnetic axis [5]. Additionally, the magnetic field-lines in a helical field typically traverse toroidal surfaces[3], and as such the top and bottom halves of a flux surface are magnetically connected. Since particles and therefore currents can flow quickly along the magnetic field, large charge imbalances can't form (due to the Pfirsch-Schlüter current) – and so the loss-of-confinement due to the large-scale $E \times B$-drift is avoided.

Unlike the toroidal field which can be generated with external coils, the poloidal field is not so straightforward to generate. In a purely toroidal system, the poloidal field needs to be generated via a current inside the plasma volume. We can't use wires for this (they'd melt immediately). Instead, since the plasma itself is conductive, we can ramp the current in a central solenoid – which leads to a time-varying magnetic field through the central solenoid, an induced electric field and current in the plasma, and a poloidal magnetic field. Alternatively, to avoid pulsed operation we can use 'non-Ohmic current drive'. Generating the poloidal magnetic field via the plasma current is the basis for 'tokamak' devices. Another approach is to generate the poloidal field with external coils, which requires breaking the rotational symmetry. This approach is used in 'stellarator' devices. Comparing the two, tokamaks are simpler to design and construct, and enjoy improved confinement due to their rotational symmetry, while stellarators are less susceptible to current-driven instabilities and are easier to operate in steady-state conditions [6].

With our magnetic confinement "windbreak" in place, what is needed to reach a self-sustaining burning fuel? The condition for ignition is famously summed up in the 'fusion-triple-product', which can be determined by balancing the α-heating rate with the power-loss rate [7]

$$n_i T_i \tau_E \gtrsim 2.6 \times 10^{21}\,\mathrm{m}^{-3}\,\mathrm{s}\,\mathrm{keV} \tag{0.1}$$

for the DT fusion reaction for $T_i \sim 15\,\mathrm{keV}$, for n_i, T_i and τ_E the ion density, ion temperature and energy confinement time respectively. The energy confinement time is a measure of how good

---

[3] Field-lines typically don't arrive back in the same place after completing a toroidal revolution. An exception to this is 'resonant surfaces', which are less stable than other magnetic surfaces.

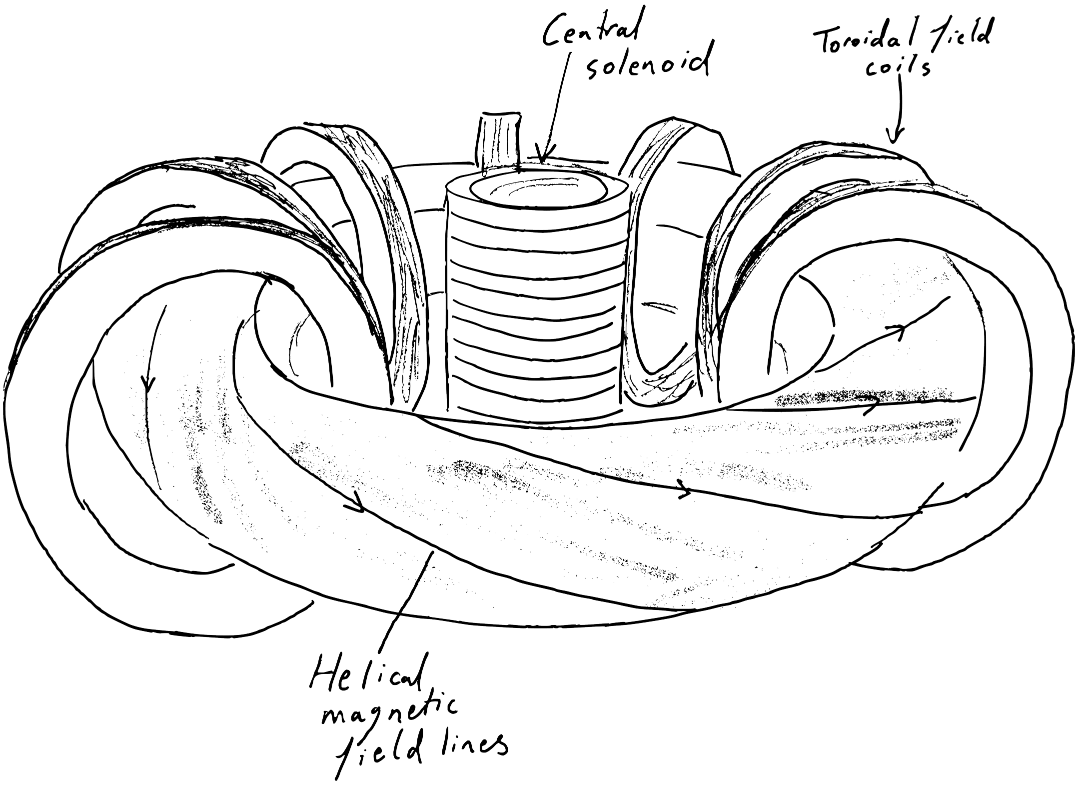

our windbreak is – the power loss rate P_{loss} is assumed to be proportional to the plasma energy density $W = \frac{3}{2}(n_D + n_T)T_i$, with an exponential decay factor τ_E, such that $\frac{\partial W}{\partial t} = P_{heat} - \frac{W}{\tau_E}$.

Remarkably, in the period after the results from the T3 tokamak were released (in 1968), the highest-achieved fusion-triple-product grew *exponentially* up until 1997, when the JET tokamak achieved the highest-recorded energy gain factor of $Q \approx 0.67$ – that is, the total fusion power was 67% of the 24 MW external heating [8]. In 1998, on the JT-60U tokamak, a record $1.53 \times 10^{21}\,\mathrm{m^{-3}\,s\,keV}$ was achieved for the fusion-triple-product – enough that, if DT was used as the fuel, the shot would have achieved $Q = 1.25$ (i.e. it would have exceeded break-even) [9]. Unfortunately, in the quarter-century since, the exponential increase in fusion-triple-product has not continued. Much of the research effort was focused on the design of the ITER tokamak, which suffered several delays [8]. In the last few years, however, fusion research has regained its optimism. ITER construction is well underway and should be completed in 2025 [10], the JT-60SA tokamak has just been completed [11], and the stellarator and inertial-confinement fusion-triple-product records have both been broken, by Wendelstein 7X [12, 13] and NIF (as this thesis was being written) respectively. In addition to the recent advances of publicly-funded fusion research, a number of privately-funded startups have also joined the effort. These range from the esoteric, to high-field tokamaks such as ARC or ST40 which, although ambitious, are based on fairly well-established physics. With so many new devices joining the research effort, we might very well be standing on the brink of break-even, ignition and the commercial application of fusion. The fusion era could well be just about to begin.

1. Introduction

> Our children will enjoy in their homes electrical energy too cheap to meter… Transmutation of the elements, unlimited power, ability to investigate the working of living cells by tracer atoms, the secret of photosynthesis about to be uncovered, these and a host of other results, all in about fifteen short years. It is not too much to expect that our children will know of great periodic famines in the world only as matters of history, will travel effortlessly over the seas and under them and through the air with a minimum of danger and at great speeds, and will experience a life span far longer than ours, as disease yields and man comes to understand what causes him to age.
>
> *(L. Strauss, 1954)*

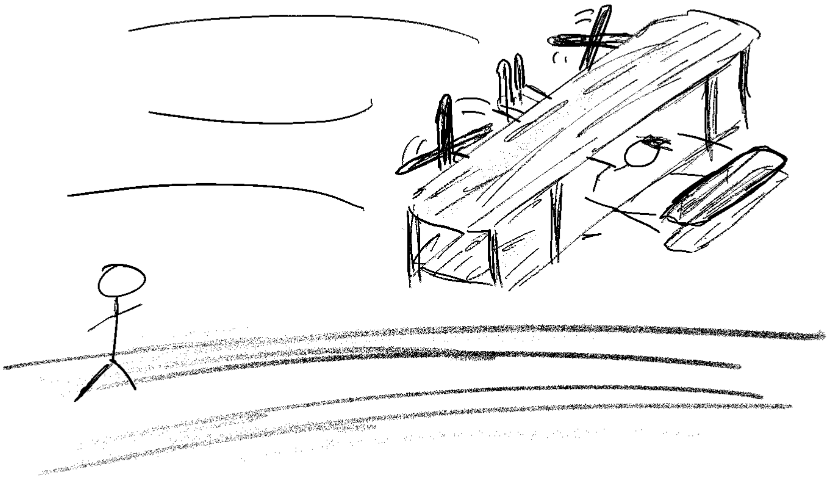

Nuclear fusion is on the edge of a breakthrough. In the next few years – most likely 2035 [10] – a fusion reactor will achieve thermal breakeven, where more energy is produced from fusion reactions than the heating energy provided to the plasma. This achievement will be more symbolic than practical: achieving break-even is sometimes compared to the Wright Brother's first powered flight in 1903 [14]. The 59 second, 260 metre flight was of little practical use, but it signified the possibility of powered flight and started the rapid development of aviation. Remarkably, the first flight across the English Channel was completed just 6 years later [15].

For fusion, break-even won't be enough for a viable reactor – it won't even produce enough energy to power the heating and auxiliary systems. Nevertheless, break-even will mean that – if we hide away all of the inefficiencies and support systems – for the first time, fusion on earth will produce a net energy gain. In that moment, fusion will no longer be just an experiment, but potentially a real source of electricity.

1.1. Fusion for energy

Once fusion achieves break-even, the next challenge will be to develop fusion into a commercially-viable source of electricity. This will be far more difficult than the technological challenge of achieving break-even. Firstly, a power reactor will need much higher energy gain factors – at least $Q = 5$ before the plasma is mostly self-heating (or 'burning'), and – for a tokamak like ITER – around $Q \sim 10$ before the electricity produced from fusion is enough to run the heating systems, the magnets and other 'balance-of-plant' electrical requirements (see p164 of reference [16]). Looking at the fusion triple product, to increase Q, we can increase either the density and temperature in the core – increasing the power output, but also increasing the power reaching the walls – or increase τ_E, requiring us to tame the zoo of plasma instabilities that cause the plasma to escape confinement. Next, we will need to design and operate the reactor in such a way that the cost of fusion electricity – at least eventually [17] – is competitive with contemporary sources. Very approximately – we can write the cost of electricity from fusion as[1]

$$€/\mathrm{kW\,h} = \frac{\text{build cost} + \text{maintenance cost}}{\text{total electrical production over lifetime}} \tag{1.1}$$

We therefore can reduce the cost of electricity by increasing the total electrical production – by reducing the amount of time that the reactor is shut-down or increasing the total power produced. Alternatively, we can reduce the build cost and maintenance cost – such as by using a smaller, simpler design, or replacing the divertor less frequently. Another option is to increase the lifetime of the reactor – since approximately 60% of the cost of electricity is the outright build cost, if we can use the same reactor for longer, it can produce more electricity and ultimately be more economically viable. A third challenge is reliability – how often will the reactor be shut down, either for maintenance or due to off-normal events? This partly affects the cost of electricity: the more time the reactor is shut down, the less total electricity it produces, and the higher the total cost of electricity. In addition to this, if fusion reactors require long maintenance periods or frequently suffer unexpected shutdowns, they become less desirable for producing baseload electricity.

These three coupled requirements – high energy gain, low cost-of-electricity and high reliability – present a complex integration problem. If we optimise a single aspect – say energy gain factor by increasing the core power – this can degrade the other factors – a high core power can lead to rapid degradation of the divertor, increasing the maintenance cost and reducing the availability.

---

[1] This is a simplification of equation 1 in reference [18]. From table 1 of reference [18], the build cost is estimated at 58% of the total cost, and the material cost of replacing components is 23%. An additional 17% is for 'maintenance and operations'; if we allocate half of that to 'maintenance cost' then 90% of the cost of fusion electricity is covered by our simple equation.

As such, while such optimisations are important, the most exciting developments are ones that simultaneously improve all three aspects. These are the 'breakthroughs' – which give rapid rather than steady progress. A recent example of this is the prospect of using high-temperature superconductors as a breakthrough technology, which led to both excitement and heated debate [19, 20, 21]. It's interesting to consider how one design – the ARC reactor [22] – explicitly highlighted that it was aiming to provide an integrated solution: the announcement paper states that the design would aim to reduce the cost ('affordable'), improve the reliability ('robust') and produce net electrical energy (unfortunately, the 'C' stands for compact). Before we connect fusion reactors to the grid there will be several challenges that we need to overcome, but we're close enough that fusion as a practical energy source might be just a breakthrough away.

1.2. The Edge and Divertor

No fusion reactions occur in the edge of a fusion reactor, but in many ways, the edge is more important than the core when it comes to building economically viable fusion reactors. It is in this region that we find some of the most pressing challenges for magnetic fusion, exotic plasma behaviour leading to remarkable improvements in plasma confinement, and also some of our widest conceptual gaps in understanding and controlling fusion plasmas [23]. This makes the edge promising ground for searching for breakthroughs – the combination of being vitally important and not fully understood means that we could find significant improvements available at accessible parameters which we simply haven't discovered yet. In this section, we will explain why the edge and divertor are important for fusion, and in the next, we will introduce current research directions.

1.2.1. The Heat Exhaust Problem

Outside the separatrix, our star meets metal[2]. A natural question to ask is: "Won't the walls melt?" To answer this crucial question, we need to consider how heat is transported out of the reactor. In steady-state conditions, the sum of the injected (heating) power and fusion power will be balanced by an equal power exhaust. We know that 80% of the fusion thermal power will be carried out of the plasma by neutrons [3], while the remaining 20% of the fusion power plus the injected power will stay in the plasma. Of the power remaining in the plasma, some fraction will be converted to radiation (photons) and lost to the walls, while the remainder will be transported across magnetic field-lines and eventually reach the last closed flux surface. For ITER, the combined neutron and photon flux to the walls will result in a heat flux on the order of a few $\mathrm{MW\,m^{-2}}$ [24, 25], which is already challenging. However, the 'directed' plasma heat flux will be even more challenging. Once plasma crosses the last closed flux surface it can stream quickly along the magnetic field to the walls, while the confining magnetic field prevents the plasma from spreading across magnetic field-lines. As a result, the plasma reaches the walls on a narrow ring near the separatrix, resulting in a large power-per-unit-area. This can lead to

---

[2] In the prelude, we showed how a fusion plasma is not like the sun's core. However, the edge plasma is arguably not that different from the photosphere (which has a temperature of $T \sim 0.5\,\mathrm{eV}$ and a density of $n \sim 10^{21}\mathrm{m}^{-3}$).

erosion of the wall material and pollution of the core plasma [26], and even localised melting (particularly during transients) [27].

The ITER divertor is being designed to handle a steady-state directed heat flux of $\sim 10\,\mathrm{MW\,m^{-2}}$ [27]. To try to put that number into context, this is similar to the heat flux on the heat shield of a spacecraft on atmospheric reentry [28]. However, unlike a spacecraft heat shield, the divertor targets must survive these heat fluxes for years, not minutes, with high neutron and particle fluences [29, 20], and with minimal particle sputtering from the surface [26] (i.e. an 'ablative' heat shield is not an option). Because of this, the divertor will need to be replaced throughout the lifetime of the reactor, and the operating conditions of the reactor will need to be constrained to minimise degradation of the divertor. If we could improve our understanding and control of the edge plasma and divertor heat flux, we could potentially build power-producing reactors with a lower maintenance cost, less downtime and with a larger operating window – which would ultimately help to improve the reliability and competitiveness of fusion energy.

1.2.2. The Divertor and H-mode

Since the plasma exhaust will stream along magnetic field-lines, we can use shaping coils to divert the directed heat flux towards specialised heat-tolerant targets. The magnetic field configuration is called a 'divertor configuration', which is compared to a simpler limiter configuration in figure 1.1. Additional poloidal field coils are used to introduce a poloidal field null called an 'X-point', which lies on a flux surface called the 'separatrix' which separates the confined region from the 'open field-line region'[3]. The 'divertor' can refer to both the wall component which absorbs the directed heat flux and the volume beyond the X-point – we will use 'divertor targets' for the former and 'divertor region' or 'divertor' for the latter, as indicated in figure 1.2.

Diverted configurations have several benefits over simpler limited configurations [31]. One key advantage is that we can move plasma-wall interactions away from the core, reducing the amount of tungsten reaching the core [26, 31]. This leads to lower radiative losses from the core, increasing the energy confinement time and therefore the energy gain factor. We can also design the divertor targets to handle extreme heat fluxes. For example, the ITER design (shown in figure 1.3) uses actively-cooled tungsten monoblocks [32]. The targets will be tilted such that the directed heat flux intersects at an angle of $\sim 1^\circ$, increasing the area over which the heat is deposited [27]. As a further defence against localised overheating the divertor targets, the divertor coil current can be ramped to sweep the strike-point position over time [33]. Divertors are also useful for particle exhaust: the neutral pressure can be increased by enclosing the divertor volume, which in turn increases how effectively the pumps work [31]. These benefits come at an economic cost (especially for 'alternative' divertors [34] – discussed later) – the divertor uses up volume inside the toroidal field coils – so a divertor configuration will have either a smaller core (less power) or need larger toroidal field coils (more cost) when compared to

---

[3] The 'separatrix' extends into the divertor region while the 'last closed flux surface' borders the confined region only – around the confined region they are equivalent. 'Open' field-lines is a misnomer – there are no known open magnetic field-lines in the universe [30]. Here, 'open' means field-lines that connect to the divertor targets.

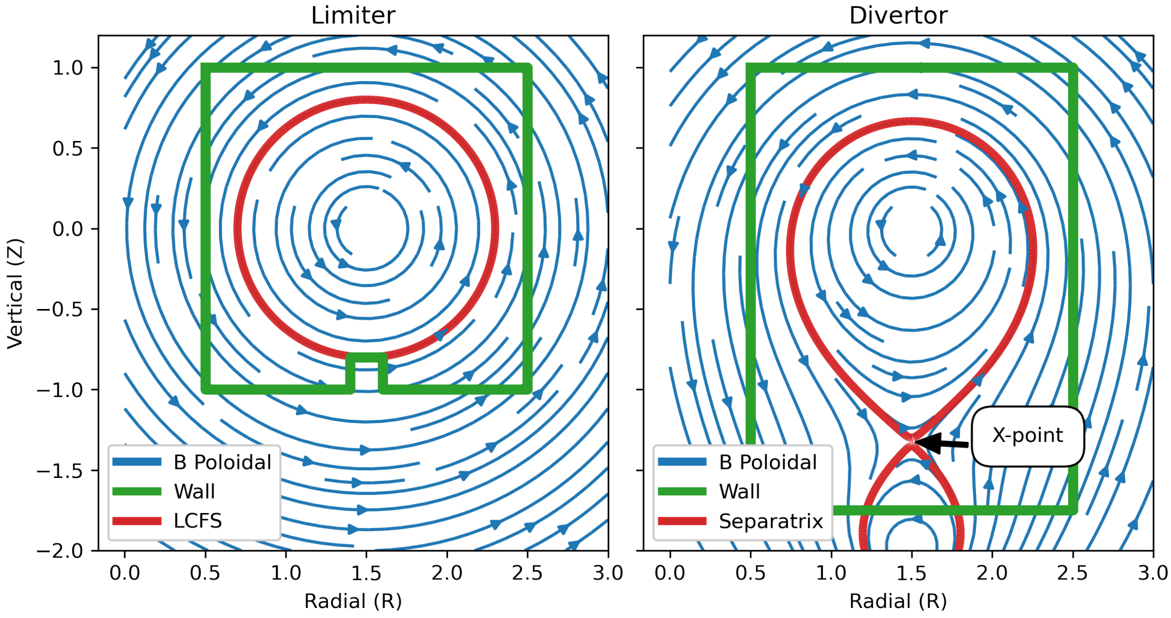

Figure 1.1.: In limiter configurations, the plasma impacts whichever part of the wall extends furthest into the plasma. The confined region is bounded by a last closed flux surface (LCFS). In tokamak divertor configurations, an additional external coil is added, which carries a current in the same direction as the plasma current. The poloidal field cancels at a poloidal field null, which is called the ‘X-point’. The flux surface which comes vanishingly close to the X-point is called the separatrix since it separates the confined region and the ‘open field-line region’ (the region where magnetic field-lines intersect the wall). In `two-wire-divertor.ipynb`, you can play around with Ampère’s law $\oint \boldsymbol{B} \cdot d\boldsymbol{l} = \mu_0 I_{enc}$ and superposition to see how to make various magnetic configurations in the large-aspect-ratio limit.

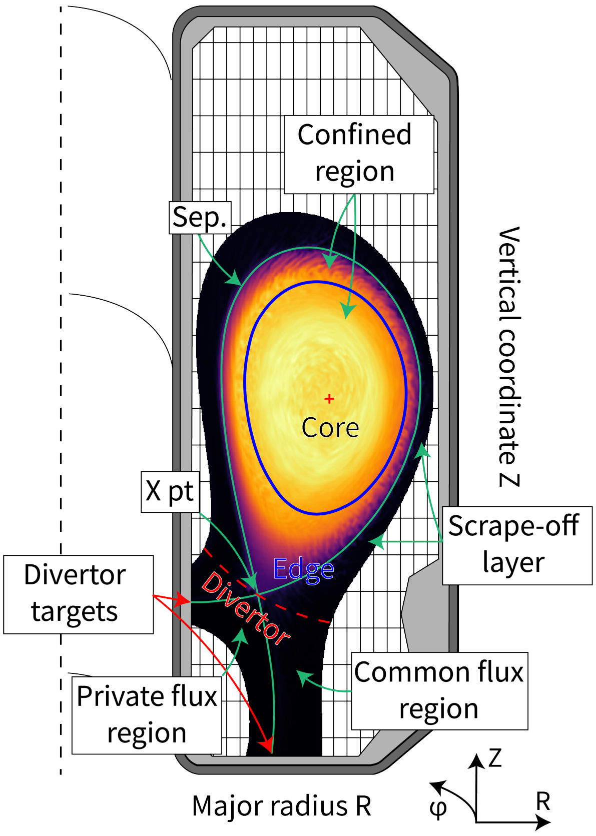

Figure 1.2.: A poloidal cross-section of TCV, showing some of the important regions of a tokamak. The green line is the separatrix, which separates the confined region from the open field-line region. We loosely divide the open field-line region at the X-point, with the scrape-off-layer (SOL) above the X-point and the divertor region below. We will further divide the divertor region into the common-flux region (CFR), which is magnetically connected to the SOL, and the private-flux region (PFR). Inside the confined region, we consider the outermost flux surfaces to be part of the edge (i.e. outside the blue surface), while flux surfaces further inside are called the core. The terminology here is not standardised: often the 'edge' excludes the open field-line region, and SOL often includes the CFR (including, at points, in this thesis).

Figure 1.3.: The ITER divertor, reproduced from reference [27].

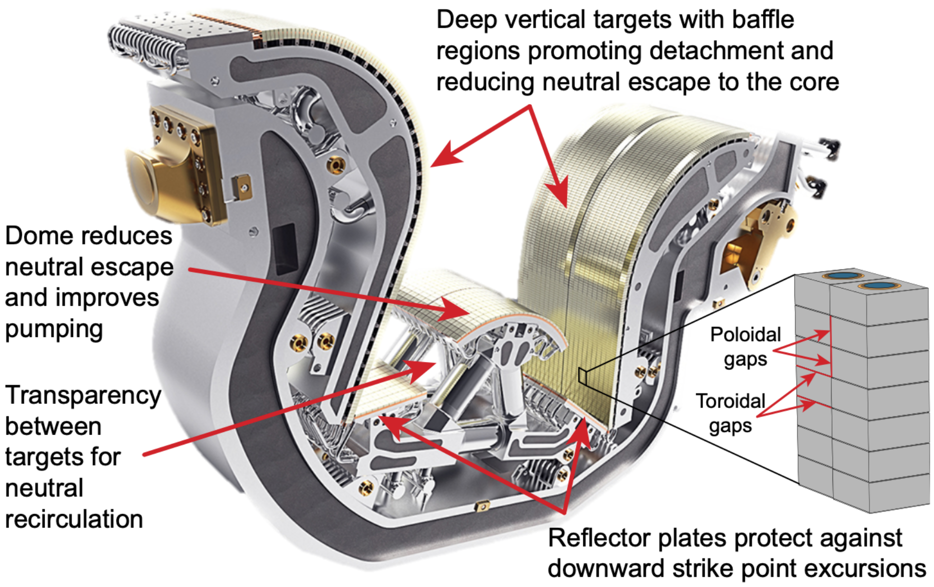

a limiter configuration. Nevertheless, the advantages of divertors justify their use in almost all fusion devices, including ITER [27], ASDEX-Upgrade [35], JET [36], TCV [37], MAST-Upgrade [38] and even the Wendelstein-7X stellarator [39, 13].

In diverted configurations, we can reduce the directed heat flux before it reaches the targets. Part of the benefit comes from the magnetic geometry itself: we can move the divertor targets to a larger major radius to increase their area, increase the flux expansion at the targets, or increase the cross-field transport (by increasing the parallel connection length, and potentially by increasing the flux expansion around the X-point [40, 41]). We also can intentionally inject gas (including fuel gas and 'seed' impurities such as neon, nitrogen and argon) into the divertor volume [42] with less impact on the core plasma performance (compared to using a limiter) since the divertor has improved confinement of neutrals and impurities. Neutrals and impurities can convert part of the directed heat flux into radiation, which is deposited over a larger area. For strong seeding conditions, the plasma can 'detach' – the plasma is radiatively cooled until it recombines before reaching the targets [43, 44, 45] – greatly reducing the heat flux to the divertor targets.

Diverted discharges are also associated with the 'high-confinement' or H-mode [23]. H-mode was discovered in diverted ASDEX experiments in 1982 [46], and has since been reproduced on several other machines (including in limited discharges, although it is still easier to access H-mode in diverted discharges [47]). Of all the breakthroughs in fusion, H-mode was one of the most surprising – 25 years after its discovery, Fritz Wagner quoted Nietzsche to describe the discovery of H-mode: "Das Wesentliche an jeder Erfindung tut der Zufall" or "the essence of all innovation is chance" [48]. Above a certain heating power, it was observed that the confinement and the energy content in the plasma improved dramatically – which increases the whole core profile, as though it were lifted onto a 'pedestal'. The H-mode is associated with a strong suppression of turbulence in the edge due to strong shearing of poloidal rotation in the edge [49], leading to very steep edge gradients [50] – although the exact mechanism which leads to the transition to and from the low-confinement mode is still being researched [51, 52, 53]. H-mode is not without its challenges (see next section), but it is estimated that power-producing fusion reactors would cost ~ 2.5× more if operated without H-mode [48].

1.3. Research questions in the edge

There are still many open questions regarding the processes and properties of the edge, especially when extrapolating to future devices. For instance, there is considerable uncertainty regarding how wide the directed heat flux channel will be for ITER (see section 3.1.2 of reference [27]). In Eich et al., 2013 [54], infrared measurements of the outer-target heat flux profiles were parametrised by a 'heat flux decay length' λ_q (roughly giving the heat transport into the SOL above the divertor) and a 'spreading factor' S (an effective cross-field diffusion in the divertor). By combining measurements from ELM-free attached discharges on JET, DIII-D, AUG, Alcator C-mod, NSTX and MAST, a strong $\lambda_q \propto 1/B_{pol,OMP}$ relationship was observed – which gives $\lambda_q = 1\,\mathrm{mm}$ when extrapolating to the ITER $Q = 10$ scenario with $B_{pol,OMP} = 1.2\,\mathrm{T}$.

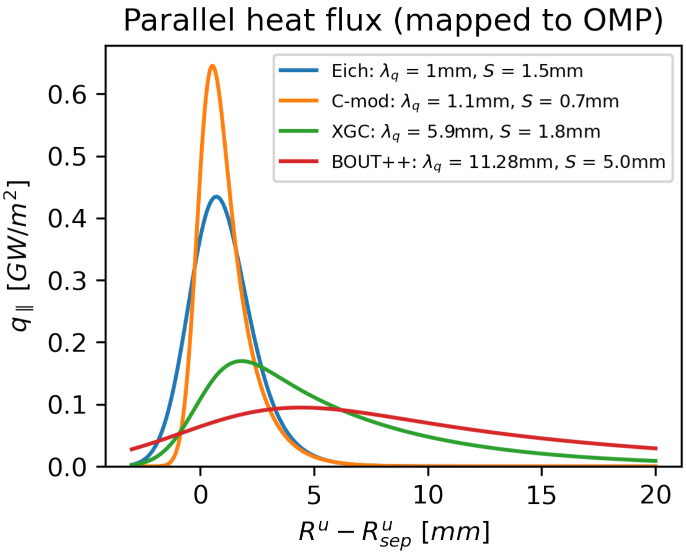

Figure 1.4.: A 'back-of-the-envelope' estimate for how the parallel heat flux density will vary for different values of λ_q and S (see reference [54]), given in `eich_fit.ipynb`. We estimate the area under each Eich profile and then normalize each profile to give the same heat flux (100 MW, although our method is only suitable for determining relative and not absolute values). The cases show the estimated parallel heat flux for the ITER $Q = 10$ scenario, mapped to the outboard midplane for the Eich scaling [54], Alcator C-Mod measurements at high B_{pol} [55], XGC [56] and BOUT++ turbulence simulations [57].

A loose correlation between λ_q and S was also seen, although it was reasoned that S is probably determined by the exact geometry of the divertor and as such the spreading factor might be $S \approx 1.5$ mm or larger [54]. Since this result was published, a series of high $B_{pol,OMP}$ discharges were performed on Alcator C-Mod [55], giving $\lambda_q = 1$ mm and $S = 0.7$ mm at $B_{pol,OMP} = 1.2$ T. By contrast, gyrokinetic modelling by XGC found $\lambda_q = 5.9$ mm and $S = 1.8$ mm for the ITER $Q = 10$ scenario [56] while also reproducing λ_q on the high $B_{pol,OMP}$ Alcator C-Mod measurements [58], and fluid modelling by BOUT++ found $\lambda_q = 11.28$ mm and $S = 5.9$ mm [57]. The effect of these different values is estimated in figure 1.4 – where we see that the XGC prediction would give a ~ 2.5× lower peak heat flux than the Eich scaling, while the peak heat flux would be ~ 4.5× lower than the Eich scaling for BOUT++ and 1.5× higher if we directly used the Alcator C-Mod result. The differences appear to be due to a shift from drift-dominated cross-field transport (the Eich result was reproduced in SOLPS with drifts activated and with a very low anomalous transport coefficient [59], or by the Goldston model [60]) to turbulence-dominated cross-field transport (trapped-electron-mode turbulence in XGC and ballooning instabilities in the pedestal in BOUT++). However, with only a few turbulence models able to simulate the edge of ITER, it is difficult to independently confirm these results, and as such, there is significant uncertainty as per what the peak heat flux will be[4]. For ITER, the range of peak heat flux values can be managed by increasing the divertor neutral pressure [27]. However, if the Eich scaling is confirmed for ITER, this will probably mean that an ITER-like divertor will not be able to handle the heat exhaust in a power-producing reactor

---

[4] The results discussed here focus on attached discharges, but ITER will be operated under partially- or fully-detached conditions (see [43] for terminology). In reference [61] a new scaling including high-density discharges is proposed.

[62].

In case the ITER lower-single-null divertor will not scale to DEMO or power-producing reactors, solutions with improved heat-flux handling are being explored. The power-handling capability and compatibility with detachment of different alternative divertor configurations (ADCs) is being studied both via modelling and experiment [63, 64, 62], to identify candidates to test in the Divertor Test Tokamak [65]. These ADCs use additional shaping coils to introduce additional poloidal-field-nulls (X-points) – giving a 'snowflake' if the secondary X-point is close to the primary X-point [66], an 'X-divertor' if the secondary X-point is close to the target [67] (or Super-X if the targets are also moved to a larger radius [68]) or a 'double-null' if the secondary X-point is on the opposite side of the magnetic axis [69]. The use of a liquid-metal divertor is also being explored as a possible way to extend the allowable heat flux to the targets [70, 71, 72]. A third option might be the use of strong neutral and impurity seeding in the divertor to promote complete detachment[5]. This has to be balanced against the risk of 'density-limit' disruptions – which may follow from the detachment front reaching the X-point and forming a MARFE [73, 74, 43]. However, recent research suggests that it is possible to control an X-point radiator via active feedback, resulting in greatly reduced steady-state and transient heat fluxes to the targets [75, 76].

Another open research question is how to handle transient heat fluxes due to edge localised modes (ELMs) and disruptions[6]. In H-mode the pedestal gradients steepen continuously until a magnetohydrodynamic instability called an ELM is triggered. This causes the edge pressure gradient to collapse and ejects a large amount of the energy stored in the edge over a short amount of time $0.1 - 1\,\mathrm{ms}$ [79, 80, 23]. For the ITER $Q = 10$ scenario, large 'Type-I' ELMs could cause melting of the divertor [27] and as such will need to be mitigated or avoided entirely. To prevent large ELMs, there is research into using resonant magnetic perturbation coils [81, 82], 'ELM-pacing' through pellet injection [83] or ELM-free improved-confinement modes such as the quiescent-H-mode [84], EDA H-mode [85] or I-mode [86, 87]. Current research explores how ELM mitigation or avoidance can be combined with good core confinement and manageable steady-state heat fluxes, and what causes plasmas to transition to and from improved confinement regimes [52, 53, 51].

1.4. Turbulence and complexity

To understand the edge, we need to understand the many physical processes which occur there and how they interact. Although we have conceptual models for many of the individual processes in the edge – several of which are indicated in figure 1.5 –, their interactions can lead to *complex behaviour*[7] such as chaos (sensitivity to initial conditions), emergence (exhibiting dynamics not present in the isolated subsystems), strongly non-linear system responses and self-organisation. To capture these dynamics we need to understand not just individual processes, but also the

---

[5] See reference [43] for a good review on detachment.

[6] Disruptions are a loss of plasma control, which leads to most or all of the stored plasma energy being lost to the walls. For an introduction, see references [77, 78, 23].

[7] See *Complexity Explained* (doi:10.17605/OSF.IO/TQGNW, complexityexplained.github.io).

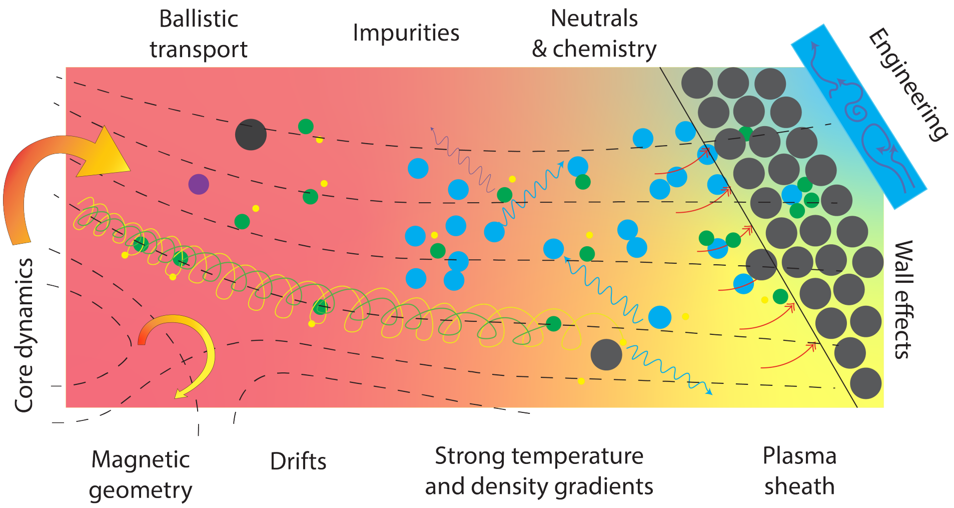

Figure 1.5.: The edge is host to several interacting physical processes, which occur over different spatial and time-scales. These include sources of energy and plasma from the confined region, the turbulent flow of plasma along and across magnetic field lines, the flux expansion and magnetic geometry of the divertor configuration, plasma drifts driven by large-scale electric field, ionisation, charge exchange and recombination reactions between plasma, neutrals and impurities, neutral and plasma chemistry, and the dynamics of the plasma sheath which forms in front of the solid targets.

dynamics of the edge as a whole.

One of the most important processes to model is the turbulent nature of the plasma flow since turbulence and background drifts drive most of the cross-field transport in the edge. Turbulence refers to a type of fluid flow where energy is transferred between fluid vortices at different spatial scales. These vortices can then interact, leading to complex behaviour which makes turbulence notoriously difficult to treat analytically[8]. In fusion plasmas, turbulence is mostly driven by small-scale instabilities which extract energy from the pressure gradient, several of which are summarised in table 1.1. Unlike other plasma instabilities, pressure-driven instabilities tend to be self-stabilising: turbulent cross-field transport leads to a flattening of the pressure gradient which in turn reduces the energy available for driving turbulence. Therefore, instead of continuously growing, pressure-driven instabilities can be dynamically balanced, providing the sustained energy injection necessary for the development of saturated turbulence. Since turbulence is characterised by the interactions of fluid vortices across a wide range of spatial scales, direct numerical turbulence simulations need to capture both large and fine-scale structures and as such are typically very computationally expensive [90]. Currently, the majority of edge modelling is performed by 'transport' codes [91] such as SOLPS [92, 93], EMC3 [94, 95], UEDGE [96] or SOLEDGE2D [97]. These codes treat turbulence as an effective cross-field diffusion, controlled by heuristic 'anomalous diffusion coefficients' which must be tuned to match

---

[8] Famously, a proof of the existence and smoothness of solutions to the Navier-Stokes equations for neutral fluids is one of the Millennium Prize problems [89].

Name	Drive	Scale	Propagation	Cross-phase
Interchange/resistive ballooning (RBM)	∇p	$> 10\rho_s$	0	$\pi/2$
Kinetic ballooning (KBM)	$\nabla T_{e,i}$	$\sim 10\rho_s$	+	$\pi/2$
Micro-tearing (MTM)	∇T_e	$\sim 10\rho_s$	−	0
Drift-wave (DW)	∇n	$1 - 10\rho_s$	−	0
Ion-temperature gradient (ITG)	∇T_i	$1 - 10\rho_s$	+	> 0
Trapped-electron (TEM)	$\nabla T_e, \nabla n$	$< 10\rho_s$	−	0
Electron-temperature gradient (ETG)	∇T_e	$\ll \rho_s$	−	$\pi/2$

Table 1.1.: Pressure-gradient-driven plasma micro-instabilities responsible for driving turbulence, modified from [88]. Micro-instabilities can be classified according to their drive mechanism, their perpendicular scale length (relative to the sound Larmor radius $\rho_s = \frac{\sqrt{T_e m_i}}{eB}$), their propagation direction (where + and − indicate the ion and electron diamagnetic directions respectively), and the cross phase between the pressure and electrostatic potential perturbations. Most pressure-driven instabilities occur at spatial scales around ρ_s or larger, except for the electron-temperature gradient mode. For a discussion of the physical mechanisms behind these instabilities, see chapter 4 of reference [88].

experimental measurements or expected results[9]. By treating turbulence diffusively, transport models are able to greatly reduce the computational cost of simulations compared to direct numerical simulations of turbulence – which in turn permits the evaluation of large multiphysics models able to capture many other processes in the edge. However, for predictive simulations or for fusion devices with limited diagnostic coverage, the prescription of anomalous diffusion coefficients can introduce significant uncertainty. Beyond this, turbulence can exhibit complex behaviour such as self-organisation and emergence, which cannot be described via diffusion [99]. This is particularly important for describing transport into the far scrape-off-layer, which is dominated by coherent ‘blobs’ [100, 101] which ballistically drive flows in otherwise stable regions. Turbulence can also drive large-scale plasma ‘zonal’ flows which are thought to be responsible for the edge transport barrier in improved confinement regimes [52]. If we want to investigate effects such as filamentary transport or edge transport barriers, or to perform predictive ab-initio simulations, we need models which can simulate turbulence directly.

To model turbulence in the edge and divertor, there are several numerical models which are actively under development – including the gyrokinetic codes XGC [56], COGENT [102], GENE-X [103], Gkeyll [104], ORB5/PICLS [105], GYSELA [106], the gyrofluid code FELTOR [107], and the fluid codes GRILLIX [108, 109], GBS [110, 111], BOUT++ [112], STORM [113], Hermes [114], GDB [115], HESEL [116] and TOKAM3X/SOLEDGE3X [91]. These codes model turbulence self-consistently, capturing the energy injection due to plasma instabilities, the transfer of energy & interactions between vortices at different scales and the dissipation of fluid kinetic energy at small scales. Once these ingredients are in place, complex behaviour such

---

[9] The use of reduced models to estimate anomalous diffusion coefficients is currently being explored [98].

as coherent transport and zonal flows should develop self-consistently, allowing us to directly investigate these effects.

1.5. Motivation and outline

Turbulence simulations are powerful tools for understanding and learning to control the edge. These simulations can capture the drive and development of turbulence, as well as its interaction with other physics such as neutral dynamics, the wall and the magnetic geometry. Compared to directly analysing experimental results, simulations have the advantage of almost limitless diagnostic access which lets us examine the dynamics of the edge in extreme detail, observing the processes and interactions which give rise to complex phenomena in the edge. However, simulations do not (and cannot) reproduce reality exactly. All models require simplifying approximations – especially if we want to reduce the computational cost enough that we can model the entire edge. These assumptions limit the applicability and accuracy of our models. Because of this, before we can use turbulence modelling to interpret and predict the edge, we need to rigorously validate these models against experimental results.

Turbulence models have previously been validated in basic plasma physics devices [117, 118, 119] and limiter configurations [120, 121]. However, there is still a need to rigorously validate turbulence models in divertor geometries[10], even though almost all relevant fusion experiments and all planned fusion reactors use a divertor. There are several reasons why this might be the case. Firstly, compared to limiter geometries, divertor geometries are more difficult to treat numerically since the X-point introduces a coordinate singularity in field-aligned coordinates [122]. Divertor geometries also have more complex dynamics than limiter geometries, both directly due to the magnetic geometry [123, 41, 124] and due to physical processes such as volumetric cooling which become important at lower temperatures [31, 43]. Finally, there are not many existing 'off-the-shelf' datasets of divertor measurements suitable for validating edge turbulence simulations. For validating the basic functionality of the models we need extremely well-diagnosed experimental cases under simple[11] operating conditions, and until turbulence simulations were shown to be able to simulate such experimental cases there was little research interest in collecting such datasets. In this work we close this validation gap, demonstrating that turbulence models are now able to perform realistic simulations of diverted experiments.

In this thesis, we extend the GRILLIX model to perform simulations of realistic divertor geometries and then validate the extended model against a series of dedicated experimental cases,

---

[10] Previous comparisons to diverted experiments have been performed, but these studies did not focus on validating the turbulence models in the divertor. In Chang et al, 2017, λ_q is successfully predicted on NSTX, DIII-D and Alcator C-mod [56], but only a single comparison observable is considered making it difficult to assess how accurately these simulations are reproducing the overall dynamics of the edge. In Riva et al., 2019, GBS is quantitatively validated against outboard midplane measurements from a MAST discharge [121], but only qualitatively compared to target measurements.

[11] Away from operational limits, and without any interesting phenomena such as detachment. Turbulence models *will* need to be validated under such conditions, but for initial tests, it is preferable to valid the models against the simplest-possible cases.

including the first-of-a-kind diverted TCV-X21 validation scenario. We start by implementing a new method for generating simulation grids in arbitrary axisymmetric geometries in section 5.4, which enables simulations in both standard and alternative divertor geometries [125]. We then isolate a numerical issue that prevented simulations of open field-line regions in section 4.5, and implement an immersed boundary method to resolve this issue in section 4.6. These modifications enable simulations across the separatrix of real experiments, using the magnetic geometry from magnetic reconstruction codes. The extended model is used to simulate two experimental cases, and the comparison of the simulated and experimental results is used to assess how accurately GRILLIX simulations are reproducing plasma dynamics in the edge and to suggest further improvements of the GRILLIX model.

The thesis is structured to give a comprehensive introduction to the GRILLIX model and to demonstrate key steps in the rigorous testing of a turbulence model. In part II we focus on introducing and developing the GRILLIX model. In chapter 2, we outline a derivation of the drift-reduced Braginskii fluid model used by GRILLIX, starting from a kinetic description. The derivation is used to highlight where simplifying assumptions are introduced into the model and to discuss where these assumptions may become invalid. Then, in chapter 3, we derive a set of sheath boundary conditions from a simple sheath model, again discussing the limits of applicability of the necessary simplifying assumptions. Together, these chapters form the basis of our *qualification* of the physical model, which helps to assess where the GRILLIX model is applicable and how inaccuracies may be introduced into the simulations. Next, in chapter 4, we show how the physical model is translated into a numerical model. We introduce the locally-field-aligned parallel discretisation method used by GRILLIX and resolve the boundary stencil collapse issue which prevented stable simulations in open field-line regions. We then discuss the *verification* of the numerical model via the Method of Manufactured Solutions (MMS), which ensures that our numerical model corresponds to our physical model. Then, in chapter 5, we introduce a new method that exploits the flexibility of the locally-field-aligned method to enable simulations of realistic diverted magnetic equilibria.

In part III, we validate the extended GRILLIX model. We shortly summarise the key aspects of model testing and the validation-driven development cycle in chapter 6, discussing how model testing can be used as an iterative process for improving the model. We then discuss the results from the ‘X-point’ scenario in the TORPEX basic plasma physics device, published as reference [126], and from the ‘TCV-X21’ scenario, published as reference [2]. We rigorously compare the GRILLIX simulations to the experimental measurements and interpret the results of the comparison to suggest the root cause of observed discrepancies and how the accuracy of the model can be further improved. We also demonstrate how numerical diagnostics can be used to provide an in-depth analysis of the results, focussing in particular on the nature and drive of turbulent transport.

Finally, in part IV, we show how validation-driven development is already being used to test new physics in the GRILLIX model, and discuss additional work towards validated reactor-relevant simulations.

1.6. Further reading

- Ongena et al., 2016, *Magnetic confinement fusion*, doi:10.1038/nphys3745: A compact paper that introduces most of the core aspects of MCF fusion. If you're new to the field or want a big picture overview, this is a great place to start reading.
- Chapman and Walkden, *An overview of shared technical challenges for magnetic and inertial fusion power plant development*, doi:10.1098/rsta.2020.0019: An introduction to the challenges of commercialising either magnetic-confinement or inertial-confinement fusion.
- Wesson, 2011, *Tokamaks*: The go-to textbook covering most aspects of fusion tokamaks.
- Stangeby, 2000, *The plasma boundary of magnetic fusion devices*: This extensive textbook covers a broad range of topics relevant to the edge. Most edge researchers have a well-read copy.
- Pitcher and Stangeby, 1997, *Experimental divertor physics*, doi:10.1088/0741-3335/39/6/001: A more compact (and free!) review of divertor physics.
- Wagner, 2007, *A quarter-century of H-mode studies*, doi:10.1088/0741-3335/49/12B/S01: A review paper covering research into high-confinement regimes, from the researcher who first discovered them.
- Pitts et al., 2019, *Physics basis for the first ITER divertor*, doi:doi.org/10.1016/j.nme.2019.100696: An recent extensive discussion on the status and open research questions regarding the ITER divertor.
- De Domenico et al., 2019, *Complexity Explained*, doi:10.17605/OSF.IO/TQGNW: A short visual introduction to complex systems.
- Manz, 2018, *The microscopic picture of plasma edge turbulence*: in particular, chapter 3 for a clear introduction to 2D turbulent dynamics, and chapter 4 for an explanation of the mechanisms behind pressure-driven plasma micro-instabilities.
- Claessens, 2019, *ITER: The Giant Fusion Reactor: Bringing a Sun to Earth*: A general introduction to the ITER project, which also introduces the broader context and part of the debate about fusion research.

Part II.

Developing GRILLIX for realistic simulations of the tokamak edge

> Predictive capability has emerged as a key goal in magnetic confinement fusion research not just for its special value in designing and operating ever costlier and more complex devices such as ITER and DEMO but, more generally, because its attainment would signify the quantitative maturity in understanding and modelling that is required for success in fusion [127].
>
> *(P. W. Terry, 2008)*

2. The plasma model

Throughout this thesis we will use SI units, except for the temperatures which are expressed as an equivalent energy in electron-volts. Wherever we write T, we implicitly mean $k_B T$ where $k_B = 11\,605\,\mathrm{K\,eV^{-1}}$ is the Boltzmann constant. Note that several plasma physics texts use c.g.s. + eV units. See the NRL plasma formulary for converting between different systems of units.

2.1. What, why, and how? The derivation and qualification of the drift-reduced Braginskii equations

A plasma consists of a large number of charged particles, interacting with each other and with external fields via the electromagnetic force. In a fusion plasma, we can use various conceptual models to describe the dynamics. For much of the plasma volume, collisions are not sufficient to thermalise the energy distribution, and as such we require gyrokinetic or kinetic models. Towards the edge, the collisionality of the plasma increases, and the plasma energy distribution approaches a local thermodynamic equilibrium. In plasma regions with near-thermal-equilibrium, we can use fluid models, which evolve moments of the kinetic equations instead of the kinetic equations themselves. Such fluid models are significantly less computationally expensive to solve, albeit at the price of reduced fidelity.

In this chapter, we derive the set of differential equations – the drift-reduced Braginskii fluid equations – which we use to model the plasma dynamics. This derivation can be found in many references, several of which are listed in the 'Further readings' section at the end of this chapter, and we don't add anything new. Nevertheless, we will present the derivation in full, for two reasons. The first is that it is difficult to understand the final set of equations unless you know where they come from. The second reason is that we use the derivation to highlight the simplifying assumptions used to derive the model and to discuss the limits of their applicability. This is used for the *qualification* of the model, where we determine the conditions under which our model is applicable.

We show how the Braginskii equations can be calculated from *moments* of the kinetic equations with a collisional-magnetised *closure*. We then apply a number of simplifying assumptions and perform a *drift-ordering*, which we use to eliminate high-frequency and small-scale dynamics from the equations. Finally, we derive equations for continuity (2.56), quasineutrality (2.58), momentum-balance (2.60), Ohm's law (2.62), electron temperature (2.67), ion temperature (2.71) and Ampère's law (2.74). If you just want the final equations listed, you can find this in Appendix A. Alternatively, if you want to derive the equations yourself, you can find a list of useful formulas in Appendix B and some of the intermediate steps of the derivations in Appendix C. Important equations will be marked in a box, and key terminology will be written in italics.

2.2. From kinetics to fluids

2.2.1. Moments of the kinetic equations

This section mostly follows the derivation of Fitzpatrick, 2011 and Freidberg, 2014

The dynamics of a charged particle in a magnetic field can be described by the Lorentz force

$$F_{Lorentz} = q(\boldsymbol{E} + \boldsymbol{v} \times \boldsymbol{B}) = m\boldsymbol{a} \tag{2.1}$$

for q, m, $\boldsymbol{v}$, $\boldsymbol{a}$, $\boldsymbol{E}$ and $\boldsymbol{B}$ the particle charge, mass, velocity, acceleration and the electric and magnetic field. In a uniform magnetic field without an electric field, this will result in helical charged particle trajectories which follow magnetic field-lines [3]. For a collection of many particles, we can describe each plasma species with a distribution function $f_\alpha(\boldsymbol{r}, \boldsymbol{v}, t)$, which gives the phase space density of particles. This can be considered as giving the number of particles within some range of velocities $d^3\boldsymbol{v}$, within some range of positions $d^3\boldsymbol{r}$ and at time t. Alternatively, we can integrate over all velocities to find the density for some species α

$$n_\alpha(\boldsymbol{r}, t) = \int f_\alpha(\boldsymbol{r}, \boldsymbol{v}, t) d^3\boldsymbol{v} \tag{2.2}$$

If we ignore processes which can transform particles into other species (i.e. fusion, ionisation, recombination), we can write the evolution of the distribution function in terms of phase space conservation. A further simplification is to separate the electromagnetic fields into a smooth large-scale component and a short-range component corresponding to collisions between particles. This gives the Boltzmann equation

$$\frac{\partial f_\alpha}{\partial t} + \boldsymbol{v} \cdot \nabla f_\alpha + \frac{q_\alpha e}{m_\alpha}(\boldsymbol{E} + \boldsymbol{v} \times \boldsymbol{B}) \cdot \nabla_v f_\alpha = \left(\frac{\partial f_\alpha}{\partial t}\right)_c \tag{2.3}$$

where $\left(\frac{\partial f_\alpha}{\partial t}\right)_c$ is a term which represents the change in the distribution function due to collisions (short-range electromagnetic interactions). This equation is coupled to Maxwell's equations (for the large-scale fields)

$$\nabla \times \boldsymbol{E} = -\frac{\partial \boldsymbol{B}}{\partial t} \tag{2.4}$$

$$\nabla \times \boldsymbol{B} = \mu_0 \boldsymbol{J} + \varepsilon_0 \mu_0 \frac{\partial \boldsymbol{E}}{\partial t} \tag{2.5}$$

$$\nabla \cdot \boldsymbol{E} = \frac{\rho_q}{\varepsilon_0} \tag{2.6}$$

$$\nabla \cdot \boldsymbol{B} = 0 \tag{2.7}$$

with current and charge densities

$$\boldsymbol{j} = \sum_\alpha q_\alpha e \int \boldsymbol{v} f_\alpha d^3\boldsymbol{v} \tag{2.8}$$

$$\rho_q = \sum_\alpha q_\alpha e \int f_\alpha d^3\boldsymbol{v} \tag{2.9}$$

The Maxwell-Boltzmann equations form the basis of kinetic models, which treat small volumes of phase-space statistically. Kinetic models contain only a few robust assumptions, so they should reproduce almost all of the dynamics of a single-particle description of the plasma. However, they are also extremely expensive to solve numerically – and so aren't going to let us model the entire edge. To make simulations of large volumes, we need to make simplifying approximations. One approximation is to treat the fast particle gyromotion as effectively instantaneous and model charged rings rather than gyrating particles, giving the *gyrokinetic* equations. By eliminating the gyromotion, gyrokinetic models can use larger time-steps than kinetic models, and additionally need to treat only two velocity-space dimensions instead of three. These simplifications reduce the computational cost enough that gyrokinetic simulations of the whole plasma edge are currently computationally feasible, albeit still expensive [56].

To further reduce the computational cost, we can compute *moments* of the distribution function, which are velocity-weighted-averages of functions $g(\boldsymbol{v})$, averaged over all velocity space

$$\left\langle g(\boldsymbol{v})\right\rangle = \frac{1}{n_\alpha}\int g(\boldsymbol{v}) f_\alpha d^3\boldsymbol{v} \tag{2.10}$$

The lowest-order moments are of interest since they correspond to quantities with well-understood interpretations and conservation properties. We've already seen the 0th-order moment – the *particle density* n_α, which we can compute by using $g(\boldsymbol{v}) = 1$. The 1st-order moment is the *bulk flow velocity* $\boldsymbol{u}_\alpha$, which we compute using $g(\boldsymbol{v}) = \boldsymbol{v}$. The velocity $\boldsymbol{u}_\alpha$ defines the centre-of-mass frame, where the net momentum of the plasma species is zero. Moving back to a fixed reference frame, the species momentum will be $m_\alpha \boldsymbol{u}_\alpha$. We can use the centre-of-mass frame to separate between a bulk plasma motion at velocity $\boldsymbol{u}_\alpha$, and a random thermal motion $\boldsymbol{w} = \boldsymbol{v} - \boldsymbol{u}_\alpha$ (which has $\langle \boldsymbol{w} \rangle = 0$). This allows us to write the 2^{nd}-order moment in terms of the random kinetic energy, temperature or pressure of the particles. We can write the mean thermal energy of the particles of species α as

$$\varepsilon_\alpha = \frac{1}{2} m_\alpha \left\langle w^2 \right\rangle \tag{2.11}$$

More often, we express the thermal motion as a pressure, which is described in full by the pressure tensor

$$\underline{\underline{\mathbf{P}}} = m_\alpha n_\alpha \left\langle \boldsymbol{w} \otimes \boldsymbol{w} \right\rangle \tag{2.12}$$

$$\text{or by components } \boxed{\left(\underline{\underline{\mathbf{P}}}\right)_{ij} = m_\alpha n_\alpha \left\langle \boldsymbol{w}_i \boldsymbol{w}_j \right\rangle}$$

The pressure tensor can be split into a scalar pressure – equal to the average of the diagonal elements (which are all equal to p_α for an isotropic system)

$$\boxed{p_\alpha = \frac{1}{3} m_\alpha n_\alpha \left\langle w^2 \right\rangle = \frac{1}{3}\,\mathrm{Tr}\,\underline{\underline{\mathbf{P}}}} \tag{2.13}$$

and the anistropic pressure tensor (for $\underline{\underline{\mathbf{I}}}$ the identity tensor), also called the generalised viscosity tensor

$$\boxed{\underline{\underline{\mathbf{\Pi}}}_\alpha = \underline{\underline{\mathbf{P}}}_\alpha - p_\alpha \underline{\underline{\mathbf{I}}}} \tag{2.14}$$

We can also use the scalar pressure to define a temperature, determined from the ideal gas law $p_\alpha = n_\alpha T_\alpha$

$$\boxed{T_\alpha = p_\alpha / n_\alpha} \tag{2.15}$$

We can write the 3rd-order moment, the heat flux due to random thermal motion, as

$$\boldsymbol{q}_\alpha = \frac{1}{2} m_\alpha n_\alpha \left\langle \boldsymbol{w} w^2 \right\rangle \tag{2.16}$$

We can find equations describing the evolution of the moments by taking moments of the Boltzmann equation. Due to the conservation of particles, momentum and energy, we can find conditions on the form of the collision operator. Generally, we treat reactions such as fusion, ionisation, recombination or radiative emission as separate sources or sinks, and only consider elastic collisions in the collision operator. As a result, the collision operator only contributes to frictional momentum transfer $\boldsymbol{R}_\alpha = \sum_\beta \boldsymbol{R}_{\alpha\beta}$ and heat transfer $Q_\alpha = \sum_\beta = Q_{\alpha\beta}$ between unlike species α and β. This lets us write the equations for the moments as

$$\frac{\partial n}{\partial t} + \nabla \cdot (n_\alpha \boldsymbol{u}_\alpha) = \mathcal{S}_{n_\alpha} \tag{2.17}$$

$$m_\alpha n_\alpha \left[\frac{\partial \boldsymbol{u}_\alpha}{\partial t} + \mathbf{u}_\alpha \cdot \nabla \boldsymbol{u}_\alpha \right] - q_\alpha e n_\alpha \left(\boldsymbol{E} + \boldsymbol{u}_\alpha \times \boldsymbol{B} \right) + \nabla \cdot \underline{\underline{\mathbf{P}}}_\alpha = \boldsymbol{R}_\alpha \tag{2.18}$$

$$\frac{3}{2} n_\alpha \left[\frac{\partial T_\alpha}{\partial t} + \mathbf{u}_\alpha \cdot \nabla T_\alpha \right] + \underline{\underline{\mathbf{P}}}_\alpha : \nabla \boldsymbol{u}_\alpha + \nabla \cdot \boldsymbol{q}_\alpha = Q_\alpha + \mathcal{S}_{\varepsilon_\alpha} \tag{2.19}$$

where the terms in the square brackets are advective derivatives $\frac{df}{dt} = \left[\frac{\partial f}{\partial t} + \mathbf{u}_\alpha \cdot \nabla f \right]$, and $\mathcal{S}_{n_\alpha}$ and $\mathcal{S}_{\varepsilon_\alpha}$ are particle and energy sources or sinks. The term $\underline{\underline{\mathbf{P}}}_\alpha : \nabla \boldsymbol{u}$ is a double-inner product, which can be calculated component-wise as $\sum_{i,j} \left(\underline{\underline{\mathbf{P}}}_\alpha \right)_{ij} \frac{\partial (\boldsymbol{u}_\alpha)_j}{\partial x_i}$.

To arrive at the above moment equations from the Maxwell-Boltzmann equations, we didn't make any further assumptions. Although we used terms like 'isotropic' and 'temperature', we can use the definitions of these terms without requiring local thermodynamic equilibrium (we could just as easily have called them something else). However, the equations aren't closed. The $\boldsymbol{q}_\alpha$ term in equation 2.19 is a 3rd-order moment which we haven't yet worked out an equation for, and haven't yet defined expressions for terms like $\boldsymbol{R}_\alpha$ and Q_α. We could, of course, find an equation for any kth-order moment from the Boltzmann equations – but this will, inevitably, depend on the $(k+1)$th-order moment due to the $\boldsymbol{v} \cdot \nabla f_\alpha$ term. To find a finite set of equations we can solve, we need to introduce a closure.

2.2.2. Fluid closure

We can close the moment equations by asymptotically expanding in some small parameter. An example of asymptotic closure is the Chapman-Enskog collisional closure, where the dynamics are expanded in terms of the Knudsen number $\mathrm{Kn} = \lambda_{mfp}/L$ (for λ_{mfp} the mean free path and

L the dimensions of the system). For neutral fluids, expansion to first-order in Kn gives the familiar Navier-Stokes equations. For plasmas, we can perform two expansions using a similar method – in terms of λ_{mfp}/L for collisional plasmas, and additionally in terms of $\rho_\alpha/L = \frac{\sqrt{T_\alpha m_\alpha}}{eBL}$ for collisional-magnetised plasmas – giving the *Braginskii equations* in the unmagnetised and magnetised limits respectively. The distribution function f_α is expanded in terms of some small parameter ϵ as

$$f_\alpha = f_0 + \epsilon f_1 + \epsilon^2 f_2 + \ldots \tag{2.20}$$

The 0^{th}-order component is always taken to be a Maxwellian distribution – the velocity distribution corresponding to a local thermodynamic equilibrium – since this causes the collision operator to vanish. However, since a Maxwellian distribution is isotropic, the associated heat flux and viscosity will be zero. To find expressions for $\boldsymbol{q}$ and $\underline{\underline{\boldsymbol{\Pi}}}$, the Boltzmann equation is linearised and f_1 is expanded in velocity space using a series of Laguerre polynomials. This gives an infinite set of simultaneous equations for f_1 in terms of f_0, which is truncated to just *two terms*, giving a set of two simultaneous equations. Finally, we take moments of our expression for f_1, to find expressions for $\boldsymbol{q}$ and $\underline{\underline{\boldsymbol{\Pi}}}$. This asymptotic closure procedure gives closed expressions for $\boldsymbol{R}$, $\underline{\underline{\boldsymbol{\Pi}}}$, $\boldsymbol{q}$ and Q, which we can use with equations 2.17–2.19. The resulting combination of equations and closure is called the Braginskii equations.

We've left out a lot of details. However, it's useful to understand the general procedure, since it can help us to identify when and how the closure approximation might give unrealistic behaviour. By using a Braginskii closure and truncating our expansion of the distribution function and the collision operator, we're making several strong implicit assumptions. Firstly, we assume that f_α is actually close to a Maxwellian – requiring that $\tau_\alpha \sim T_\alpha^{3/2}/n$ is much shorter than the time-scales that we're interested in, or alternatively that $\lambda_{mfp} \sim T^2/n$ is much shorter than the spatial scales that we're investigating. In magnetised fusion plasmas, this is generally true perpendicular to the magnetic field, but not along the magnetic field [128]. However, at very small (sub-Larmor radius) scales, the fluid approximation also breaks down perpendicular to the magnetic field – once finite-Larmor-radius effects start to become significant. Additionally, by neglecting the higher-order moments, we lose 'collisionless' effects which involve particles with specific energies. This means that particle trapping and Landau-damping are not contained in the model – and so we miss instabilities like the trapped-electron-mode and can find unrealistic heat fluxes.

This raises an interesting question: what happens if we try to model the plasma with a fluid model, even after it is no longer formally valid? The density, velocity and isotropic pressure are all determined by the f_0 Maxwellian component, and so should remain reasonably well-behaved (albeit not necessarily realistic – since they're affected by the higher-order moments) as the fluid approximation becomes marginal. The heat flux $\boldsymbol{q}$ and viscous stress tensor $\underline{\underline{\boldsymbol{\Pi}}}$ are not determined by the Maxwellian component, but rather by the f_1 and higher-order components of the distribution. Since the Braginskii closure only includes a truncated-series-expansion of f_1, it is unsurprising that these terms most quickly become unreasonable as we approach the limits of the fluid approximation.

Although the Braginskii equations are closed and therefore solvable, they include phenomena across vastly different spatial and time scales. This is a problem for modelling – a lot of the fast and small-scale dynamics aren't of much interest for us, but if we simply ignore them they can cause numerical problems. As such, we make further approximations to focus only on the turbulent dynamics.

2.2.3. Quasineutrality

Despite consisting of charged particles, most plasmas have very little space-charge. Highly mobile electrons can respond extremely quickly to any charge imbalance, such that over large-enough spatial and time scales the plasma is close to neutral. Despite this, the plasma can internally generate electric fields – indeed, these are crucial for turbulent transport. We want to eliminate dynamics at the very fast time-scales and small spatial scales where single-particle motion leads to charge imbalances (since these are expensive to simulate), but to retain the larger electric fields which lead to transport. This separation is referred to as the *quasineutrality approximation.* The time and spatial scales over which charge imbalances occur due to single-particle motion are, respectively, the inverse electron plasma frequency $t \sim \omega_{p,e}^{-1} = \left(\frac{ne^2}{\epsilon_0 m}\right)^{-1/2}$ and the electron Debye length $\lambda_{D,e} = v_{th,e}\omega_{p,e}^{-1}$, for $v_{th,e} = \sqrt{T_e/m_e}$ the electron thermal velocity. We want to eliminate dynamics which vary at these scales, and so assume that the dynamics of interest follow

$$\omega_{p,e}^{-1}\frac{\partial}{\partial t} \ll 1 \quad \text{and} \quad \lambda_{D,e}\nabla \ll 1 \tag{2.21}$$

We can use this to find a condition on Gauss's law

$$\lambda_{D,e}^2\nabla\phi \ll \phi \tag{2.22}$$

$$\frac{\varepsilon_0}{en}\nabla^2\phi \ll \frac{e\phi}{T_e} \tag{2.23}$$

We can identify $\nabla\cdot\boldsymbol{E} \sim \nabla^2\phi$ (assuming that the electromagnetic part is of the same order as the electrostatic part). The term $\frac{e\phi}{T_e}$ is of the order as the electron perturbation in response to a perturbing potential ϕ (i.e. see a derivation of the Debye length), and so we expect $\frac{e\phi}{T_e} \lesssim 1$. Therefore,

$$\frac{\rho_q}{en} = \frac{\varepsilon_0}{en}\nabla\cdot\boldsymbol{E} \ll 1 \tag{2.24}$$

Therefore, on spatial scales larger than $\lambda_{D,e}$, only a small fraction of the total plasma density leads to a charge density and the resulting electric fields are required to smoothly vary. Then, taking the divergence of Ampere's law and we find

$$\nabla\times\boldsymbol{B} = \mu_0\boldsymbol{J} + \mu_0\varepsilon_0\frac{\partial\boldsymbol{E}}{\partial t} \tag{2.25}$$

$$0 = \nabla\cdot\boldsymbol{J} + \frac{\partial\rho_q}{\partial t} \tag{2.26}$$

Since we have assumed that $\rho_q \ll en$ and $\omega_{p,e}^{-1}\frac{\partial}{\partial t} \ll 1$, we further assume that $\nabla \cdot \boldsymbol{J} \simeq 0$. Although we have some small finite charge density, its time derivative is even smaller and as such we assume that $\nabla \cdot \boldsymbol{J}$ is negligible. Finally, looking again at Ampere's law, we can multiply by the entire equation by $\lambda_{D,e} = v_{th,e}\omega_{p,e}^{-1}$ to see that

$$v_{th,e}^2\omega_{p,e}^{-2}\nabla \times \boldsymbol{B} = \mu_0 v_{th,e}^2\omega_{p,e}^{-2}\boldsymbol{J} + \frac{v_{th,e}^2}{c^2}\omega_{p,e}^{-2}\frac{\partial \boldsymbol{E}}{\partial t} \tag{2.27}$$

If we assume that $v_{th,e}/c \ll 1$, then the second term on the RHS is an order smaller than the other terms. Therefore, using the non-relativistic and quasineutral orderings, we can drop the displacement current term and write Ampere's law as

$$\nabla \times \boldsymbol{B} = \mu_0 \boldsymbol{J} \tag{2.28}$$

2.2.4. Small β limit

We additionally require that the effective magnetic pressure is much stronger than the thermal pressure. We can write this as a condition on the electron dynamical β_e

$$\beta_e = \frac{2\mu_0 p_e}{B^2} = \frac{c_s^2}{v_A^2} \ll 1, \tag{2.29}$$

where c_s is the sound speed and $v_A = B/\sqrt{\mu_0 n_i m_i}$ is the Alfvén speed. $v_A \gg c_s$ implies that the response of the magnetic field to pressure perturbations will be effectively instantaneous compared to the evolution of the pressure perturbation. This is used to assume that the magnetic field is always in a static equilibrium with the perpendicular pressure profile, which lets us ignore compressional Alfvén (fast magnetosonic) waves. We do, however, keep the magnetic tension response to pressure perturbations – which represents a competition between electron inertia $\frac{\partial j_\parallel}{\partial t}$ and magnetic induction $\frac{\partial A_\parallel}{\partial t}$. This leads to shear Alfvén waves (also called torsional Alfvén or slow magnetosonic waves) which travel along the magnetic field. A small perpendicular variation in the magnetic field will be induced by the change in $A_\parallel$. This can lead to 'magnetic flutter' cross-field transport, which occurs when the perturbed field-lines connect regions of different pressure. However, for the very low β_e values in this thesis, the effect was found to be minimal[1], and so the term was disabled to reduce computational cost.

2.2.5. Flute-mode and drift approximation

In a magnetised plasma, the confining magnetic field impedes particle motion across the magnetic field but permits motion parallel to the field. As such, it is generally reasonable to assume that perturbations will be spatially small perpendicular to the magnetic field, but elongated parallel to the magnetic field. (This assumption may become marginal in the presence of strong parallel gradients due to neutrals or the divertor targets). The resulting structures look a little

---

[1] The flutter term is stabilising and so the initial instability starts later, but the saturated states with and without flutter were more-or-less equivalent at low β_e [129].

like elongated tubes or flutes, bent to follow a magnetic field-line, and so this is called the 'flute-mode' approximation. Under the flute-mode approximation, we assume that the parallel and perpendicular dynamics are strongly separated. As such, instead of solving a 3D vector equation, we instead solve a 2D equation for the perpendicular dynamics and a 1D equation for the parallel dynamics. By itself, this doesn't help much, but if we combine this with the small-β_e assumption we can strongly simplify the perpendicular dynamics. With the small-β assumption, the perpendicular magnetic pressure will evolve much faster than small perpendicular (kinetic) pressure excitations. We can use this to perform an *ordering*: we assume that the time-scales τ which we're interested in are much longer than the inverse cyclotron frequency Ω^{-1},

$$\Omega_\alpha^{-1} = \frac{q_\alpha B}{m_\alpha} \gg \tau \tag{2.30}$$

that the frequencies and time-evolution scales of interest $\omega \sim d/dt$ are lower than the cyclotron frequency,

$$(d/dt) \ll \Omega_\alpha \tag{2.31}$$

that the parallel spatial wave-number is less than the perpendicular spatial wave-number,

$$k_\parallel \ll k_\perp \tag{2.32}$$

and that the perpendicular spatial wave-number is much larger than the inverse gradient length of the magnetic field.

$$k_\perp \gg \frac{\nabla B}{B} \tag{2.33}$$

We can use the *drift ordering* to isolate the dynamics of interest. In section 2.4 we will show how this ordering lets us linearise the perpendicular momentum balance.

2.3. The magnetised two-fluid Braginskii equations

Having introduced our approximations, we now need to combine them to simplify the moment equations. For simplicity we assume a single ion species with $q = +1$, plus a single electron species. We also use the quasineutrality approximation, such that $n_e = n_i = n$. We then take the moment equations (2.17–2.19) and use the magnetised limit ($\Omega_\alpha \tau_\alpha \gg 1$, for τ_α the collision frequency) of the Braginskii closure to find expressions for $\boldsymbol{R}$, $\underline{\underline{\boldsymbol{\Pi}}}$, Q and $\boldsymbol{q}$. As a shorthand we adopt the notation

$$\boxed{\boldsymbol{u}_i = \boldsymbol{u} \text{ and } \boldsymbol{u}_e = \boldsymbol{v}}$$

From quasineutrality and continuity, we have two equations for n

$$\frac{\partial n}{\partial t} + \nabla \cdot (n\boldsymbol{v}) = \frac{\partial n}{\partial t} + \nabla \cdot (n\boldsymbol{u}) = \mathcal{S}_n \tag{2.34}$$

We usually keep the electron continuity equation, and replace the ion continuity equation with the quasineutrality condition

$$\nabla \cdot \boldsymbol{j} = e\nabla \cdot n\left(\boldsymbol{u} - \boldsymbol{v}\right) = 0 \tag{2.35}$$

where $\boldsymbol{j} = en\left(\boldsymbol{u} - \boldsymbol{v}\right)$ is the current density. Since the Maxwellian distribution is isotropic, we separate the pressure tensor (2.12) into an isotropic pressure (p_α, equation 2.13) and a viscosity ($\underline{\underline{\boldsymbol{\Pi}}}_\alpha$, equation 2.14). Under the Braginskii closure, the electron viscosity will be a factor of $\sqrt{m_i/m_e} \approx 42\sqrt{m_i/m_p}$ smaller than the ion viscosity, and so we drop the terms which aren't involved in diamagnetic cancellation. An expression for the components of the ion viscosity can be found on p.15 of Zeiler, 1999 (called the *stress tensor* and denoted as P).

A further simplification is made by keeping only the parallel components of the friction $R_{\|} = \boldsymbol{R} \cdot \hat{\mathbf{b}} = \boldsymbol{R} - \boldsymbol{R}_\perp$. The perpendicular friction is important for setting the dissipation scale of the turbulence. However, since we often don't resolve all the way down to the dissipation scale, we use a tunable 'hyperdiffusion' instead of perpendicular friction. These simplifications allow us to write the momentum balance equations as

$$m_e n\left[\frac{\partial}{\partial t} + \boldsymbol{v}\cdot\nabla\right]\boldsymbol{v} = -\nabla p_e - en\left[\boldsymbol{E} + \boldsymbol{v}\times\boldsymbol{B}\right] + R_{\|}\hat{\mathbf{b}} \tag{2.36}$$

$$m_i n\left[\frac{\partial}{\partial t} + \boldsymbol{u}\cdot\nabla\right]\boldsymbol{u} = -\nabla p_i - \nabla\cdot\underline{\underline{\boldsymbol{\Pi}}}_i + en\left[\boldsymbol{E} + \boldsymbol{u}\times\boldsymbol{B}\right] - R_{\|}\hat{\mathbf{b}} \tag{2.37}$$

For the temperature equations, we again neglect the electron viscosity, giving

$$\frac{3}{2}n\left[\frac{\partial}{\partial t} + \boldsymbol{v}\cdot\nabla\right]T_e + p_e\nabla\cdot\boldsymbol{v} = -\nabla\cdot\boldsymbol{q}_e + \left(Q_e - Q_{ei}\right) + \mathcal{S}_{\varepsilon_e} \tag{2.38}$$

$$\frac{3}{2}n\left[\frac{\partial}{\partial t} + \boldsymbol{u}\cdot\nabla\right]T_i + p_i\nabla\cdot\boldsymbol{u} + \underline{\underline{\boldsymbol{\Pi}}}_i : \boldsymbol{u} = -\nabla\cdot\boldsymbol{q}_i + Q_{ei} + \mathcal{S}_{\varepsilon_i} \tag{2.39}$$

where $\mathcal{S}_{\varepsilon_e}$ and $\mathcal{S}_{\varepsilon_i}$ are local sources of energy which change the electron and ion temperatures.

2.4. Applying the drift-approximation and small-β limit to the magnetised Braginskii equations

Next, we apply the drift approximation to separate the parallel and perpendicular flows. The electric field is assumed to be electrostatic perpendicular to the magnetic field, and electromagnetic parallel to the magnetic field[2]. Therefore, we only need to retain the parallel component of the magnetic vector potential $A_{\|}$, and we can write the electric field as

$$E_{\|} = -\frac{\partial A_{\|}}{\partial t} - \nabla_{\|}\phi \text{ and } E_\perp = -\nabla_\perp\phi \tag{2.40}$$

We then solve the ion momentum balance equation for the perpendicular ion velocity $\boldsymbol{u}_\perp = \boldsymbol{u} - u_{\|}\hat{\mathbf{b}}$. To isolate the perpendicular component of the velocity $\boldsymbol{u}$, we use the 'drift operator' (equation B.17) on equation 2.37.

$$\frac{m_i n\hat{\mathbf{b}}}{B}\times\left[\frac{\partial}{\partial t} + \boldsymbol{u}\cdot\nabla\right]\boldsymbol{u} = -\frac{\hat{\mathbf{b}}\times\nabla p_i}{B} - \frac{\hat{\mathbf{b}}\times\nabla\cdot\underline{\underline{\boldsymbol{\Pi}}}_i}{B} - \frac{en\hat{\mathbf{b}}\times\nabla\phi}{B} + en\boldsymbol{u}_\perp \tag{2.41}$$

---

[2] This assumption is justified a posteriori on p3.15 of Scott.

$$\boldsymbol{u}_\perp = \frac{\hat{\mathbf{b}} \times \nabla\phi}{B} + \frac{\hat{\mathbf{b}} \times \nabla p_i}{enB} + \frac{m_i \hat{\mathbf{b}}}{eB} \times \left[\frac{\partial}{\partial t} + \boldsymbol{u} \cdot \nabla\right] \boldsymbol{u} + \frac{\hat{\mathbf{b}}}{enB} \times \nabla \cdot \underline{\underline{\mathbf{\Pi}}}_i \tag{2.42}$$

We have $\boldsymbol{u}$ on both sides of the equation. To solve this, we can *linearise* the equation in terms of $(d/dt)/\Omega_i = m_i (d/dt)/(q_i B) \ll 1$, which is assumed to be small due to the drift-ordering (equation 2.30). We can directly see this small parameter in the inertial term, and if we explicitly expand the $\hat{\mathbf{b}} \times \nabla \cdot \underline{\underline{\mathbf{\Pi}}}_i$ term we see that it is of the same order as the inertial term. Therefore, to leading order, we can write

$$\boldsymbol{u}_\perp = \boldsymbol{u}_{E\times B} + \boldsymbol{u}_{dia} + O\left(\frac{d/dt}{\Omega_i}\right) \tag{2.43}$$

for the $E \times B$ *drift*

$$\boxed{\boldsymbol{u}_{E\times B} = \frac{\hat{\mathbf{b}} \times \nabla\phi}{B}} \tag{2.44}$$

and the *ion diamagnetic drift*

$$\boxed{\boldsymbol{u}_{dia} = \frac{\hat{\mathbf{b}} \times \nabla p_i}{enB}} \tag{2.45}$$

Similarly, for the electrons

$$\boldsymbol{v}_\perp = \boldsymbol{u}_{E\times B} + \boldsymbol{v}_{dia} + O\left(\frac{d/dt}{\Omega_e}\right) \tag{2.46}$$

for the *electron diamagnetic drift*

$$\boxed{\boldsymbol{v}_{dia} = -\frac{\hat{\mathbf{b}} \times \nabla p_e}{enB}} \tag{2.47}$$

We then use the leading-order drifts to find the ion inertial response, expanding equation 2.42 to first-order in $(d/dt)/\Omega_i$. We will not, however, determine the electron inertial response, since this is much smaller than the ion inertial response since $\frac{m_e}{m_i} \ll 1 \implies O\left(\frac{d/dt}{\Omega_e} \sim \frac{m_e}{m_i}\frac{d/dt}{\Omega_i} \ll \frac{d/dt}{\Omega_i}\right)$. Substituting the leading order perpendicular ion drifts plus the parallel velocity $u_\| \hat{\mathbf{b}}$ into equation 2.42 gives

$$\boldsymbol{u}_\perp = \boldsymbol{u}_{E\times B} + \boldsymbol{u}_{dia} + \boldsymbol{u}_{pol} + O\left(\frac{d/dt}{\Omega_i}\right)^2 \tag{2.48}$$

for the *polarisation drift*

$$\boldsymbol{u}_{pol} = \frac{m_i \hat{\mathbf{b}}}{eB} \times \left[\frac{\partial}{\partial t} + \boldsymbol{u} \cdot \nabla\right] \left(u_\| \hat{\mathbf{b}} + \boldsymbol{u}_{E\times B} + \boldsymbol{u}_{dia}\right) + \frac{\hat{\mathbf{b}}}{enB} \times \nabla \cdot \underline{\underline{\mathbf{\Pi}}}_i \tag{2.49}$$

Provided that the characteristic scale for magnetic field variations is much larger than the scale of the turbulence (assumption 2.33), we can commute the $\hat{\mathbf{b}}\times$ operator through the advective derivative[3] to cancel the parallel component, which lets us write the polarisation velocity as

$$\boldsymbol{u}_{pol} = \frac{-m_i}{eB^2}\left[\frac{\partial}{\partial t} + \boldsymbol{u}\cdot\nabla\right]\left(\nabla_\perp\phi + \frac{\nabla_\perp p_i}{en}\right) + \frac{\hat{\mathbf{b}}}{enB}\times\nabla\cdot\underline{\underline{\mathbf{\Pi}}}_i \tag{2.50}$$

We need to explicitly write out the velocity term inside the advective derivative. Due to a property of the diamagnetic drift called *diamagnetic cancellation*, the diamagnetic drift does not contribute to advection, since the term $\frac{-m_i n}{B}\boldsymbol{u}_{dia}\cdot\nabla\boldsymbol{u}$ cancels with part of $\hat{\mathbf{b}}\times\nabla\cdot\underline{\underline{\mathbf{\Pi}}}_i$ (we write the remaining part as $\underline{\underline{\mathbf{\Pi}}}_{dia}$). This can be seen directly from the expansion of $\nabla\cdot\underline{\underline{\mathbf{\Pi}}}_i$ given on p.18 of Zeiler, while the general principle of diamagnetic cancellation is discussed on p.2.37 of Scott. Conversely, to ensure energy conservation, we *do* need to include the polarisation velocity in the advection[4]. Unfortunately, this is very difficult to treat numerically, so in the numerical model we drop the polarisation velocity from advective derivatives, and we approximate the polarisation velocity as

$$\boxed{\boldsymbol{u}_{pol} = \frac{-m_i}{eB^2}\left[\frac{\partial}{\partial t} + \left(u_\parallel\hat{\mathbf{b}} + \boldsymbol{u}_{E\times B} + \cancel{\boldsymbol{u}_{pol}}\right)\cdot\nabla\right]\left(\nabla_\perp\phi + \frac{\nabla_\perp p_i}{en}\right) + \frac{\hat{\mathbf{b}}}{enB}\times\nabla\cdot\underline{\underline{\mathbf{\Pi}}}_{i,dia}} \tag{2.51}$$

This was quite a bit of work for a 'correction' term! Couldn't we have just dropped this term and saved ourselves the effort? Unfortunately, no. Although the polarisation velocity is small compared to the $E\times B$ and diamagnetic drifts, its divergence is of the same order. Therefore, wherever $\boldsymbol{u}_{pol}$ appears under a divergence, we need to keep it. Physically, if particles are able to instantly respond to pressure perturbations, the perturbation will not grow. It is only due to terms like inertia and electromagnetic induction that we get a non-instantaneous response and an energy source for our turbulence.

2.5. The final equation set

With the drift approximation, our electron and ion velocities can be written as

$$\boldsymbol{v} = \boldsymbol{u}_{E\times B} + \boldsymbol{v}_{dia} + \left(u_\parallel - \frac{j_\parallel}{en}\right)\hat{\mathbf{b}} \tag{2.52}$$

$$\boldsymbol{u} = \boldsymbol{u}_{E\times B} + \boldsymbol{u}_{dia} + \boldsymbol{u}_{pol} + u_\parallel\hat{\mathbf{b}} \tag{2.53}$$

where the *parallel current density is*

$$j_\parallel = en\left(u_\parallel - v_\parallel\right) \tag{2.54}$$

---

[3] Using the product rule we see that $\hat{\mathbf{b}}\times\left[\frac{\partial}{\partial t} + \boldsymbol{u}\cdot\nabla\right]\boldsymbol{u} = \left[\frac{\partial}{\partial t} + \boldsymbol{u}\cdot\nabla\right]\left(\hat{\mathbf{b}}\times\boldsymbol{u}\right) - \boldsymbol{u}\times\left[\frac{\partial}{\partial t} + \boldsymbol{u}\cdot\nabla\right]\hat{\mathbf{b}}$. Provided that the magnetic field doesn't change too quickly in space or time compared to the velocity, it is reasonable to drop the second term since it should be much smaller than the first.

[4] This is curious, since $\boldsymbol{u}_{pol}$ is formally an order down compared to $\boldsymbol{u}_{E\times B}$ or $u_\parallel\hat{\mathbf{b}}$. However, its divergence is of the same order as $\nabla\cdot\boldsymbol{u}_{E\times B}$ (see Scott p3.6). If we consider vector identity B.9, we can see that a $\boldsymbol{u}\cdot\nabla$ operator acting on some arbitrary vector function $\boldsymbol{A}$ can be related to a divergence $\nabla\cdot\boldsymbol{u}$.

Although we need it for energy conservation, we will drop the polarisation drift from $\boldsymbol{u} \cdot \nabla$ because this term is difficult to treat numerically, and will further drop $\boldsymbol{u}_{pol}$ unless it appears under a divergence. We can substitute the expressions for the velocities into equations 2.34–2.39 and add the constitutive terms from the magnetised-Braginskii closure to find a set of equations. The final equations are expressed in terms of the ion stress function G (defined on p.18 of Zeiler and given in equation A.1), which gives the component of the ion viscosity which remains after diamagnetic cancellation.

Continuity equation

Since we neglected the perpendicular electron inertia, the electron continuity equation is simpler than the ion equation. As such, we use equation the electron continuity equation (2.34) with the electron velocity (2.52) to give the evolution of the common density n

$$\frac{\partial n}{\partial t} + \nabla \cdot n\boldsymbol{u}_{E\times B} + \nabla \cdot n\boldsymbol{v}_{dia} + \nabla \cdot n v_{\|}\hat{\mathbf{b}} = 0 \tag{2.55}$$

We expand the $\boldsymbol{E} \times \boldsymbol{B}$ flux using the vector identity B.5 and write

$$\boxed{\left[\frac{\partial}{\partial t} + \boldsymbol{u}_{E\times B} \cdot \nabla\right] n = -n \left(\frac{\nabla \times \hat{\mathbf{b}}}{B}\right) \cdot \nabla\phi - \left(\frac{\nabla \times \hat{\mathbf{b}}}{B}\right) \cdot \frac{\nabla p_e}{e} + \nabla \cdot \left(\frac{j_{\|}}{e} - n u_{\|}\right) \hat{\mathbf{b}}} \tag{2.56}$$

Quasineutrality equation

We substitute both the electron and ion velocities (equations 2.52 and 2.53) into the quasineutrality equation (equation 2.35), and then rearrange to find an expression for the polarisation flux

$$-e\nabla \cdot n\boldsymbol{u}_{pol} = \nabla \cdot j_{\|}\hat{\mathbf{b}} + e\nabla \cdot n\boldsymbol{u}_{dia} - e\nabla \cdot n\boldsymbol{v}_{dia} \tag{2.57}$$

$$\boxed{\begin{aligned} \nabla \cdot \frac{m_i n}{B^2} \left[\frac{\partial}{\partial t} + u_{\|}\nabla_{\|} + \boldsymbol{u}_{E\times B} \cdot \nabla\right] \left(\nabla_{\perp}\phi + \frac{\nabla_{\perp} p_i}{en}\right) \\ = \nabla \cdot j_{\|}\hat{\mathbf{b}} + \left(\frac{\nabla \times \hat{\mathbf{b}}}{B}\right) \cdot \nabla_{\perp}\left(p_e + p_i\right) - \frac{1}{6}\left(\frac{\nabla \times \hat{\mathbf{b}}}{B}\right) \cdot \nabla G \end{aligned}} \tag{2.58}$$

The quasineutrality equation gives the evolution of the electrostatic potential ϕ.

Momentum balance

To find an equation for the parallel velocity, we project both momentum equations (2.36,2.37) into the parallel direction by applying the $\hat{\mathbf{b}}\cdot$ operator. We then cancel the diamagnetic velocity terms $\boldsymbol{u}_{dia} \cdot \nabla$ and $\boldsymbol{v}_{dia} \cdot \nabla$ with corresponding terms in $\nabla \cdot \underline{\underline{\mathbf{\Pi}}}_i$ and $\nabla \cdot \underline{\underline{\mathbf{\Pi}}}_e$. Finally, we add the two parallel components together and drop $\boldsymbol{u}_{pol}$ since it is hard to evaluate numerically, giving

$$m_i n \left[\frac{\partial}{\partial t} + \boldsymbol{u}_{E\times B} \cdot \nabla + \cancel{\boldsymbol{u}_{pol} \cdot \nabla} + u_{\|}\nabla_{\|}\right] u_{\|} = -\nabla_{\|}\left(p_e + p_i\right) - \nabla \cdot \left(\underline{\underline{\mathbf{\Pi}}}_i\right)_{\|} \hat{\mathbf{b}} \tag{2.59}$$

$$\boxed{m_i n \left[\frac{\partial}{\partial t} + \boldsymbol{u}_{E\times B}\cdot\nabla + u_{\|}\nabla_{\|}\right] u_{\|} = -\nabla_{\|}\left(p_e + p_i\right) + \frac{m_i p_i}{e}\left(\frac{\nabla\times\hat{\mathbf{b}}}{B}\right)\cdot\nabla u_{\|} - \frac{2}{3}B^{3/2}\nabla_{\|}\frac{G}{B^{3/2}}} \tag{2.60}$$

Ohm's law

The parallel component of the electron momentum equation can be used to find an equation for the evolution of the parallel current density. We again cancel $\boldsymbol{v}_{dia}\cdot\nabla$ with part of $\nabla\cdot\Pi_e$, and then drop the rest of the electron viscosity tensor. The electric field is written in terms of the electromagnetic four-potential $\boldsymbol{E} = -\nabla\phi - \frac{\partial \boldsymbol{A}}{\partial t}$, which we project into the parallel direction. The parallel friction is written using the constitutive equations from the Braginskii closure as $R_{\|} = \boldsymbol{R}\cdot\hat{\mathbf{b}} = e^2 n^2 \eta_{\|}(u_{\|} - v_{\|}) - 0.71 n\nabla_{\|}T_e = en\eta_{\|}j_{\|} - 0.71n\nabla_{\|}T_e$ for $\eta_{\|} = \left(1.96\frac{ne^2\tau_e}{m_e}\right)^{-1}$ the *parallel Spitzer resistivity*. The first term in the parallel friction is simply friction, while the second is the *thermal force*[5]. We can therefore write

$$\frac{m_e}{e}\left[\frac{\partial}{\partial t} + \boldsymbol{u}_{E\times B}\cdot\nabla + v_{\|}\nabla_{\|}\right]\left(u_{\|} - \frac{j_{\|}}{en}\right) - \frac{\partial A_{\|}}{\partial t} = -\frac{\nabla_{\|}p_e}{en} + \nabla_{\|}\phi + \eta_{\|}j_{\|} - 0.71\frac{1}{e}\nabla_{\|}T_e \tag{2.61}$$

We can use equation 2.60 to show that $\frac{du_{\|}}{dt}$ will be a factor of m_e/m_i smaller than the $\frac{dj_{\|}}{dt}$ term, and so we drop it from the left-hand-side, giving

$$\boxed{\frac{m_e}{e}\left[\frac{\partial}{\partial t} + \boldsymbol{u}_{E\times B}\cdot\nabla + v_{\|}\nabla_{\|}\right]\frac{j_{\|}}{en} + \frac{\partial A_{\|}}{\partial t} = \frac{\nabla_{\|}p_e}{en} - \nabla_{\|}\phi - \eta_{\|}j_{\|} + 0.71\frac{1}{e}\nabla_{\|}T_e} \tag{2.62}$$

Since this equation relates the current density to the electric field via a resistivity, we refer to it as the generalised Ohm's law.

Electron temperature equation

An expression for the evolution of the electron temperature can be found by expanding the electron temperature equation (2.38) in terms of constitutive equations from the Braginskii closure. These are the frictional heating $Q_e = (u_{\|} - v_{\|})R_{\|} = \eta_{\|}j_{\|}^2 - 0.71\frac{1}{e}j_{\|}\nabla T_e$, the electron-ion heat exchange $Q_{ei} = \frac{3m_e}{m_i}\frac{n(T_e - T_i)}{\tau_e}$ and the electron heat flux

$$\boldsymbol{q}_e = -\chi_{\|,e}\nabla_{\|}T_e\hat{\mathbf{b}} - \frac{5}{2}\frac{p_e}{eB}\hat{\mathbf{b}}\times\nabla T_e - 0.71\frac{1}{e}T_e j_{\|}\hat{\mathbf{b}} \tag{2.63}$$

representing a random-walk thermal diffusion, a diamagnetic heat flux (see p2.34–2.35 of Scott) and a 'hot-tail' term. The last term accounts for the fact that current is primarily carried by

---

[5] The thermal force acts in the direction opposite to the temperature gradient, since higher temperature electrons have a *lower* collision cross-section and therefore experience *less* friction. The thermal force can be considered a correction to the bulk friction, and it acts against the temperature gradient.

high-energy electrons, and as such we can associate a current with an additional advective heat flux. The electron heat conductivity is written as

$$\chi_{\parallel,e} = 3.16\frac{nT_e\tau_e}{m_e} \tag{2.64}$$

for the electron collision time

$$\tau_e = \frac{6\sqrt{2}\pi^{3/2}\epsilon_0^2\sqrt{m_e}T_e^{3/2}}{\ln\Lambda e^4 n} \sim \frac{T_e^{3/2}}{n} \tag{2.65}$$

and the Coulomb logarithm

$$\ln\Lambda \simeq 6.6 - 0.5\ln\left(\frac{n}{10^{20}\mathrm{m}^{-3}}\right) + 1.5\ln\left(\frac{T_e}{1\mathrm{eV}}\right) \tag{2.66}$$

which we approximate as a constant, evaluated at the reference density and electron temperature (see Appendix A). We don't introduce new assumptions in the derivation of the electron temperature equation (although we do use some of the approximations that we made earlier), so won't show the derivation here. However, it's not entirely straightforward, and so you can find the derivation in Appendix C.1. The final result is

$$\boxed{\begin{aligned}\frac{3}{2}\left[\frac{\partial}{\partial t} + \boldsymbol{u}_{E\times B}\cdot\nabla + v_\parallel\nabla_\parallel\right]T_e = &-T_e\left(\left(\frac{\nabla\times\hat{\mathbf{b}}}{B}\right)\cdot\nabla\phi + \nabla\cdot v_\parallel\hat{\mathbf{b}} + \frac{1}{n}\left(\frac{\nabla\times\hat{\mathbf{b}}}{B}\right)\cdot\nabla p_e\right)\\ &+\frac{1}{n}\nabla\cdot\left[\chi_{\parallel,e}\nabla_\parallel T_e\hat{\mathbf{b}}\right] + \frac{5}{2}\frac{T_e}{e}\left(\frac{\nabla\times\hat{\mathbf{b}}}{B}\right)\cdot\nabla T_e\\ &+\frac{0.71}{e}\frac{T_e}{n}\nabla\cdot j_\parallel\hat{\mathbf{b}} + \frac{1}{n}\eta_\parallel j_\parallel^2 - \frac{3m_e}{m_i}\frac{(T_e - T_i)}{\tau_e} + \mathcal{S}_{T_e}\end{aligned}} \tag{2.67}$$

Ion temperature equation

Similarly to the electrons, we can rewrite the ion temperature equation (2.39) using the constitutive equations from the Braginskii closure. In this case, the relevant terms are Q_{ie} (defined in the previous section) and the ion heat flux

$$\boldsymbol{q}_i = -\chi_{\parallel,i}\nabla_\parallel T_i\hat{\mathbf{b}} - \frac{5}{2}\frac{p_i}{eB^2}\boldsymbol{B}\times\nabla T_i \tag{2.68}$$

representing a random-walk thermal diffusion and a diamagnetic heat flux. The ion heat conductivity is

$$\chi_{\parallel,i} = 3.9\frac{nT_i\tau_i}{m_i} \tag{2.69}$$

for the ion collision time

$$\tau_i = \frac{12\pi^{3/2}\epsilon_0^2\sqrt{m_i}T_i^{3/2}}{\ln\Lambda e^4 n} \sim \frac{T_i^{3/2}}{n} \tag{2.70}$$

for the Coulomb logarithm defined in the previous section. The derivation of the final T_i equation is similar to the derivation for the T_e equation, except we now have $\boldsymbol{u}_{pol}$ in our velocity. We use the continuity equations to replace $\nabla \cdot \boldsymbol{u}$ with $\nabla \cdot \boldsymbol{v} + \frac{1}{n}(\boldsymbol{v} - \boldsymbol{u}) \cdot \nabla n$, which is why we have the *electron diamagnetic velocity* in the top row. The derivation is given in Appendix C.2, and the final result is

$$\boxed{\begin{aligned}\frac{3}{2}\left[\frac{\partial}{\partial t} + \boldsymbol{u}_{E\times B} \cdot \nabla + u_\parallel \nabla_\parallel\right] T_i = &- T_i \left(\left(\frac{\nabla \times \hat{\mathbf{b}}}{B}\right) \cdot \nabla\phi + \nabla \cdot u_\parallel \hat{\mathbf{b}} + \frac{1}{n}\left(\frac{\nabla \times \hat{\mathbf{b}}}{B}\right) \cdot \nabla p_e\right) \\ &+ \frac{1}{n}\nabla \cdot \left[\chi_{\parallel,i} \nabla_\parallel T_i \hat{\mathbf{b}}\right] + \frac{5}{2}\frac{T_i}{e}\left(\frac{\nabla \times \hat{\mathbf{b}}}{B}\right) \cdot \nabla T_i \\ &+ \frac{T_i}{n}\nabla \cdot \frac{j_\parallel}{e}\hat{\mathbf{b}} + \frac{3m_e}{m_i}\frac{(T_e - T_i)}{\tau_e} + \frac{G^2}{3n\eta_i} + \mathcal{S}_{T_i}\end{aligned}} \tag{2.71}$$

Ampère's law

The set of equations is closed with Ampère's circuital law $\nabla \times \boldsymbol{B} = \mu_0 \boldsymbol{j}$. From the quasineutrality condition, we use the quasi-static form of Ampère's law. We can write the curl of the magnetic field in terms of the vector potential (which is divergence-free in the non-relativistic limit)

$$\begin{aligned}\mu_0 \boldsymbol{j} &= \nabla \times (\nabla \times \boldsymbol{A}) && (2.72) \\ &= \nabla\left(\cancel{\nabla \cdot \boldsymbol{A}}\right) - \nabla^2 \boldsymbol{A} && (2.73)\end{aligned}$$

Taking only the parallel component then gives

$$\boxed{\nabla_\perp^2 A_\parallel = \mu_0 j_\parallel} \tag{2.74}$$

2.6. Normalised equations

The equations for continuity (2.56), quasineutrality (2.58), momentum-balance (2.60), Ohm's law (2.62), electron temperature (2.67), ion temperature (2.71) and Ampère's law (2.74) form a complete set. We could solve them as they are, although we'd need to be careful to make sure that we're consistent with our units. Instead, we normalise the equations to a set of reference values, which leads to a number of *dimensionless (unit-less) parameters* appearing in the equations. The normalisation parameters, dimensionless parameters and normalised equations are given in Appendix A.

Our choice of reference parameters should not affect the simulations[6], while the dimensionless parameters *do* have a strong influence since they set the relative strength of terms in the equations. One slight exception is the use of a constant Coulomb logarithm $\ln\Lambda$ which is calculated from the reference parameters, which gives a (weak) dependence on the choice of reference density and electron temperature.

---

[6] Reference parameters *could* have an effect numerically, particularly if the choice of reference parameter leads to overflow errors. However, since double-precision numbers can represent values between $10^{-308} - 10^{308}$, any reasonable choice of reference value will not lead to overflow errors (for single precision, the range is $10^{-38} - 10^{38}$, which could conceivably be reached with a poor choice of reference values).

2.7. Further reading

- Braginskii, 1965, *Transport Processes in a Plasma*: the book chapter where the 'Braginskii model' was originally published. Remarkably relevant and readable.
- Zohm, 2015, *Magnetohydrodynamic Stability of Tokamaks*: section 1.1.1 gives the derivation of the fluid equations from the Boltzmann equation.
- Freidberg, 2014, *Ideal MHD*, section 2.3 up to 2.3.3, also giving the derivation of the fluid equations, in complement to derivation in Zohm.
- Scott, 2001, *Low-frequency Fluid Drift Turbulence in Magnetised Plasmas*: a comprehensive thesis that rigorously derives the drift-reduced Braginskii equations and provides an extensive commentary on their use and analysis.
- Zeiler, 1999, *Tokamak Edge Turbulence*: a more brisk introduction to the drift-reduced Braginskii equations, with some useful perspectives on plasma turbulence.

3. Sheath boundary conditions

3.1. What, why, and how? Using a sheath model to find boundary conditions for our model

For all fusion experiments on earth, at some point – via classical, neoclassical or turbulent transport – the plasma will collide with the solid walls of the device. Once plasma particles reach the walls, they mostly recombine into neutral particles which are reflected back into the plasma volume, where they are reionised. As such, the walls act as a sink for plasma particles and a source for neutral particles. However, due to the very different masses of electrons and ions, random thermal transport to the walls will lead to different rates of electron and ion loss, resulting in a net current to the walls. To keep the plasma volume quasineutral, the bulk velocity of electrons and ions must be modified to (approximately) balance the losses. This requires a strong electric field in a small ($\sim \lambda_{D,e}$) region near the walls called the *sheath*, which breaks the quasineutrality assumption (2.2.3). The electric field extends some short distance into the plasma ($\sim \rho_i$), in a region called the *magnetic presheath*, where it deflects ions from the field-lines and breaks the ion-drift-ordering (2.2.5). As such, the model that we derived in chapter 2 is valid only up until the magnetic presheath entrance (MPSE).

Despite being small, the sheath has a significant effect on the bulk plasma. As such, if we want to accurately model the edge plasma, we need to either model the sheath directly – which would require coupling to a kinetic model [130] – or at least approximate its effects on the bulk plasma. Since kinetic models are extremely expensive, we instead look for solutions to (strongly-simplified) sheath models to find a set of *sheath boundary conditions* which give expressions for the MPSE plasma in terms of the bulk plasma properties. The assumptions required to arrive at an implementable set of equations are less rigorous than those made in chapter 2, and there is little consensus amongst the modelling community per what sheath boundary conditions should be used. As such, we need to use validation (Part III) to test our model and boundary conditions against experiment.

In this chapter, we first present the boundary conditions for a normal sheath in an unmagnetised plasma. This closely follows results available in literature, although we modify the standard result to allow for sub and supersonic sheath entrance ion velocities. We then discuss the magnetised case, introducing the magnetic presheath and drifts, and boundary conditions for the simulations in this thesis. Finally, we discuss part of what makes this topic so challenging, and what an improved set of boundary conditions might include.

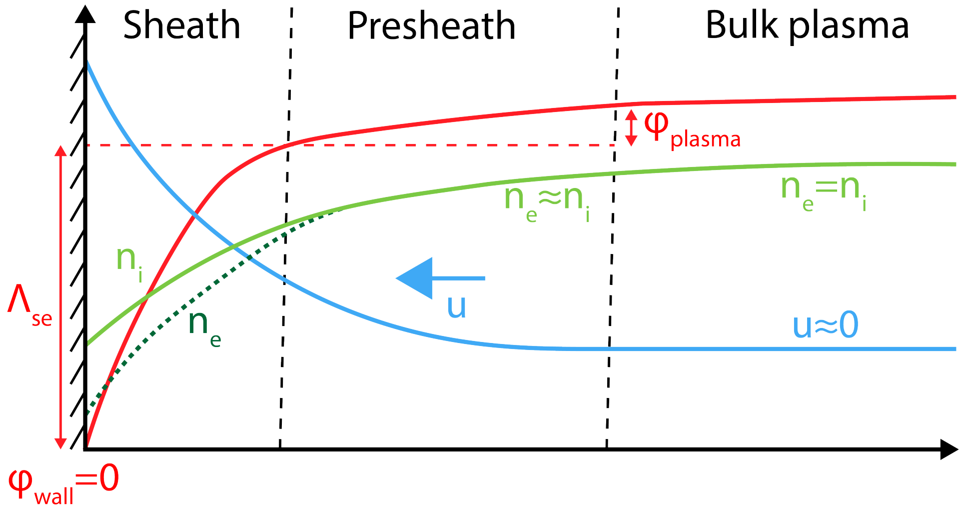

Figure 3.1.: A normal sheath for an unmagnetised plasma with $q = 1$. The plasma is divided into regions – the bulk plasma, the presheath and the sheath. As we move towards the wall, the electric field increases, accelerating the ions towards the wall and repelling the electrons. In the presheath, this electric field is weak enough that we can still apply quasineutrality, while in the sheath the electric field is stronger and a significant space-charge develops, with $n_e < n_i$. In this thesis, we assume that the wall is conducting and grounded.

3.2. The normal sheath

3.2.1. The Bohm criterion

In a simple unmagnetised plasma, as depicted in figure 3.1, an electric field develops spontaneously to balance the electron and ion fluxes. This electric field accelerates ions towards the wall, and repels electrons, leading to a region of space charge where the quasineutrality condition is broken. If we neglect collisions, we can derive the Bohm condition for the ion velocity at the Debye sheath entrance. We assume that the electron energy distribution function can be approximately described as a Maxwellian, so that we can relate the electron density at some position x near the sheath entrance to the electrostatic potential, via the Boltzmann relation

$$n_e(x) = n_{se} \exp\left[\frac{e\left(\phi(x) - \phi_{se}\right)}{T_e}\right] \tag{3.1}$$

where n_{se} and ϕ_{se} are the electron density and electrostatic potential at the sheath entrance. Then, if we assume that the ion thermal velocity is negligible compared to the bulk flow velocity, and that the ion velocity is due only to the acceleration by the electric field, via energy conservation we have

$$\frac{1}{2}m_i u(x)^2 + e\phi(x) = \frac{1}{2}m_i u_{se}^2 + e\phi_{se} \tag{3.2}$$

We assume that there are no sources in the sheath, and if we further assume that the flow is incompressible we can write the ion continuity equation as

$$n_i(x)u(x) = n_{se}u_{se} \tag{3.3}$$

$$n_i(x) = n_{se}\left(u_{se}/u(x)\right) \tag{3.4}$$

which we can rewrite using equation 3.2 as

$$n_i(x) = n_{se}\left[1 - \frac{e\left(\phi(x) - \phi_{se}\right)}{K_{se}}\right]^{-1/2} \tag{3.5}$$

for $K_{se} = \frac{1}{2}m_i u_{se}^2$. Then, using the electrostatic form of Poisson's equation (for $q_i = 1$)

$$\nabla \cdot \boldsymbol{E} = -\frac{\partial^2\phi}{\partial x^2} = \frac{e}{\varepsilon_0}\left(n_i(x) - n_e(x)\right) \tag{3.6}$$

$$\frac{\varepsilon_0 \nabla \cdot \boldsymbol{E}}{e n_{se}} = -\frac{\varepsilon_0}{e n_{se}}\frac{\partial^2\phi}{\partial x^2} = \left[1 - \frac{e\left(\phi(x) - \phi_{se}\right)}{K_{se}}\right]^{-1/2} - \exp\left[\frac{e\left(\phi(x) - \phi_{se}\right)}{T_e}\right] \tag{3.7}$$

Rather than attempting to solve for ϕ, lets consider the values which the right-hand-side

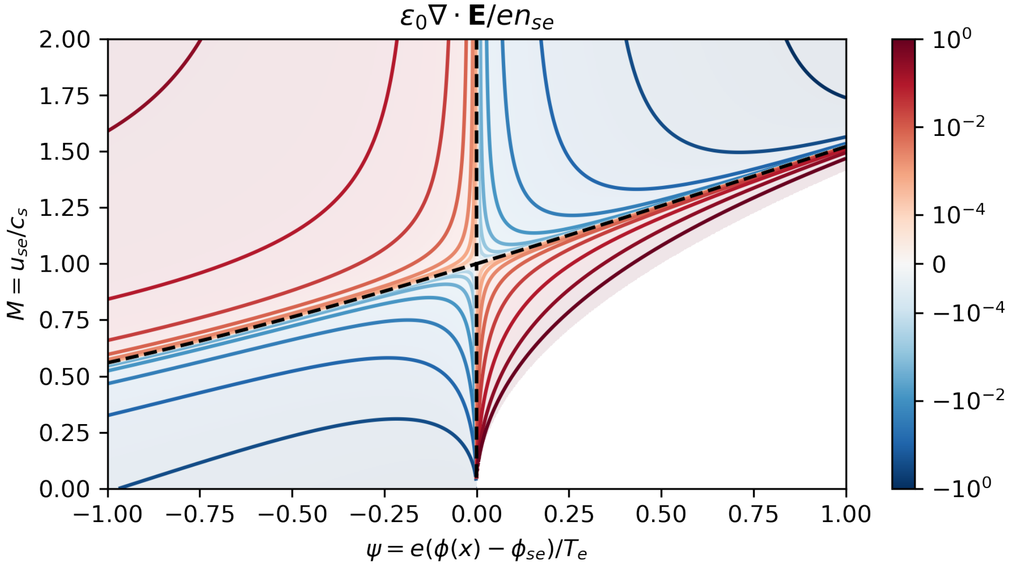

Figure 3.2.: The right-hand-side of equation 3.8, for different values of the normalised potential difference $\psi = \frac{e}{T_e}\left(\phi(x) - \phi_{se}\right)$ and the Mach number $M_{se} = u_{se}/c_{se} = u_{se}/\sqrt{T_e/m_i}$. There are two distinct branches which give a minimum space charge ρ_q – one with $\phi(x) = \phi_{se}$ (a field-free plasma) and another with $u_{se}/c_s \propto \phi(x) - \phi_{se}$.

of the equation can take. First of all, since the entrance to the sheath is still quasineutral, we know that $\left|\frac{\varepsilon_0 \nabla \cdot \boldsymbol{E}}{e n_{se}}\right| \ll 1$. Then, if we make the change of variables $\psi = \frac{e}{T_e}\left(\phi(x) - \phi_{se}\right)$ and

$M_{se} = u_{se}/c_s = u_{se}/\sqrt{T_e/m_i}$ we can write

$$\left|\frac{\varepsilon_0 \nabla \cdot \boldsymbol{E}}{e n_{se}}\right| = \left|\left[1 - \frac{2\psi}{M^2}\right]^{-1/2} - \exp\left[\psi\right]\right| \ll 1 \tag{3.8}$$

In figure 3.2 we have evaluated $\left|\frac{\varepsilon_0 \nabla \cdot \boldsymbol{E}}{e n_{se}}\right|$ as a function of ψ and M. There are two branches which fulfil the quasineutrality condition – $\psi = 0$ or a $M \propto \psi$. $\psi = 0$ would imply that the electric field is negligible, which is the solution valid for the bulk plasma. Near the sheath entrance, we want some electric field pointing towards the wall, to accelerate the ions and repel electrons. Looking at $\phi(x)$ in figure 3.1 (generated using `sheath_potential.ipynb`), if we pick x at some point in the bulk plasma $\phi_{se} - \phi(x) = \phi_{plasma} > 0$, which corresponds to

$$\boxed{M \geq 1 \iff u_{se} \geq c_s = \sqrt{\frac{T_e}{m_i}}} \tag{3.9}$$

This is the 'Bohm criterion', which states that the ion velocity perpendicular to the wall must be at least the local sound speed at the entrance to the sheath. To account for non-negligible ion temperature, we can modify the local sound speed [131] to

$$c_s = \sqrt{\frac{\gamma_{a,e} T_e + \gamma_{a,i} T_i}{m_i}} \tag{3.10}$$

where the γ_a terms are the adiabatic indices for the electrons and ions. We always set $\gamma_a = 1$ for both the electrons and ions, which corresponds to the isothermal case[1].

3.2.2. Insulating-sheath boundary conditions

The sheath balances the electron and ion wall fluxes via an electric field. We can calculate the required electric field, and use this to set a boundary condition for the potential. We assume that the wall is grounded at $\phi = 0$, and calculate the potential difference Λ_{se} across the sheath required to give zero net current. Since the ions are accelerated towards the wall, we assume that any ions reaching the sheath entrance will arrive at the wall. As such, the ion flux to the wall will be

$$\Gamma_i \geq e n_{se} c_s \tag{3.11}$$

$$= n_{se} c_s M_{se} \tag{3.12}$$

where $M_{se} = u_{se}/c_s$ is the Mach number at the sheath entrance, which must be ≥ 1 for the Bohm criterion to hold. We assume that the electron flux is equal to $\Gamma_e = \frac{1}{4} n \bar{c}_e$ with $\bar{c}_e = \sqrt{\frac{8 T_e}{\pi m_e}}$, which is the flux to an infinite planar surface for particles with temperature T_e. We further assume the electron density $n_e = n_{se} \exp\left[\frac{e\Lambda_{se}}{T_e}\right]$ is the electron density at the wall determined

---

[1] The adiabatic index for adiabatic flow is $\gamma_a = 5/3$ in 3D and $\gamma_a = 3$ in 1D. Since the strong electric field at the sheath leads to essentially one-dimensional flow for the ions we might consider setting $\gamma_{a,i} = 3$.

by the Boltzmann relation, with Λ_{se} the potential drop from the sheath to the wall. Then, for ambipolar flows ($j_{\|} = 0$) with single-charged ions, the fluxes must balance

$$\Gamma_i = \Gamma_e \tag{3.13}$$

$$n_{se} c_s M_{se} = \frac{1}{4} n_{se} \exp\left[\frac{e\Lambda_{se}}{T_e}\right] \bar{c}_e \tag{3.14}$$

$$c_s M_{se} = \frac{1}{4} \exp\left[\frac{e\Lambda_{se}}{T_e}\right] \bar{c}_e \tag{3.15}$$

$$\frac{\gamma_{a,e} T_e + \gamma_{a,i} T_i}{m_i} = \frac{1}{16} \exp\left[\frac{2e\Lambda_{se}}{T_e}\right] \frac{8T_e}{\pi m_e} \tag{3.16}$$

$$\boxed{\begin{aligned} \frac{e\Lambda_{se}}{T_e} &= \frac{1}{2} \ln\left[2\pi \frac{m_e}{m_i} M_{se}^2 \left(\gamma_{a,e} + \gamma_{a,i} \frac{T_i}{T_e}\right)\right] && (3.17) \\ \Lambda_{se} &\approx -2.8 \frac{T_e}{e} \text{ for } M_{se} = 1,\ T_i = T_e,\ \gamma_{a,i} = \gamma_{a,e} = 1 \text{ in Deuterium} && (3.18) \end{aligned}}$$

Currently, we take $\frac{e\Lambda_{se}}{T_e}$ as a constant, assuming $M_{se} = 1$, equal electron and ion temperatures and using the adiabatic index corresponding to the isothermal case. However, this is mainly for ease of implementation – we could considering adding the temperature ratio and M_{se} dependencies, or using a different adiabatic index. The effect of this is shown in figure 3.3 (generated using `sheath_potential.ipynb`).

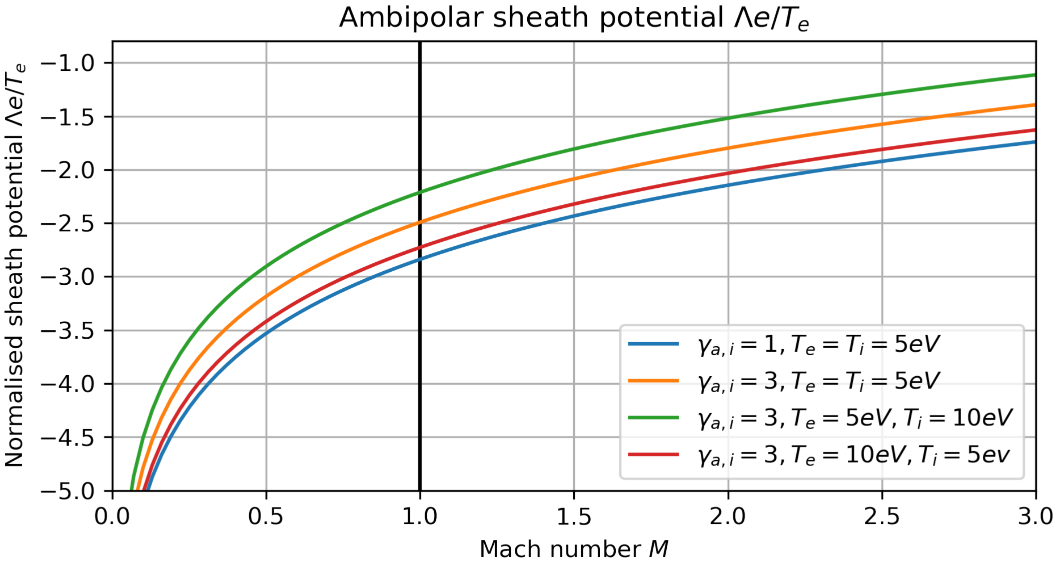

Figure 3.3.: The ambipolar sheath potential Λ_{se}, normalised to T_e/e. Although the Bohm criterion requires $M_{se} \geq 1$, subsonic solutions exist provided $M_{se} > 0$. We fix $\gamma_{a,e} = 1$ and show the effect of changing the ion adiabatic index $\gamma_{a,i}$, for solutions with $T_e = T_i$, $T_e > T_i$ and $T_e < T_i$.

3.2.3. Conducting-sheath boundary conditions

What happens if the potential drop across the sheath is not Λ_{se}? So long as the electric field points towards the wall, we assume that the ion flux should still equal the flux reaching the sheath entrance. The electron flux, however, will be modified by the new potential (which we denote ϕ_{se}, since we have assumed $\phi_{wall} = 0$), leading to a net current density

$$\begin{aligned} j &= e(\Gamma_i - \Gamma_e) && (3.19) \\ &= e n_{se} \left(c_s M_{se} - \frac{1}{4} \exp\left[\frac{e\phi_{se}}{T_e} \bar{c}_e \right] \right) && (3.20) \end{aligned}$$

Equation 3.15 lets us to rewrite this as

$$\boxed{\begin{aligned} j = j_{sat} \left(1 - \exp\left[\frac{e(\phi_{se} - \Lambda_{se})}{T_e} \right] \right) \\ \text{where } j_{sat} = e n_{se} M_{se} c_s \text{ is the } \textit{ion saturation current} \end{aligned}} \quad \begin{aligned} (3.21) \\ (3.22) \end{aligned}$$

Therefore, if $\phi_{se} \neq \Lambda_{se}$, there will be some finite current across the sheath. As $\phi_{se} \longrightarrow -\infty$ the positive current will saturate at j_{sat} (usually defined with $M_{se} = 1$) – which is the current associated with the ion flux and no electron flux (the strong electric field completely excludes electrons from entering the sheath) – while for large positive ϕ_{se} there is no limit in our model on the maximum negative current. However, we have used a very simple sheath model – in reality, the positive current can exceed j_{sat} due to electron emission from the wall [132], and the negative current also (approximately) saturates at the electron saturation current [133].

This then raises the question, what sets the value of ϕ_{se}? One way that we could find a boundary condition for ϕ is to find an expression for $\nabla_{\|}\phi$ from a simplified Ohm's law (by approximating terms in equation 2.62) [134]. Alternatively, if we assume that the current to the boundary is given, we can rearrange equation 3.21 to give a boundary condition for ϕ in terms of $j_{\|}$

$$\begin{aligned} 1 - \frac{j}{j_{sat}} &= \exp\left[\frac{e(\phi_{se} - \Lambda_{se})}{T_e} \right] && (3.23) \\ \frac{e(\phi_{se} - \Lambda_{se})}{T_e} &= \ln\left[1 - \frac{j}{j_{sat}} \right] && (3.24) \\ \phi_{se} &= \Lambda_{se} + \frac{T_e}{e} \ln\left[1 - \frac{j}{j_{sat}} \right] && (3.25) \end{aligned}$$

which only gives meaningful values for ϕ_{se} if $j < j_{sat}$.

3.3. The magnetic presheath entrance

In the previous section, we considered the case of an unmagnetised plasma. For a magnetised plasma, we still have a Debye sheath like the one discussed in the previous section, but also have

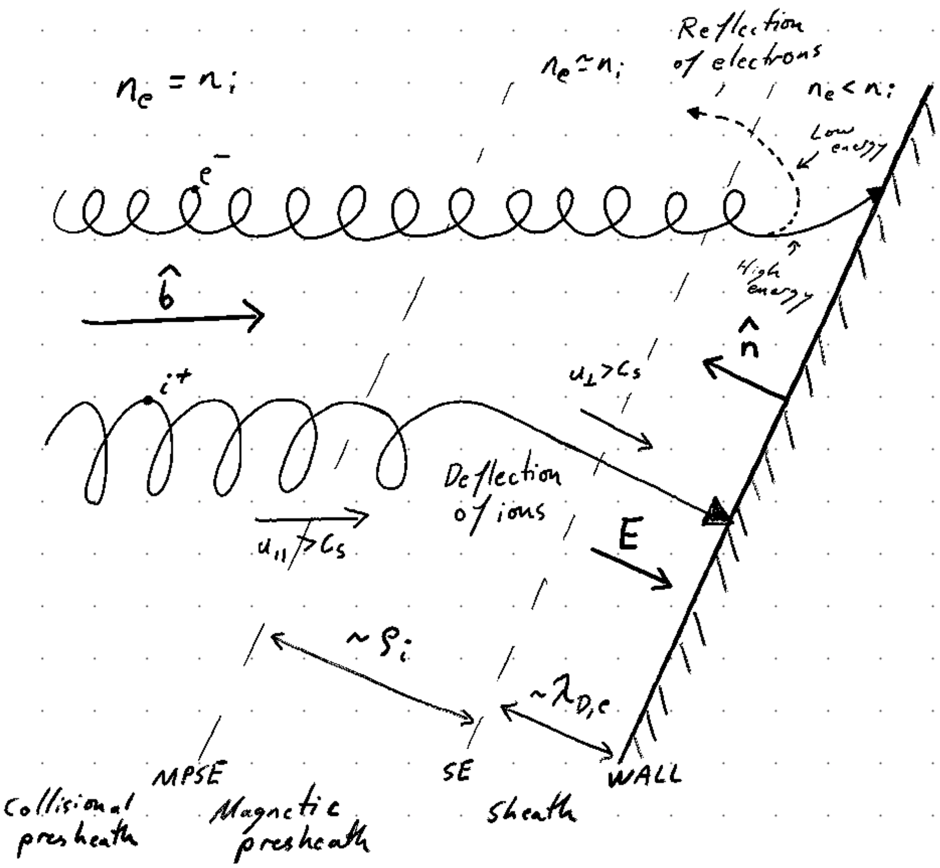

Figure 3.4.: Plasma-wall interface regions (modified from reference [135]). In a magnetised plasma, the plasma-wall interface can be broken into three distinct regions [136]. In the first, called the 'collisional presheath', the electron flux is driven by the pressure gradient, while an electric field ensures that the ion flux matches the electron flux. Moving towards the wall, at $\sim \rho_i$ from the wall the electric field (in the $\hat{\mathbf{n}}$ direction) becomes strong enough to deflect ions from the magnetic field, in the 'magnetic presheath'. Finally, within a few $\lambda_{D,e}$ of the wall, the electric field completely dominates the magnetic field, deflecting both ions and electrons. This region is called the 'Debye sheath'. In this figure, we show the magnetic field in 2D only – if you'd like, you can think of this as showing only the poloidal component of the magnetic field. Additionally, we have shown a 2D wall-normal vector, which is valid for the assumption of an axisymmetric wall, but which in general would also be in 3D. Irrespective of the representation shown here, the angle $\alpha = \cos^{-1}\left(-\hat{\mathbf{n}} \cdot \hat{\mathbf{b}}\right)$ should be calculated using 3D vectors.

an additional ‘magnetic presheath’, as indicated in figure 3.4. In the magnetic presheath the plasma is still quasineutral, but the electric field is strong enough to deflect ions from following the magnetic field. This breaks the ion drift ordering (2.30), and as such, we need boundary conditions for our model to apply at the magnetic presheath entrance (MPSE). To derive these, we need to have a model both for the sheath – which we discussed in the previous section – and another for the magnetic presheath – which we discuss here.

The size and effect of the magnetic presheath depends on the angle between the magnetic field $\hat{\mathbf{b}}$ and the wall normal vector $\hat{\mathbf{n}}$. If $\hat{\mathbf{b}} \parallel \hat{\mathbf{n}}$ (magnetic field perpendicular to the wall), the magnetic presheath disappears and we only have a sheath [136]. Conversely, for $\hat{\mathbf{b}} \perp \hat{\mathbf{n}}$ (magnetic field parallel to the wall), we need to model the finite Larmor radius of the particles [137, 138] and our simple sheath model breaks down. In between these two limits, we can modify our sheath boundary conditions to account for the magnetic presheath.

3.3.1. Bohm-Chodura and drift-corrections

The Bohm criterion is replaced by the Bohm-Chodura criterion [136, 139], which states that the *parallel* ion velocity $u_\parallel$ must exceed the local sound speed

$$u_{\parallel,mpse} = M_{mpse} c_s \text{ for } M_{mpse} \geq 1 \tag{3.26}$$

In a magnetised plasma, we can also have poloidal transport due to drifts. The $E \times B$ drift leads to an additional transport to the targets, and since usually $B_{pol}/B \ll 1$ the poloidal transport due to the drift can be as large as the poloidal transport due to $u_\parallel$ [139, 140]. Conversely, it is expected that the diamagnetic velocity does not lead to transport to the targets since the drift is deflected away from the targets, forming closed loops within the plasma [141]. We can ‘correct’ the parallel velocity boundary condition (3.26) to take into account the $E \times B$ transport. One way to do this would be to calculate the parallel velocity which would give as much poloidal transport as the $E \times B$ drift, and then add this to $u_\parallel$ in equation 3.26

$$\left(u_\parallel + \boldsymbol{u}_{E\times B} \cdot \hat{\mathbf{b}}_{pol} \frac{|B|}{B_{pol}} \right)_{mpse} = M_{mpse} c_s \tag{3.27}$$

$$\left(u_\parallel + \frac{\hat{\mathbf{b}} \times \nabla\phi}{B_{pol}} \cdot \hat{\mathbf{b}}_{pol} \frac{B}{|B|} \right)_{mpse} = M_{mpse} c_s \text{ where } \frac{B}{|B|} = \pm 1 \tag{3.28}$$

However, in the simulations in this thesis, we instead set

$$\boxed{\left(u_\parallel \hat{\mathbf{b}} \cdot \hat{\mathbf{n}} + \boldsymbol{u}_{E\times B} \cdot \hat{\mathbf{n}} \right)_{mpse} = M_{mpse} c_s \hat{\mathbf{b}} \cdot \hat{\mathbf{n}}} \tag{3.29}$$

which prevents $E \times B$ influx across the boundary. The motivation for this was to try prevent a strong ion heating observed near the boundaries, which was originally thought to be due to a spurious source of T_i via $E \times B$ transport across the boundary. However, it was later realised that this heating was caused by the $\frac{T_i}{n} \nabla \cdot j_\parallel \hat{\mathbf{b}}$ (compression of $v_\parallel$) term in equation 2.71, and so in future work we could consider using equation 3.27, or the more involved boundary condition in reference [140] (our boundary condition corresponds to the 'intuitive' solution in this reference, which is valid only for insulating boundary conditions) or reference [142].

3.3.2. Current and potential in the magnetic presheath

Using kinetic modelling Chodura showed that the potential difference across the sheath and magnetic presheath does not vary significantly with the angle $\alpha = \cos^{-1}\left(-\hat{\mathbf{n}} \cdot \hat{\mathbf{b}}\right)$ – although the fraction of the total potential drop in the magnetic presheath does vary – provided that $\alpha > 10°$ [136]. For most tokamaks of interest, however, $\alpha < 10°$ and so we should consider the effect of the incidence angle on ϕ_{mpse}. Unfortunately, a closed form solution for ϕ_{mpse} as a function of α is not available, and so we assume that ϕ_{mpse} is the same the sheath entrance potential for the normal sheath. In reference [130], kinetic modelling finds that $\phi_{se}\frac{T_e}{e} \approx 3$ for $\alpha \in [1.5°, 3°]$, which is close to the result from the normal sheath.

For the current, since the magnetic pre-sheath is quasineutral we require $\nabla \cdot j = 0$. We can additionally neglect the diamagnetic current (since the diamagnetic drift doesn't lead to transport to the plates) and the $E \times B$ drift (since this drift is ambipolar), so we simply set the parallel current density at the magnetic presheath entrance equal to the sheath current

$$\boxed{j_{\|,mpse} = e n_{mpse} M_{mpse} c_s \left(1 - \exp\left[\frac{e(\phi_{mpse} - \Lambda_{se})}{T_{e,mpse}}\right]\right)} \tag{3.30}$$

3.4. Density boundary condition and recycling

When a plasma reaches the solid walls of the reactor, the ions and electrons recombine on the surface. As such, the walls act as a sink for plasma and a source for neutral particles. We can find a boundary condition for the plasma density by simplifying the ion continuity equation, by neglecting drifts, assuming no sources and ignoring the time-derivative, such that

$$\nabla \cdot \left(n u_{\|} \hat{\mathbf{b}}\right) = 0 \tag{3.31}$$

Therefore, under these strong assumptions, the particle flux across the boundary $n u_{\|}$ should be constant. Alternatively, we could use the electron continuity equation (2.56), replacing the drifts with parallel velocities which give the same poloidal transport (see equation 3.27). However, these boundary conditions have not yet been tested, and for numerical stability in this thesis we use a Neumann boundary condition

$$\boxed{\nabla_{\|} n = 0} \tag{3.32}$$

The neutrals at the wall can either be removed by pumps or be excited and re-ionised, acting as a source of plasma and a sink of energy[2]. For typical fusion plasmas, the plasma source and sink due to *recycling* of particles at the walls is *much* stronger than the source due to gas injection and the sink due to pumping. However, we don't include a neutral model in this thesis, so we use a density source to try to mimic neutral ionisation.

3.5. Temperature boundary conditions: sheath heat transmission factors

As well as providing a particle sink, the walls also act as an energy sink. This is a distinctively kinetic effect: the sheath acts as a high-energy filter for the electrons, and therefore *cools* the interior electron distribution beyond what is expected from the advected energy loss. For the ions, the velocity distribution in the sheath is strongly non-Maxwellian, and so we need to adjust our energy loss term. Rather than trying to determine the effective heat loss from a simple model, we usually rely on *sheath heat transmission coefficients*. These coefficients give the ratio of the total heat flux crossing the sheath entrance to the advected heat flux at the sheath entrance, and they require kinetic modelling to get reasonable estimates for [143, 130]. As such, the sheath heat coefficients are *inputs* to our simulations, with typical values between $\gamma_e \sim 1.5 - 8$ and $\gamma_i \sim 1 - 2$ (due to the large uncertainty, it doesn't make sense to distinguish between the sheath and the magnetic presheath) [135]. From the definition of the sheath heat coefficients

$$q_{s,mpse} = n_{mpse} u_{mpse} T_{s,mpse} - \chi_{\parallel,s} \nabla_\parallel T_{s,mpse} \tag{3.33}$$

$$\gamma_s = \frac{q_{s,mpse}}{n_{mpse} u_{mpse} T_{s,mpse}} \tag{3.34}$$

$$= 1 - \frac{\chi_{\parallel,s} \nabla_\parallel T_{s,mpse}}{n_{mpse} u_{mpse} T_{s,mpse}} \tag{3.35}$$

$$\boxed{-\frac{\chi_{\parallel,s} \nabla_\parallel T_{s,mpse}}{n_{mpse} u_{mpse} T_{s,mpse}} = \gamma_s - 1} \tag{3.36}$$

This gives a Robin boundary condition for the electron and ion temperatures.

3.6. Discussion

The walls have a leading-order effect on the edge plasma, and accurately capturing the effects of the sheath on the bulk plasma is a serious challenge for edge modelling. In this chapter, we arrived at a set of boundary conditions to apply at the magnetic presheath entrance by making

---

[2] In addition to recycling the main plasma species, the walls also act as a source of non-fuel impurities. These impurities typically radiate much more efficiently than the fuel, and so have a significant effect even when present only in small concentrations. The rates at which wall impurities are generated is determined by processes such as direct erosion and implantation of ions in the wall – which are difficult to model. Additionally, impurities may also be intentionally injected, to enhance the radiative power dissipation. In this thesis, impurities are neglected entirely.

some very haphazard assumptions. The first (implicit) assumption that we made was that there actually exists a sensible way to couple a fluid model to the sheath. Since the sheath requires a full-kinetic description and it strongly modifies the distribution function in the edge, there may not be an accurate way to model the plasma near the sheath with a fluid model [130]. Then, to arrive at a set of solvable boundary conditions, we made several simplifying assumptions, without considering what the limits of these assumptions are (or even if they are valid at all). A further challenge is to find boundary conditions that are compatible with the interior model and numerics. As we will show in section 4.5, this is far from trivial – the sheath acts like a shock, and so this prevents us from always using physically motivated boundary conditions.

To test different boundary conditions and determine which ones give reasonable results, comparisons against experiment are extremely helpful. Here, we care more about the impact of the boundary conditions on the measured plasma profiles, rather than accurately modelling the sheath itself. As such, we validate the bulk plasma and boundary conditions together, rather than trying to investigate the boundary conditions by themselves.

In part III, we show that the choice of boundary conditions has a significant effect on the interior plasma and that much of the disagreement can be linked to boundary conditions. As such, this is a topic which we should focus on in future work. One solution might be to try to build boundary conditions from the interior equations, substituting in physically reasonable estimates of the boundary values where possible, and then simplifying until we can prescribe boundary values or gradients from the equations. Alternatively, we could aim to include more physics effects in the boundary conditions, generalising them to be valid at higher collisionality [144, 143] or including kinetic modifications [145, 130]. For either approach, it is likely that analytical solutions will not be available, and as such we could consider including an additional iterative model to find consistent solutions for the MPSE [140]. As an additional note – since our boundary conditions are not self-consistent, we will need to carefully test them across a range of plasma conditions. In particular, for fully-detached plasmas, our simple sheath model will probably be too inaccurate, and so we will need to determine a new set of boundary conditions (see the discussion in section 2.3 of reference [43]).

3.7. Further reading

- Loizu, 2013, *The role of the sheath in magnetized plasma turbulence and flows (PhD thesis)*: a long-form introduction to sheath physics in the context of turbulence simulations
- Stangeby, 2000, *The plasma boundary of magnetic fusion devices*: although mainly focussed on steady-state transport modelling, this classic text describes the sheath in great detail.

4. Numerical implementation

4.1. What, why, and how? Local field-alignment for computationally efficient simulations

In fusion plasmas, the strong confining magnetic field leads to very different dynamics parallel and perpendicular to the magnetic field. The magnetic field mostly prevents particles from being transported perpendicular to the field, while particle transport parallel to the field is mostly unaffected and therefore much faster than perpendicular transport. As a result, perturbations are typically highly elongated parallel to the magnetic field and comparatively small perpendicular to the magnetic field. We already used this ‘flute-mode’ nature of the turbulence to perform the drift ordering in section 2.2.5, but we can also use it to build efficient computational grids.

In this chapter, we discuss how the model and boundary conditions developed in previous chapters (our conceptual model) are *discretised*[1] and implemented as code (our numerical model). In particular, we discuss in depth the parallel discretisation method – the ‘flux-coordinate-independent field-aligned’ – since this discretisation method is a large part of why GRILLIX is able to flexibly and efficiently simulate arbitrary magnetic geometries. We first sketch the basic idea behind local field-alignment (section 4.3), then introduce the actual parallel operators used, and explain why we need to use toroidally staggered grids. We discuss a peculiarity of the discretised equations which leads to strong corrugations near the sheath boundaries, and the immersed boundary method used to resolve this issue. Finally, we use the *method of manufactured solutions* to *verify* our implementation, and close with a discussion of current research efforts.

4.2. Field alignment

Within the confined region, many grid-based codes use a field-aligned grid, using a coordinate system such as those described in references [146, 147, 148]. In field-aligned coordinate systems, the coordinates are defined in such a way that the magnetic field-lines appear as straight lines in the coordinate system. Aligning the grid to the magnetic field greatly simplifies both analytic and numerical computations. Additionally, with the flute-mode assumption, we can reduce the resolution in the parallel direction. This directly reduces the computational cost by reducing the number of computational points, and also allows for a larger time-step since the fast parallel dynamics have the most severe CFL criterion. However, such coordinate systems cannot be applied across the separatrix [122].

---

[1] Discretisation is the representation of the continuous dynamics over some finite-resolution grid.

To treat the separatrix and the open field-line region, we instead use a ‘locally field-aligned’ (LFA) coordinate system. This method was originally developed in references [149, 150, 151], to preserve the benefits of field-aligned methods while also being able to cross the separatrix. A method for reducing spurious cross-field diffusion was developed in references [122, 152], which forms the basis for the method used in GRILLIX. This method was extended to treat complex boundaries and arbitrary geometry in references [109, 125]. Beyond GRILLIX, the locally field-aligned method is also used in FELTOR [107], a gyrofluid code, BOUT++/BSTING [153], a fluid code capable of modelling stellarators, GDB, a fluid which uses a toroidal coordinate system [115] and recently GENE-X [103], a gyrokinetic code. As a note on terminology, the method is usually termed the ‘flux-coordinate-independent field-aligned’ or ‘FCI’ method, although we prefer ‘locally field-aligned’ for describing what the method is, rather than what it is not.

4.3. Local field-alignment – the basic concept

The basic concept of the locally field-aligned method is refreshingly simple. It is easiest to describe by considering how we would build a grid for some arbitrary tokamak configuration. First of all, we assume that the configuration is perfectly axisymmetric – which isn’t actually necessary (see reference [154]), although it does simplify the book-keeping. We divide the torus into N_{pol} equal sections, and at the centre of each section we define a R, Z plane at some constant toroidal angle $\phi = i\frac{2\pi}{N_{pol}}$ for $i = 1, 2, \ldots$. For each poloidal R, Z plane, we define a two-dimensional grid. In GRILLIX, we always use a regularly spaced Cartesian grid, although again this isn’t strictly necessary [153]. With axisymmetry and a Cartesian grid in the poloidal planes, the resulting grid is simply a R, ϕ, Z cylindrical grid[2]. From each R, ϕ, Z point, we trace $\pm\Delta\phi$ along the magnetic field using an ordinary-differential-equation integrator, as shown in figure 4.1

$$\frac{\partial R}{\partial \phi} = \frac{B_R}{B_\phi} \iff R(\phi + \Delta\phi) = R(\phi) + \int_0^{\Delta\phi} \frac{B_R(\gamma)}{B_\phi} R d\phi \tag{4.1}$$

$$\frac{\partial Z}{\partial \phi} = \frac{B_Z}{B_\phi} \iff Z(\phi + \Delta\phi) = Z(\phi) + \int_0^{\Delta\phi} \frac{B_Z(\gamma)}{B_\phi} R d\phi \tag{4.2}$$

$$\frac{\partial l_\|}{\partial \phi} = \frac{B}{B_\phi} \iff l_\|(\phi + \Delta\phi) = \int_0^{\Delta\phi} \frac{B(\gamma)}{B_\phi} R d\phi \tag{4.3}$$

where $\gamma(\phi) = (R(\phi), \phi, Z(\phi))$ is the characteristic curve of the magnetic field-line (see III.A of reference [109]), $l_\|$ is the length along the magnetic field-line, and the factor of R comes from the cylindrical coordinate system. We can use numerical field-line tracing to find the points

---

[2] We could directly discretise the equations using expressions for the operators in cylindrical coordinates, which is called the non-aligned discretisation method. Non-aligned methods are useful for isotropic systems, while for flute-mode turbulence aligned methods are typically more computationally efficient.

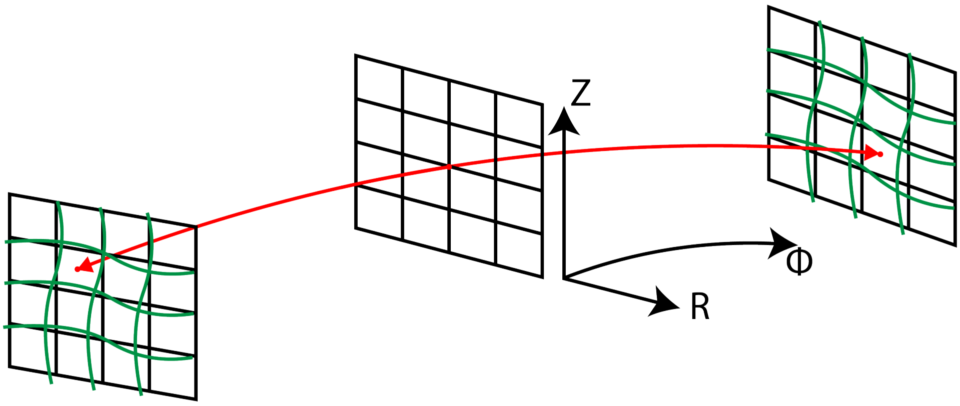

Figure 4.1.: The basic concept behind the locally-field-aligned method. For each point, we trace in both field-directions to neighbouring poloidal planes. The values at the intersection points can be computed via interpolation and used to compute parallel operators. *N.b. the actual method used in GRILLIX is slightly more complicated – see figure 4.2.*

which are field-line connected to our start point, allowing us to calculate parallel gradients. Typically, the points where the magnetic field intersect the neighbouring planes are not actual grid points, and so we use interpolation to find the value at the intersection point. Then, we can simply calculate perpendicular derivatives using standard two-dimensional finite differences, and parallel derivatives from the interpolated values.

4.4. Parallel operators and toroidal staggered grid

In GRILLIX, the actual parallel discretisation method is similar to a finite-volume method [122, 152, 108]. In addition to the cell-centred poloidal planes introduced in the previous section, we also introduce toroidally-staggered poloidal planes at the faces between the cells. Scalar quantities like the density, temperature and electrostatic potential are defined at the cell-centres, while vector quantities like the parallel velocity, current and vector potential are defined at the cell-faces. We then introduce two parallel operators – a *parallel derivative* which takes quantities on the scalar grid and returns a value on the vector grid, and a *parallel divergence* which takes quantities on the vector grid and returns a value on the scalar grid.

For the parallel derivative, around each point on the vector grid we define a hexahedral flux box, indicated in figure 4.2. The points of the cell are determined by field-line tracing $\phi \pm \frac{1}{2}\frac{2\pi}{N_{pol}}$ from the four corners of a square $R \pm h/2, Z \pm h/2$ around the point R, ϕ, Z. The parallel derivative is defined in terms of a volume integral over the cell. This lets us resolve regions like the X-point where neighbouring field-lines separate quickly, without having to increase the

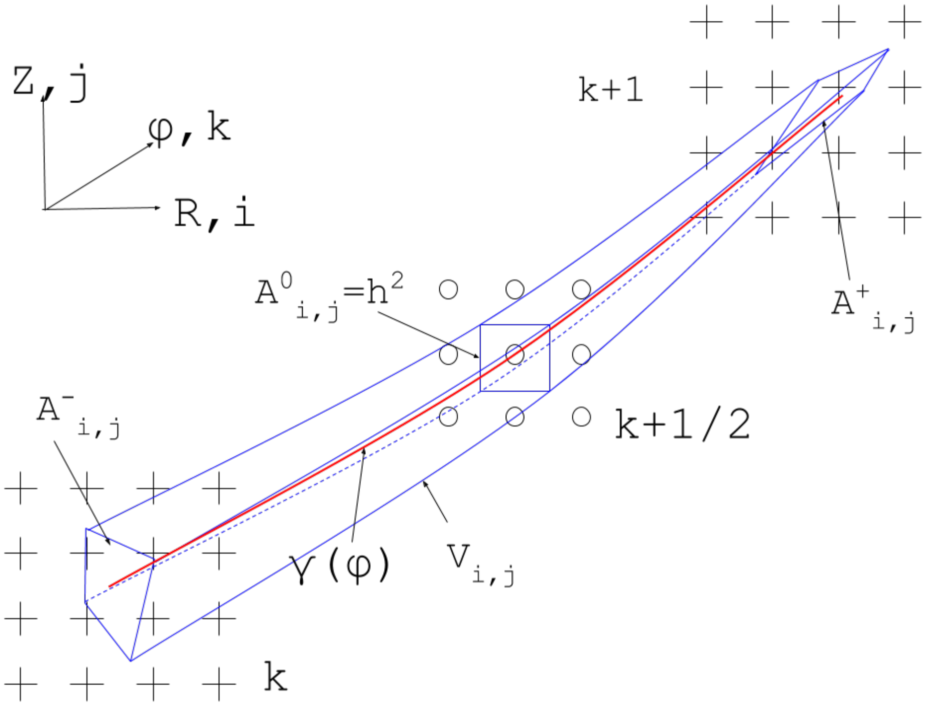

Figure 4.2.: In GRILLIX (figure 7 from the GRILLIX manual), the parallel gradient for the (i, j) point on the $\left(k+\frac{1}{2}\right)^{\text{th}}$ plane is defined in terms of an integration over a flux box (*marked in blue*). The flux box is defined via tracing to the k^{th} and $(k+1)^{\text{th}}$ toroidal planes from the corners of a square of side length h (the poloidal grid spacing) centred at the point. Integration is performed at the ends of the flux box via numerical integration over interpolated points.

toroidal resolution [152]. The parallel derivative in GRILLIX is defined as

$$\nabla_{\parallel} u = \frac{1}{B} \nabla \cdot (u\boldsymbol{B}) \tag{4.4}$$

$$= \lim_{V_{cell} \to 0} \frac{1}{BV_{cell}} \int_{\partial V_{cell}} u\boldsymbol{B} \cdot d\boldsymbol{S} \tag{4.5}$$

Only the ends of the flux box contribute to the integral, so we can discretise this as

$$\left(\nabla_{\parallel} u\right)_{i,j,k+\frac{1}{2}} = \frac{1}{B_{i,j} V_{i,j}} \left[\int_{A^{+}_{i,j}} u_{k+1} B_{\phi} dA - \int_{A^{-}_{i,j}} u_k B_{\phi} dA \right] \tag{4.6}$$

where the integrals are evaluated using numerical integration of interpolated points on the k^{th} and $(k+1)^{\text{th}}$ toroidal planes. The parallel divergence is then constructed from the parallel gradient using the method of support operators (see the GRILLIX manual and reference [155]). We define an inner product between two arbitrary test functions u and v as

$$\langle u, v \rangle = \oiiint_{\mathcal{V}} uv d\mathcal{V} \tag{4.7}$$

On a continuous level, via integration-by-parts

$$\oiiint_{\mathcal{V}} u \nabla \cdot \left(\nabla_{\parallel} v \hat{\mathbf{b}}\right) d\mathcal{V} = - \oiiint_{\mathcal{V}} \nabla_{\parallel} u \nabla_{\parallel} v d\mathcal{V} + \text{surface terms} \tag{4.8}$$

We discretise $\nabla_{\parallel}$ according to equation 4.6 and $\langle \cdot, \cdot \rangle$ as a sum over all grid points. The parallel gradient and divergence are expressed as matrices $\boldsymbol{Q}$ and $\boldsymbol{Q}^*$. Since the parallel gradient maps vectors from the scalar grid onto the vector grid, the left and right hand sides of equation 4.8 will be on different grids and so at first we sum these over different indices (dropping the surface terms)

$$\sum_{\alpha_1, \beta_1, \gamma_1} \mathbf{u}_{\alpha_1} \mathbf{Q}^*_{\alpha_1 \beta_1} \mathbf{Q}_{\beta_1 \gamma_1} \mathbf{v}_{\gamma_1} V_{\alpha_1} = - \sum_{\alpha_2, \beta_2, \gamma_2} \mathbf{Q}_{\alpha_2 \beta_2} \mathbf{u}_{\beta_2} \mathbf{Q}_{\alpha_2 \gamma_2} \mathbf{v}_{\gamma_2} V_{\alpha_2} \tag{4.9}$$

However, without losing generality, we can relabel the indices. We set $\beta_2 = \alpha_1$, $\alpha_2 = \beta_1$ and $\gamma_2 = \gamma_1$ to let us cancel the arbitrary test functions, then drop the subscripts on the indices. Since the test functions are arbitrary (i.e. they could also be δ-functions), each term in the sum must also be equal and so

$$\mathbf{u}_{\alpha} \mathbf{Q}^*_{\alpha\beta} \mathbf{Q}_{\beta\gamma} \mathbf{v}_{\gamma} V_{\alpha} = \mathbf{Q}_{\beta\alpha} \mathbf{u}_{\alpha} \mathbf{Q}_{\beta\gamma} \mathbf{v}_{\gamma} V_{\beta} \tag{4.10}$$

$$\mathbf{Q}^*_{\alpha\beta} = \mathbf{Q}_{\beta\alpha} \frac{V_{\alpha}}{V_{\beta}} \tag{4.11}$$

Therefore, the discrete parallel divergence is equal to the transpose of the discrete parallel gradient, multiplied by a volume correction factor. This method ensures that the discretise parallel gradient will be the negative adjoint of the parallel divergence

$$\left(\nabla_{\parallel}\right)^{\dagger} = -\nabla \cdot \circ\hat{\mathbf{b}} \tag{4.12}$$

on a discrete level. It also ensures that second-order differential operators of the form $\mathcal{L}\left(u(x)\right) = \frac{d}{dx}\left(p_0(x)\frac{du}{dx}\right) + p_2(x)u(x)$ such as the parallel diffusion will be *self-adjoint.* In equations 34 and 35 of reference [122] it is shown that this method reduces spurious perpendicular diffusion, which is extremely important for turbulence simulations. Since the physical cross-field transport due to turbulence is slow compared to the parallel transport, additional cross-field transport due to numerical pollution can quickly to lead to unphysical plasma profiles. As such, the self-adjoint method is necessary for accurate turbulence simulations.

4.5. Boundary stencil collapse

The locally field-aligned method works well when the turbulence is strongly elongated along the magnetic field. However, as we discussed in chapter 3, in the vicinity of the solid walls the plasma dynamics lose field-alignment due to the strong sheath electric field. As well as modifying our equations, the sheath can be difficult to treat numerically. This is true for all turbulence codes, but the use of a toroidally-staggered grid for GRILLIX makes this issue particularly severe.

To illustrate the issue we will consider a simplified 1D advection model. If we consider only the parallel components of the continuity and momentum balance equations and ignore the effect of anything that isn't the density or velocity, we can write a simplified set of equations

$$\partial_t n = -\nabla \cdot (n u_{\parallel} \hat{b}) + \mathcal{S}_n \tag{4.13}$$

$$\partial_t u_{\parallel} = -u_{\parallel}\nabla_{\parallel}u_{\parallel} - \frac{\nabla_{\parallel} n}{n} \tag{4.14}$$

As discussed in the previous section, the scalar grid (SG, for n) and vector grid (VG, for $u_{\parallel}$) are toroidal staggered (i.e. the vector grid lies halfway between two scalar grid planes, and vice-versa – see figures 4.4 and 4.5). The parallel operators map from one grid to another

$$(\nabla_{\parallel} f)_{i+1/2} = \frac{f_{i+1} - f_i}{\Delta x} \text{ maps } f \in SG \rightarrow (\nabla_{\parallel} f) \in VG$$

and

$$\nabla \cdot (\hat{b} q)_i = \frac{q_{i+1/2} - q_{i-1/2}}{\Delta x} \text{ maps } q \in VG \rightarrow \nabla \cdot (\hat{b} q) \in SG$$

We additionally define mapping operators

$$f^*_{i+1/2} = \frac{f_{i+1} + f_i}{2} \text{ maps } f \in SG \rightarrow f^* \in VG$$

and

$$q^*_i = \frac{q_{i+1/2} + q_{i-1/2}}{2} \text{ maps } q \in VG \rightarrow q^* \in SG$$

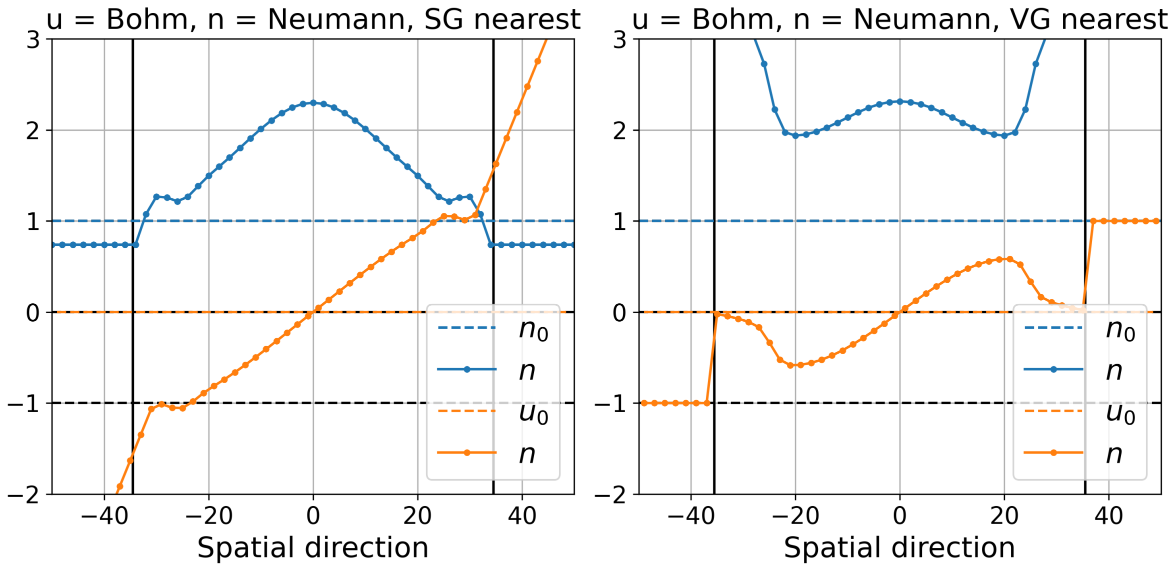

Figure 4.3.: Density and velocity after 100 time-steps of the advection equations, with $u_{\|} \geq c_s$ and $\nabla_{\|} n = 0$ used as boundary conditions. In the left figure, the scalar grid is the closest point to the boundary (as in figure 4.4), while in the right figure the vector grid is the closest point to the boundary (as in figure 4.5).

We can discretise the system of equations, to see how the system evolves for different choices of boundary conditions. We assume that $\mathcal{S}_n$ is a constant Gaussian density source, located at the centre of the domain. For simplicity, we make our domain symmetric around $x = 0$, and define left and right boundaries at $-x_B$ and x_B. Grid points are added at integer values, with even-integer values assigned to the scalar grid and odd-integer values assigned to the vector grid. We do not require that the boundary is on a grid point since in the 3D system a magnetic field-line can intersect the boundary at any position along the wall, and not necessarily on a poloidal plane. A Jupyter notebook showing the discretisation of this set of equations is available at `boundary_advection.ipynb`, which uses a simple diffusion-stabilised FTCS scheme.

We defined boundary conditions to apply at the walls in chapter 3. Ignoring the drift

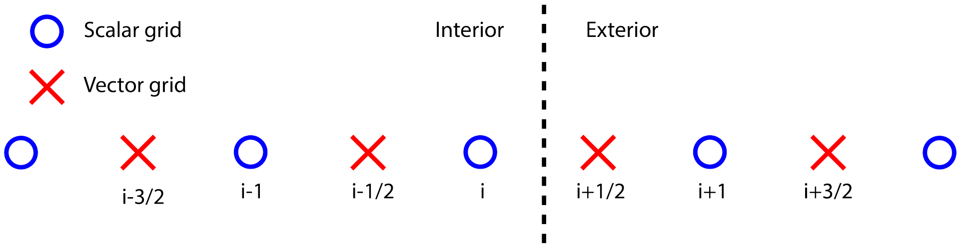

Figure 4.4.: Grid with scalar-grid point nearest to the boundary

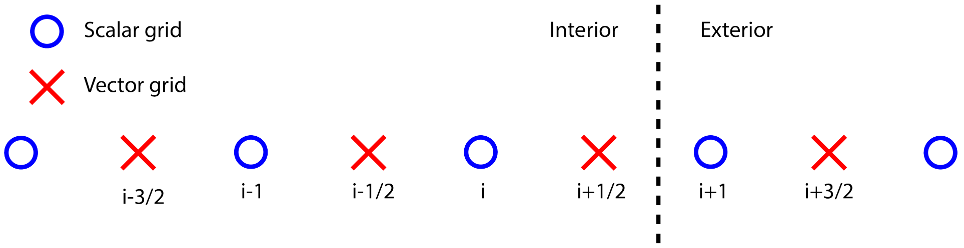

Figure 4.5.: Grid with vector-grid point nearest to the boundary

corrections since we are in 1D, the boundary conditions for the velocity and density are

$$u_{\|} \geq c_s \text{ and } \nabla_{\|} n = 0 \tag{4.15}$$

which is a Bohm boundary condition for velocity and a Neumann boundary condition for density. A snapshot of the density and velocity is shown after 100 time-steps in figure 4.3. The left-hand figure looks like a reasonable solution to the advection equations. The right-hand figure, on the other hand, looks completely different. The difference between these figures is that we shifted our boundary by a small distance Δx (the distance between the scalar and vector grid points) and have found a completely different result. This is a problem: we can't constrain the parallel distance from grid-points to the sheath boundaries in 3D, so have a continuous range of boundary positions. As shown in figure 4.6 where we scan the boundary position, the evolution of the interior points is determined by whether the grid point closest to the boundary in on the scalar grid (figure 4.4) or the vector grid (figure 4.5). Therefore, two neighbouring field-lines can have dramatically different dynamics, leading to severe corrugations in the poloidal plane. We can explain why this is by looking at the discrete forms of the equations

$$n_i^{t+1} = n_i^t - \frac{\Delta t}{\Delta x}\frac{1}{2}\left(u_{i+1/2}(n_{i+1}+n_i) - u_{i-1/2}(n_i+n_{i-1})\right) \tag{4.16}$$

$$u_{i+1/2}^{t+1} = u_{i+1/2}^t - \frac{\Delta t}{\Delta x}\left(u_{i+1/2}\frac{u_{i+3/2}-u_{i-1/2}}{2} + 2\frac{n_{i+1}-n_i}{n_{i+1}+n_i}\right) \tag{4.17}$$

In the scalar-grid-adjacent case shown in figure 4.4, the density at point i evolves according to the interior dynamics, while the velocity at point $i+1/2$ is set according to the boundary condition. If $u_{i+1/2} \neq u_{i-1/2}$ or $n_{i+1} \neq n_{i-1}$, the time-derivative of n in equation 4.16 will be non-zero. This in turn leads to a density gradient, and as such the time-derivative of u in equation 4.17 is also non-zero. In the vector-grid-adjacent case shown in figure 4.5, both n_i and $u_{i+1/2}$ evolve according to the interior dynamics, and boundary conditions are applied at n_{i+1} and $u_{i+3/2}$. If we pick an intentionally-difficult initial condition with $u = 0$ and $n = 1$, the issue is easy to see. Both $u_{i+1/2} = u_{i-1/2} = 0$, so the time-derivative of n in equation 4.16 will be zero. Then, if $n_{i+1} = n_i$, the time-derivative of u in equation 4.17 will also be zero. Therefore, regardless of what boundary condition is set on the velocity, if the density gradient across the boundary is zero, the equations will *never evolve*. At this point, it is natural to ask whether this is a peculiarity of our initial condition. However, regardless of what we select as our initial condition, in the vector-grid-adjacent case the continuity equation (equation 4.16) the

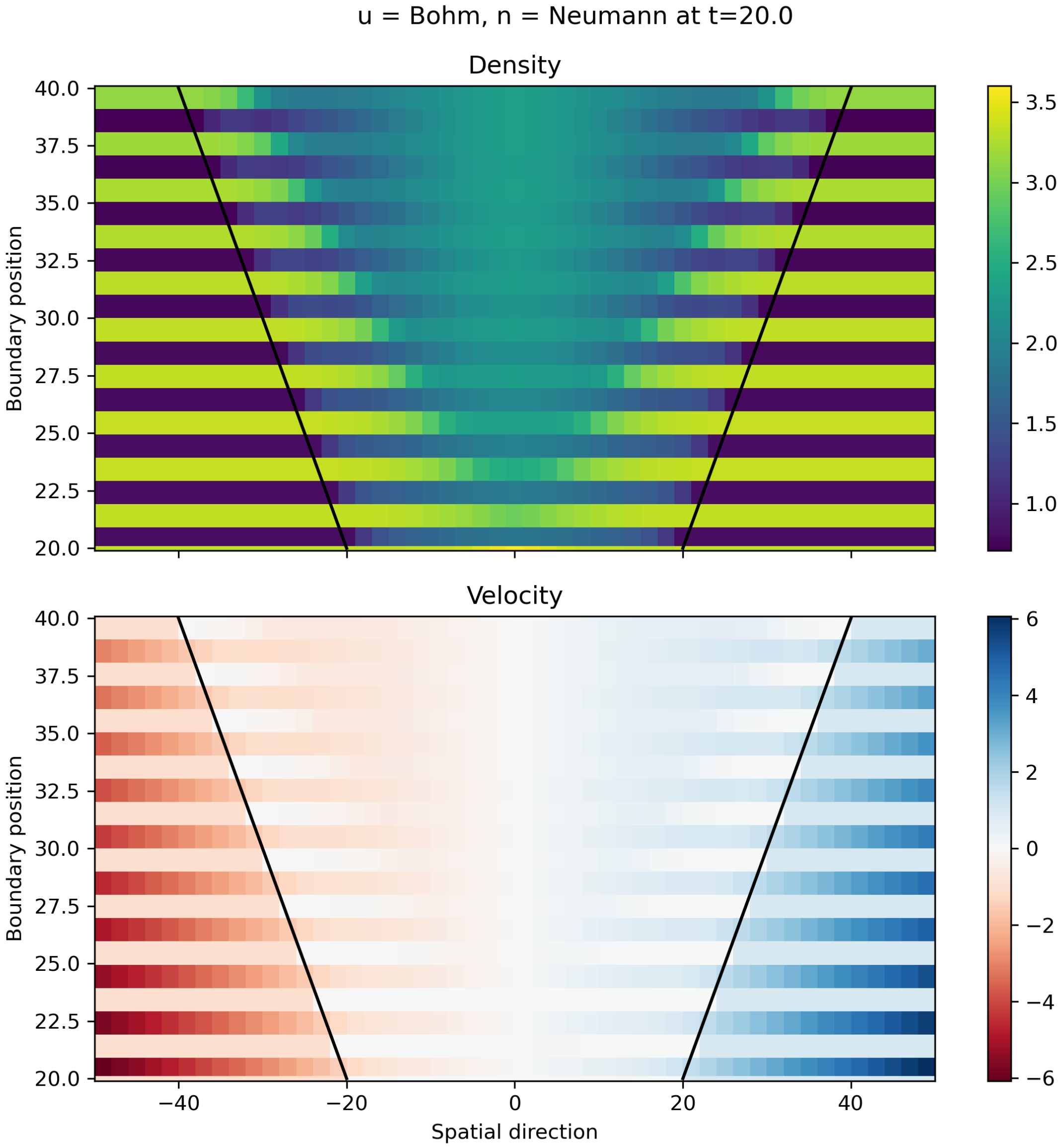

Figure 4.6.: Density and velocity profiles after 100 time-steps of the advection equations, with $u_{\|} \geq c_s$ and $\nabla_{\|} n = 0$ used as boundary conditions. The vertical coordinate gives the boundary position. Distinctive behaviour is seen depending on whether the boundary is between a scalar grid point inside and vector grid point outside (for boundary position between an even and an odd number), or vice-versa.

velocity boundary condition is not in any density evolution stencil. In the case of the $u \geq c_s$, $\nabla_{\|} n = 0$ boundary conditions, $\partial_t u = -u \nabla_{\|} u - \frac{1}{n}\cancel{\nabla_{\|} n}$, an increasing velocity gradient (due to the boundary condition) and a zero density gradient (also due to the boundary condition) causes a *decrease* in the velocity in front of the boundary, and therefore an increase in the density in front of the boundary – leading to the profile seen on the right in figure 4.3.

4.6. Immersed boundary method

To deal with the boundary conditions in GRILLIX, we have two methods for setting boundary conditions. The first method is to directly compute the value of ghost cells, as described in section 3.4 of reference [108]. This method works by calculating what values are required at exterior points such that derivatives are the same as those which would be calculated if a boundary condition was applied exactly at the boundary, which is used for perpendicular boundary conditions. However, for the parallel boundary conditions we need to ensure that neighbouring field-lines evolve continuously – and in particular, need to avoid the corrugations discussed in the previous section. As such, we use an immersed boundary method[3] for setting parallel boundary conditions, which is described in section III.B of reference [109] and section 3.4 of reference [125]. Instead of setting boundary conditions directly on some interior dynamics $\partial_t f = F_f$, we use a modified equation which we solve over a larger domain (which encompasses the interior, plus a region around it)

$$\frac{\partial f}{\partial t} = (1 - \chi_P) F_f + \frac{\chi_P}{\epsilon_P}(f_P - f) \tag{4.18}$$

where χ_P is a mask function, equal to 0 in the interior and 1 in the exterior, ϵ_P is a small user-defined number and f_P is a value of the field f which would give the desired boundary condition. The advantage of this method is that the mask function can be modified to improve numerical stability. We typically define

$$\chi_P = 1 + \mathcal{S}_3(\Delta\phi_{rev}, w_P) - \mathcal{S}_3(\Delta\phi_{forw}, w_P) \tag{4.19}$$

where $\mathcal{S}_3$ is a third-order smooth-step function

$$\mathcal{S}_3(x, w_P) = 6\,(x/w_P)^5 - 15\,(x/w_P)^4 + 10\,(x/w_P)^3 \tag{4.20}$$

By adjusting the width w_P of the smooth-step function, we can smooth the corrugations due to the boundary stencil collapse. As an example, we show χ_P for the TCV-X21 case in figure 4.7. The method has proven to be useful and numerically stable. Since we switched to using the immersed boundary method in GRILLIX, we have performed simulations with the full model in open-field-line geometries, which were unstable with the Taylor-expansion boundary method [108]. However, it is far from an optimal method. One issue is that the boundary is no longer

---

[3] In previous publications, we called this a penalisation method. However, the method is distinct from the method described in reference [156] – instead, we directly select the values of f_P to enforce a desired boundary condition.

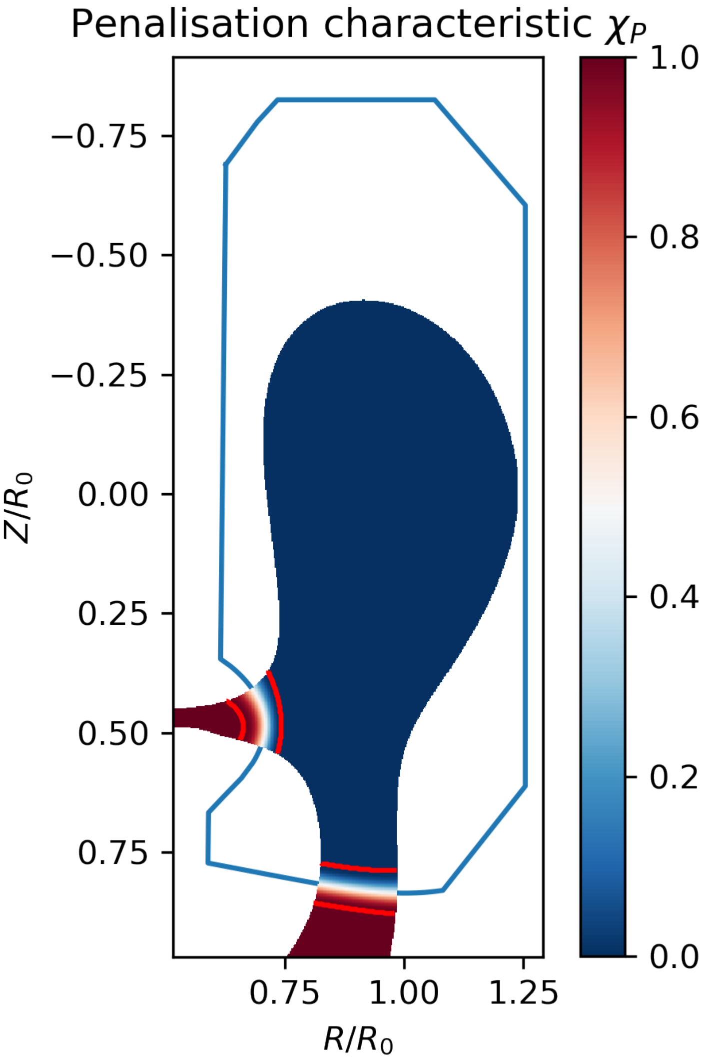

Figure 4.7.: The penalisation characteristic function used for the TCV-X21 case discussed in chapter 8. The χ_P function varies smoothly from 0 inside the domain to 1 outside the domain, over some number of toroidal planes. The boundaries where the function is exactly 0 or exactly 1 are marked in red. Here, we modified the position of the boundaries (relative to the real TCV divertor targets) to fit a large penalisation transition region.

defined at a single point, which makes it difficult to evaluate conservative boundary conditions such as particle recycling. Another issue is that the transition region required is usually quite wide – and as such, we need magnetic data for a region outside of the reactor vessel. We can pad numerical equilibria with artificial magnetic data, although this isn't always well-behaved and so we sometimes have to shift the boundaries inwards (as seen in figure 4.7). As such, it would be extremely beneficial to identify a set of boundary conditions which are both physically reasonable and which eliminate the need for a finite transition width. This is an active area of research, discussed more in Appendix C.3.

4.7. Verification with MMS

Using the discretisation, numerical method and boundary conditions discussed in this chapter, we can convert our conceptual model (equations) into a computational model (code). This is easier said than done: our model equations are quite complicated and we need to do a lot of work to set up the simulations! As of writing, the current version of GRILLIX has just under 30,000 lines of Fortran code[4]. It's almost inevitable to introduce translation errors – a `2` instead of a `2.0` for instance. While a lot of translation errors can be caught by code review or by a good compiler, these methods aren't guaranteed to catch everything. Another more subtle error arises if our numerical scheme is non-convergent. As we increase our spatial and time resolution, our solution from our discrete model should approach the continuous solution. If this is not the case, then our discretised equations are not consistent with our continuous equations. Both translation errors and non-convergent numerical schemes cause our simulations to give results which are not consistent with our numerical model. Due to the complexity and computational cost of our simulations, these errors are almost inevitably disastrous. Since the dynamics in our model are non-linear, it is extremely difficult to determine the effect of an error discovered after a simulation – so repeating expensive simulations (if you still have budget) is usually the only recourse. More dangerous still is not catching the error at all – especially as simulation is increasingly used to design and interpret experiments. How can we avoid easy-to-make, difficult-to-repair errors? We can't compare to an analytical solution, since there is are analytical solutions for turbulence, but thankfully we can manufacture our own solution to compare to.

To test the complete model, we use the *Method of Manufactured Solutions* (MMS), which is explained well in Chapter 12 of *Computer Simulation Validation* [157]. The basic idea of MMS is that, instead of searching for an exact physical solution, we modify our equations slightly and use a manufactured solution. First of all, we can write our differential equations in the form

$$\mathcal{L}(u(x,t)) = 0 \tag{4.21}$$

where $\mathcal{L}$ is some operator which acts on our system state $u(x,t)$. Then, we select an arbitrary solution $U = U(x,t)$, which should be sufficiently complicated that all terms in $\mathcal{L}$ are non-zero. If we then apply our differential operator on our manufactured solution, it will give some residual

$$\mathcal{L}(U(x,t)) = \mathcal{S}(x,t) \tag{4.22}$$

---

[4] Excluding comments, measured using the CLOC tool.

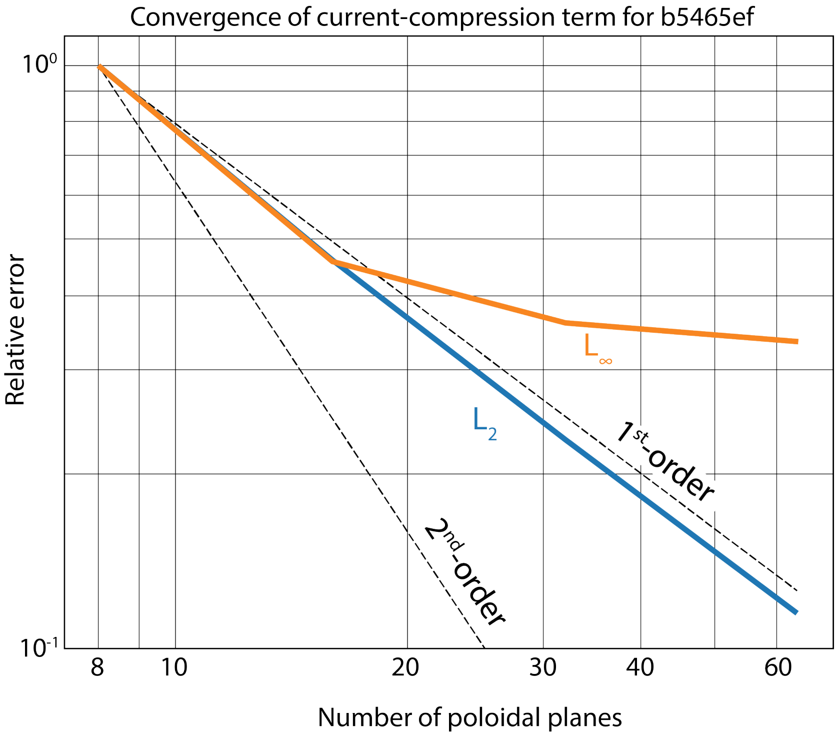

Figure 4.8.: In GRILLIX, we can switch individual evolution equations on or off (or even individual terms in the evolution equations). This lets us use MMS to isolate issues, such as in this figure where we see that the error was not converging at second-order for the $\nabla \cdot j_{\|}\hat{\mathbf{b}}$ term for commit `b5465ef`. The y-axis gives the difference between the prescribed solution and the computed solution, and the x-axis gives the number of toroidal planes (we also increase the perpendicular resolution at the same rate). The dashed lines give first and second-order convergence. From our numerical scheme we expect second-order, but we see first-order or worse convergence here, indicating an error. This allowed us to catch and fix the error (a toroidal shift in the mapping of the density from the scalar to the vector grid), which might not have otherwise been caught in code review.

We rearrange this to give a new differential operator

$$\mathcal{L}_{mms}(u(\boldsymbol{x},t)) = \mathcal{L}(u(\boldsymbol{x},t)) - \mathcal{S}(\boldsymbol{x},t) \tag{4.23}$$

which, by definition, has a solution

$$\mathcal{L}_{mms}(U(\boldsymbol{x},t)) = \mathcal{L}(U(\boldsymbol{x},t)) - \mathcal{S}(\boldsymbol{x},t) = 0 \tag{4.24}$$

Therefore, the *analytical solution* to $\mathcal{L}_{mms}(u(\boldsymbol{x},t)) = 0$ with an initial condition $u(\boldsymbol{x},t=0) = U(\boldsymbol{x},t=0)$ will, by definition, be $U(\boldsymbol{x},t)$. This is insofar quite straight-forward, if a little circular – we've found an analytic solution to a differential equation because we defined it to be the analytic solution. However, this method is very powerful if we apply it to our numerical model.

An analytical solution to our differential equations is exactly what we need to make sure that we haven't made coding errors and that our numerical scheme is convergent. We first select a numerical solution of sufficient complexity to test all of the terms in our scheme, but which is simple enough that the residual of the differential operators can be computed by a symbolic-maths program like Mathematica or SymPy. We then add this term as a source to our equations and compute the difference between the analytic and computed solutions for each dynamic quantity (i.e. the density or velocity)

$$\delta_{mms}(\boldsymbol{x},t) = u(\boldsymbol{x},t) - U(\boldsymbol{x},t) \tag{4.25}$$

and then compute the L^2 error norm. The structure of $\delta_{mms}(\boldsymbol{x},t)$ can sometimes help to identify issues – i.e. if a particular region has a higher error than average. To fully test the system, however, we increase the resolution in time and space and check that the norm of $\delta_{mms}(\boldsymbol{x},t)$ decreases at the rate expected from the order of the numerical scheme[5]. If this is the case, we can be confident that our numerical model is both correctly implemented and convergent.

MMS is used to continuously verify the refactored version of GRILLIX (introduced in chapter 9.2). For each commit pushed to the Gitlab repository, a battery of tests is performed using continuous-integration continuous-development (CI/CD) tools. For changes which do not modify the model, these tests check that the lowest-resolution MMS result is unchanged for separate executables compiled with each supported compiler. For changes to the model, a full convergence analysis is performed, and the MMS reference values are updated. In addition to MMS, we also perform unit and integration tests for the model, again with multiple compilers. By constantly verifying the model, the CI/CD suite helps to catch errors quickly in development and ensures that our simulations match our conceptual model.

---

[5] For example, a second-order finite difference scheme should have $\delta_{mms}(\boldsymbol{x},t) \propto h^2$. To see the second-order convergence of the spatial discretisation, the time-step must be small enough that the discretisation error dominates. As such, we typically increase spatial resolution and reduce the time-step simultaneously.

5. Realistic magnetic geometries

5.1. What, why, and how? Using the magnetic field from real experiments

One of the key advantages of the locally-field-aligned discretisation method is extremely flexible for treating magnetic geometries. Locally-field-aligned codes have been used to treat standard limited [115] and diverted [108] geometries, as well as advanced divertor configurations [125] and non-axisymmetric geometries [154]. In principle, all that is required is to provide information about the magnetic field to the field-line tracing routines (4.3) used to build parallel operators and information about the boundary positions.

In this chapter, we first introduce the concept of magnetic equilibria. We then derive the Grad-Shafranov equation used in magnetic reconstruction, although this is mainly as a convenient way to introduce the necessary terminology since we will simply use the results from magnetic reconstruction codes. Finally, we discuss the design of `parallax`-format equilibrium NetCDF files and how they are generated using `parallax-equilibrium`, and how they are handled in `GRILLIX`. The resulting machinery allows for any axisymmetric magnetic equilibrium to be modelled using the same code – only the equilibrium files need to be built to adapt the code to a new case.

5.2. Magnetohydrodynamic equilibrium

In turbulence modelling, we are typically interested in modelling cases where the magnetic field evolves over a longer time-scale than the evolution of the plasma profiles (the 'transport' time-scale). However, the evolution of the magnetic field occurs due to processes which are much *faster* than transport processes. We have excluded the effects of these fast processes via the drift-ordering (2.2.5), and so we cannot model the dynamic evolution of the magnetic field. Instead, we model plasma turbulence in *magnetic equilibria*, where the structure of the magnetic field varies slower than the evolution of pressure-driven instabilities.

The magnetic field evolution is usually studied via the magnetohydrodynamic (MHD) equations. These equations are fluid equations, like the model that we derived in chapter 2, but the MHD equations are derived using a different ordering. The MHD ordering assumes that the dynamics of interest occur around the thermal velocity – which is much faster than the ion drift velocities of the drift-ordering. Perhaps counter-intuitively, the MHD-ordering generally yields a *simpler* set of equations than the drift-ordering – since terms like viscosity and heat conduction are 'slow' and therefore excluded. There are several different flavours of MHD-ordered equations, which use different simplifying assumptions, but we will consider only the simplest 'ideal MHD' equations.

The ideal MHD equations are derived and applied in references [128, 5], but for this chapter we are only interested in the steady-state solutions with $\frac{\partial}{\partial t} \rightarrow 0$. This simplifies the force balance equation to

$$\boxed{\nabla p = \boldsymbol{j} \times \boldsymbol{B}} \tag{5.1}$$

This is an extremely helpful expression! We'll use it several times in this chapter to determine the properties of magnetohydrodynamic equilibria. Immediately, we can see that $\boldsymbol{B} \cdot \nabla p = \boldsymbol{j} \cdot \nabla p = 0$, and so in an equilibrium state the magnetic field and current vectors must both be tangent vectors to surfaces of constant pressure, which we call *flux surfaces.* We can also cross both sides of equation 5.1 with the magnetic field

$$\begin{align} \nabla p \times \boldsymbol{B} &= \left(\boldsymbol{j} \times \boldsymbol{B}\right) \times \boldsymbol{B} \tag{5.2} \\ &= -\left(B^2 \boldsymbol{j} - \left(\boldsymbol{j} \cdot \boldsymbol{B}\right) \boldsymbol{B}\right) \tag{5.3} \\ \boldsymbol{j}_\perp &= \frac{\boldsymbol{B} \times \nabla p}{B^2} \tag{5.4} \\ &= en\boldsymbol{u}_{dia} \tag{5.5} \end{align}$$

In an MHD equilibrium, there must be some current which is perpendicular to both the magnetic field and the pressure gradient. By comparing this to equation 2.45, we see that it is equal to the current due to the ion diamagnetic drift, and as such, we identify this as the *diamagnetic current.* To ensure $\nabla \cdot \boldsymbol{j} = 0$, this current must be balanced by another current (called the *Pfirsch-Schlüter current*), which develops instantaneously and flows parallel to the magnetic field. Therefore, for any equilibrium with a non-zero pressure gradient, we need a parallel current.

5.3. Axisymmetric equilibria

5.3.1. The poloidal magnetic flux function

MHD equilibria can be found for various magnetic confinement devices, including linear devices and stellarators. However, in this thesis we will focus on tokamaks, and assume that the magnetic field is perfectly axisymmetric since this will simplify our equilibrium calculations. If we have perfect toroidal symmetry, all derivatives in the toroidal direction can be dropped $\frac{\partial}{\partial \phi} \rightarrow 0$. If we expand the curl of the vector derivative using B.24, we can write

$$\begin{align} \boldsymbol{B} &= \nabla \times \boldsymbol{A} \tag{5.6} \\ &= \frac{1}{R} \begin{vmatrix} \hat{\mathbf{R}} & R\hat{\phi} & \hat{\mathbf{Z}} \\ \frac{\partial}{\partial R} & \cancel{\frac{\partial}{\partial \phi}} & \frac{\partial}{\partial Z} \\ A_R & RA_\phi & A_Z \end{vmatrix} \tag{5.7} \\ &= -\frac{\partial A_\phi}{\partial Z}\hat{\mathbf{R}} + \frac{1}{R}\frac{\partial RA_\phi}{\partial R}\hat{\mathbf{Z}} + \left(\frac{\partial A_Z}{\partial R} - \frac{\partial A_R}{\partial Z}\right)\hat{\phi} \tag{5.8} \\ &= \nabla \times \left(A_\phi \hat{\phi}\right) + B_\phi \hat{\phi} \tag{5.9} \end{align}$$

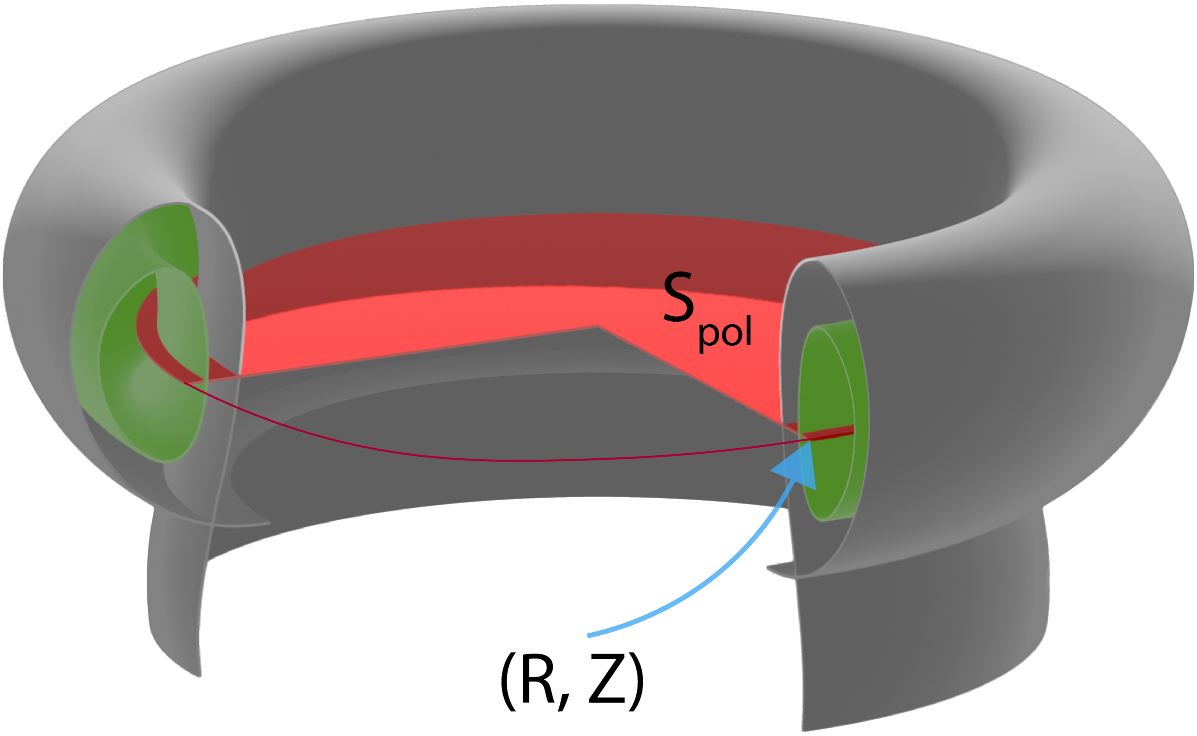

Figure 5.1.: The poloidal magnetic field components can be expressed in terms of the poloidal flux function $\Psi(R, Z)$. This is defined as the magnetic flux through a horizontal surface S_{pol} which extends from the axis of symmetry ($R = 0$) to some radial position R at some vertical position Z, as indicated by the red surface (note that the actual surface is defined via a full toroidal rotation, while part of the surface indicated here has been cut away to see inside). To find the two-dimensional poloidal flux function, we would need to define several surfaces $S_{pol}(R, Z)$ at different (R, Z) positions, and compute the magnetic flux for each surface. Thankfully, we don't have to do this manually. Instead, we take the poloidal flux function from magnetic reconstruction codes, discussed in section 5.3.4. For reference, we have also indicated the separatrix and a confined region flux-surface, in grey and green respectively.

For an axisymmetric field, we can write our poloidal field in terms of a single scalar function $A_\phi(R, Z)$. However, we are usually given the *poloidal magnetic flux* function. This is defined as the magnetic flux through a horizontal cylindrical surface of radius R at a constant height Z, as indicated in figure 5.1. In cylindrical coordinates, the differential normal area (B.28) to a horizontal surface will be $\boldsymbol{dS} = RdRd\phi\hat{\mathbf{Z}}$, and so the poloidal flux function will be

$$\Psi(R, Z) = \int_0^{2\pi} \int_0^R B_Z(R', Z)R'dR'd\phi = 2\pi R A_\phi(R, Z) \tag{5.10}$$

Rather unhelpfully, there is a related quantity which is defined as $\psi(R, Z) = RA_\phi(R, Z)$ (sometimes distinguished as the poloidal magnetic field stream function, written in lower case without the factor of 2π, but not always). We will only ever use the poloidal magnetic flux function (in this section, and also in `parallax-equilibrium`), but whenever processing a new equilibrium you should take extreme care to distinguish between the two[1]. Combining equations 5.8 and 5.10 gives that

$$\boxed{\begin{aligned} B_R(R, Z) = \boldsymbol{B}(R, Z) \cdot \hat{\mathbf{R}} &= \frac{-1}{2\pi R}\frac{\partial \Psi(R, Z)}{\partial Z} && (5.11) \\ B_Z(R, Z) = \boldsymbol{B}(R, Z) \cdot \hat{\mathbf{Z}} &= \frac{1}{2\pi R}\frac{\partial \Psi(R, Z)}{\partial R} && (5.12) \end{aligned}}$$

which we can write compactly as a cross product (B.3)

$$\boxed{\begin{aligned} \boldsymbol{B}_{pol} = \boldsymbol{B}_R\hat{\mathbf{R}} + \boldsymbol{B}_Z\hat{\mathbf{Z}} &= \frac{1}{2\pi R}\left(-\frac{\partial \Psi}{\partial Z}\hat{\mathbf{R}} + \frac{\partial \Psi}{\partial R}\hat{\mathbf{Z}}\right) && (5.13) \\ &= \frac{1}{2\pi R}\nabla\Psi \times \hat{\phi} && (5.14) \end{aligned}}$$

5.3.2. The toroidal magnetic field

From Ampère's law (using B.25 and then expanding j_ϕ using 5.11 and 5.12)

$$\begin{aligned} \mu_0 \boldsymbol{j} = \nabla \times \boldsymbol{B} &= -\frac{\partial B_\phi}{\partial Z}\hat{\mathbf{R}} + \frac{1}{R}\frac{\partial R B_\phi}{\partial R}\hat{\mathbf{Z}} + \left(\frac{\partial B_R}{\partial Z} - \frac{\partial B_Z}{\partial R}\right)\hat{\phi} && (5.15) \\ &= \frac{1}{R}\left(-\frac{\partial R B_\phi}{\partial Z}\hat{\mathbf{R}} + \frac{\partial R B_\phi}{\partial R}\hat{\mathbf{Z}}\right) - \frac{1}{2\pi R}\left(R\frac{\partial}{\partial R}\left(\frac{1}{R}\frac{\partial \Psi}{\partial R}\right) + \frac{\partial^2 \Psi}{\partial Z^2}\right)\hat{\phi} && (5.16) \\ &= \frac{1}{R}\nabla\left(R B_\phi\right) \times \hat{\phi} - \frac{1}{2\pi R}\Delta^*\Psi\hat{\phi} && (5.17) \end{aligned}$$

where Δ^* is the Stokes operator

$$\Delta^*\Psi = R\frac{\partial}{\partial R}\left(\frac{1}{R}\frac{\partial \Psi}{\partial R}\right) + \frac{\partial^2 \Psi}{\partial Z^2} = -\frac{1}{2\pi R\mu_0}j_\phi \tag{5.18}$$

---

[1] The notebook for the TCV-X21 equilibrium compares the q-profile from the eqdsk file to one calculated from the processed equilibrium, which helps to make sure that we're not out by a factor of 2π.

We can find an expression for B_ϕ by using the integral form of Ampère's law. We use a horizontal disk S_{pol} as defined in figure 5.1 and its bounding curve ∂S_{pol} with a differential line element $\boldsymbol{dl} = Rd\phi\hat{\phi}$. Therefore, the toroidal field B_ϕ is related to the vertical current I_{pol} through S_{pol}

$$\oint_{\partial S_{pol}} \boldsymbol{B}\cdot\boldsymbol{dl} = 2\pi R B_\phi = \mu_0 \iint_{S_{pol}} \boldsymbol{j}\cdot\boldsymbol{dS} = \mu_0 I_{pol} \tag{5.19}$$

$$B_\phi = \mu_0 \frac{I_{pol}}{2\pi R} \tag{5.20}$$

For a tokamak, the current in the toroidal field coils will usually be *much* larger than the poloidal current in the plasma and so $I_{pol} \approx I_{coil}$, which is called the *vacuum field approximation.* Using this approximation, the toroidal magnetic field can be written as a function of radius and a single reference value

$$\boxed{B_\phi = \mu_0 \frac{I_{coil}}{2\pi R} = B_0 \frac{R_0}{R}} \tag{5.21}$$

where $B_0 = B(R = R_0)$ (where R_0 is usually taken to be the radius of the magnetic axis). We use this form for defining the toroidal field in `parallax-equilibrium`.

5.3.3. Flux surfaces

By writing $\boldsymbol{B}_{pol}$ in the form of equation 5.14, we can see that the magnetic field must be a tangent vector along isosurfaces[2] of Ψ, which we call *flux surfaces.* Furthermore, from the MHD force balance (equation 5.1), we know that $\boldsymbol{B}\cdot\nabla p = \boldsymbol{j}\cdot\nabla p = 0$ – that is, the magnetic field and the current must tangent vectors to isosurfaces of the pressure. We can further show that the pressure and Ψ isosurfaces are the same. From axisymmetry, we assume the toroidal derivative of the pressure is zero, and therefore $\boldsymbol{B}\cdot\nabla p = 0 \implies \boldsymbol{B}_{pol}\cdot\nabla p = 0$. Then, using equations 5.14 and B.1, we find that

$$\left(\nabla p \times \nabla\Psi\right)\cdot\hat{\phi} = 0 \tag{5.22}$$

Since both ∇p and $\boldsymbol{\Psi}$ have poloidal components, the toroidal component will only be zero if p or Ψ have zero gradient or if ∇p is parallel to $\nabla\Psi$. Therefore, if we want a non-trivial magnetic equilibrium, the pressure gradient must be a function of Ψ, and so flux surfaces are also surfaces of constant pressure. Similarly, for the current, $\boldsymbol{j}\cdot\nabla p = 0 \implies \boldsymbol{j}_{pol}\cdot\nabla p = 0$ since $\frac{\partial p}{\partial\phi} = 0$. Additionally, since $p = p(\Psi)$, we can rewrite $\nabla p = \nabla\Psi\frac{dp}{d\Psi}$. Using equation 5.17, we can show

$$\frac{1}{R}\left(\nabla(RB_\phi)\times\hat{\phi}\right)\cdot\nabla\Psi\frac{dp}{d\Psi} = 0 \tag{5.23}$$

$$\left(\nabla\Psi\cdot\nabla(RB_\phi)\right)\cdot\hat{\phi} = 0 \tag{5.24}$$

This is of the same form as equation 5.22, and so $RB_\phi = \frac{\mu_0}{2\pi}I_{pol}$ must also be constant over a magnetic flux surface. Since I_{coil} is constant, the contribution from the poloidal currents must also be constant. Therefore, if a flux surface intersects some constant-Z surface at two positions R_1 and R_2, then $R_1\boldsymbol{j}(R_1, Z)\cdot\hat{\mathbf{z}} = -R_2\boldsymbol{j}(R_2, Z)\cdot\hat{\mathbf{z}}$, ensuring $\nabla\cdot\boldsymbol{j} = 0$.

---

[2] The poloidal magnetic field at any point in space will point along a contour of Ψ.

5.3.4. Magnetic reconstruction

We now have several ingredients for defining a magnetohydrodynamic equilibrium – the poloidal flux function $\Psi(R, Z)$, the pressure profile $p(\Psi)$ and the poloidal current profile $I_{pol}(\Psi)$. To put these together, we need a recipe for how the profiles are related in the direction across to the flux surfaces. We can use our expressions for the poloidal magnetic field (equation 5.14), the toroidal magnetic field (equation 5.20) and the current density (equation 5.17) in the MHD force balance, expanding the terms in $\nabla p = \boldsymbol{j} \times \boldsymbol{B}$ to give

$$\begin{aligned}\frac{dp}{d\Psi}\nabla\Psi &= \frac{1}{(2\pi R)^2}\left(\frac{dI_{pol}}{d\Psi}\nabla\Psi\times\hat{\phi} - \frac{1}{\mu_0}\Delta^*\Psi\hat{\phi}\right)\times\left(\nabla\Psi\times\hat{\phi} + \mu_0 I_{pol}\hat{\phi}\right) \qquad (5.25)\\ &= \frac{1}{(2\pi R)^2}\left(\left(\frac{dI_{pol}}{d\Psi}\mu_0 I_{pol}\right)\left(\nabla\Psi\times\hat{\phi}\right)\times\hat{\phi} + \left(\frac{-\Delta^*\Psi}{\mu_0}\right)\hat{\phi}\times\left(\nabla\Psi\times\hat{\phi}\right)\right) \qquad (5.26)\end{aligned}$$

Using B.4, $\left(\nabla\Psi\times\hat{\phi}\right)\times\hat{\phi} = \left(\cancel{\nabla\Psi\cdot\hat{\phi}}\right)\hat{\phi} - \left(\hat{\phi}\cdot\hat{\phi}\right)\nabla\Psi = -\nabla\Psi$, and so

$$\frac{dp}{d\Psi}\nabla\Psi = \frac{-1}{(2\pi R)^2}\left(\frac{dI_{pol}}{d\Psi}\mu_0 I_{pol} + \frac{\Delta^*\Psi}{\mu_0}\right)\nabla\Psi \tag{5.27}$$

$$\boxed{-(2\pi R)^2\mu_0\frac{dp}{d\Psi} - \mu_0^2 I_{pol}\frac{dI_{pol}}{d\Psi} = \Delta^*\Psi = R\frac{\partial}{\partial R}\left(\frac{1}{R}\frac{\partial\Psi}{\partial R}\right) + \frac{\partial^2\Psi}{\partial Z^2}} \tag{5.28}$$

This equation is called the *Grad-Shafranov* equation. This is an elliptic differential equation which relates the poloidal flux function Ψ (or, alternatively, the toroidal current function since $\Delta^*\Psi = -\frac{1}{2\pi R\mu_0}j_\phi$) to the pressure gradient profile $\frac{dp}{d\Psi}(\Psi)$ and the poloidal current profile $I_{pol}(\Psi)$. This must be combined with a suitable boundary condition – usually the value of the poloidal flux along the boundary. However, ideal-MHD doesn't tell us how $p(\Psi)$ or $I_{pol}(\Psi)$ evolve over time – and so these must be provided either from experiment or another model.

To find a solution to the Grad-Shafranov equation, we use typically *magnetic reconstruction* codes such as EFIT [158], CLISTE [159], LIUQE [160] and IDE [161]. These codes combine measurements of the poloidal flux from wall magnetic sensors as well as pressure and current chord measurements (if available) to iteratively find a consistent solution for $\Psi(R, Z)$. The accuracy of the solution therefore depends on the available diagnostics [162] and whether the allowed solutions are further constrained (such as by using a current diffusion equation to limit how quickly the magnetic equilibrium can change in time) [161, 163]. For example, on ASDEX-Upgrade, Fischer et al., 2020 found that the uncertainty of the separatrix was as much as $\sim 6\,\mathrm{mm}$ – $12\times$ the sound Larmor radius at the outboard midplane separatrix. This uncertainty can affect the results of the integrated data analysis (since profiles from different diagnostics are often combined as functions of Ψ). For our simulations, uncertainty in the magnetic geometry technically should be quantified via sensitivity scans [163], but these are currently unfeasibly expensive.

5.4. Numerical equilibria in `GRILLIX`

If we want to perform realistic simulations of real devices, we need to use the realistic magnetic field geometry. This is, in principle, very straight-forward. Magnetic reconstruction codes can provide us with gridded numerical values of $\Psi(R,Z)$, the radial dependence of $B_\phi(R)$ (if this is significantly different to the vacuum field) or a reference value B_0 for the toroidal field on-axis (if the $B_\phi \propto 1/R$ approximation is valid), allowing us to define our magnetic field using equations 5.11, 5.12 and 5.21 as

$$\boldsymbol{B}(R,Z) = \frac{1}{2\pi R}\left(-\frac{\partial \Psi(R,Z)}{\partial Z}\hat{\mathbf{R}} + \frac{\partial \Psi(R,Z)}{\partial R}\hat{\mathbf{Z}}\right) + B_0\frac{R_0}{R}\hat{\phi} \tag{5.29}$$

We pass gridded values of $\Psi(R,Z)$ to `GRILLIX`, and evaluate $\partial_R\Psi$ and $\partial_Z\Psi$ at the grid-point positions using a bicubic spline interpolator [164]. For this, we modified the spline interpolation routines from `github.com/jacobwilliams/bspline-fortran` for thread-safety, and verified that the spline interpolator gave the same result as `FITPACK`. This approach helps to reduce the numerical divergence of $\boldsymbol{B}_{pol}$, as shown in figure 5.2. Using Ψ instead of $\boldsymbol{B}_{pol}$ also ensures that if we smooth the poloidal field to eliminate fine structure, our magnetic field is still divergence-free.

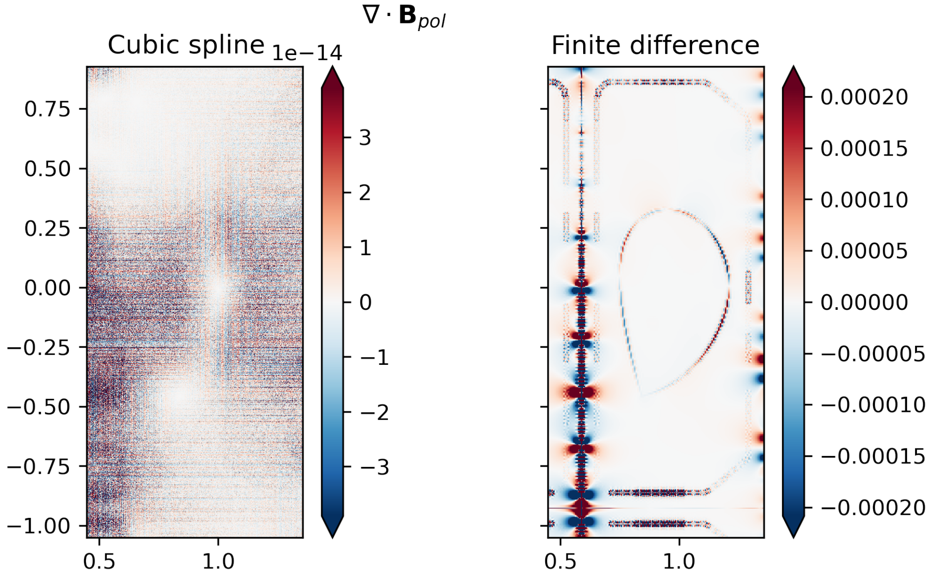

Figure 5.2.: Comparison of the numerical divergence of the poloidal magnetic field, for $\boldsymbol{B}_{pol}$ computed from the poloidal flux function Ψ, using either a bicubic spline interpolator (left) or a first-order finite difference method (right) to evaluate the poloidal derivatives of Ψ. For both methods, we use a bicubic spline interpolator to evaluate $\nabla \cdot \boldsymbol{B} = \frac{1}{R}\left(\partial_R(RB_R) + \partial_Z(RB_Z)\right)$.

We additionally require a polygon $\mathcal{P}_{wall}$, which give the (R,Z) position of the first wall and divertor (which is assumed to be axisymmetric). This allows us to efficiently determine whether points are inside or outside of the vessel, by the winding algorithm [165, 166]. We

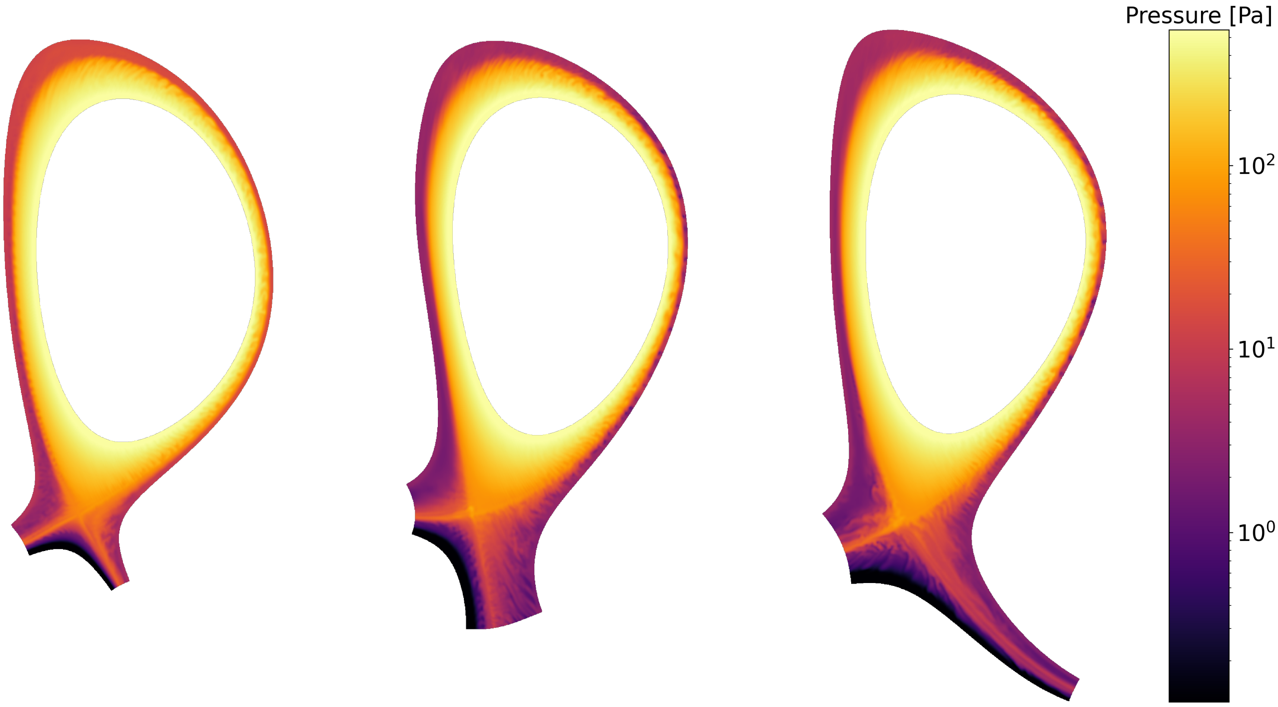

Figure 5.3.: Simulations in advanced divertor configurations proposed for DEMO, at TCV parameters. From left, the pressure in a configuration with a single-null, an X-divertor and a Super-X divertor, from simulations performed with GRILLIX. We are currently exploring how turbulence interacts with magnetic geometry in various ADCs, including in the planned ASDEX Upgrade upper divertor [167].

also modified the field-line tracing routines such that they can use the winding algorithm as a stopping condition, which allows for the computation of the along-field-line distance to the boundaries used for setting the penalisation characteristic function.

By convention, we define $\mathcal{P}_{wall}$ as a non-intersecting, closed polygon with points defined in an anticlockwise order and with no repeated points (such that all edges have a non-zero length). This allows us to consistently define the vector normal $\hat{\mathbf{n}}$ to the polygon – which is useful for determining which sign of the parallel direction is towards the wall via $\hat{\mathbf{b}} \cdot \hat{\mathbf{n}}$. We can additionally define the shortest poloidal distance to the wall for any (R, Z) point, by computing the minimum vector rejection of the point-to-vertex displacement vector onto the corresponding edge vector.

We can use this methodology to treat any axisymmetric magnetic geometry – including limiter, divertor and advanced divertor configurations (several of which are shown in figure 5.3). One minor limitation is our use of the vacuum-field assumption for the toroidal field, which excludes cases with non-negligible poloidal current, but it is straightforward to include a computed toroidal-field profile is straight-forward[3]. Although `parallax` can handle essentially any axisymmetric magnetic geometry, not all geometries are compatible with the `GRILLIX` model and numerics (or, more specifically, the boundary conditions). In particular, due to the finite-width transition region for the immersed boundary condition (section 4.6), we require well-behaved magnetic data outside of the vessel. This isn't always available, in which case we need to pad the magnetic data with artificial data. Another challenge is that our boundary conditions aren't well-behaved in the limit of very shallow glancing angles ($\hat{\mathbf{n}} \cdot \hat{\mathbf{b}} \to 0$). For this reason, rather than extending the simulation to the first wall, we use a limiting flux surface so that parallel boundary conditions are only applied in the divertor. We usually trim our grid just before the secondary separatrix in X-point geometries[4], but if this surface is close to the primary separatrix it can result in an extremely narrow scrape-off-layer.

5.5. Preprocessing with `parallax-equilibrium`

In the previous step, we skipped over an important step. There are several different magnetic reconstruction codes, which produce magnetic data in several different file-formats. Some formats – such as eqdsk or IMAS – are widely used, but even within formats there are different standards[5]. As such, rather than implementing several different readers into `parallax`, we use a Python preprocessor to convert various formats into our own '`parallax`-standard equilibrium NetCDF' format, the structure of which is given in Appendix D. The preprocessor is called `parallax-equilibrium` (or `pxequi` for short), and it is available from the `phoenix` at `gitlab.mpcdf.mpg.de/phoenix/parallax_equilibrium`. Each case is processed in a Jupyter notebook in `pxequi_notebooks`, which allows for interactive data processing and in-place documentation for each case.

The `pxequi` library currently supports eqdsk and arbitrary MATLAB files, as well as interfacing to the ASDEX-Upgrade EQI equilibria. All equilibrium formats are used to build a common `ProcessEquilibrium` instance, which is a derived class based on the `NumericalEquilibrium` class from `TorX`. This design means that, as the necessary data is added to the `ProcessEquilibrium`, it can use the functionality of `TorX` to test the equilibrium during pre-processing. Additionally, it allows for new readers to be added with minimal difficulty. Once the data is mapped onto a `ProcessEquilibrium` object, the remaining pre-processing steps can share the same code. The remaining steps depend on the availability and quality of the data, although the algorithm is roughly as follows;

1. **Filtering**: `GRILLIX` requires smooth derivatives of Ψ up to 1st order, and `GENE-X` requires smooth derivatives up to 2nd order. However, the contours of Ψ define flux surfaces, so

---

[3] The original version of the numerical equilibrium routines included this term, but it was dropped to avoid constructing a second interpolator, since the given profiles were very close to the vacuum field.

[4] In X-point geometries, a second shaping coil is often used to make a second poloidal-field-null (which might be outside the vessel). The secondary separatrix is the flux surface that goes through this second poloidal-field-null.

[5] Searching for documentation of the `eqdsk` format, one of the first results warns that "*The G–EQDSK file format is unstable and unreliable. Use with caution.*"

we need to smooth fine structures (which affect the derivatives) while having a minimal effect on large-scale structures. Several image filters were tested, with the best results found for a Fourier-Gaussian image filter from `scipy.ndimage.fourier_gaussian`, with an additional edge padding[6].

2. **Axis and X-point optimisation**: The magnetic axis and X-point correspond to local nulls of the poloidal field. To find their positions to high accuracy we use the BGFS algorithm implemented in `scipy.optimize.minimize` to find minima of $B_{pol}(R,Z) = \sqrt{B_R(R,Z)^2 + B_Z(R,Z)^2}$. The starting points can be either supplied manually or taken from the equilibrium data.
3. **Axis and separatrix poloidal flux**: The axis and X-point positions are used to define the values of Ψ_0 and Ψ_X. These are used to calculate the normalised poloidal flux $\rho(R,Z) = \sqrt{\frac{\Psi(R,Z)-\Psi_0}{\Psi_X-\Psi_0}}$, which is 0 at the magnetic axis and 1 at the separatrix.
4. **Divertor and first-wall polygon**: The divertor and first-wall polygon is approximated as a collection of R, Z points (an axisymmetric wall is assumed). Currently, only the divertor points are used (since we limit our grid with some limiting flux surface), but nevertheless, we provide the full first-wall in case the codes are extended to model the first-wall interaction. The wall points are not always provided with the magnetic data – but this can be quickly extracted from any figure of the device via a tool such as `automeris.io/WebPlotDigitizer/`.
5. **Private-flux region polygon**: Another polygon is used to designate the private-flux region. This can be drawn very coarsely, using the position of the X-point.
6. **Limiting flux surfaces**: For a simple single-null geometry, we need to identify an inner flux-surface (which is usually, fairly arbitrarily, defined at $\rho = 0.9$) to exclude the core. We also need to define an outer flux-surface, which should be placed just before the first wall (such that parallel boundary conditions are applied only within the divertor). A third minimum-ρ flux-surface is defined in the private flux region, to exclude the glancing-angle region between the divertor targets. This flux limit is only applied at points within the private-flux-region polygon identified in the previous step.
7. **Exclusion polygon**: A third polygon is used to define the region of points which should be considered for grid creation. This is useful for eliminating regions near the magnetic field coils, which can have poloidal flux values similar to the confined region. It also defines the end-of-grid for the finite-width immersed boundary transition region used in `GRILLIX`.
8. **Double-checking**: The last pre-processing step is to check that the equilibrium matches your expectations. **Important: You should always check that your poloidal field**

---

[6] Artificial data was added to the edges of the $\Psi(R,Z)$ array via `np.pad(array, (pad_x, pad_y), mode='reflect', reflect_type='odd')`. The padded array was then filtered, and then the padded edges were removed. The edge-padding eliminated edge distortion introduced by the Fourier filter, and the Fourier-Gaussian filter was found to strongly reduce high-frequency components while leaving the flux-surfaces visually unchanged.

(and preferably your q-profile) comes out correctly[7]. It is also worth ensuring that your limiting flux-surfaces avoid any glancing-angle boundary conditions and that there are no points within the exclusion polygon that should not be modelled.

Once an equilibrium is pre-processed and mapped to a `ProcessEquilibrium` object, it can be written to a `parallax`-standard NetCDF using the `PX2Writer`.

5.6. Simulations in arbitrary magnetic geometry

This equilibrium-handling infrastructure permits simulations with `GRILLIX` and `GENE-X` in numerically-defined limited, single-null, double-null, X-divertor, Super-X, snowflake-plus and snowflake-minus geometries. This unlocks several possibilities – such as investigations of real devices, including those with negative triangularity and advanced divertor configurations. In part III, we will use this infrastructure to run simulations in the experimentally-reconstructed magnetic geometry several, allowing us to quantitatively validate and assess the predictive capabilities of `GRILLIX`.

We could extend the equilibrium-handling infrastructure further, to consider more cases and with increased realism. One interesting possibility would be to permit non-axisymmetric equilibria since this is within the capabilities of the locally-field-aligned method [154]. This would of course be interesting for modelling stellarators such as Wendelstein-7X, but also for including effects such as resonant magnetic perturbation coils or modelling the effects of field ripple due to non-continuous toroidal field coils. Another possibility would be allowing for the time-evolution of the magnetic field during turbulence simulations. We could, for instance, implement a Grad-Shafranov solver to update the magnetic equilibrium according to the pressure and current profiles computed within a turbulence simulation, or could extend the model to explore non-equilibrium events such as edge-localised modes. Including realistic axisymmetric magnetic equilibria in turbulence modelling is a significant development and a starting point of investigating turbulence in realistic magnetic fields.

---

[7] The poloidal flux function Ψ and the poloidal magnetic field stream function $\psi = \frac{1}{2\pi}\Psi$ are often used interchangeably. If your poloidal field is out by a factor of 6.283, you've likely been given ψ, while all of the routines in `pxequi` and `parallax` assume that you are using Ψ. If in doubt, check again – a factor of 2π in the poloidal field in your simulations means throwing everything out and starting again.

Part III.

Validation

> All models are approximations. Assumptions, whether implied or clearly stated, are never exactly true. All models are wrong, but some models are useful. So the question you need to ask is not "Is the model true?" (it never is) but "Is the model good enough for this particular application?"
>
> *(G. E. P. Box)*

6. What, why, and how? Comparing against experiment to validate our model

> Validation is the process of determining the degree to which a conceptual model is an accurate representation of the real world from the perspective of its intended uses. Validation is an essentially physical problem, one that can be as difficult and complex as the underlying science itself. Despite the implications from the standard English usage for the word, validation should not be viewed as a one-time, binary process where codes are accepted for all time or rejected and discarded. Validation is instead part of a cyclic process, whereby models are continuously improved [168].
>
> *(M. Greenwald, 2010)*

In part II, we developed a powerful tool able to simulate plasma turbulence in any axisymmetric geometry. What should we do with it? Before we use simulations to predict turbulence in new and novel magnetic geometries, we need to *validate* the model by making sure that it can correctly predict results from existing machines. We can use validation to identify errors in our conceptual model, such as erroneous assumptions in the derivation of our model or unphysical model inputs. We can also use validation to help us to *qualify* whether our model is valid at different physical parameters and to *calibrate* uncertain input parameters. The results of validations can be used to guide model development by helping to identify where the model needs improvement [168] – although due to the non-linear and coupled nature of the system this is by no means trivial.

By using *validation-driven* development, we can focus our development effort on parts of the model which are leading to poor agreement with experiment and we can quantify how the fidelity of the model improves as we extend the model. Through careful and rigorous validation, we rapidly improve the predictive capability of the model with a modest number of developers, can provide estimates of how uncertain the simulation results are, and ultimately can make the simulations more useful for the fusion effort.

"How much can I trust the results of my simulation?" Numerical errors and uncertainties can be introduced into simulations in many ways – such as coding errors, uncertain input parameters and discretisation errors due to finite grid resolutions. In addition to these, there are also (both explicit and implicit) conceptual errors due to the assumptions we made in the derivation of our model. We can use *verification* (section 4.7) to eliminate or reduce numerical errors and

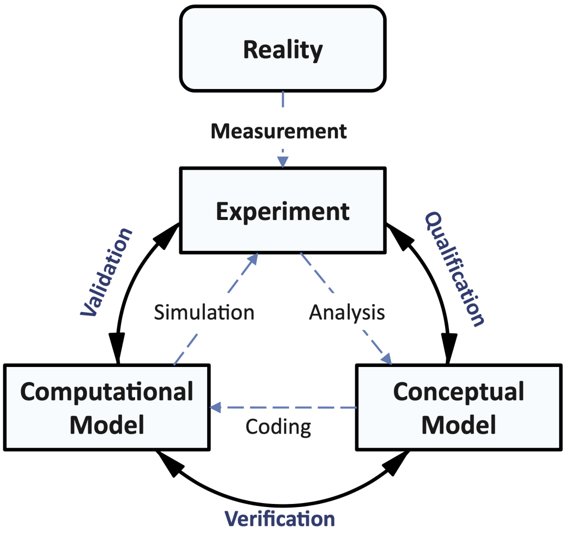

Figure 6.1.: The model testing cycle, from Greenwald, *Verification and Validation for magnetic fusion*, Physics of Plasmas, 2010 [168]

qualification to highlight erroneous assumptions. However, we can't entirely eliminate many of these errors – such as discretisation errors or simplifying assumptions. As such, we need to be able to quantify their effects. Since the plasma response is non-linear, it's difficult to estimate how errors and assumptions affect the simulation results via theoretical considerations alone, and so we instead compare our simulations to experimental results to evaluate their accuracy. This process is termed *validation*. It is typically combined with verification and qualification in a combined model-testing process (as depicted in figure 6.1 from reference [168]), since these other steps can help to interpret the results of the comparison to experiment and to prevent bugs that can invalidate the comparison.

To validate our model, we need an experiment to compare to. We could validate our model against available experimental data, but there are several reasons why it is helpful to compare to a dedicated experimental case. We want to first validate our model against simple (even boring) cases to test the basic functionality of the code. However, there is little research interest in these cases except for the validation of models and, currently, not many dedicated validation cases since turbulence models have only recently been able to simulate realistic cases. We want to be able to determine where our model gives good or poor agreement, and why that is the case. For this, it's helpful to have extremely well-diagnosed experimental cases, with multiple observables available for comparison. Not all edge and SOL diagnostics are routinely operated, and often we need to combine data from multiple shots to get good experimental statistics and diagnostic coverage. We also need to know things like the magnetic geometry, heating power or radiation measurements, to set the input parameters for our simulations. The data needed isn't always easily available, and when it is it isn't always well documented – so we need to work carefully with experimentalists to make sure that we're providing realistic inputs to the simulations.

We worked with the Swiss Plasma Centre under the EUROFusion Enabling Research Project `MFE19.EPFL-02`, led by Christian Theiler, to validate the model against dedicated experimental cases. The first of these was performed on the TORPEX basic plasma physics device, in a new 'X-point' scenario, discussed in chapter 7 and published in reference [126]. We then performed a validation against a dedicated TCV scenario, which we called `TCV-X21`. The results from this validation are discussed in chapter 8, and published in reference [2].

6.1. Further reading

There are several excellent references regarding the validation of numerical models, including specifically for validation in fusion. If you are interested in the topic, the following references are highly recommended.

- Terry et al., 2008, *Validation in fusion research: Towards guidelines and best practices* doi:10.1063/1.2928909: the key concepts of model testing, and how they can be applied to fusion. Section III.A introduces key terms such as validation metrics, and section V outlines a series of best practices for model validation [127].
- Greenwald, 2010, *Verification and validation for magnetic fusion* doi:10.1063/1.3298884: similar to reference [127], defines key terminology and best practices for model validation. States that model testing should be performed iteratively rather than once-off, to guide development of the models [168].
- Beisbart and Saam, 2019, *Computer Simulation Validation* doi:10.1007/978-3-319-70766-2: a textbook on validating numerical simulations. Recommend chapters 5 (on simulation uncertainty), 12 (on the Method of Manufactured Solutions) and 13 (on validation metrics). Part IX, on the philosophy of computer simulations and their validations, is also an interesting read.
- Oberkampf and Trucano, 2002, *Verification and validation in computational fluid dynamics* doi:10.1016/S0376-0421(02)00005-2: a classic text on validating numerical models. Section 4.7 gives a useful overview of advantages and deficiencies of validation metrics [169].
- Ricci et al., 2015, *Approaching the investigation of plasma turbulence through a rigorous verification and validation procedure: A practical example)* doi:10.1063/1.4919276: introduces the validation methodology which was used in reference [2], based on a composite metric introduced in reference [118].
- Ho et al., 2019, *Application of Gaussian process regression to plasma turbulent transport model validation via integrated modelling* doi:10.1088/1741-4326/ab065a: an alternative validation metric based on Gaussian process regression [170].
- White, 2019, *Validation of nonlinear gyrokinetic transport models using turbulence measurements* doi:10.1017/S0022377818001253: an extensive 'tutorial' discussing the validation of non-linear gyrokinetic simulations [171]

7. Validation against the TORPEX basic plasma physics device

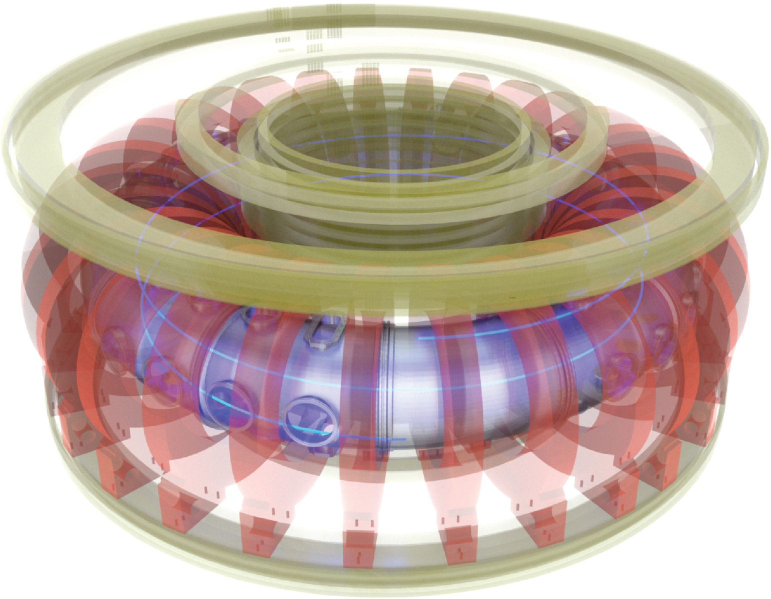

Figure 7.1.: A CAD-drawing of the TORPEX device, reproduced with modification from `epfl.ch`. The toroidal field coils are marked in red, and shaping coils are marked in olive-green. The vacuum vessel and a representative magnetic field line are indicated. Note that, in contrast to a tokamak, there is no central solenoid and therefore no plasma current drive mechanism.

TORPEX is a basic plasma physics experiment operated by the Swiss Plasma Centre [172, 173]. Like a tokamak, TORPEX uses toroidal magnetic field coils to generate an axisymmetric toroidal field. However, there is no central solenoid and so the poloidal field cannot be generated via the plasma current. Instead, a poloidal field can be generated via an in-vessel toroidal conductor [172], which is possible since TORPEX is operated at very low plasma densities and temperatures. The use of in-vessel coils and shaping coils means that a wide range of magnetic geometries can be achieved in TORPEX, including geometries with a poloidal field null like an X-point. Additionally, due to the low densities and temperatures, the entire plasma volume can be studied with immersed probes, giving good diagnostic coverage. TORPEX has previously been used for validating the basic functionality of plasma turbulence models [119], including

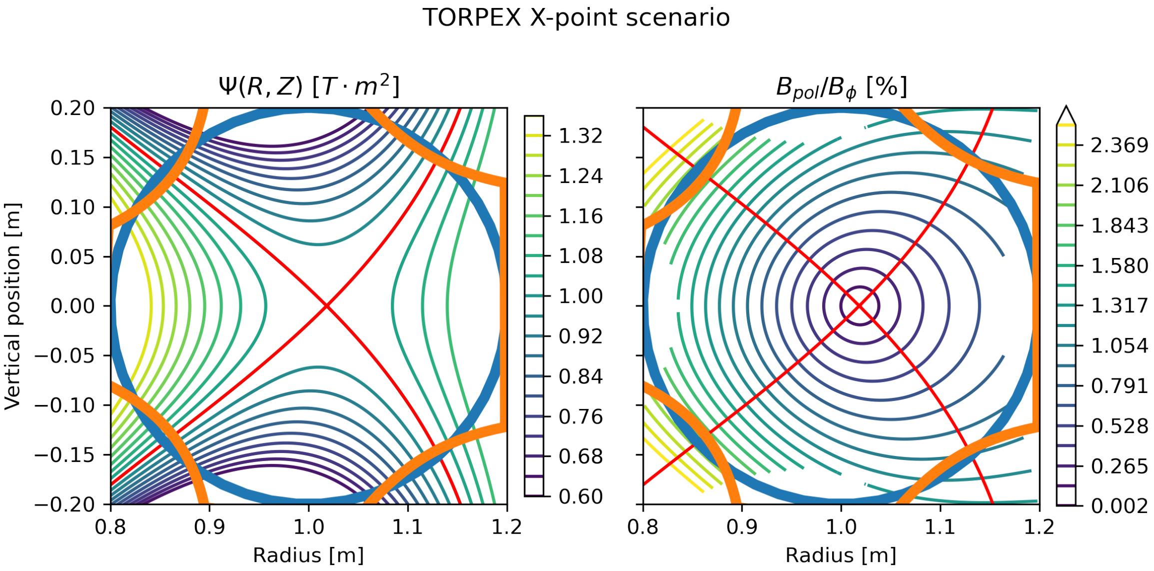

Figure 7.2.: Flux surfaces (*left*) and field-line pitch B_{pol}/B_ϕ (*right*, as a percentage) in the TORPEX X-point scenario. Data is shown between the limiting flux surfaces. The 'separatrix' – the flux surface of the poloidal field null – is shown in red, and contours of the poloidal flux are shown in white. The actual boundary is shown in blue, and the position where the boundary is applied is shown in orange.

GRILLIX [108]. As part of a EUROFusion Enabling Research Project[1] this validation effort was extended to an X-point-like magnetic geometry. The results of this project have been published as Galassi et al., 2021, '*Turbulence dynamics around the X-point in TORPEX and comparison with multi-code 3D flux-driven simulations*' [126], comparing the results from the GRILLIX, GBS, STORM and FELTOR codes. In this chapter, we will introduce the TORPEX 'X-point' validation case, describe how the GRILLIX simulations were performed, and discuss the match between the experiment and simulation.

7.1. The TORPEX X-point scenario

For this validation, a magnetic geometry with a poloidal field null was generated using external shaping coils. A magnetic equilibrium is analytically computed from the coil currents only, instead of using a magnetic reconstruction code. The vacuum field assumption is used to write the toroidal field as $B_\phi(R,Z) = B_0 \frac{R_0}{R}$ where the reference magnetic field value $B_0 = 76\,\mathrm{mT}$ (in the anti-clockwise direction, if viewed from above) is taken at the centre of the device at $R_0 = 1\,\mathrm{m}$. The equilibrium is assumed to be axisymmetric, allowing us to use the poloidal flux function $\Psi(R,Z)$ to define the magnetic field via the method described in section 5.4. A poloidal cross-section of the resulting flux surfaces and the computed field-line pitch is shown in

---

[1] EUROFusion ENR `MFE19.EPFL-02`, led by Christian Theiler.

figure 7.2. The geometry is up-down symmetric, with a poloidal field null close to the centre of the device. Using analogous terminology from a tokamak, the poloidal field is termed an X-point and its flux-surface is termed a ‘separatrix’, although there is no confined region in this geometry. The plasma volume was fuelled with neutral H_2 gas, which was then ionised with a Electron-cyclotron Resonance microwave Heating (ECRH) system. The total injected power was $\sim 300\,\mathrm{kW}$, giving an ionisation fraction of $n_e/n_{H_2} \sim 1\%$, a plasma density of $n_e \sim 1 \times 10^{16}\,\mathrm{m}^{-3}$ and an electron temperature of $T_e \sim 5\,\mathrm{eV}$. The position of the particle and energy source was estimated via the method described in reference [174], by measuring the change in the ion saturation current when the microwave heating was switched on. The determined source position was localised in the left (high-field-side) sector, and was fitted analytically as

$$\mathcal{S}(R,Z) = \begin{cases} \exp\left[-\left(\frac{R-R_0}{a}\right)^2 - \left(\frac{Z-Z_0}{b}\right)^2\right] \text{ if } R > R_0 \\ \frac{1}{2}\exp\left[-\left(\frac{R-R_0}{a}\right)^2 - 2c\,(R-R_0)(Z-Z_0) - \left(\frac{Z-Z_0}{b}\right)^2\right] \\ +\ \frac{1}{2}\exp\left[-\left(\frac{R-R_0}{a}\right)^2 + 2c\,(R-R_0)(Z-Z_0) - \left(\frac{Z-Z_0}{b}\right)^2\right] \text{ if } R \leq R_0 \end{cases} \tag{7.1}$$

with $R_0 = 0.98\,\mathrm{m}$, $Z_0 = -0.02\,\mathrm{m}$, $a = 0.0335\,\mathrm{m}$, $b = 0.050\,\mathrm{m}$ and $c = 565\,\mathrm{m}^{-2}$. The power and particle source rates were not given, and as such the simulations were permitted to vary their source rates to match $n \simeq 2.1 \times 10^{16}\,\mathrm{m}^{-3}$ and $T_e \simeq 5.3\,\mathrm{eV}$ at $R_{ref} = 0.96\,\mathrm{m}$, $Z_{ref} = 0.0\,\mathrm{m}$.

Validation data was collected by three Langmuir probe arrays. Two arrays were mounted on a fixed hexagonal grid covering most of the poloidal cross-section, while the other probe array was mounted on a vertical arm that could be swept horizontally. The probe directly measured the ion saturation current density[2] $J_{sat} = 0.5enc_s$ and the floating potential[3] $V_{fl} = \phi - \Lambda_{sh}$. The mean, standard deviation and skew of J_{sat} and V_{fl} was computed from the measured signals. Additionally, the plasma density and electron temperature were estimated via a four-parameter fit to the I-V characteristic.

7.2. Cold-ion model with neutral friction

Although GRILLIX includes terms for ion thermal effects, these were disabled for TORPEX modelling since only electrons are heated via ECRH and electron-ion heat transfer is likely small since there is no confined region in the X-point scenario[4]. Additionally, the neutral dynamics were not treated self-consistently. Instead, it was assumed that the neutrals provided a constant background, and the electron-electron collision time τ_{ee} was replaced with the electron-neutral

---

[2] The ion saturation current density is computed from the ion saturation current by estimating the collection area of the probes. Compared to the expression for J_{sat} given by equation equation 3.21, there is an additional factor of 0.5 because the probes are immersed rather than wall-mounted, and it is assumed $M_{sh} \approx 1$.

[3] The floating potential is defined in terms of the sheath potential Λ_{sh}, given by equation 3.17 and here approximated as $\Lambda_{sh}\frac{e}{T_e} \approx 3$.

[4] This assumption was also partly motivated to reduce the differences between the models used by GRILLIX, GBS, STORM and FELTOR.

collision time $\tau_{en} \approx 1.4\,\mathrm{ms}$. Therefore, the model used for this validation was (in SI-units)

$$\left[\frac{\partial}{\partial t} + \boldsymbol{u}_{E\times B}\cdot\nabla\right] n = n\mathcal{K}(\phi) - \frac{n}{e}\mathcal{K}(T_e) - \frac{T_e}{e}\mathcal{K}(n) + \nabla\cdot\left[\left(\frac{j_\parallel}{e} - n u_\parallel\right)\mathbf{b}\right] + \mathcal{D}_n(n) + S_n \tag{7.2}$$

$$\nabla\cdot\left[\frac{m_i n}{B^2}\left(\frac{\partial}{\partial t} + \boldsymbol{u}_{E\times B}\cdot\nabla + u_\parallel\nabla_\parallel\right)\nabla_\perp\phi\right] = -T_e\mathcal{K}(n) - n\mathcal{K}(T_e) + \nabla\cdot\left(j_\parallel\mathbf{b}\right) + \mathcal{D}_\Omega(\Omega) \tag{7.3}$$

$$m_i n\left(\frac{\partial}{\partial t} + \boldsymbol{u}_{E\times B}\cdot\nabla + u_\parallel\nabla_\parallel\right)u_\parallel = -\nabla_\parallel p_e + \mathcal{D}_u(u_\parallel) \tag{7.4}$$

$$-\frac{m_e}{e}\left(\frac{\partial}{\partial t} + \boldsymbol{u}_{E\times B}\cdot\nabla + v_\parallel\nabla_\parallel\right)\frac{j_\parallel}{en} - \frac{\partial}{\partial t}A_\parallel = \frac{0.51 m_e}{e^2\tau_{en}} j_\parallel + \nabla_\parallel\phi - \frac{1}{en}\nabla_\parallel p_e - 0.71\frac{1}{e}\nabla_\parallel T_e + \mathcal{D}_\Psi(\Psi_m) \tag{7.5}$$

$$\begin{aligned}\frac{3}{2}\left(\frac{\partial}{\partial t} + \boldsymbol{u}_{E\times B}\cdot\nabla + v_\parallel\nabla_\parallel\right)T_e = &-\frac{7}{2}\frac{T_e}{e}\mathcal{K}(T_e) - \frac{T_e^2}{en}\mathcal{K}(n) + T_e\mathcal{K}(\phi) - T_e\nabla\cdot\left(v_\parallel\mathbf{b}\right) + 0.71\frac{T_e}{en}\nabla\cdot\left(j_\parallel\mathbf{b}\right)\\ &+ \frac{0.51 m_e}{e^2\tau_{en}}\frac{j_\parallel^2}{n} + \frac{1}{n}\nabla\cdot\left(3.16\frac{n T_e\tau_{en}}{m_e}\nabla_\parallel T_e\right) + \frac{3}{2}\mathcal{D}_{T_e}(T_e) + \frac{3}{2}S_{T_e}\end{aligned} \tag{7.6}$$

$$\nabla_\perp^2 A_\parallel = -\mu_0 j_\parallel \tag{7.7}$$

corresponding to the continuity equation, quasineutrality equation, parallel momentum balance, Ohm's law with electromagnetic induction and electron inertia, electron temperature equation and Ampere's law in the cold-ion limit, with the curvature operator $\mathcal{K}$ defined by equation B.18. The $\mathcal{D}$ terms correspond to numerical (hyper)diffusion terms used to stabilise the numerical scheme, which is applied on the vorticity Ω and modified electromagnetic potential Ψ_m (described in reference [109]). Compared to the equations presented in Appendix A, the main differences are the assumption of cold ions ($T_i \longrightarrow 0$) and the use of τ_{en} instead of τ_{ee} in the resistivity and heat-conductivity.

At the parallel boundary conditions, we used an $E \times B$-drift corrected velocity boundary condition (given by equation 3.27), a zero-current assumption $j_\parallel \longrightarrow 0, \phi \longrightarrow \Lambda_{sh} T_e$, a sheath-heath-transmission boundary condition (equation 3.36) with $\gamma_{s,e} - 1 = 2.5$ for T_e and a Neumann condition $\nabla_\parallel n = 0$ for the density. At the perpendicular boundaries, Neumann boundary conditions were used for all quantities except for the current (set to 0) and the potential (set to Λ_{sh}). Simulations using the realistic boundary surface (the blue circle in figure 7.2) were numerically unstable due to the shallow angle-of-incidence between the magnetic field and the wall[5]. A modified boundary surface (the orange line in figure 7.2) which maximised the angle-of-incidence between the poloidal field and the wall was found to be more stable, and as such the modified boundary was used for the validation.

---

[5] The drift-corrected boundary conditions are expected to be valid for angles-of-include $\geq 1.3°$ [175]

7.3. Simulating the TORPEX X-point scenario

The TORPEX magnetic field was processed using `parallax-equilibrium`, following the method developed in chapter 5. 16 poloidal planes were used to resolve the toroidal direction and the poloidal resolution was set to 1 mm, giving a total of $16 \times 1.5 \times 10^5 = 2.4 \times 10^6$ grid points. The time-step was set to $4 \times 10^{-5} \times R_0/c_{s0} = 2.7 \times 10^{-9}$ s, which was slightly below the CFL stability limit. A constant density and temperature was used as the initial condition, and the sources were tuned to approximately match the reference density and temperature values. The tuned source rates were 2.18×10^{18} particles-per-second and 8.83 W – notably less than the 300 W used in the experiment. To prevent the equations from becoming stiff due to low values of density and temperature, an additional adaptive source was used to prevent the density from dropping below $5 \times 10^{-15}\,\mathrm{m}^{-3}$ and the electron temperature below 2.21 eV. The simulations were performed on the Draco cluster and the Marconi supercomputer, at a cost of 6104 CPU-hrs per millisecond[6]. Tuning the sources took 0.15 ms, after which the simulation was continued for 7.36 ms to collect statistics[7].

7.4. Comparison to experiment

The results of the simulation were post-processed using the `TorX` analysis library. The mean profiles from the TORPEX simulation are shown in figure 7.3. These profiles are interpolated to the measurement positions of the swept Langmuir probe array and compared to the experimental measurements in figure 7.4. The density is shown to match fairly well between experiment and simulation. The simulated profile correctly predicts a higher density near the source region (in the left sector) and captures the up-down asymmetry. The most notable difference is that the simulated density doesn't reach as low a density value as the experiment, due to a density floor which is used for numerical reasons. Additionally, the density peak in the simulation is slightly less localised than in the experiment. An overall correlation of $\rho = 0.79$ is found between the simulation and experiment, which is remarkably high considering our strongly simplified treatment of the neutrals.

By contrast, the electron temperature profile is not well-predicted by the simulation. The simulated T_e profile has a similar spatial structure to the simulated n profile, while the measured experimental profile has a very different structure. The measured profile appears to be aligned vertically, with a peak temperature near the wall on the lower high-field-side. The poor agreement is most likely due to the lack of neutral ionisation and radiation in the simulations. This missing energy sink could explain the large difference in the simulated (8 W) and experimental power (300 W) – we are missing 97% of the power, so the power loss to the walls must be only a small fraction of the total power loss! Therefore, by neglecting the neutrals, we've dramatically changed the energy source and sink terms. This explains the poor match in the T_e profile

---

[6] Average value of 2500 time-steps, taking 1180 s on the Skylake partition of Marconi, using 16 MPI tasks and 8 OpenMP threads-per-task.

[7] This is a long time to gather statistics for a turbulence simulation. To get reasonable values of the skew, more sample points are necessary than for a lower-order statistical moment.

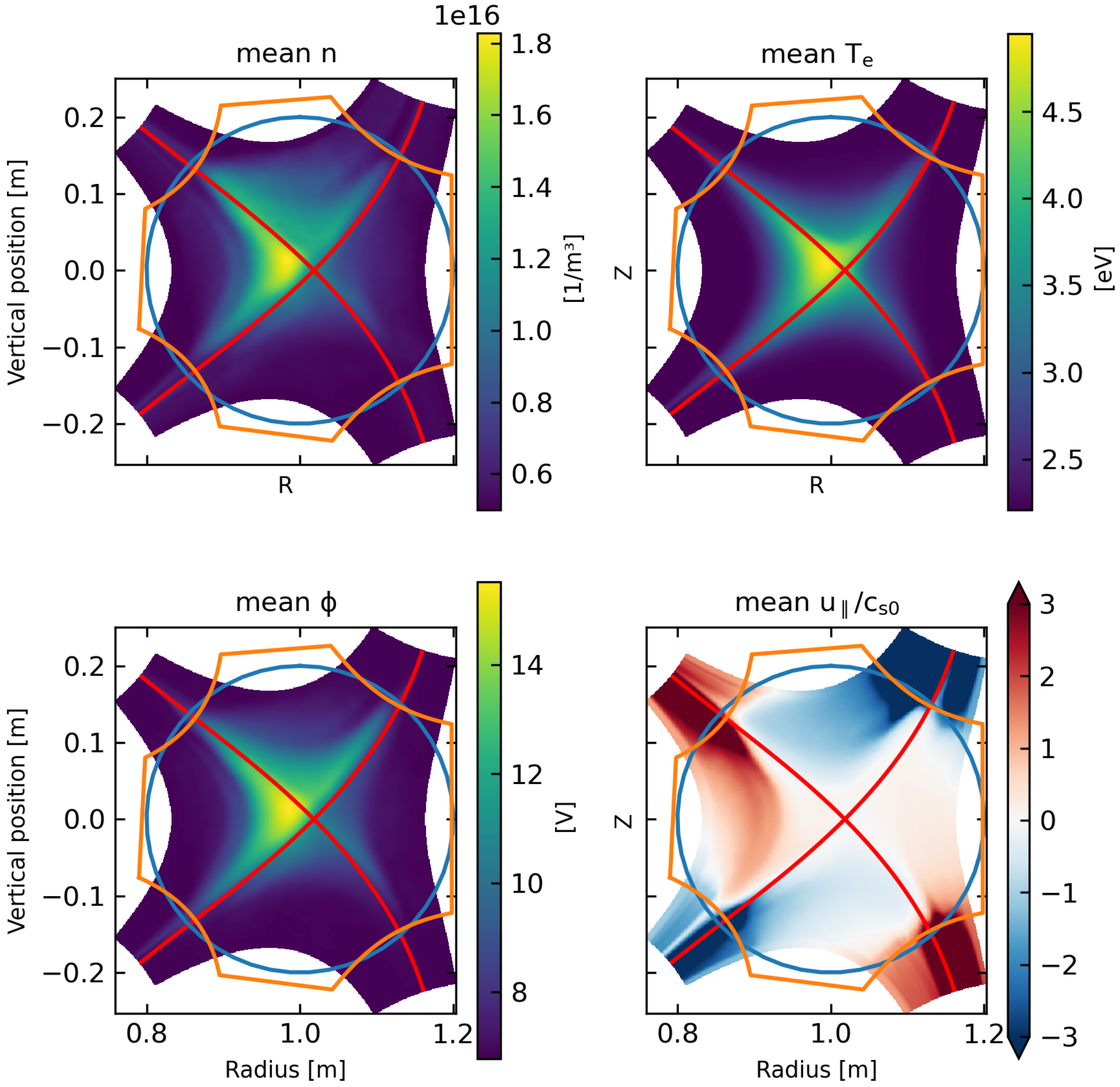

Figure 7.3.: Poloidal profiles of the mean density, electron temperature, electrostatic potential and velocity. The velocity is normalised to the reference sound speed $c_{s0} = 14.6\,\mathrm{km\,s^{-1}}$

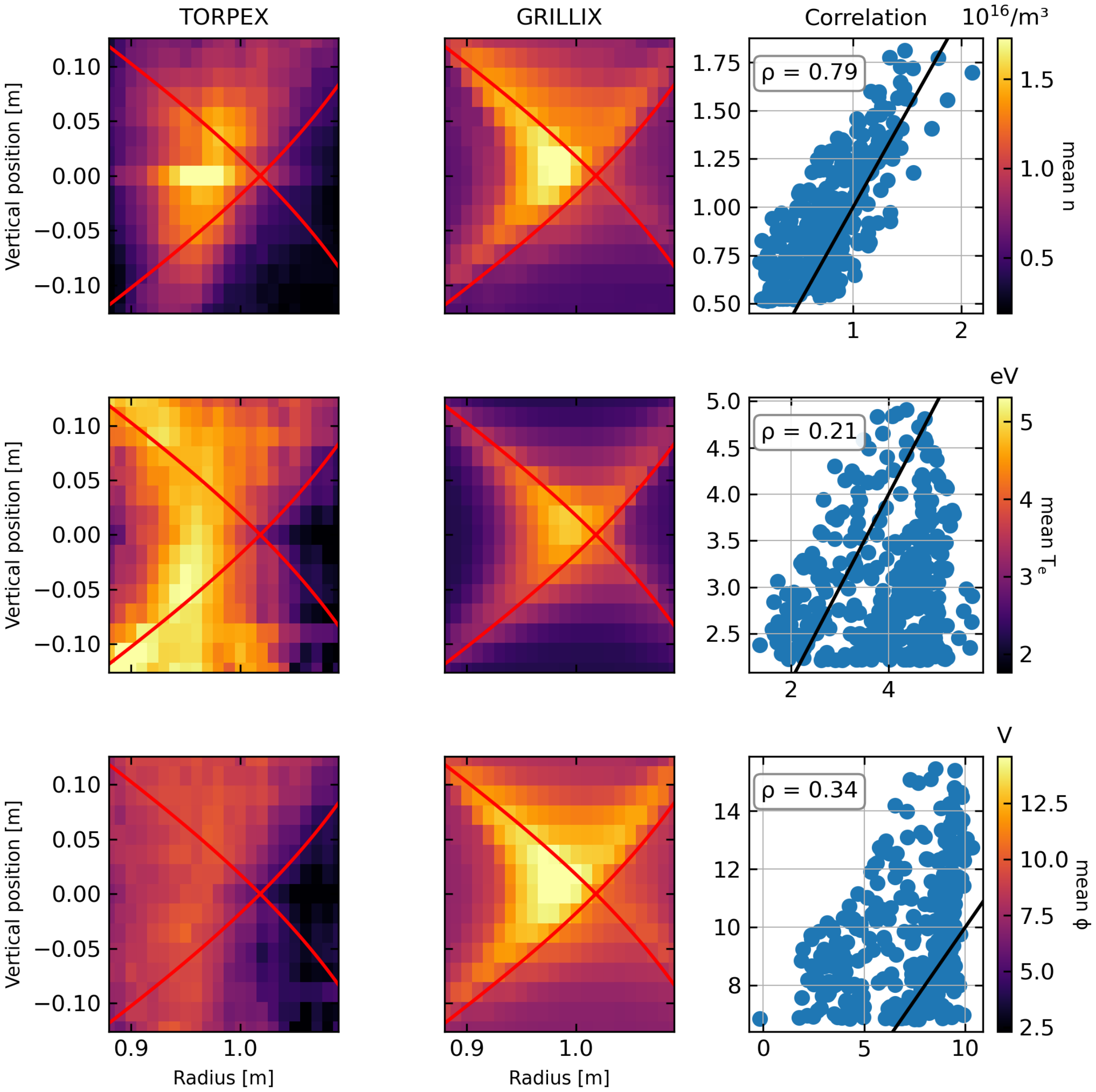

Figure 7.4.: Comparison of the simulated and measured profiles of the mean density (top row), electron temperature (middle row) and electrostatic potential (bottom row) at the measurement positions of the swept Langmuir probe array. The left column gives the experimental measurement and the middle column gives the corresponding GRILLIX simulation. The right column gives the correlation between the simulated and measured profiles. The x-value of each point corresponds to an experimental measurement, and the y-value gives the simulated value at the same position. The Pearson correlation coefficient ρ is given in the annotation, and the black solid line gives the perfect-correlation $y = x$.

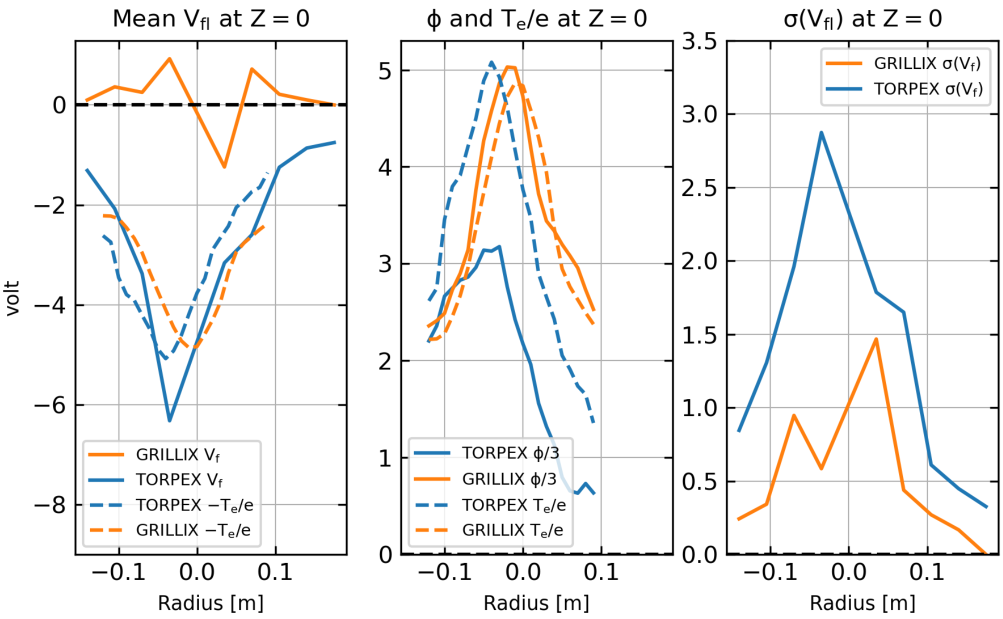

Figure 7.5.: Comparison of the simulated and measured profiles of the mean floating potential (left) and its standard deviation (right), along a line at $Z = 0$. The central figure compares the simulated and measured profiles of the plasma potential and the electron temperature (divided by the elementary charge to give units of volts).

(correlation $\rho = 0.21$) – and actually, it is surprising that we managed to match the density profile so well.

The match for the potential is similar to the match for the electron temperature. Again, the simulation predicts a similar structure to the density profile, while the measured profile appears to be vertically aligned, and the resulting correlation ($\rho = 0.34$) is poor. The relationship between the potential and the electron temperature is given by the floating potential $V_{fl} = \phi - \Lambda_{sh}$. We compare the simulated and measured floating potential at the $Z = 0$ position of the swept Langmuir probe array in figure 7.5. Here, we see that the mean simulated V_{fl} is closer to zero than in the experiment. Since we have set $V_{fl} \to 0$ at the boundaries, the low V_{fl} values near the boundaries are expected, but it is not immediately obvious how this affects the interior dynamics since we also don't match the T_e profile. In the central plot of figure 7.5, we see that both T_e and ϕ vary with position in both the experiment and in the simulation. In the simulation, $T_e/e \approx \phi/3$ such that the floating potential is always $V_{fl} \approx 0$, while in the experiment it appears that $V_{fl} \propto -T_e/e$. From equation 7.5 we see that the parallel gradients of T_e and ϕ are related via the parallel current, which may suggest that the insulating boundary conditions for ϕ and $j_{\|}$ need to be reconsidered. Interesting, despite the poor agreement in the mean floating potential, its standard deviation agrees more closely with the experiment – suggesting that we might be capturing the turbulence more accurately than the background drifts.

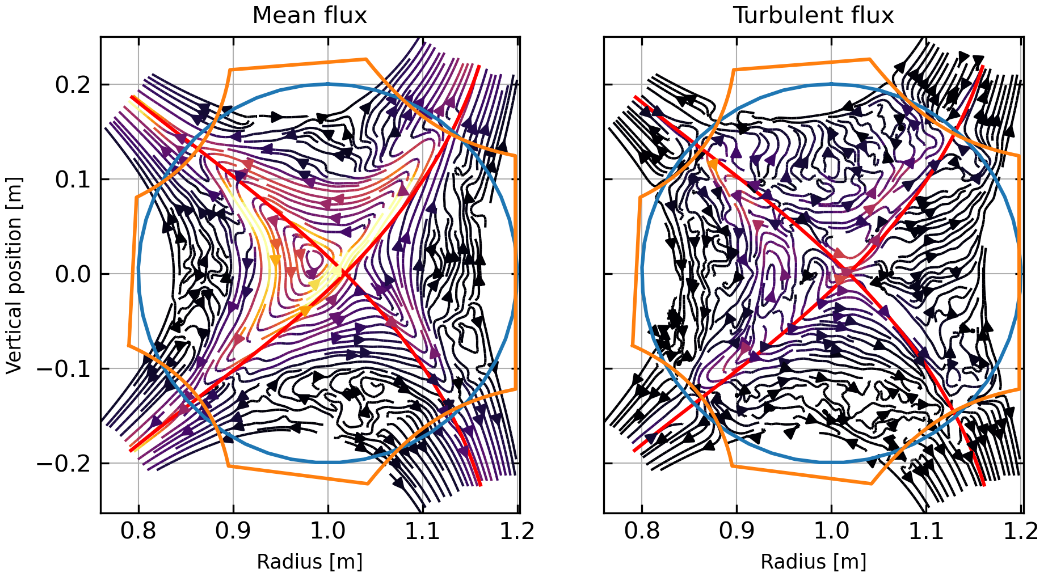

Figure 7.6.: Stream-plots of the mean and turbulent poloidal ion fluxes in TORPEX. The mean flow is calculated as $\text{mean}(\boldsymbol{\Gamma}_i) = \text{mean}(n\boldsymbol{u}_{tot})$, where $\boldsymbol{u}_{tot} = \boldsymbol{u}_{E\times B} + \boldsymbol{u}_{dia} + u_{\|}\hat{\mathbf{b}}$. The turbulent flux is calculated as $\text{mean}(n \times (\boldsymbol{u}_{tot} - \text{mean}(\boldsymbol{u}_{tot})))$. The colour scale gives the magnitude of the poloidal components of the vector field, and the stream-plot is computed from the poloidal components of the vector field. The maximum of the colour scale for the mean flux is set to ten times the maximum for the turbulent flux, since the turbulent flux is much smaller than the mean flux.

Although there is no available experimental data for the parallel velocity, it is surprising that the parallel velocity profile (shown in figure 7.3) is highly supersonic throughout the plasma volume. By following the time evolution of the profiles and comparing the results to the TCV validation in the next chapter, it seems that there is a numerical feedback loop causing extremely high velocities, discussed more in section 8.6.2. Despite the high velocities, it is interesting to consider the flow profile observed in the simulation. This is shown both for the mean particle flux $\Gamma = n\boldsymbol{u}$ and turbulent flux $n\,(\boldsymbol{u} - \text{mean}(\boldsymbol{u}))$ in figure 7.6. In the mean-flow profile, we see a distinctive flow pattern that transports particles from the source region (left) into the upper region. There, the asymmetry observed in the density profile can be attributed to the mean $E \times B$-drift which preferentially transports particles into the upper sector (the mean electric field points from the source region across the separatrix, and the asymmetry of the drift can be found via the right-hand-rule). This would correspond to a preferential transport towards the high-field-side target in a lower-single-null favourable-field-direction tokamak discharge – suggesting that convective cells around the X-point may contribute to in-out asymmetries. The turbulent flux is much weaker than the mean flux, and it is conspicuously absent in the right sector – which is roughly analogous to the private-flux-region of a tokamak. We see that the mean flow is consistently outwards at the boundaries, while the turbulent component appears to stagnate near the boundaries.

7.5. Comparison to other models

The TORPEX X-point scenario was also simulated by the GBS [110, 111], STORM [113] and FELTOR [107] models [126]. For all models, neutrals were not directly included, but rather assumed to modify the plasma resistivity and heat conductivity as in section 7.2, permitting a direct comparison of the codes. The other fluid models, GBS and STORM, found similar results to GRILLIX for the ion saturation current, electron temperature and injected power. Conversely, the plasma potential in these simulations had a lower minimum value and a range closer to the experimental values due to the use of different potential boundary conditions. The gyrofluid FELTOR model showed significantly different results to the fluid codes, predicting ion saturation current and potential profiles lower than the other codes (and lower than the measurements). However, since FELTOR also used a fixed electron temperature, it is unclear whether these differences are due to the gyrofluid model or the isothermal approximation. A qualitative validation metric (introduced in reference [118] and discussed in section 8.7) was used to assess the overall match for each of the codes. It was found that GRILLIX achieved a slightly better overall match ($\chi = 0.85$) compared the other codes ($\chi \geq 0.89$), although the result is still far from what could be considered as indicating a match.

7.6. Discussion

The overall result from the TORPEX was not particularly encouraging. Although we tried to include the effect of neutrals by modifying the resistivity and heat conductivity, it appears that this simple treatment is insufficient to match the experiment. The omission of self-consistent neutral dynamics led to unrealistic power sources and sinks, leading to a poor match to the T_e profile. This in turn led to a poor match for the electrostatic potential, which was seen to closely follow Λ_{sh} throughout the plasma volume. Nevertheless, the density profile was found to match well, which is surprising since the background drifts will be affected by the (erroneous) ϕ profile. The simulation reached extremely high parallel velocities, which might indicate a feedback loop. The sensitivity to neutral dynamics and boundary conditions, unfortunately, make this case extremely difficult to match. Presumably, a significantly improved match could be achieved by including self-consistent neutral dynamics. However, the lack of a confined region means that this case will be dominated by sheath effects, and the low pitch angle between 0.5° and 1.2° at the boundaries means that our sheath boundary conditions (which require $\geq 1.3°$) are not valid [176]. Additionally, the low electron temperatures mean that we need a surprisingly large number of grid-points despite the small size of the device, which increases the computational cost. As such, rather than acting as a simple test of the basic functionality of the simulations, this case could be useful for experimenting with various sheath models.

8. Validation against the TCV-X21 diverted tokamak scenario

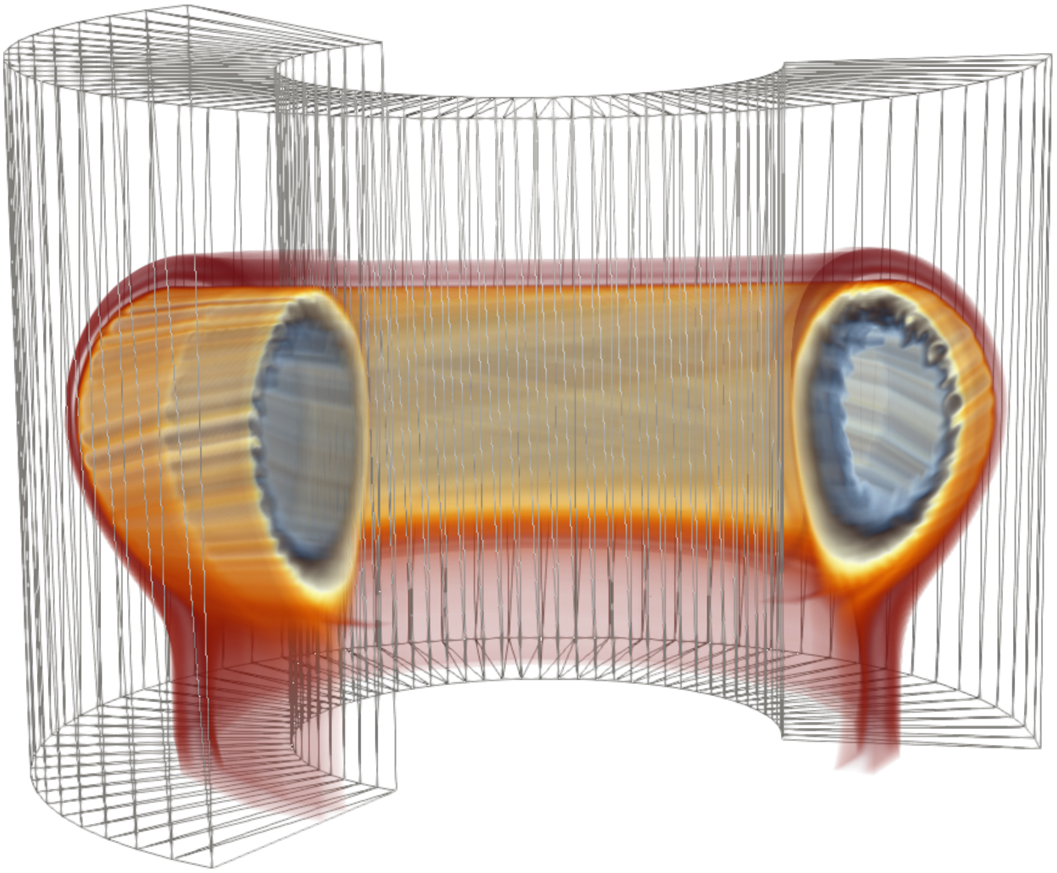

Figure 8.1.: The edge plasma density from a GRILLIX simulation, and the TCV vessel. Rendering performed with NVIDIA IndeX and Paraview.

All reactor-relevant tokamaks or stellarators use a divertor. For a burning plasma, the divertor is required to remove helium ash from the plasma, making them essential for reactor operations. Beyond this, there are several advantages of the divertor geometry compared to the simpler limited geometry, discussed in section 1.2.2, and so almost all fusion experiments are operated with a divertor. Despite this, edge validations have often focussed on limited discharges [120, 121, 126] or basic plasma devices [117, 118, 177, 119], to avoid the additional complexity introduced by the divertor magnetic geometry. This is useful for developing the basic functionality of the codes, but to move towards reactor-relevant simulations it is clear that validations in diverted geometry are essential. In this chapter, we describe a landmark validation project – the TCV-X21 validation case, developed as part of EUROFusion Enabling Research Project `MFE19.EPFL-02` led by Christian Theiler. The results of this project have been submitted for publication as Oliveira and Body[1] et al., 2021, '*Validation of edge turbulence codes against the TCV-X21 diverted L-mode reference case*' [2], comparing the results from the GRILLIX, GBS and TOKAM3X codes. In this chapter, we will discuss the results of this validation, focussing mainly on the GRILLIX results and presenting them in more detail than in the combined paper.

8.1. The TCV-X21 diverted L-mode scenario

TCV is a medium-sized tokamak, operated by the Swiss Plasma Centre [37]. It can achieve a wide variety of plasma configurations – including advanced divertor configurations – due to the unshaped (rectangular) vacuum vessel and 16 independently-powered shaping coils. For this work, a new scenario was specifically developed for the validation of turbulence codes. The scenario was designed to be as easy as possible to match – a simple Deuterium-fuelled lower-single-null with a reduced field (for reduced computational cost), with a reduced density targetting a strongly sheath-limited regime (to reduce the effect of neutrals), in L-mode (since H-mode requires the formation of a transport barrier) and with only Ohmic heating.

The toroidal field was reduced from the nominal 1.43 T to 0.95 T, which increased the reference ion Larmor radius ρ_{s0} and therefore the spatial scale of several microinstabilities (see table 1.1). Compared to the nominal field, in the reduced field $\rho_{s0} = \sqrt{T_{e0} m_i}/eB_0 \propto 1/B_0 \approx 1.54\times$ larger, reducing the number of grid-points required by $\left(R_0/\rho_{s0}\right)^2 \propto 1/B^2 \approx 2.37\times$. This either reduces the cost of the simulations by half or allows for simulations with effectively double the resolution at the same computational cost. To keep a similar q-profile and field-line pitch to a TCV discharge at nominal parameters, the plasma current was reduced to $I_p \simeq 165\,\mathrm{kA}$.

To reduce the effect of the neutrals, a low density corresponding to $\sim 25\%$ of the Greenwald density was used, and the plasma was fuelled from the top seeding value (indicated in figure 8.3). The electron temperature dropped by a factor of between ~ 2 (at the separatrix) to ~ 0.8 (at $\Psi_N = 1.08$) from the divertor-entrance (measured by Thomson scattering) to the low-field-side divertor target (measured by the wall-embedded Langmuir probe array). This suggests that the discharge is sheath-limited and in low-recycling conditions. For the initial modelling, we use this to assume that all of the density source is in the confined region and neglect the ionisation in the divertor. We don't include neutrals and so need to add a density source, which was assumed to be constant along flux-surfaces and localised to a region just inside the confined region, as indicated in figure 8.2. The applied density source function was

$$\mathcal{S}_n(R,Z) = c_n \exp\left[-\left(\frac{\Psi_N(R,Z)^2 - \Psi_{N,c}^2}{\Psi_{N,w}^2}\right)^2\right] \tag{8.1}$$

with the source centre at $\Psi_{N,c} = 0.915$ and the source width $\Psi_{N,w} = 0.0838$. The source rate

---

[1] Co-first authorship.

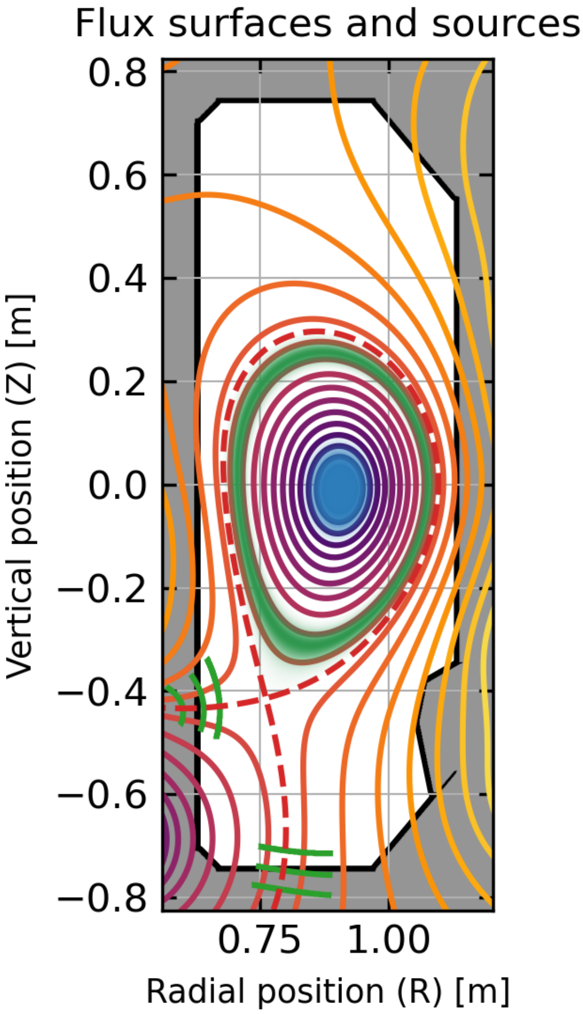

Figure 8.2.: Flux-surfaces and estimated source positions in the TCV-X21 scenario. The energy source position is indicated by the blue shaded region, and the particle source position is indicated by the green shaded region. The divertor is marked in black, and points outside the vessel are indicated by the grey shaded region. The 0, 0.5 and 1 levels of the penalisation characteristic function are shown in green (near the targets), and the separatrix is indicated by a red-dashed line.

c_n was unknown and so it was tuned by each simulation group to give a reasonable match of the outboard midplane density at the separatrix. This gave a total particle injection rate of $1.85 \times 10^{21}\,\mathrm{s}^{-1}$ – which is reasonably close to the $\approx 3 \times 10^{21}\,\mathrm{s}^{-1}$ inferred from the total flux reaching the wall Langmuir probes.

The discharge was heated Ohmically, to reduce the number of heating systems which had to be considered by the modelling groups. Since Ohmic heating is proportional to the plasma current, it is assumed that the power source is localised near the magnetic axis (current measurements were not available). Ohmic heating will preferentially heat the electrons since $P_{Ohm} = \sigma E^2$ and $\sigma \propto 1/\sqrt{m_\alpha}$, so we apply a T_e source only. The applied core power source is indicated in figure 8.2. Rather than applying a temperature source as per usual, we modified the source such that it injected a constant power. The general form for the total power is

$$P = \frac{3}{2}\int n(\boldsymbol{x})\left(S_{T_e}(\boldsymbol{x}) + S_{T_i}(\boldsymbol{x})\right) + \left(T_e(\boldsymbol{x}) + T_i(\boldsymbol{x})\right) S_n(\boldsymbol{x})\mathrm{d}^3V \tag{8.2}$$

where $\boldsymbol{x} = (R, \phi, Z)$. For the TCV modelling we set

$$S_{T_e}(\boldsymbol{x}) = \frac{1}{n(\boldsymbol{x})}\left[S_P(\boldsymbol{x}) - \left(T_e(\boldsymbol{x}) + T_i(\boldsymbol{x})\right) S_n(\boldsymbol{x})\right] \text{ and } S_{T_i}(\boldsymbol{x}) = 0 \tag{8.3}$$

which simplifies the power source to

$$P = \frac{3}{2}\int S_P(\boldsymbol{x}) d^3V \tag{8.4}$$

The resulting power is independent of the density source rate, since the energy associated with adding particles is subtracted from T_e. We don't use an external source for the ion temperature, and instead heat them via equipartition. For the validation, S_P was adjusted to give 150 kW of power, matching the total Ohmic heating power. A later bolometry analysis estimated that ~ 30 kW was being lost to confined-region radiation, while the ionisation associated with the particle source would require a further 4.0 kW (using the particle source rate and an ionisation energy of 13.6 eV), so probably a value of 115 kW may have been more appropriate. Nevertheless, as we will discuss later in this chapter, it would be preferable to include self-consistent neutral dynamics, rather than increasing the complexity of the source functions.

8.2. The TCV-X21 validation dataset and repository

The SPC team collected an experimental dataset by performing several discharges based on the TCV-X21 scenario. An extensive dataset was collected by combining data from different diagnostics and discharges, giving a total of 45 observables from the 5 diagnostic systems indicated in figure 8.3, measured in two toroidal field directions. The diagnostic systems and the methods for calculating the experimental uncertainty are detailed in reference [2]. The dataset observables include the plasma density n, electron temperature T_e, plasma potential ϕ, ion saturation current density j_{sat} and floating potential $V_{fl} = \phi - \Lambda_{sh}$ from the FHRP (outboard midplane), RDPA (divertor volume), LFS-LP (low-field-side target) and HFS-LP (high-field-side target) Langmuir probe arrays. Additionally, the immersed probes (FHRP and RDPA) measure the parallel Mach number $M_{\|}$, and the wall-mounted probes (LFS-LP and HFS-LP) measure the parallel current density $j_{\|}$. In addition to the probe measurements, the TS (Thomson scattering) system gives measurements of n and T_e at the divertor entrance, and the IR-LFS (infrared camera) system gives $q_{\|}$ at the low-field-side target. No edge-data is available for the ion temperature, while the value in the confined region is determined via charge-exchange recombination spectroscopy.

To enable future validations against this dataset, the experimental data, extended documentation of the validation case, the routines used to process the simulations and the simulation

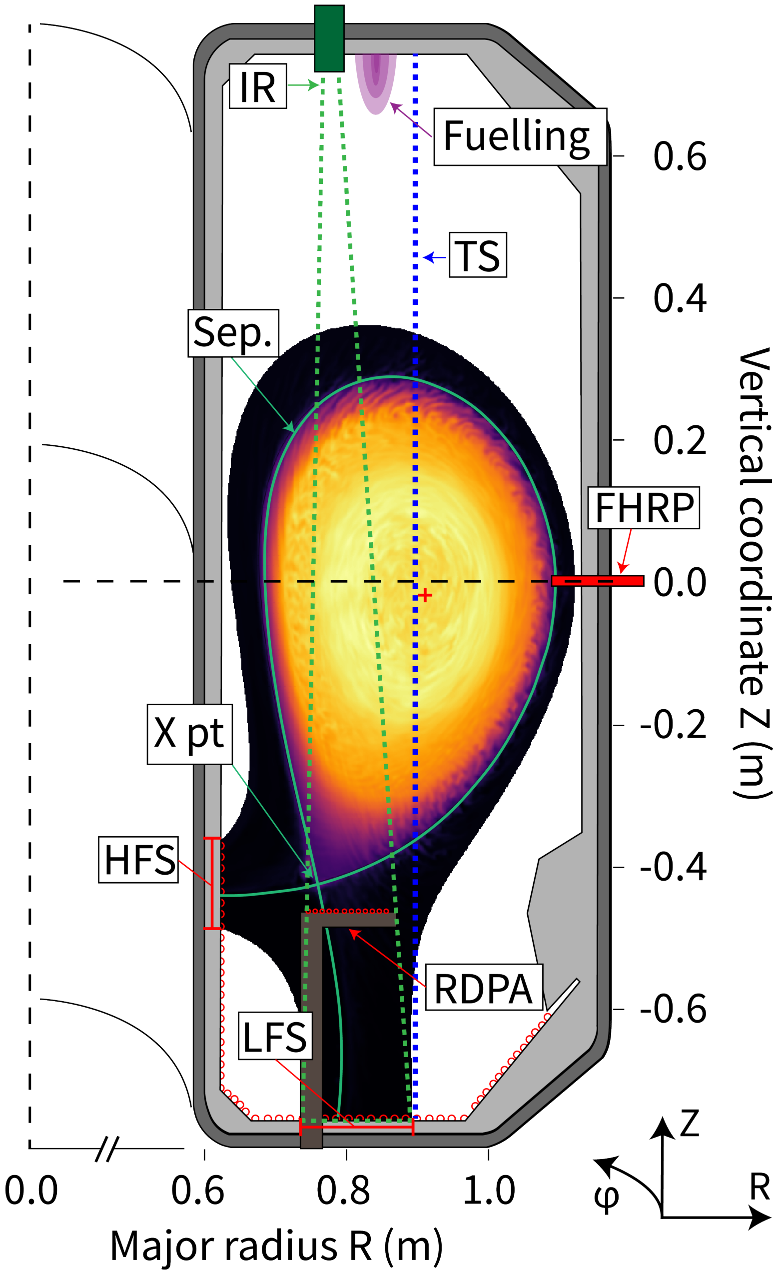

Figure 8.3.: The diagnostics used to collect experimental data in the TCV-X21 scenario, overlayed onto the density from a GRILLIX simulation. Experimental data was collected via a fast horizontally-reciprocating midplane probe (FHRP), the Thomson scattering system (TS, using only points below the magnetic axis), wall-embedded Langmuir probes at the low-field-side (LFS) and high-field-side (HFS) targets, an infrared camera (IR) measuring the heat flux at the low-field-side target and a vertically-reciprocating divertor probe array (RDPA).

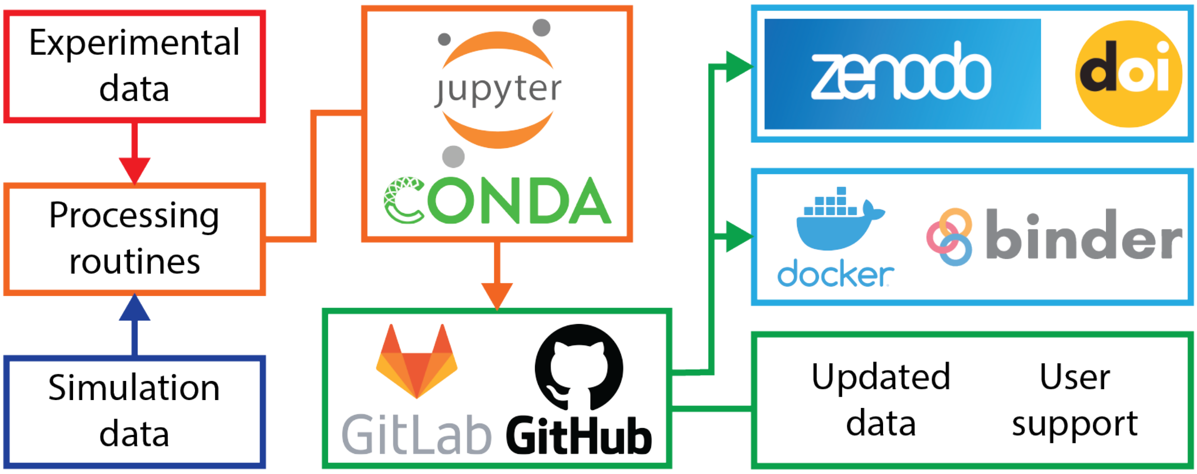

Figure 8.4.: For the TCV-X21 validation case, the experimental and simulation data is stored in an interoperable data format (NetCDF) and processed using an open-source library of Python scripts. The functionality of this library is built on packages from Conda-forge, and in-place documentation is provided with Jupyter notebooks. These are shared via `gitlab.mpcdf.mpg.de` and `github.com` repositories. The repository is also permanently stored on `zenodo.org`, and a Docker image of the library is used to provide in-browser interactivity via `mybinder.org`. By using a public `github.com` mirror, we can provide user-support via issues and accept user-submitted data via merge requests.

results are provided according to the Findable Accessible Interoperable Reproduce (FAIR) open data principles. The dataset and resources are shared at `github.com/SPCData/tcv-x21` and `gitlab.mpcdf.mpg.de/tcv-x21/tcv-x21`. In addition to the scientific outcomes of this work, this project can also be considered an experiment for the public release of fusion data. We're hoping that this will make the dataset and validation case more widely used and that this will encourage more sharing of fusion data and more openness in code validation. If you're considering something similar, as early as possible in the project you should decide how you will store your data, how you will share it, and under what licence. This data management plan can be informal, although having a formal structure in place and getting your contributors to sign up can avoid future conflicts. For the licence, the Creative Commons licences are recommended if you're sharing a dataset. We selected a standard CC-BY 4.0 Attribution licence which includes a requirement for attribution and marking any changes, while we decided against adding a non-commercial clause since this can prevent the use of datasets in things like textbooks.

The licence and a data management plan are the most important parts of sharing a dataset, but if you want to make it easier to use your dataset there are a few additional tools that you can use. These are outlined in figure 8.4. For user-support, a public `github.com` repository lets anyone with a GitHub account make issues and merge requests for your repository, although there are a few oddities such as charging for Git-LFS which make this service less than optimal. As such, we also kept the institutional `gitlab.mpcdf.mpg.de` repository, which is easier to do development and testing in. We also stored a copy of the repository with CERN's `zenodo.org`, which offers permanent versioned storage of datasets up to 50GB, a DOI for each version, an interface to `github.com` and a Python-based REST API for sending and retrieving files. I additionally built a Docker image based on a `jupyter/scipy-notebook` image from `github.com/jupyter/docker-stacks`. This allowed for in-browser interactive data exploration via `mybinder.org` – which was rather complicated to set up and somewhat frivolous, although it is useful to have a snapshot of the data analysis as of paper submission available at the click of a button. The paper was only recently published but the work is already gaining interest, with at least 5 groups aiming to reproduce and extend the simulations[2] and more experimental data being collected to include in the repository. These are promising signs that TCV-X21 will be a significant work setting the standards for rigorous validations, and also for the open and accessible sharing of fusion data.

8.3. Hot-ion electromagnetic model

To simulate the TCV-X21 scenario, we used a hot-ion, electromagnetic model which evolves the plasma density n, the electron and ion temperatures T_e and T_i, the electrostatic potential ϕ, the parallel velocity $u_\parallel$, the parallel current density $j_\parallel$ and the parallel component of the electromagnetic vector potential $A_\parallel$. Self-consistent neutral dynamics were not included, nor was the electromagnetic 'flutter' transport. The equations are implemented in GRILLIX in a dimensionless form, given in appendix A and appendix A of reference [129], included here in SI units for reference;

$$\left[\frac{\partial}{\partial t} + \boldsymbol{u}_{E\times B}\cdot\nabla\right] n = n\mathcal{K}(\phi) - \mathcal{K}(p_e) + \nabla\cdot\left[\left(j_\parallel - n u_\parallel\right)\mathbf{b}\right] + \mathcal{D}_n(n) + S_n$$

$$\nabla\cdot\left[\frac{n}{B^2}\left(\frac{\partial}{\partial t} + \boldsymbol{u}_{E\times B}\cdot\nabla + u_\parallel\nabla_\parallel\right)\left(\nabla_\perp\phi + \frac{\nabla_\perp p_i}{n}\right)\right] = -\mathcal{K}(p_e + p_i) + \nabla\cdot\left(j_\parallel\mathbf{b}\right) - \frac{1}{6}\mathcal{K}(G) + \mathcal{D}_\Omega(\Omega)$$

$$\left(\frac{\partial}{\partial t} + \boldsymbol{u}_{E\times B}\cdot\nabla + u_\parallel\nabla_\parallel\right) u_\parallel = -\frac{\nabla_\parallel\left(p_e + p_i\right)}{n} + T_i\mathcal{K}(u_\parallel) - \frac{2}{3}\frac{B^{3/2}}{n}\nabla_\parallel\frac{G}{B^{3/2}} + \mathcal{D}_u(u_\parallel)$$

$$\beta_0\frac{\partial}{\partial t}A_\parallel + \frac{m_e}{m_i}\left(\frac{\partial}{\partial t} + \boldsymbol{u}_{E\times B}\cdot\nabla + v_\parallel\nabla_\parallel\right)\frac{j_\parallel}{n} = -\left(\frac{\eta_{\parallel 0}}{T_e^{3/2}}\right) j_\parallel - \nabla_\parallel\phi + \frac{\nabla_\parallel p_e}{n} + 0.71\nabla_\parallel T_e + \mathcal{D}_\Psi(\Psi_m)$$

$$\begin{aligned}\frac{3}{2}\left(\frac{\partial}{\partial t} + \boldsymbol{u}_{E\times B}\cdot\nabla + v_\parallel\nabla_\parallel\right) T_e &= T_e\mathcal{K}(\phi) - \frac{T_e}{n}\mathcal{K}(p_e) - \frac{5}{2}T_e\mathcal{K}(T_e) - T_e\nabla\cdot\left(v_\parallel\mathbf{b}\right) + 0.71\frac{T_e}{n}\nabla\cdot\left(j_\parallel\mathbf{b}\right)\\ &+ \frac{1}{n}\nabla\cdot\left[\left(\chi_{\parallel e0}T_e^{5/2}\right)\mathbf{b}\nabla_\parallel T_e\right] - \frac{2}{\tau_{e0}}\frac{m_e}{m_i}\left(\frac{n}{T_e^{3/2}}\right)(T_e - T_i) + \left(\frac{\eta_{\parallel 0}}{T_e^{3/2}}\right)\frac{j_\parallel^2}{n} + \frac{3}{2}\left(\mathcal{D}_{T_e}(T_e) + S_{T_e}\right)\end{aligned}$$

---

[2] GRILLIX, GENE-X, GBS, SOLEDGE3X, SOLPS – that I know of.

$$\frac{3}{2}\left(\frac{\partial}{\partial t} + \boldsymbol{u}_{E\times B}\cdot\nabla + u_{\|}\nabla_{\|}\right)T_i = T_i\mathcal{K}(\phi) - \frac{T_i}{n}\mathcal{K}(p_e) + \frac{5}{2}T_i\mathcal{K}(T_i) - T_i\nabla\cdot\left(u_{\|}\mathbf{b}\right) + \frac{T_i}{n}\nabla\cdot\left(j_{\|}\mathbf{b}\right)$$

$$+\frac{1}{n}\nabla\cdot\left[\left(\chi_{\|i0}T_i^{5/2}\right)\mathbf{b}\nabla_{\|}T_i\right] + \frac{2}{\tau_{e0}}\frac{m_e}{m_i}\left(\frac{n}{T_e^{3/2}}\right)(T_e - T_i) + \frac{2}{9\eta_{i0}}\frac{G^2}{nT_i^{5/2}} + \frac{3}{2}\left(\mathcal{D}_{T_i}(T_i) + S_{T_i}\right)$$

$$\nabla_{\perp}^2 A_{\|} = -\mu_0 j_{\|}$$

corresponding to the continuity (2.56), quasineutrality (2.58), momentum-balance (2.60), Ohm's law (2.62), electron temperature (2.67) and ion temperature (2.71) equations, plus Ampère's law (2.74), with the curvature operator $\mathcal{K}$ defined by equation B.18. The $\mathcal{D}$ terms correspond to numerical hyper-diffusion terms used to stabilise the numerical scheme, which is applied on the vorticity Ω and modified electromagnetic potential Ψ_m (described in reference [109]).

We limit the heat conductivity in the core, since the Braginskii heat flux diverges at low collisionality (high temperatures). To calculate a reasonable value for the heat flux limit on closed flux-surfaces, we use equation B.63 from the SOLPS-ITER manual [92], where

$$\chi_{\|e} = \chi_{\|e0}T_e^{5/2} \text{ is replaced by } \chi_{\|e,limited} = \chi_{\|e0}T_e^{5/2}\left(1 + \frac{\lambda_{HC}}{qR_0}\right)^{-1} \tag{8.5}$$

where λ_{HC} is the mean-free-path of hot-tail electrons, given as

$$\lambda_{HC}[\mathrm{m}] = 7.5\times 10^{16}\frac{(T_e[\mathrm{eV}])^2}{n[\mathrm{m}^{-3}]} \tag{8.6}$$

and q is the safety factor. At the time these simulations were run, we didn't have the functionality to set a variable heat-flux. Instead, a value was calculated by analysing a partially-converged simulation and finding a heat flux limit that was reasonably representative of the actual result of the above equation.

As in the TORPEX validation, the TCV simulations were found to be strongly affected by boundary conditions. For the first simulations performed, we used the same insulating boundary conditions as in the TORPEX validation, with $j_{\|} \to 0, \phi \to \Lambda_{sh}$. However, it was found that strong internal currents were driven in TCV, including in the SOL. Using the insulating boundary conditions, these currents had to be forced to zero in the boundary region, leading to a strong parallel gradient in $j_{\|}$. Due to the $\frac{T}{n}\nabla\cdot\left(j_{\|}\hat{\mathbf{b}}\right)$ terms in the T_e and T_i equations, this led to a strong heating near the boundaries. For the electron temperature, due to the larger sheath-heat transmission coefficient, this heating could be transported to the targets, while for the ions the heat is not lost as effectively and so the overall T_i increases. Eventually, this would cause the simulations to crash with $T_i \sim 100\,\mathrm{eV}$ in the SOL – higher than in the confined region. To avoid this heating term, the parallel current boundary condition was changed to $\nabla_{\|}j_{\|} = 0$ – a simple Neumann boundary condition, setting the boundary current to the nearest interior value. As we will later show, this led to surprisingly good agreement with the experimentally measured current profiles. However, the potential was still set to the insulating value $\phi = \Lambda_{sh}$.

The other boundary conditions were an $E \times B$-drift corrected velocity boundary condition (given by equation 3.27), a sheath-heath-transmission boundary condition (equation 3.36) with $\gamma_{s,e} - 1 = 2.5$ for T_e and $\gamma_{s,i} - 1 = 0.1$ for T_i, and a Neumann condition $\nabla_{\parallel} n = 0$ for the density. At the perpendicular boundary conditions, Neumann boundary conditions are used for all quantities except for the current (set to 0) and the potential (set to Λ_{sh}).

8.4. Simulating the TCV-X21 scenario

The magnetic equilibrium corresponding to TCV shot 65402 at time $t = 1\,\mathrm{s}$ was computed using the LIUQE code [160]. This equilibrium was processed with `parallax-equilibrium`, and used for the simulations in both field directions. For all simulations, we used 16 toroidal planes to resolve the parallel dynamics. To calculate the required perpendicular resolution, the reference electron temperature was set to the separatrix value measured by Thomson scattering $T_{e0} = 41.3\,\mathrm{eV}$, giving a reference sound Larmor radius

$$\rho_{s0} = \frac{\sqrt{T_{e0} m_i}}{e B_0} = \frac{\sqrt{41.3\,\mathrm{eV} \cdot 2.014\,\mathrm{u}}}{e \cdot 0.95\,\mathrm{T}} = 0.977\,\mathrm{mm}$$

To resolve microinstabilities which mostly occur on scales around $1 - 10\rho_s$ (see table 1.1), we need a perpendicular grid resolution of $\sim \rho_s$ or finer. However, in GRILLIX we use a regularly-spaced perpendicular grid, and so set a single perpendicular resolution in terms of ρ_{s0}. The relationship between the reference and local Larmor is shown in figure 8.5. Most of the confined region has $\rho_s > \rho_{s0}$, except for the outermost flux-surfaces on high-field-side (which has a larger ρ_s due to the higher magnetic field). Conversely, all of the open field-line region has $\rho_s < \rho_{s0}$.

The resolution required to resolve the turbulent drive and transport depends both on the spatial scale of the instabilities and on the numerical scheme. Ideally, we would scan the resolution, increasing it until an increase of resolution no longer causes any noticeable change in the dynamics. However, due to the strong variation of ρ_s it's very expensive to run simulations that are globally converged with respect to resolution. As such, we instead pick a resolution which gives a reasonable balance between cost and accuracy.

For TCV-X21, we used a perpendicular resolution of $2\rho_{s0}$ for quickly scanning input parameters. At this perpendicular resolution and with 16 poloidal planes and a timestep of $1.02\,\mathrm{ns}$, the simulations cost around 1.69×10^4CPU-hrs per millisecond – giving about $2\,\mathrm{ms}$ per week on 4 nodes of Marconi-Skylake[3]. Once the $2\rho_{s0}$ simulations reached a quasisteady state, we interpolated the solution to a $1\rho_{s0}$-resolution grid and then continued the simulation, at a cost of 9.14×10^4CPU-hrs per millisecond. This changed the turbulence drive and so we needed to find a new quasisteady state, but reaching convergence was faster than reaching convergence from a clean initial condition – suggesting that this method might also be helpful for economising simulations of larger devices. Visually, the higher-resolution simulations looked similar in the confined-region, but had more filaments in the open-field-line region and especially the private-flux-region – which is consistent with what we would expect from figure 8.5.

---

[3] (at realistic resistivity and heat conductivity) – this is *extremely* cheap for a turbulence simulation.

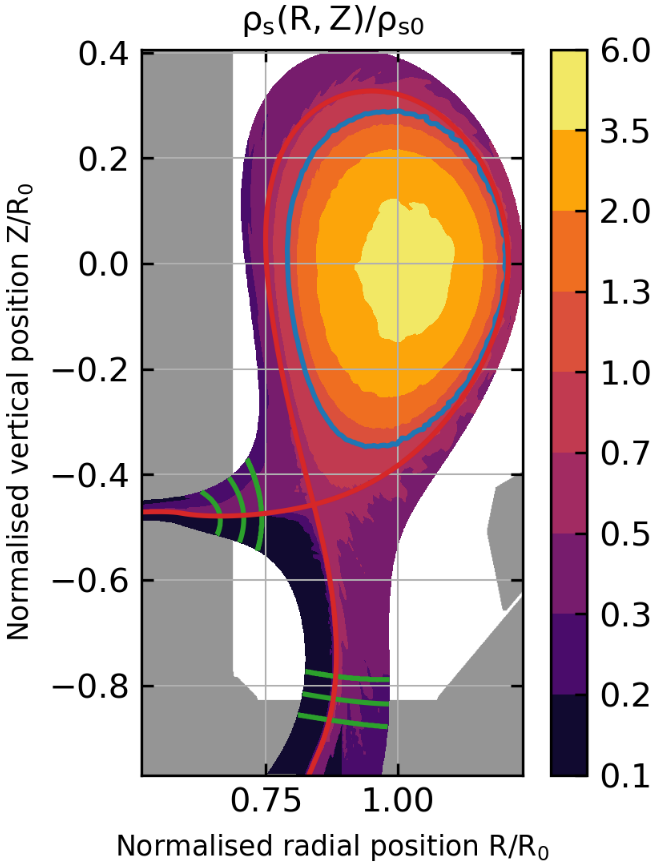

Figure 8.5.: The ratio of the local sound radius ρ_s, normalised to the reference sound Larmor radius $\rho_{s0} \simeq 1\,\mathrm{mm}$, using a T_e profile from a GRILLIX simulation. To resolve microinstabilities that drive turbulence, we need a perpendicular resolution equal to some number of the local sound-Larmor-radii ρ_s (see table 1.1). However, we don't know the temperature profile in advance and use a constant perpendicular resolution, so we set our perpendicular resolution equal to some number of the reference sound-Larmor-radius ρ_{s0}. The contour where $\rho_s = \rho_{s0}$ is marked in blue.

8.5. Comparison of simulation to experiment

The simulations were processed using a subset of the `TorX` library which was publicly released with the `TCV-X21` repository. The simulations were interpolated to the positions of the experimental diagnostics and either compared directly to the experiment or used to calculate synthetic diagnostics (the expected value measured by an experimental diagnostic if it was measuring a plasma with the simulated profiles). The simulated and experimental profiles were compared both graphically and via a quantitative composite validation metric introduced in reference [118]. Due to the sheer number of observables – in total, 90 one- and two-dimensional profiles, 45 in each field direction, from 5 diagnostic systems – this is no small task. One result of the validation is that the confined region agrees quite well, while the open field-line region does not, and as such we present the results by region, starting from the core and working our way towards the divertor and targets.

8.5.1. Uncertainty quantification

For the experimental data, the uncertainty was given as the root-mean-square sum of the intrinsic diagnostic uncertainty, the standard deviation across repeat discharges and the uncertainty of the models used to calculate comparison observables from raw experimental data. For the GRILLIX simulations, the statistical uncertainty was calculated via a bootstrap analysis [178]. The basic principle of this is as follows: if you have N data points, randomly sample N values from the data set *with replacement* (i.e. you can draw the same value twice) and calculate the statistical moments (mean, standard deviation, skew and kurtosis). Then, repeat this procedure a number of times, each time redrawing another N data points and recalculating the statistical moments. Eventually, you will have a *distribution* of results for each statistical moment, with a mean and a standard deviation for each moment. The expected value of the moment is set to the mean of the moment, and the statistical uncertainty (due to calculating statistical datasets from a finite number of time-points and poloidal planes) is set to the standard deviation of the moment. When taking data from 16 poloidal planes and from 500 time-points (about 1 ms), the bootstrap method was found to give negligible statistical uncertainty for the mean, a small statistical uncertainty for the standard deviation, and large statistical uncertainty for the skew and kurtosis. In addition to statistical uncertainty, there are several other sources of uncertainty – notably, sensitivity to uncertain input parameters such as the sheath heat transmission coefficients or the density source rate, uncertainty in the magnetic reconstruction and the discretisation error due to finite time- and space-resolution – although these are not evaluated in this work[4].

8.5.2. Core profiles

Since GRILLIX uses a collisional-magnetised fluid closure, we don't expect that the model will accurately model the plasma in regions where the collisionality is low. For TCV-X21, this means that the model is not formally valid in the core. Nevertheless, it is interesting to consider what happens when we apply the model outside of its region of applicability. Since the TCV-X21 scenario is small, we decided to include the core region, removing the need to apply boundary conditions at some confined-region flux surface. To avoid extremely high conductivities due to the Braginskii expressions, a heat-flux limiter (equation 8.5) was used. This permitted stable simulations in both toroidal field directions, which we compare to measurements from Thomson scattering and charge-exchange recombination spectroscopy in figure 8.6. We are also interested in the profiles of the radial electric field but do not have experimental data, and so show the simulated profiles in figure 8.7. These comparisons are not included in reference [2], although the data is available in the repository.

In figure 8.6, we see that all of the profiles agree fairly well near the separatrix ($\Psi_N \rightarrow 1$). Additionally, the T_e profile matches further into the core. However, the flattening of the profile observed around $\Psi_N \sim 0.25$ is not seen in the simulations, which might be due to the shape of our T_e source or due to the lack of fast MHD instabilities near the magnetic axis. Conversely, the n and T_i profiles don't match the experiment in the core. For the density profile, the density

---

[4] We performed simulations at 2 mm and 1 mm in both field directions. We could use this to estimate the discretisation error via Richardson extrapolation [118]. However, this method should only be used when the numerical solution is close to the asymptotic solution obtained at infinite resolution. When we refined our grid, the solution changed significantly, suggesting that we are not in the asymptotic region and that the Richardson error estimation is invalid. See references [179, 163] for more discussion of simulation uncertainties

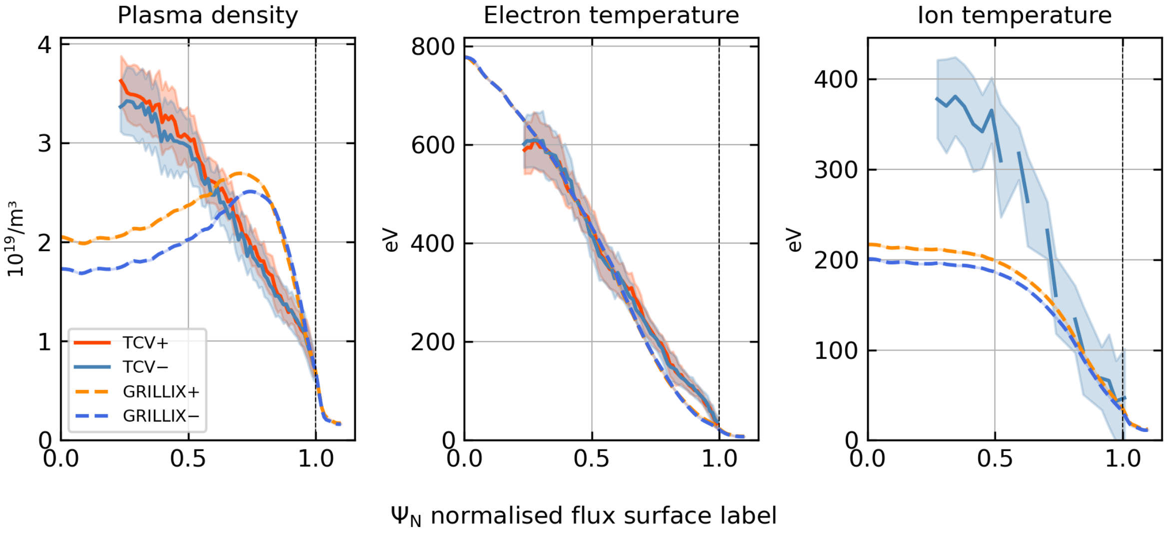

Figure 8.6.: Core profiles from Thomson scattering (n and T_e) and charge-exchange-recombination-spectroscopy (T_i) diagnostics. The experimental data is given in forward field (*light blue*) and reversed field (*red*), which is compared to the simulated profiles in forward field (*blue*) and reversed field (*orange*).

source is clearly visible, although the density profile peaks around $\Psi_N \sim 0.75$ instead of at the source position at $\Psi_N \sim 0.915$. To recover the experimental density profile, we need to increase the inward particle transport, which might require modelling the neutrals [180] or trapped particles [181]. The T_i looks reasonable in the edge, albeit with extremely high uncertainty, but is cooler in the core. This might indicate that we need either an additional T_i source (such as the small contribution from the Ohmic heating) or additional coupling mechanisms between T_e and T_i.

In figure 8.7, we show the radial electric field and the electrostatic potential. We see that the radial electric field structure does not change significantly with the toroidal field direction, although the reversed field simulation has $E_{rad} \sim 1-2\,\mathrm{keV}$ more negative than the forward-field case. This slight difference in the radial electric field corresponds to a significant difference in the electrostatic potential – the simulations are similar in the SOL since the absolute value of the potential is fixed via the boundary conditions[5], while in the core the forward-field simulation has a potential difference (with respect to the walls) of $\approx 0\,\mathrm{V}$, while in the reversed field case we have a core potential of $\approx -200\,\mathrm{V}$. Relating this back to the profiles; an inhomogeneous radial electric field can cause shearing of the plasma poloidal rotation, which can suppress turbulence [129] and affect the plasma profiles. Since the structure of E_{rad} is similar in both toroidal field directions, the plasma n, T_e and T_i profiles are similar despite the large difference in ϕ.

---

[5] We set the sheath entrance potential equal to the potential drop across the sheath – which implies that the potential at the wall must be 0.

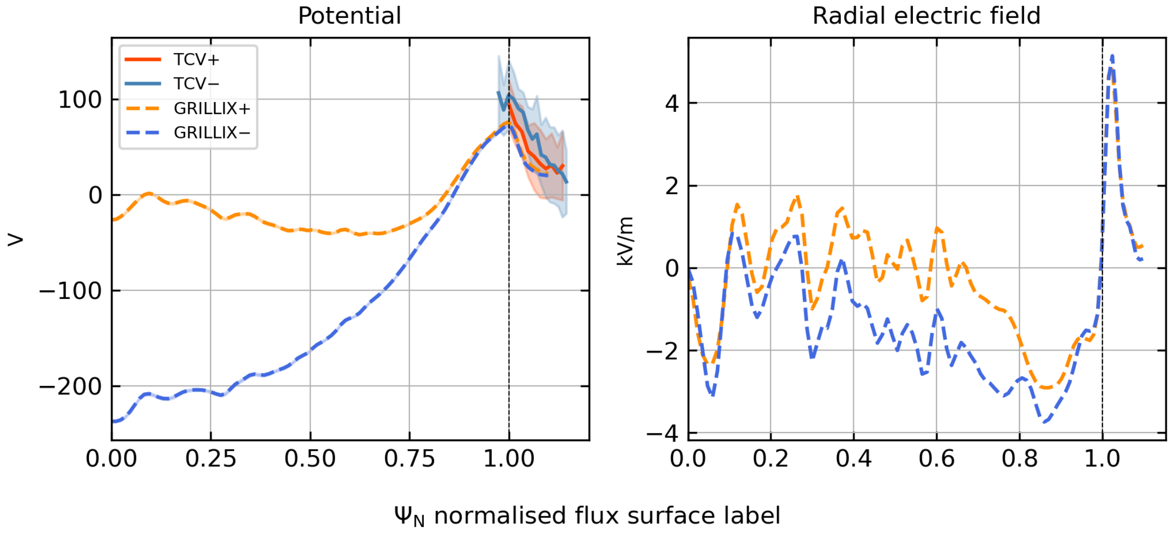

Figure 8.7.: Core profiles for the electrostatic potential (measured in the SOL by the FHRP) and the radial electric field. The experimental data is given in forward field (*light blue*) and reversed field (*red*), which is compared to the simulated profiles in forward field (*blue*) and reversed field (*orange*).

8.5.3. Outboard midplane profiles

Comparison of mean plasma profiles

Next, we consider the simulated outboard midplane and divertor entrance profiles. These are compared to measurements from the fast horizontally-reciprocating probe (FHRP, at the OMP) and Thomson scattering (TS, at the DE) systems in figure 8.8 and 8.9. We see that for all of the OMP and DE profiles, the toroidal field reversal doesn't have a large effect in the simulations. Similarly, for the experimental measurements, the toroidal field reversal doesn't have much of an effect, except for the electrostatic potential ϕ and the floating potential $V_{fl} = \phi - \Lambda_{sh}$. From equation 3.21, this suggests that the current density j at the outboard midplane might be changing with the toroidal field direction, although since the current isn't measured directly we can't confirm this. Additionally, the measured parallel velocity $u_{\|}$ (shown normalised to the local sound speed as $M_{\|}$) is faster in reversed field, and the separatrix density is smaller ($\sim 2/3^{\text{rd}}$s of the forward-field value) in reversed field. However, when comparing the outboard-midplane and divertor entrance density measurements, it is surprising that the DE n is higher than the OMP n in reversed-field while it is about the same in forward-field. Since the T_e separatrix values are about the same between the OMP and DE, the difference in the n measurements would imply a pressure gradient along confined-region flux surfaces, and it is unclear if this is physically

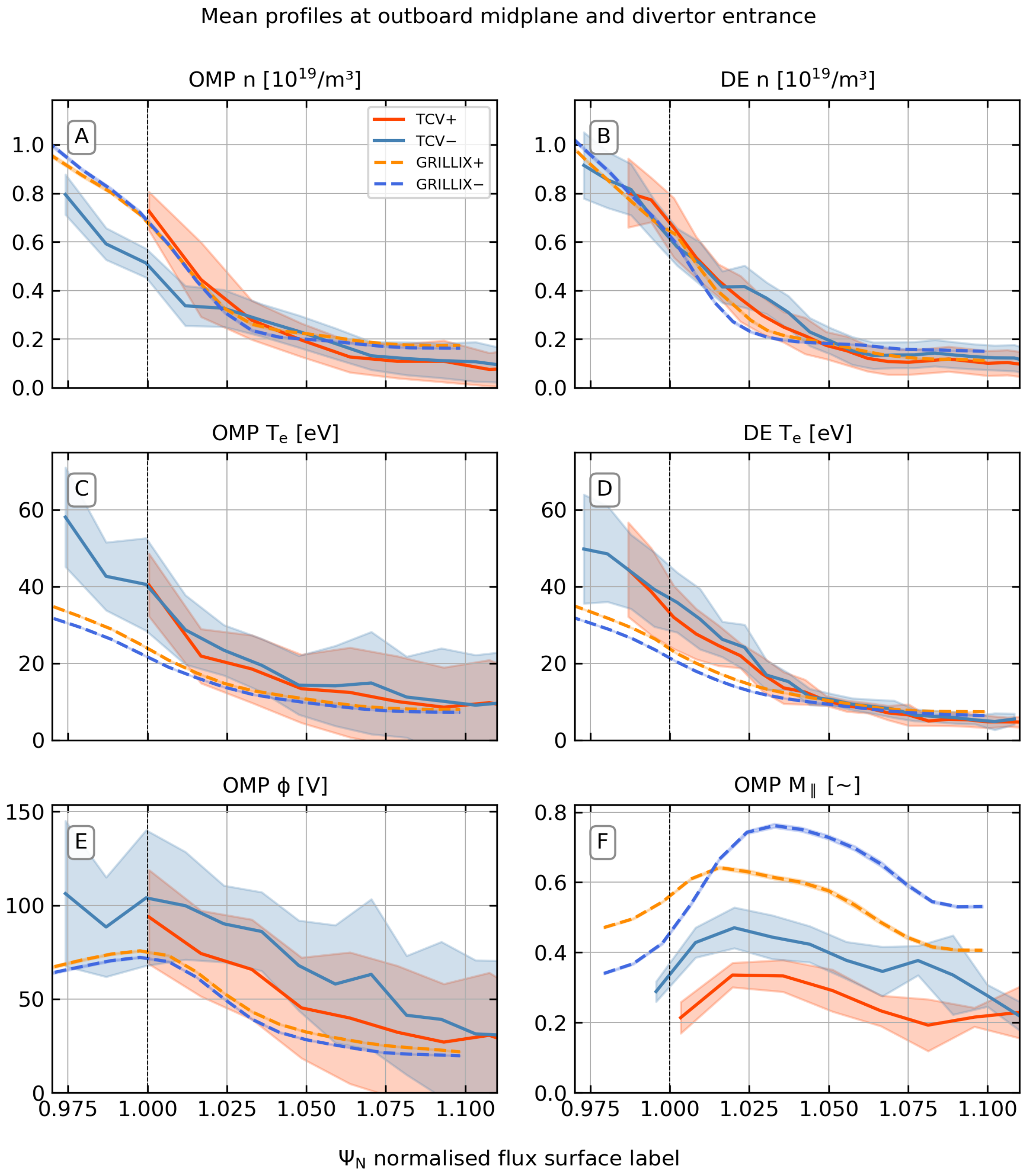

Figure 8.8.: Mean profiles at the outboard midplane (OMP, measured by the FHRP) and divertor entrance (DE, measured by TS). The experimental data is given in forward field (*light blue*) and reversed field (*red*), which is compared to the simulated profiles in forward field (*blue*) and reversed field (*orange*). We have multiplied both the simulated and measured forward-field parallel Mach number $M_{\parallel} = u_{\parallel}/c_s$ by -1, such that we can compare its magnitude against the reversed-field.

reasonable or indicative of an underestimated experimental uncertainty[6].

Comparing the simulations to the experiment, we see that the simulations match the density profile fairly well (with the exception of the OMP-separatrix n in reversed-field). The T_e profiles are underestimated by approximately a factor of 2 at the separatrix, while a good agreement is found from $\Psi_N \gtrsim 1.05$. The ϕ profile matches within the (large) experimental uncertainty in forward-field, while it is underestimated in the reversed-field SOL. For the simulations, the separatrix corresponds to a maximum of ϕ, while this is less clearly visible in the experimental measurements. The parallel Mach number $M_{\|} = u_{\|}/c_s$ is overestimated in the simulations. Since T_e is underestimated, part of the disagreement could be because the simulated $c_s = \sqrt{T_e/m_i}$ is underestimated, but even after correcting for this we see that the parallel velocity $u_{\|}$ is overestimated. This will increase the parallel transport relative to the perpendicular transport, which may explain why the density profiles fall off faster into the SOL in the simulations.

Comparison of mean profiles from synthetic diagnostics

We also calculate synthetic probe measurements from the simulated profiles and compare these to the direct experimental measurements. This is interesting particularly for the ion saturation current density – since the n, T_e and ϕ profiles determined by the FHRP are calculated using a model which assumes that $T_e = T_i$, while in the simulations we instead find that $T_i \approx T_e + 10\,\mathrm{eV}$ around the separatrix. The j_{sat} profiles agree at both the separatrix and in the far-SOL, while in the near-SOL the simulations predict that j_{sat} should fall off more quickly than in the experiment. Since we see similar behaviour in both the j_{sat} and DE-n profiles, the lower reversed-field OMP-n measured by the FHRP is probably not realistic. The floating potential V_{fl} shows poor agreement in both field directions. While in the experiment the V_{fl} profile changes significantly with the toroidal field direction, in the simulations this effect is not observed. The forward-field simulation appears to match the shape and magnitude of the profile reasonably well, but the simulated V_{fl} profile is shifted towards the confined region by $\Delta\Psi_N \sim 0.02$. Conversely, for the reversed-field simulation, the V_{fl} is both underestimated in the SOL and shifted towards the confined region. This may a consequence of the $\phi \longrightarrow \Lambda_{sh}$ boundary condition. As we will discuss in section 8.5.4, the simulated and measured $j_{\|}$ at the targets change with the toroidal field direction, and so if we set the potential at the boundaries consistently this could improve our description of the potential across the separatrix.

Comparison of statistical moments from synthetic diagnostics

Since the experimental profiles of j_{sat} and V_{fl} are measured directly rather than determined from experimental measurements via a model, we can also compute the statistical moments of these observables. These are compared to the corresponding statistical moments from the synthetic diagnostics in figure 8.9. For the standard deviations of j_{sat} and V_{fl} we see a reasonable

---

[6] Since the FHRP has a probe head which is small compared to the ion Larmor radius, the probe collection area was calculated using the sheath-expanded surface area (valid for a weakly-magnetised plasma) rather than its parallel-projected area (valid for a strongly-magnetised plasma) [182]. Additionally, it was assumed that $T_e = T_i$.

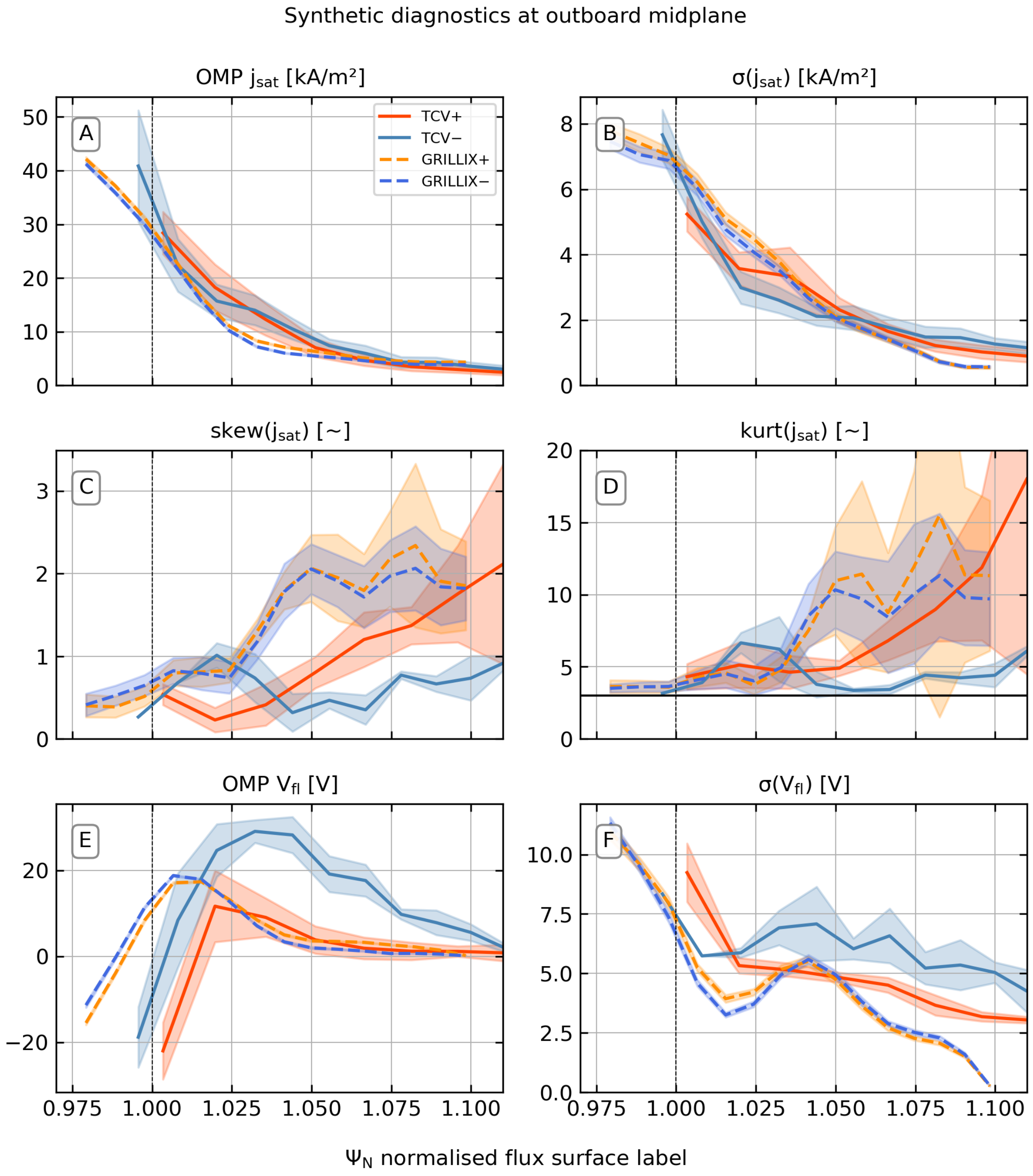

Figure 8.9.: Statistical moments of the profiles at the outboard midplane (measured by the FHRP). σ indicates the standard deviation, 'skew' indicates the unbiased skewness and 'kurt' indicates the Pearson kurtosis. The experimental data is given in forward field (*light blue*) and reversed field (*red*), which is compared to the simulated profiles in forward field (*blue*) and reversed field (*orange*).

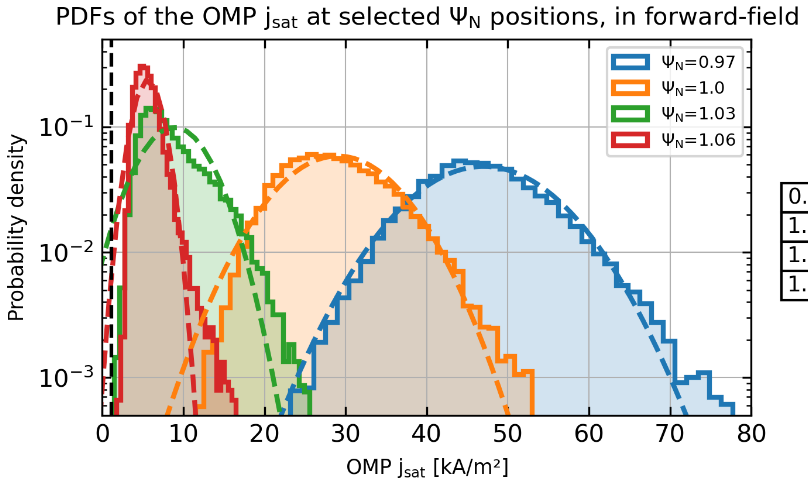

	mean	std	skew	kurt
0.97	47.02	8.26	0.40	3.61
1.0	29.03	6.81	0.54	3.44
1.03	8.89	4.02	1.11	4.17
1.06	5.64	1.68	2.04	12.14

Figure 8.10.: Probability distribution functions of j_{sat} at various positions along the outboard midplane for the forward-field simulations. Each colour indicates a different radial position, representing the outer-confined region (*blue*), the separatrix (*orange*), the near-SOL (*green*) and the far-SOL (*red*). A histogram is shown for each position, giving the normalised counts from 16000 samples binned into 50 equally-spaced bins. For each histogram, we also fit a Gaussian distribution from the mean and standard deviation of the distribution, shown by the dashed line. The statistical moments corresponding to each position are given in the table. The black dashed line gives the minimum j_{sat} value achievable for an immersed probe for the density and temperature floors used in the simulations

agreement for both the shape and order-of-magnitude. Since these can be related back to the fluctuations of n, T_e and ϕ, this suggests that we are capturing the turbulent fluctuation levels reasonably well. One interesting point is that the simulations seem to be reproducing the standard deviation of V_{fl} more accurately than its mean, particularly in reversed-field. This could imply that the simulations are capturing small-scale $E \times B$ turbulence more accurately than the large-scale background drifts.

We also have experimental measurements for the skewness and kurtosis of j_{sat}. These are defined in terms of the *statistical moments about the mean* [183]

$$m_r = \frac{1}{n}\sum_{i=1}^{n}(x_i - \bar{x})^r$$

The (unbiased) skew is given as

$$\text{skew}(x) = m_3/m_2^{3/2} \tag{8.7}$$

which is zero for the normal distribution. The (Pearson) kurtosis is given as

$$\text{kurt}(x) = m_4/m_2^2 \tag{8.8}$$

which is 3 for the normal distribution. Somewhat confusingly, the kurtosis is sometimes given as

$$\text{excess kurt}(x) = m_4/m_2^2 - 3 \tag{8.9}$$

which we call the excess (Fisher) kurtosis (this is zero for the normal distribution).

These higher-order statistical moments help to characterise non-normally distributed data. The profiles for the mean, standard deviation, skew and kurtosis of j_{sat} at the OMP are given in figure 8.9. The skewness and excess kurtosis are close to zero in the confined region in both field directions, in both the simulations and the experiment. Moving into the SOL, in the forward-field the skewness and kurtosis increase for both the simulation and experiment, although the simulated values increase more steeply than in the experiment. Conversely, in the reversed-field, the experimental skewness and excess kurtosis increase slightly and then return to almost zero – suggesting Gaussian-distributed turbulence. This is not reproduced in the simulation.

To understand the meaning of these statistical moments, we also show the raw probability density function from the forward-field simulation at several radial positions in figure 8.10. The PDFs are all seen to be positively skewed: that is, there are more high-amplitude data points than would be expected from Gaussian-distributed data. Physically, this means that the plasma has an overabundance of coherent structures which have more particles than the background (compared to a normal distribution) – which are termed ‘blobs’ or ‘filaments’ – and/or an absence of ‘holes’ (background minus a filament) [100]. As we move further into the SOL, the skewness of the distribution increases. We also see that the kurtosis increases into the SOL. This implies that j_{sat} signal is increasing dominated by very-high or very-low amplitude events, rather than by events with j_{sat} close to the mean [113]. Combined with the skew, we conclude that as we move further into the SOL, the j_{sat} signal is increasingly dominated by coherent blobs rather than random transport. We expect that these blobs are sourced from a region with negative skewness (since the ejection of the blob will leave a corresponding hole) seen between $\Psi_N = 0.8$ and 0.95 in the simulations. Filaments generated in this region drive SOL turbulence *ballistically*, leading to non-Gaussian statistics in the SOL [99].

8.5.4. Target profiles

Comparison of mean plasma profiles

We next consider the profiles measured at the divertor targets. We are interested in both the toroidal field reversal and the in-out asymmetry, so we plot both field directions and both divertor targets for each observable. The plasma density, electron temperature and electrostatic potential are shown in figure 8.11, and the current and floating potential are shown in figure 8.12. We see that in the experimental measurements, the density, current density and floating potential show a strong effect of toroidal field reversal and a strong in-out asymmetry. The potential changes with field direction but is similar at both targets, while the electron temperature is similar at both targets and in both field directions.

In the simulations, a weaker effect of toroidal field reversal and in-out asymmetry is found, which might suggest that the background drifts are having a weaker effect in the simulations

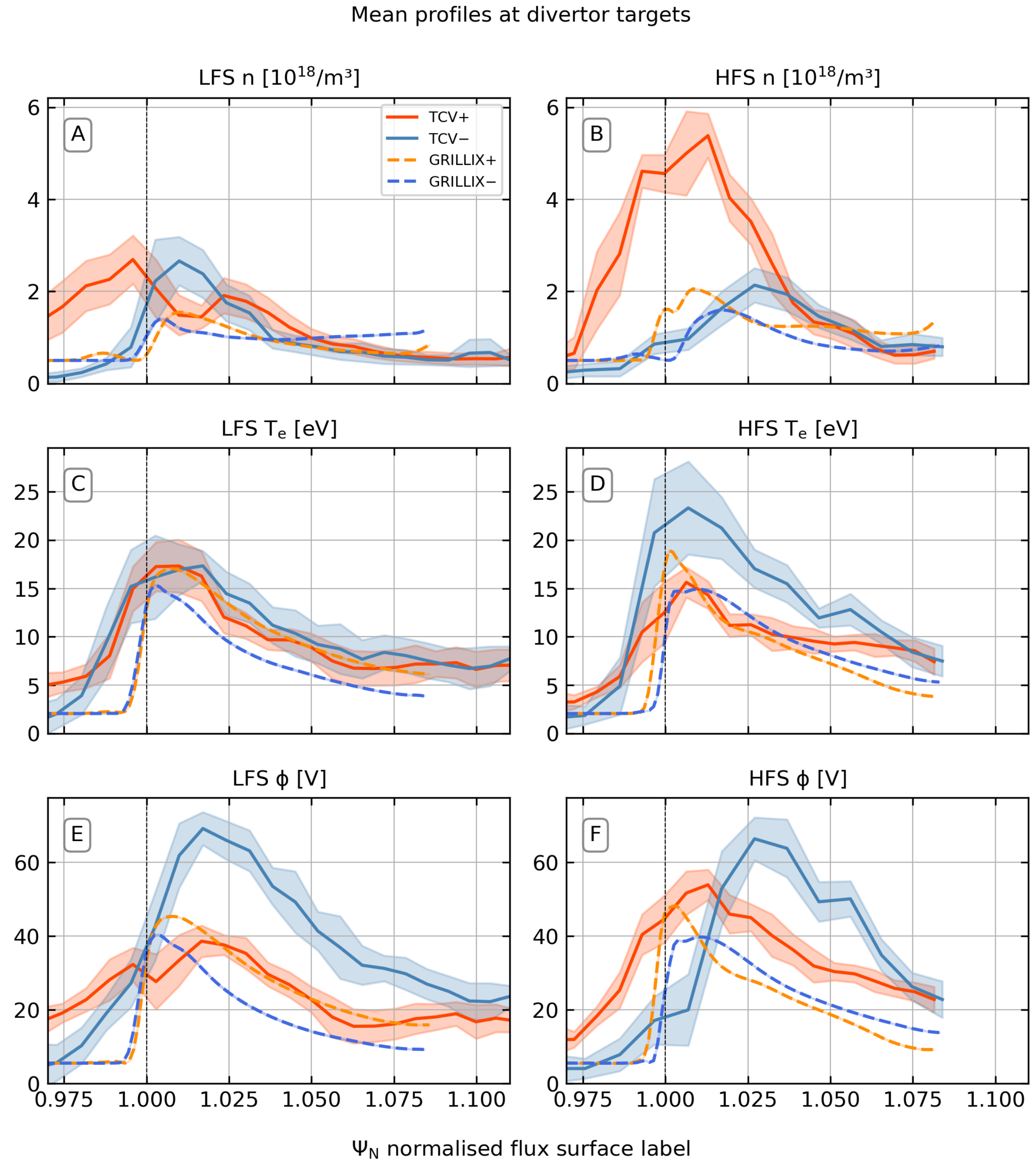

Figure 8.11.: Mean profiles at the low-field-side (LFS) and high-field-side (HFS) divertor targets, measured by the wall-embedded Langmuir probes. The experimental data is given in forward field (*light blue*) and reversed field (*red*), which is compared to the simulated profiles in forward field (*blue*) and reversed field (*orange*).

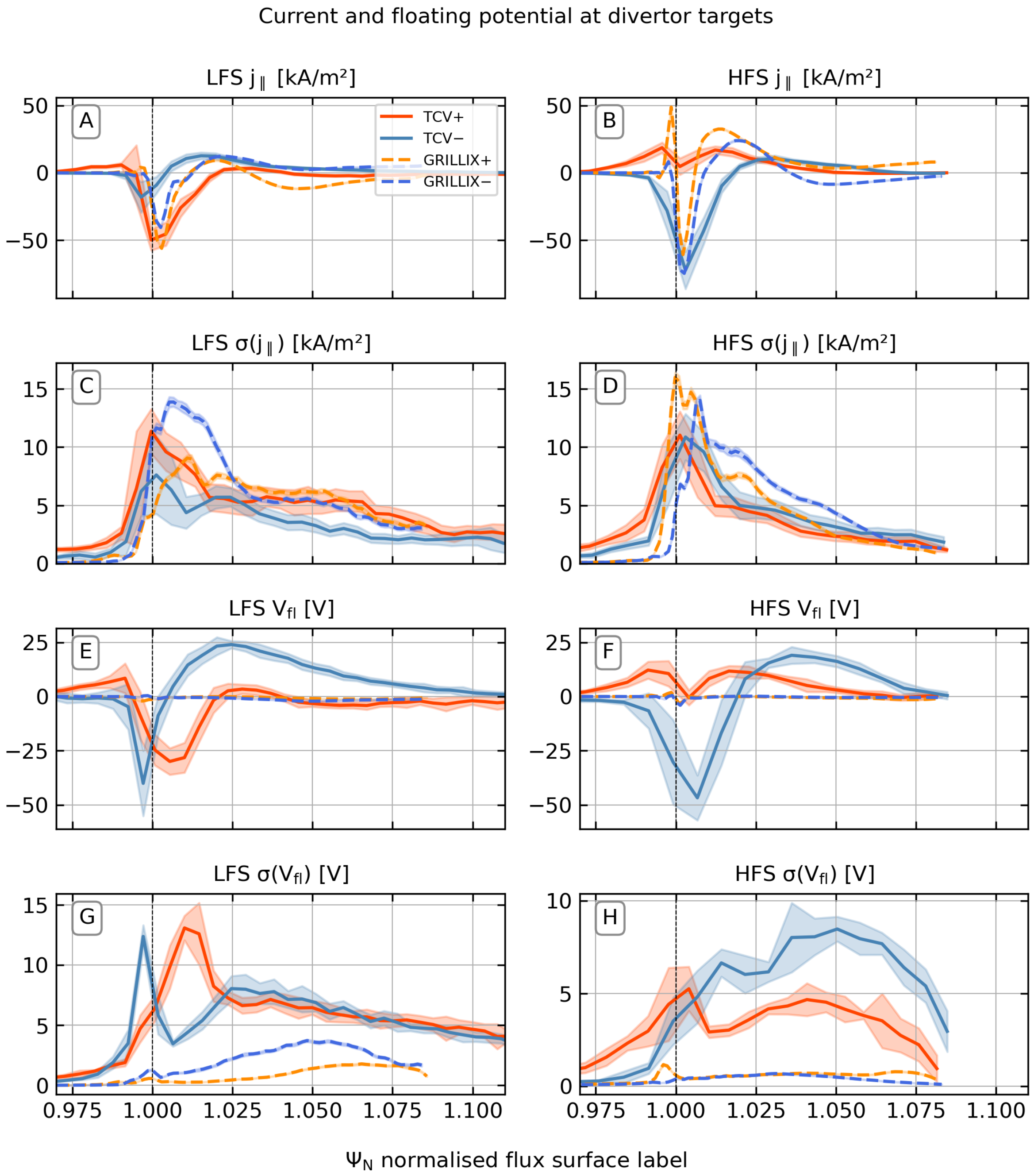

Figure 8.12.: The parallel current density and floating potential at the low-field-side (LFS) and high-field-side (HFS) divertor targets, measured by the wall-embedded Langmuir probes. The mean and standard deviation for each observable is shown. The experimental data is given in forward field (*light blue*) and reversed field (*red*), which is compared to the simulated profiles in forward field (*blue*) and reversed field (*orange*).

than in the experiment. The target n is underestimated by a factor of $\sim 2-3$, and the profile shape is only loosely recovered. One interesting feature is the small secondary peak visible on both the LFS and HFS targets in the forward-field direction. The position of this secondary peak roughly corresponds to the prominent private-flux-region peak seen on the LFS target and the split peak seen on the HFS target – although the magnitude of the simulated peaks is much lower than the corresponding experimental features. A mechanism for a similar double-peaked n profile is described via UEDGE transport modelling in reference [124], primarily due to background $E \times B$ drifts. The effect of the n floor value is visible on the targets, and the increase of the n profile at the limiting flux surface may indicate a numerical issue.

The T_e profiles agree remarkably well – matching both the shape in the SOL for both field directions and the magnitude of the profile for the forward-field field simulation. The reversed field simulation slightly underestimates T_e, although this is just outside of uncertainty. In the private flux region, T_e drops much more sharply than in the experiment, such that the private-flux-region is mostly at the T_e floor. Since we have set $\phi = \Lambda_{sh}$ (where Λ_{sh} is roughly proportional to T_e, equation 3.17), the T_e profile also affects the ϕ profile. This gives reasonably good agreement in the forward-field SOL, while the shape of the simulated reversed-field ϕ is significantly different to the experiment. In both field directions, the steep T_e gradient into the private flux region leads to a strong radial electric field, which will, in turn, drive poloidal $E \times B$ flows across the boundary surface.

Current density and floating potential

The mean and standard deviation of the current density and floating potential are shown in figure 8.12. We see that the simple extrapolation of the internal current is able to predict the approximate shape and magnitude of $j_{\parallel}$, except for at the HFS in forward-field. The simulations also predict $\sigma(j_{\parallel})$ remarkably well, capturing the profile shape in both field-directions and the magnitude in forward-field, while overpredicting the magnitude in reversed-field. Since we are setting the boundary current equal to the current at the nearest interior point, this suggests that the currents observed at the targets must be driven mostly within the plasma volume – such as via thermoelectric currents – rather than by the sheath.

In a sharp contrast to $j_{\parallel}$, the floating potential and its standard deviation are matched very poorly by the simulations. In the simulations, we have set $V_{fl} \rightarrow 0$ as a boundary condition (corresponding to $j_{\parallel} \rightarrow 0$, see equation 3.25), but this does not agree with the experimental measurements. Our simple sheath model in chapter 3 gives the relationship between V_{fl} and $j_{\parallel}$ at the targets as equation 3.25. Our relatively good agreement for $j_{\parallel}$ suggests that we might be able to set ϕ in terms of $j_{\parallel}$, which is discussed more in section 8.6.

Statistical moments of j_{sat}

The mean, standard deviation, skew and kurtosis of j_{sat} at the targets is shown in figure 8.13 (see section 8.5.3 for the definition of the skew and kurtosis). We see that the mean j_{sat} value is underestimated at both targets and in both field directions – likely due to the low target n. This also leads to an underestimated $\sigma(j_{sat})$, while the relative fluctuation level (not shown) is closer

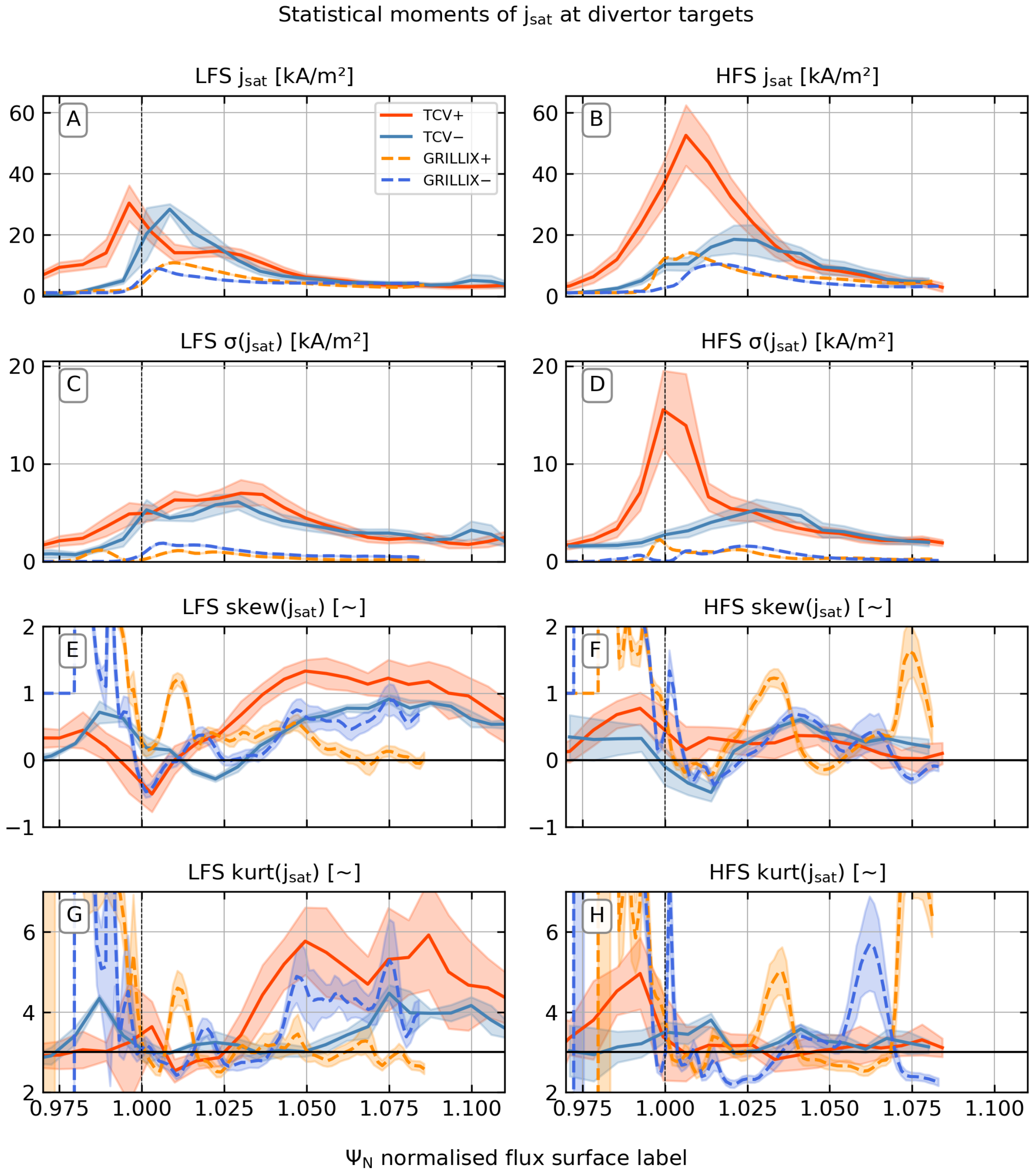

Figure 8.13.: Statistical moments of the ion saturation current at the low-field-side (LFS) and high-field-side (HFS) divertor targets, measured by the wall-embedded Langmuir probes. σ indicates the standard deviation, 'skew' indicates the unbiased skewness and 'kurt' indicates the Pearson kurtosis. The experimental data is given in forward field (*light blue*) and reversed field (*red*), which is compared to the simulated profiles in forward field (*blue*) and reversed field (*orange*).

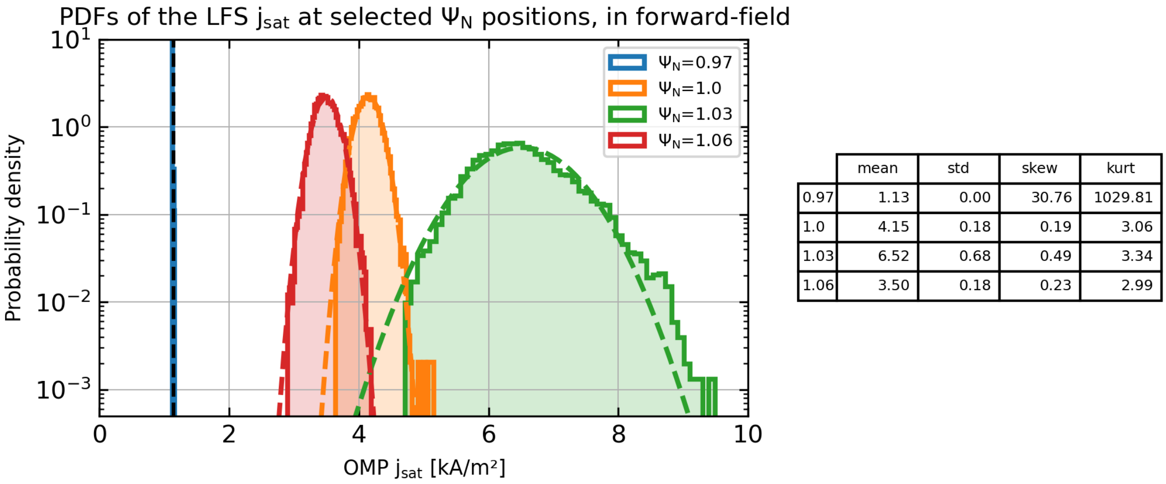

	mean	std	skew	kurt
0.97	1.13	0.00	30.76	1029.81
1.0	4.15	0.18	0.19	3.06
1.03	6.52	0.68	0.49	3.34
1.06	3.50	0.18	0.23	2.99

Figure 8.14.: Probability distribution functions of j_{sat}, at various positions along the low-field-side target for the forward-field simulations. Each colour indicates a different radial position, representing the private-flux region (*blue*), the separatrix (*orange*), the near-SOL (*green*) and the far-SOL (*red*). A histogram is shown for each position, giving the normalised counts from 16000 samples binned into 50 equally-spaced bins. For each histogram, we also fit a Gaussian distribution from the mean and standard deviation of the distribution, shown by the dashed line. The statistical moments corresponding to each position are given in the table. The black dashed line gives the minimum j_{sat} value achievable for a wall-embedded probe for the density and temperature floors used in the simulations.

to the experimental value near the separatrix (the far-SOL and PFR are again underestimated). The skewness and kurtosis j_{sat} are seen to oscillate wildly and to give extreme values. The non-smooth profiles may suggest that we don't have enough data points to characterise these higher-order moments, while the extreme values suggest that we have points that are not described by Gaussian statistics. To investigate this further, we plot the raw probability density function at several positions in figure 8.14.

We see that at the separatrix and in the SOL, the PDFs of j_{sat} appear reasonably close to the Gaussian profiles. However, in the private-flux region, the PDF is essentially a δ function at $j_{sat} = 1.14\,\mathrm{kA\,m^{-2}}$, which is the minimum possible value of j_{sat}, given floor values of $n_{floor} = 5 \times 10^{17}\,\mathrm{m^{-3}}$ and $T_{floor} = 2.1\,\mathrm{eV}$. If we allowed j_{sat} to drop further, we would presumably find a more reasonable PDF in the PFR. However, since there are several $1/n$ and $1/T$ terms in the equations, very low values of n and T can lead to numerical difficulties. Furthermore, comparing to the profiles in figure 8.11, we see that the experimental measurements are above the floor values, so it would be instead better to find why the n and T profiles in the PFR are so low.

Heat flux to targets

From our sheath-heat transmission boundary conditions (equation 3.36), we can calculate the heat flux to the targets as the sum of a convective heat flux $nu_{\|}T_e$ and a conductive heat flux $-\chi_{\|}\nabla_{\|}T$. Additionally, since the poloidal $E \times B$-drifts are found to be strong, we add an addition convective component with a velocity equal to the effective parallel transport due to the $E \times B$-drift (i.e. a convective flux with a value of $u_{\|}$ which gives the same poloidal transport). The resulting parallel heat flux profile is compared to measurements from an infrared camera which measures the heat flux to the LFS target, with the results shown in figure 8.15.

For each $q_{\|}$ profile, we use Levenberg-Marquardt algorithm [184] to fit a Eich-type profile (see reference [54]) of the form

$$q_{\|}(r) = \frac{q_0}{2}\exp\left[\left(\frac{S}{2\lambda_q}\right)^2 - \frac{r-r_0}{\lambda_q}\right] \times \operatorname{erfc}\left(\frac{S}{2\lambda_q} - \frac{r-r_0}{S}\right) + q_{BG} \tag{8.10}$$

where $r = R^u - R^u_{sep}$ is the radial distance from a flux surface to the separatrix evaluated at the outboard midplane[7], q_0 is the peak heat flux, λ_q is the heat flux decay length, S is a 'spreading factor', r_0 allows for a radial shift of the separatrix position (to correct for uncertainty in the separatrix position or a radial shift due to drifts), and q_{BG} is the background heat flux. The relevant fitted values are given in the table in figure 8.15.

We see that the Eich-type profiles fit the experimental results fairly well, while they provide a poor fit for the simulated profiles. This might suggest that the simulations are not reproducing the heat flux spreading correctly, or alternatively, that our expression for the heat flux isn't capturing all of the necessary components. The forward-field simulation is able to recover the experimental peak heat flux, while the reversed-field simulation underestimates the peak heat flux by almost a factor of 4. The simulations in both field directions predict narrow

---

[7] For PFR flux surfaces, a confined region flux surface with the same Ψ_N is used.

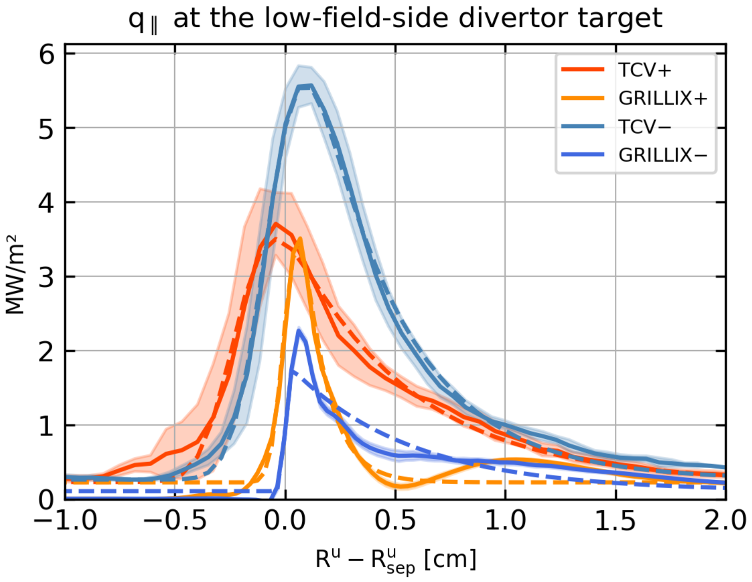

	q_{peak}	λ_q	S
TCV+	4.99±0.13	5.49±0.20	1.78±0.09
GRX+	6.47±0.55	1.07±0.11	0.71±0.07
TCV-	9.09±0.15	3.98±0.09	1.76±0.05
GRX-	1.75±0.08	5.44±0.45	0.20±0.16

Figure 8.15.: Computed heat flux to the divertor targets, compared to Eich-type fits. The corresponding fit parameters are given in the table. The experimental data is given in forward field (*light blue*) and reversed field (*red*), which is compared to the simulated profiles in forward field (*blue*) and reversed field (*orange*).

peaks, leading to a very small λ_q for the forward-field simulation and a poorly-fit profile for the reversed-fit profile. The simulated spreading factor is much lower than the experiment, for both field directions.

This is a problem! We need accurate predictions of λ_q, since this determines the area over which the heat flux is spread and ultimately the peak heat flux. To figure out why we aren't getting the expected profiles, we show the different components included in the heat flux in figure 8.16. The heat flux is dominated by the electron heat convection $\frac{5}{2}nT_e v_\parallel$, which has a narrow profile. This can be partly explained by the narrower-than-measured $j_\parallel$ profile in figure 8.12, and partly because we have missed the density peak at $\Psi_N = 1.025$ ($R^u - R^u_{sep} = 0.6\,\mathrm{cm}$) in figure 8.11. The double-peak structure is due to the electron conductive heat flux $3.16\frac{nT_e\tau_e}{m_e}\nabla_\parallel T_e$, which gives a heat flux *into* the simulation at $R^u - R^u_{sep} = 0.5\,\mathrm{cm}$, indicating higher temperatures at the targets than in the domain. This seems to be balanced by the $E \times B$ convected heat flux, so the double-peaked profile might be related to the strong poloidal $E \times B$ flow. This suggests that we could improve our prediction of the heat flux by improving the match of other target profiles. We could also add additional terms to the heat flux, such as the kinetic energy of the particles or the energy associated with recombination of the particle flux, and should carefully consider how to calculate heat fluxes across the sheath from a fluid model.

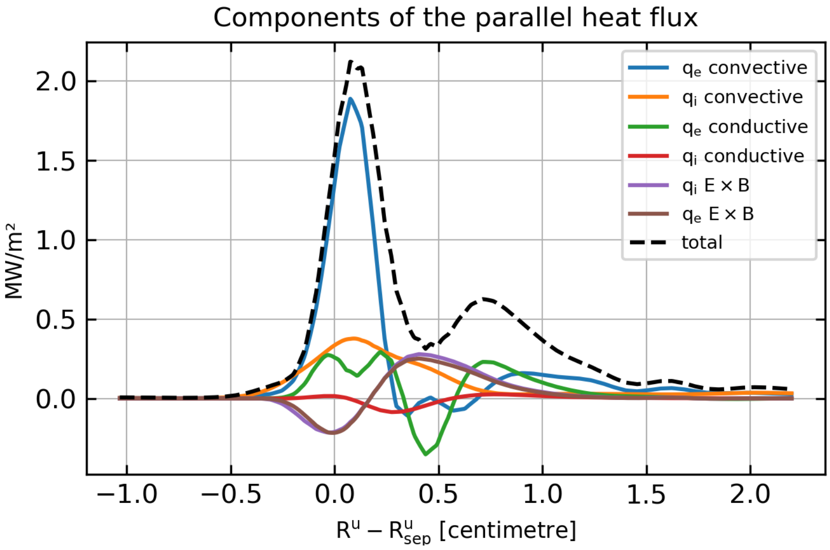

Figure 8.16.: Components of the computed heat flux, from a single time-point and single poloidal plane from the forward-field simulation.

8.5.5. Divertor volume profiles

Finally, we show the divertor volume profiles measured by the reciprocating divertor probe array, in figure 8.17. For the density profile, we see that the profile is underestimated throughout the divertor volume. Additionally, the experimental results show only a small drop in the direction parallel to the magnetic field (vertical in these figures), while a strong parallel density gradient was seen in the simulations. In the forward-field, a strong transport into the PFR was seen experimentally, while for the simulations this isn't reproduced. Conversely, the T_e profiles in the SOL match quite well, although the experimental broadening into the PFR isn't seen in the simulations. For ϕ, both experiment and simulation are roughly constant along the magnetic field, but the experimentally observed shape isn't recovered in the simulations. For the parallel Mach number, a large deviation from the experiment is found. The simulations show $\left|M_\parallel\right| \gg 1$, while the experiment shows $\left|M_\parallel\right| < 1$. Despite the much-higher-than-measured magnitudes, the direction of the parallel flow appears to be roughly correct – including the reversal of the PFR flow with the toroidal field reversal.

8.6. Discussion

Putting everything together, we have shown that it is now possible to run simulations in realistic divertor geometries, at realistic physical parameters, and at a relatively modest computational cost. By comparing multiple observables and at multiple positions, the TCV-X21 validation lets us find where the model is working well, where it isn't and, crucially, to interpret the causes of disagreement and determine how we can improve the fidelity of the model. We see that the model is able to match the outboard midplane and divertor entrance profiles remarkably

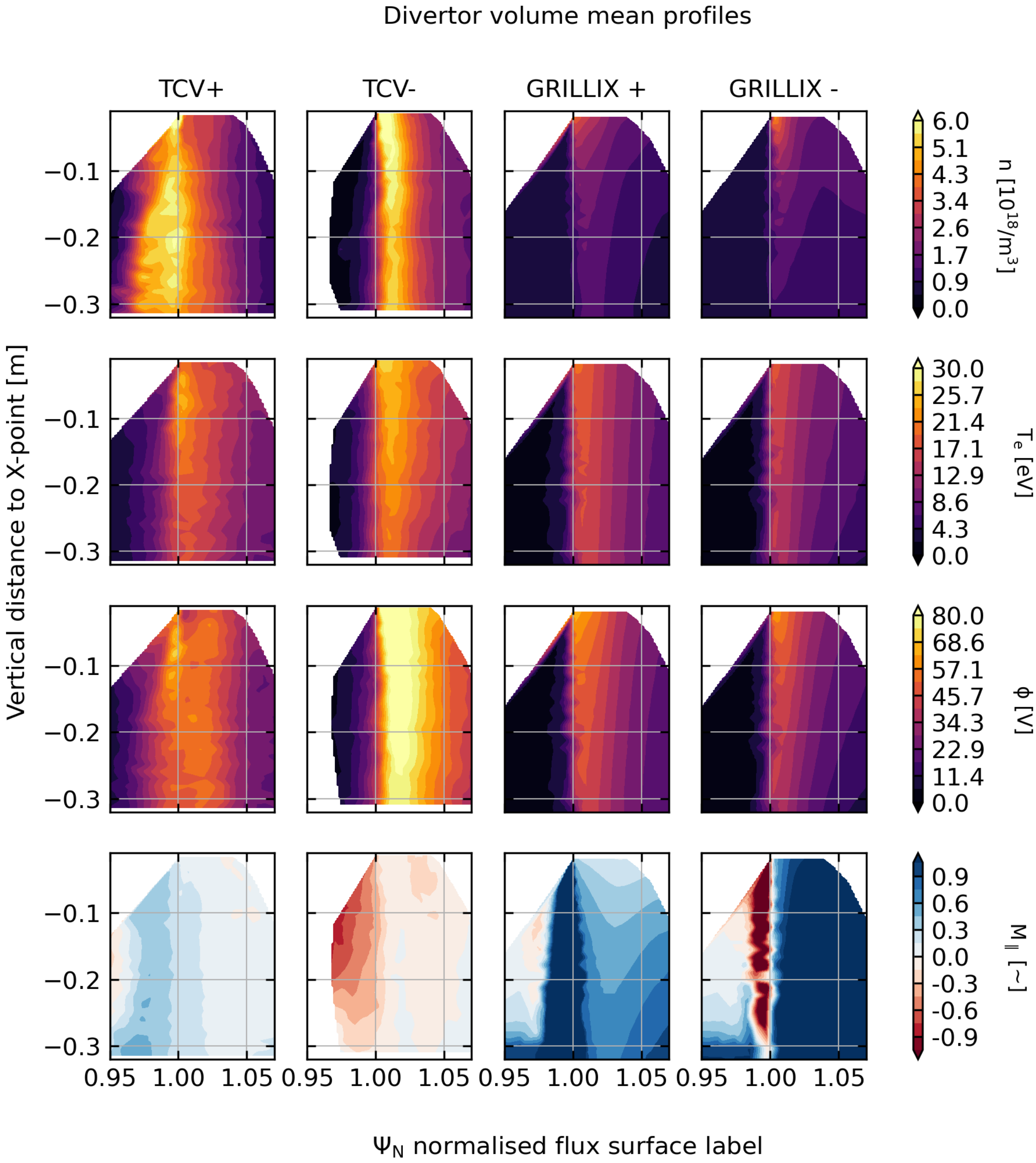

Figure 8.17.: Mean profiles in the divertor volume, measured by the reciprocating divertor probe array. The rows (*from top*) correspond to the density, electron temperature, electrostatic potential and parallel Mach number, with each row sharing a colour-bar. For each subplot, the vertical direction gives the vertical displacement in metres from the X-point. We have cropped the colour-bar range for $M_{\|}$ to keep detail in the experimental results: the actual range of values are $(-0.58, 0.67)$ for TCV in forward-field, $(-0.78, 0.14)$ for TCV in reversed-field, $(-0.23, 6.4)$ for GRILLIX in forward-field and $(-3.4, 2.6)$ for GRILLIX in reversed-field.

well, except for the parallel Mach number which is overestimated. By contrast, the divertor volume and divertor targets show a poorer match, except for the T_e profile in the SOL which matches remarkably well. This might be due to our choice of sheath boundary conditions or due to the omission of neutrals. Further into the confined region, the n, T_e and T_i profiles all look reasonable in the edge, but the n and T_i profiles do not agree in the core – although we didn't expect our model to apply there anyway. In the outlook (section 9.2), we discuss how the model will be extended to improve its accuracy at lower collisionality, which would let us simulate the core more accurately.

8.6.1. What is driving the turbulence?

At the outboard midplane, both the simulations and the experimental measurements found non-Gaussian probability density functions for j_{sat}. Positive skewness and excess kurtosis indicate that the j_{sat} signal is dominated by coherent filaments with an amplitude larger than the mean j_{sat}, which is the behaviour typically expected in the SOL [101, 100]. In the simulations, we identified a range of flux surfaces in the confined region with negative skewness, between $\Psi_N = 0.8$ and 0.95. We can use the `lineouts` feature in `torx` to investigate this flux surface in more detail. We first interpolate the fields to the flux surface and then use the symmetry angle[8] to interpolate from our 16 poloidal planes to a much higher toroidal resolution (the figure uses 1000 points in the toroidal direction). We then calculated the z-score for each point in the upscaled n, ϕ, T_e and T_i profiles for a single time-point, and show the result in figure 8.18. We also perform a Fourier analysis and show the magnitude of each poloidal mode as well as the phase shift between the n, T_e and T_i profiles and the ϕ profile. The magnitude helps to identify which are the dominant modes, while the phase shift can be used to identify whether the mode exhibits drift-mode or ballooning characteristics[9].

We find that the n and T_i modes have approximately the same amplitude as the ϕ modes, while the T_e modes have a lower amplitude. All fields show a localised peak around a poloidal wavenumber of between $30-40$ (which corresponds to a toroidal wavenumber of between $15-20$, since the q-factor of the flux surface is 2.11). This peak could be identified as the energy injection scale (the spatial scale of the dominant instability). For both the n and T_i profiles, the phase shift is much less than $\pi/2$, indicating that the turbulence is driven predominantly by drift-wave rather than interchange turbulence. The T_i profile has higher z-scores than the n profile, which we could associate with the coherent filaments ejected into the SOL. To confirm this, it would be helpful to develop a blob tracking algorithm such as in reference [187]. This would also be useful for investigating what sets the frequency and size of blobs, and studying how they are transported through the edge and SOL. Another extension could be to apply the Fourier analysis in the open field-line region, to study secondary instabilities which lead to profile broadening.

---

[8] We use the 'ballooning' or 'straight-field-line' coordinates. See equation 6.3.20 in reference [185] and the `Fourier_analysis` notebook in the `torx` repository – particularly the section on upscaling in the toroidal direction.

[9] See the discussion on page 7.13 of reference [186]. Interchange modes should have a phase shift around $\pi/2$, while drift-wave turbulence has a phase shift closer to 0.

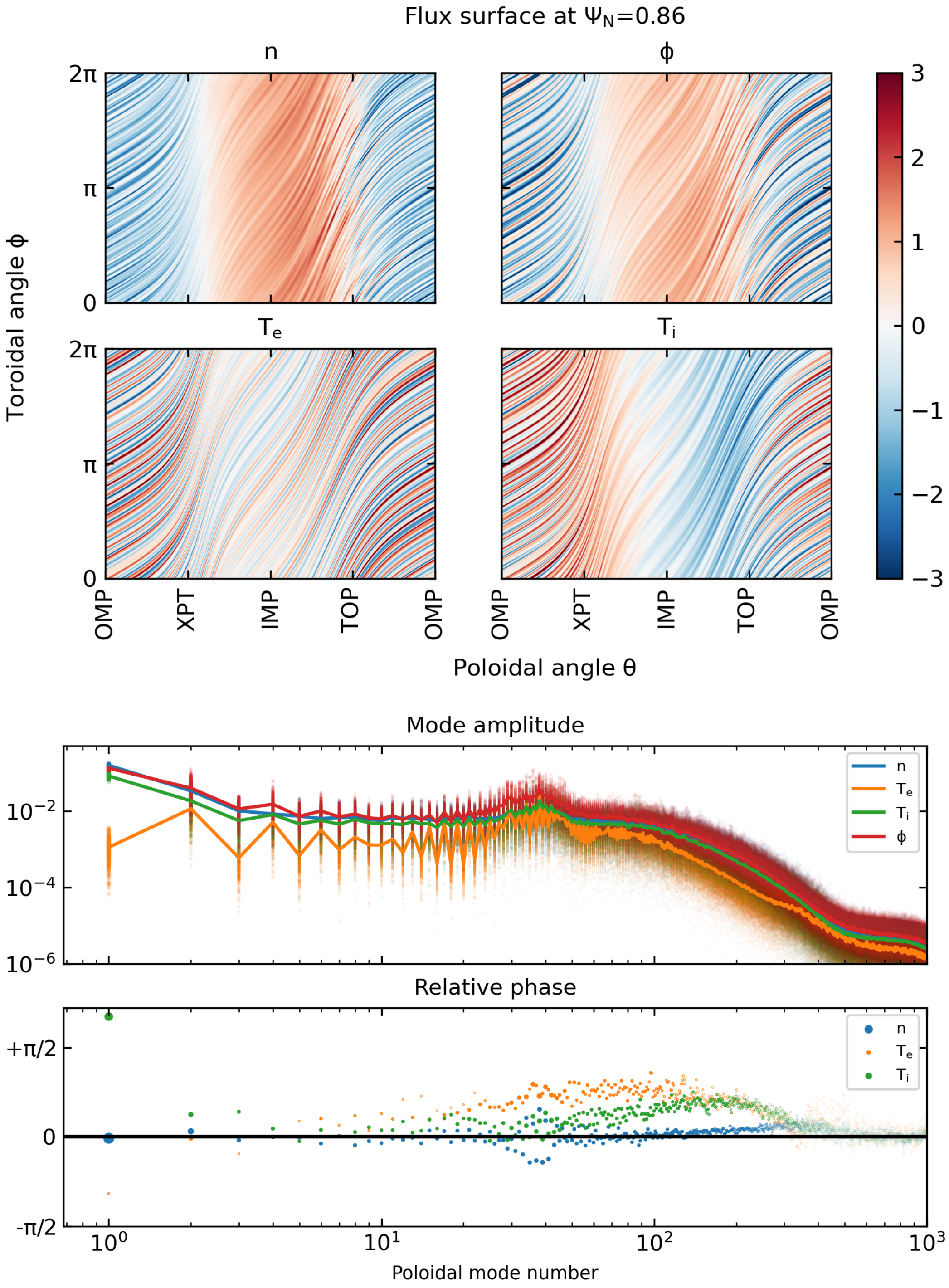

Figure 8.18.: The profiles and a Fourier analysis of the $\Psi_N = 0.86$ flux-surface, which is identified as the source region for SOL filaments. The colour-bar in the upper set of plots gives the z-score at each point, calculated as $(x - \bar{x})/\sigma(x)$. The x-labels are the outboard midplane, X-point, inboard midplane, and top of the device.

8.6.2. Fast parallel advection

Despite the promising initial result, there's still room for improvement, especially at the divertor targets. Rather than focussing on what is matching well, it is interesting to find where and how the code is diverging from the experiment since this lets us see how to improve the result in the future. The most striking disagreement is the parallel Mach number, especially in the divertor, which is much higher than measured. Since our T_e profiles are realistic, this indicates that we are overestimating the parallel velocity. To balance our particle source and sinks, the fast advection will require us to increase our particle source rate or to reduce the target density to reduce the outgoing particle flux $\Gamma = nu_\|$. This explains why we are underestimating the target density, and this causes us to underestimate other profiles such as j_{sat}. We may also be setting our particle source too high, although this is less clear than the reduced target density. Our total source rate appears reasonable when compared to the total flux reaching the Langmuir probes, but the outboard midplane T_e separatrix value is lower than measured. This might indicate that the core density source is too high since we added a negative T_e source proportional to the density source (to achieve a constant power).

The overestimated parallel advection will affect the balance of parallel and perpendicular transport. Increased parallel transport will lead to narrower SOL profiles and a reduced effect of the background drifts since plasma entering the SOL has less time to be advected across field-lines before it reaches the divertor targets. This gives a reasonable explanation for the narrowed parallel-heat-flux profiles and for the reduced effect of toroidal field reversal. The depletion of the private-flux-region can also be partly be explained by this mechanism, although it appears that we're also not fully resolving the local drive of turbulence due to the very small sound Larmor radius in the PFR, since the PFR activation increases slightly with increasing resolution. The two mechanisms likely affect either other – the parallel advection reduces T_e and therefore ρ_s in the PFR, which in turn leads to less cross-field transport since we aren't resolving the locally-generated turbulence.

What is driving this fast advection? Since we observed something similar in TORPEX, it appears that this is a peculiarity of the model or boundary conditions, rather than something specific to the case we are modelling. By following the time evolution of the simulation, we see that $u_\|$ starts increasing after the initial T_e pulse travels from the OMP to the targets. This leads to a radial electric field at the targets due to the $\phi \propto T_e$, which then modifies the parallel velocity to compensate for the $E \times B$ transport across the targets, via the mechanism depicted in figure 8.19. At this point this is desirable, since the modified $u_\|$ prevents spurious $E \times B$ fluxes across the boundary, and additionally the modification of $u_\|$ by return flows is physically motivated [139, 140]. However, the influx from $E \times B$ should be exactly balanced by $u_\|$. Instead, the electric field along the target increases, probably due to the coupling of the target T_e and ϕ. This leads to self-steepening, and eventually to the extremely high velocities observed. It's not entirely clear why this is occurring. Due to the stencil-collapse issue described in section 4.5, we gradually switch from the interior to boundary dynamics and therefore there is no exact boundary surface. Going back to a ghost-cell method (or at least using a zero-width penalisation) might therefore improve the issue, but this would require resolving the stencil

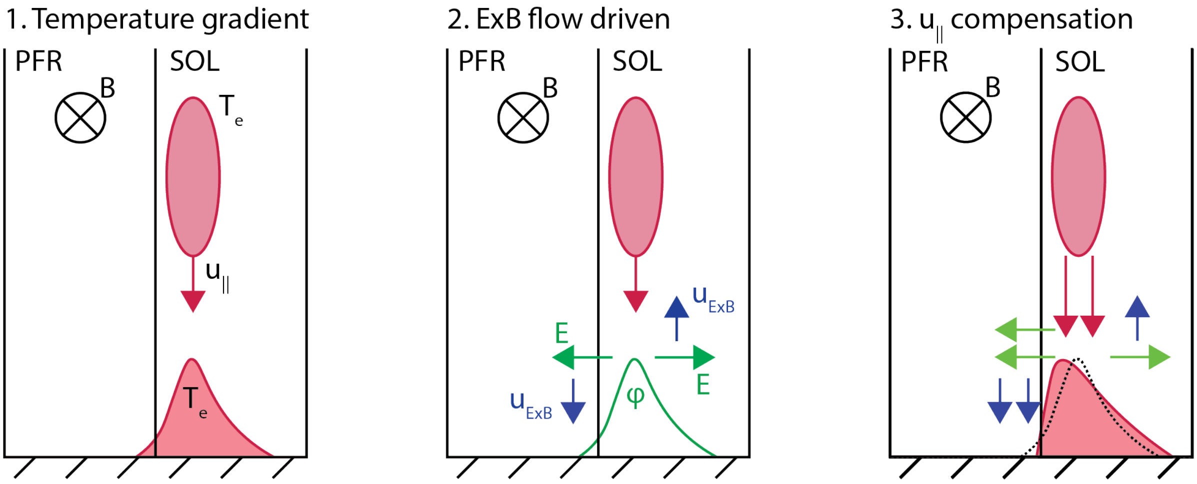

Figure 8.19.: The interaction of the $\phi = \Lambda_{sh}$ and drift-corrected velocity boundary conditions can lead to a feedback loop. First, there is usually a temperature gradient across the separatrix at the targets, since the scrape-off-layer is parallel-connected to a higher temperature region. Due to the $\phi = \Lambda_{sh}$ boundary condition, this leads to an electric field and therefore an $E \times B$ velocity *across the boundary.* If the $E \times B$ velocity is inflowing, the parallel velocity is accelerated to compensate, while if the $E \times B$ velocity is out-flowing, the parallel velocity is decelerated. However, we do not drive reverse flows in the parallel velocity, so above a certain out-flowing $E \times B$ velocity there is a net outflow in the private-flux-region, leading to a steepening of the temperature gradient and a feedback loop.

collapse. Alternatively, if we used consistent conducting boundary conditions we could change the target electric field, but it is unclear if this would be stabilising.

Furthermore, resolving the feedback loop is only part of the puzzle. If we instead just set $u_{||} = \pm c_s$ at the divertor targets, we will still have faster-than-measured parallel flows in the divertor, and we will not have a mechanism to reproduce the experimentally-observed flow reversal (seen in figure 8.17). The experimental measurements show flows significantly below sound speed throughout most of the divertor, while even for simulations with simple Bohm boundary conditions the parallel velocity will be close to sound speed in the divertor volume. We might be able to reduce the divertor flows by introducing neutrals. In previous transport modelling, subsonic flows in the divertor volume were possible *only* if neutrals were included [123]. Neutrals can reduce $u_{||}$ by adding an additional viscosity into the $u_{||}$ equation or by acting as an energy sink near the targets. Additionally, if the density increases faster than the temperature drops, the neutrals will cause a positive pressure gradient towards the targets, which will oppose the parallel flow. Another more radical way to reduce $u_{||}$ would be to not use a Bohm criterion at all, and instead drive advection across the targets via a particle source. In a simple 1D model, this was found to still give a target velocity $u_{||} \rightarrow c_s$ when the flow is driven by a sufficiently strong density source (i.e. the flow will become 'choked'). However, for a weakly sourced region like the PFR, the outflow velocity would be subsonic.

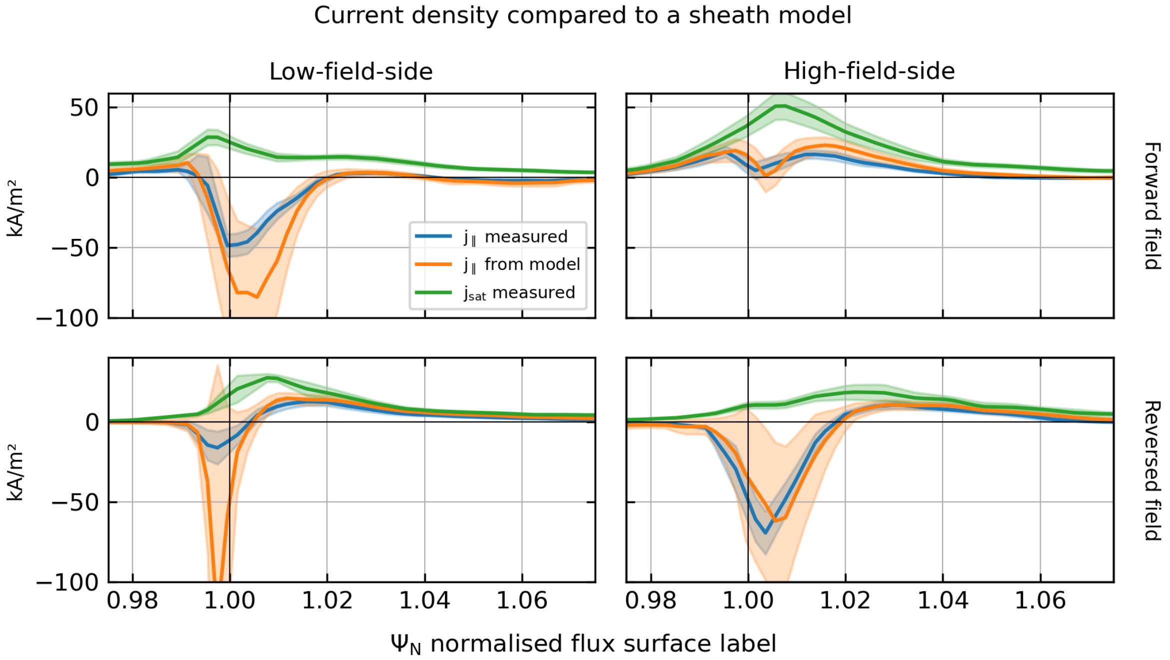

Figure 8.20.: The experimental parallel current density $j_\parallel$ at the divertor targets (in *blue*), compared to the experimental ion saturation current density j_{sat} (in *green*) and the expected current density $j_{sat}\left(1-\exp\left[\frac{e}{T_e}V_{fl}\right]\right)$ (in *orange*) from a simple sheath model, using the experimental j_{sat}, V_{fl} and T_e measurements.

8.6.3. Conducting boundary conditions

According to the sheath model we discussed in chapter 3, our boundary conditions for the parallel current are inconsistent with our potential boundary conditions. As such, the match for $j_\parallel$ at the targets is remarkably (and unexpectedly) good. Firstly, as a caveat, it's unclear whether this is a fluke, or whether it represents real physics. If we assume the latter, this could let us set ϕ in terms of $j_\parallel$ using equation 3.21. In the simulations, we have $j > j_{sat}$ so can directly compute V_{fl} from the simulated $j_\parallel$. However, to see whether this condition is reasonable we can use

$$j_\parallel = j_{sat}\left(1-\exp\left[\frac{e}{T_e}V_{fl}\right]\right) \tag{8.11}$$

$$V_{fl} = \frac{T_e}{e}\ln\left(1-\frac{j_\parallel}{j_{sat}}\right) \tag{8.12}$$

with the experimental data. We show the $j_\parallel$ profile calculated by equation 8.11 with $\sigma(j_\parallel)^2 = \left[\sigma(j_{sat})\frac{\partial j_\parallel}{\partial j_{sat}}\right]^2 + \left[\sigma(T_e)\frac{\partial j_\parallel}{\partial T_e}\right]^2 + \left[\sigma(V_{fl})\frac{\partial j_\parallel}{\partial V_{fl}}\right]^2$ compared to the measured $j_\parallel$ and j_{sat} in figure 8.20. We see that there is a good agreement between equation 8.11 and the measured $j_\parallel$, suggesting that the simple sheath model is reasonably accurate.

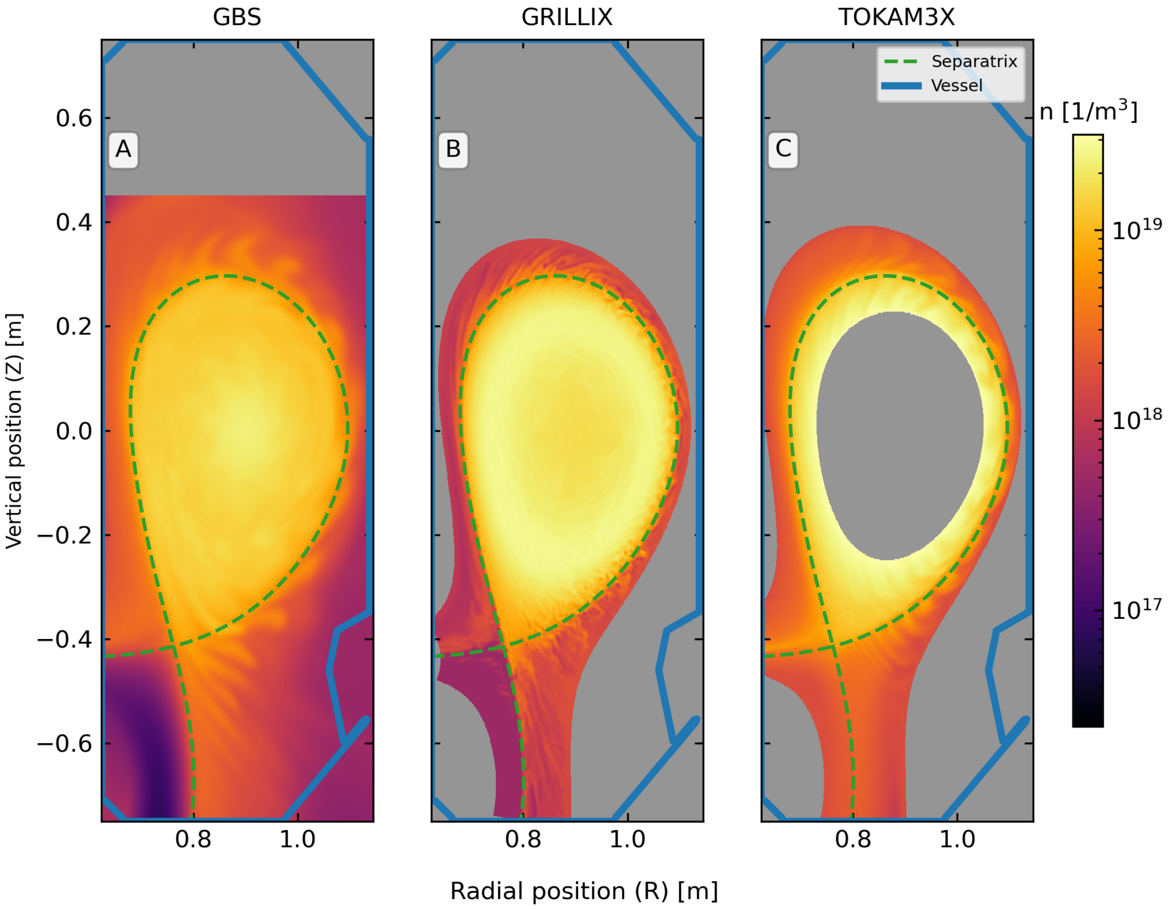

Figure 8.21.: A poloidal snapshot of the plasma density from the GBS, GRILLIX and TOKAM3X simulations. Here, GBS and GRILLIX show the reversed-field case, while TOKAM3X shows the forward-field case. The simulations have visually differently-sized structure – large for GBS, medium for TOKAM3X and small for GRILLIX.

In our equations we have $j_\| = -\nabla_\| \phi$. This term would be destabilising if we use equation 8.12 as the ϕ boundary condition with a free-flowing $j_\|$ boundary condition – since as $\phi \longrightarrow -\infty$ at the targets we have that $j_\| \longrightarrow \infty$ (which makes sense – as we generate strong electric fields, the positive current should increase). There is no obvious mechanism in the interior dynamics that would limit $j < j_{sat}$, and so this would drive our system unstable. To resolve this, we could set a current limiter, or simultaneously set a coupled boundary condition on $j_\|$ and ϕ such as in reference [134].

8.7. Comparison to other models and validation metrics

The TCV-X21 case was also used to validate the GBS [111] and TOKAM3X [134] models, with the results of the validations published in a combined paper [2]. The models also use the

		GBS(+)		GBS(−)		GRILLIX(+)		GRILLIX(−)		TOKAM3X(+)	
Diagnostic	observable	d_j	S	d_j	S	d_j	S	d_j	S	d_j	S
Fast horizontally-reciprocating probe (FHRP) for outboard midplane	n	1.35	0.841	0.712	0.899	0.698	0.865	1.73	0.91	2.6	0.893
	T_e	0.66	0.765	0.426	0.825	0.866	0.733	1.21	0.776	0.916	0.756
	V_{pl}	0.482	0.774	2.21	0.78	0.52	0.738	1.3	0.773	0.801	0.75
	J_{sat}	1.27	0.89	0.663	0.893	1.24	0.9	1.4	0.882	4.09	0.918
	$\sigma(J_{sat})$	4.73	0.889	1.64	0.939	1.9	0.927	1.9	0.934	3.25	0.933
	skew (J_{sat})	2.44	0.81	1.81	0.912	3.78	0.898	12.1	0.942	1.85	0.847
	kurt (J_{sat})	2.8	0.829	2.37	0.934	4.78	0.886	20.2	0.954	2.4	0.83
	V_{fl}	4.52	0.833	6.38	0.901	2.15	0.749	4.99	0.824	1.65	0.696
	$\sigma(V_{fl})$	5.11	0.949	8.78	0.963	5.67	0.953	4.98	0.94	4.22	0.952
	$M_\parallel$	2.18	0.925	7.9	0.92	6.53	0.942	4.61	0.944	2.46	0.901
	$(\chi; Q)_{\text{FHRP}}$	**(0.62;**	**4.02)**	**(0.61;**	**4.25)**	**(0.59;**	**4.06)**	**(0.69;**	**4.2)**	**(0.75;**	**4.01)**
Thomson scattering (TS) for divertor entrance	n	1.09	0.877	0.59	0.908	0.435	0.887	0.992	0.907	2.63	0.914
	T_e	3.28	0.89	3.93	0.907	1.09	0.872	1.37	0.871	2.72	0.874
	$(\chi; Q)_{\text{TS}}$	**(0.52;**	**0.883)**	**(0.5;**	**0.908)**	**(0.018;**	**0.88)**	**(0.1;**	**0.889)**	**(0.99;**	**0.894)**
Wall Langmuir probes for low-field-side target	n	1.81	0.861	4.2	0.89	1.81	0.859	2.35	0.862	3.28	0.902
	T_e	6.01	0.937	3.63	0.911	1.76	0.907	1.94	0.868	1.88	0.908
	V_{pl}	9.63	0.951	3.79	0.925	2.55	0.912	4.8	0.896	2.26	0.915
	J_{sat}	2.9	0.891	16.1	0.942	3.22	0.884	3.62	0.88	2.76	0.91
	$\sigma(J_{sat})$	4.93	0.859	3.34	0.894	5.52	0.854	5.3	0.872	5.38	0.85
	skew (J_{sat})	3.02	0.849	9.03	0.922	71.3	0.957	45.5	0.943	5.4	0.808
	kurt (J_{sat})	1.96	0.904	15.5	0.971	1290	0.994	68.1	0.982	2.7	0.895
	$J_\parallel$	2.93	0.765	7.53	0.863	7.78	0.841	4.16	0.85	4.29	0.735
	$\sigma(J_\parallel)$	3.26	0.884	10.4	0.92	2.71	0.896	3.51	0.905	4.24	0.844
	V_{fl}	6.54	0.854	5.66	0.794	2.14	0.64	5.9	0.734	2.74	0.662
	$\sigma(V_{fl})$	5.83	0.907	6.88	0.916	7.49	0.894	6.1	0.909	7.4	0.893
	$(\chi; Q)_{\text{LFS-LP}}$	**(0.96;**	**4.83)**	**(1.0;**	**4.97)**	**(0.94;**	**4.82)**	**(0.98;**	**4.85)**	**(0.98;**	**4.66)**
Overall	χ; Q	**(0.87;**	**18.9)**	**(0.86;**	**19.4)**	**(0.83;**	**19.0)**	**(0.87;**	**19.2)**	**(0.92;**	**18.6)**

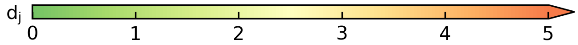

Table 8.1.: **Quantitative validation result for each observable**. For each code and field direction (indicated by (+) for forward field and (−) for reversed field), the d_j ('normalised distance', equation 8.13) and S_j ('sensitivity', equation 8.17) terms are given. The normalised distance d_j gives the root-mean-square Z-score of the difference between the experiment and simulation, with *green* cells indicating good agreement ($d_j \rightarrow 0$) and *red* cells indicating poor agreement ($d_j \rightarrow \infty$, with the colour scale limited to $d_j \leq 5.0$). The sensitivity S_j indicates the precision of each observable, with $S_j \rightarrow 0$ for observables with high relative uncertainty and $S_j \rightarrow 1$ for observables with low relative uncertainty. The combined level-of-agreement χ (equation 8.14 for $d_0 = 1.0$ and $\lambda = 0.5$) and the comparison quality Q (equation 8.15) are given for the FHRP, TS, LFS-LP and for the overall validation.

drift-reduced Braginskii equations, although both GBS and TOKAM3X omit electromagnetic effects and GBS uses a different set of sheath boundary conditions [188]. The models use different parallel discretisations – a fully non-aligned method in GBS, a locally field-aligned method in GRILLIX (described in chapter 4) and a domain-decomposed flux-aligned method in TOKAM3X. Additionally, while GRILLIX used the Braginskii resistivity and heat-conductivities directly, GBS and TOKAM3X artificially modified these parameters to reduce computational cost and improve numerical stability[10]. GBS increased the resistivity by a factor of 3 and reduced the heat conductivities by a factor of between 20 and 4.8 (see section 4.1 of reference [2] for details), while TOKAM3X increased the resistivity by a factor of 1.8 and reduced the heat conductivities by a factor of 1.8. The simulations also used different heating sources – 170 kW for GBS and only 30 kW for TOKAM3X, compared to 150 kW for GRILLIX and 150 kW of Ohmic heating in TCV-X21 (of which ≈ 120 kW crossed the separatrix).

The different models had markedly different simulation results. In figure 8.21 we compare poloidal snapshots of the plasma density, where we see that the scrape-off-layer filaments are large in GBS, medium-sized in TOKAM3X and small in GRILLIX. This is likely due to the increased resistivity used in GBS and TOKAM3X, since the resistivity affects the perpendicular size of electrostatic perturbations [134]. Comparing the profiles (see figures in reference [2]), we see that the models are not too dissimilar at the outboard midplane, but they predict significantly different divertor profiles. We find that GBS captures more of the effect of toroidal field reversal, especially for the density profiles, and also predicts parallel velocities closer to the experiment – which is consistent with our interpretation that the parallel velocity in GRILLIX is the primary cause of the disagreement in the target density profile. We also find that both GBS and TOKAM3X predict extremely flat divertor electron temperature profiles. For GBS, this is probably due to the reduced heat conductivity which changes the balance of parallel and perpendicular transport. For TOKAM3X, the outboard midplane electron temperature profile is also extremely flat so this might be due to the very low power source used in that simulation.

To help interpret and compare the validation results we used a *validation metric* which summarises the agreement between simulation and experiment in terms of a single number[11]. The methodology is described in reference [118] and in section 2 of reference [2]. For this discussion we will briefly summarise it here. For each model, the level of agreement for each observable (i.e. the plasma density measured by the FHRP, for instance) is quantified using the RMS of the Z-scores for each measurement point

$$d_j = \left[\frac{1}{N_j} \sum_{i=1}^{N_j} \frac{\left(e_{j,i} - s_{j,i}\right)^2}{\Delta e_{j,i}^2 + \Delta s_{j,i}^2} \right]^{1/2} \tag{8.13}$$

where j indicates some particular observable, and $e_{j,i}$ and $\Delta e_{j,i}$ are the experimental values and uncertainties defined at some set of discrete measurement points $i = \left\{1, 2, \ldots, N_j\right\}$. The simulation result is assumed to be continuous and so is interpolated to the experimental

---

[10] A discussion on why this is particularly necessary for electrostatic models is given in reference [189] and also in section III.E of reference [109].

[11] For more discussion of validation metrics and why they are useful, see references [127, 168].

measurement positions, giving computed values $s_{j,i}$ and uncertainties $\Delta s_{j,i}$. However, for this study, we didn't calculate simulation uncertainties, and so set $\Delta s = 0$ for all observables and models. The results from all observables are combined into a composite metric

$$\chi = \frac{\sum_j R(d_j) H_j S_j}{\sum_j H_j S_j} \tag{8.14}$$

which returns values between 0 (perfect agreement) and 1 (disagreement), and a 'quality'

$$Q = \sum_j H_j S_j \tag{8.15}$$

Here, R is a smooth-step function (with constants $d_0 = 1$ and $\lambda = 0.5$)

$$R(d_j) = \frac{\tanh\left[\left(d_j - 1/d_j - d_0\right)/\lambda\right] + 1}{2} \tag{8.16}$$

S_j is the 'sensitivity' which gives a measure of the total relative uncertainty

$$S_j = \exp\left(-\frac{\sum_i \Delta e_{j,i} + \sum_i \Delta s_{j,i}}{\sum_i |e_{j,i}| + \sum_i |s_{j,i}|}\right) \tag{8.17}$$

and H_j is a 'primacy hierarchy'

$$H_j = \left[h_{Exp} + h_{Sim} - 1\right]_j^{-1} \tag{8.18}$$

defined in terms of two manually-set hierarchies, given in table 1 of reference [2]. The hierarchies are chosen to increase the weight of direct measurements (i.e. the plasma density for h_{Sim} or the ion saturation current for h_{Exp}) in the calculation of the composite metric, compared to observables which have to be calculated from a model (i.e. $q_{\parallel}$ for both h_{Sim} and h_{Exp})[12]. The results of the validation analysis for the midplane probe, the divertor entrance Thomson scattering and the low-field-side Langmuir probes are shown in table 8.1, as well as the overall validation result. We see that the validation metric gives a similar result to what we found by directly comparing profiles – namely, that the match is better at the outboard midplane and divertor entrance. Despite achieving an impressive match at the OMP and divertor entrance, the large number of poorly-matched observables in the divertor means that the overall quantitative result for GRILLIX of $\chi = 0.83$ in forward-field and $\chi = 0.87$ in reversed-field is about the same as for TORPEX ($\chi = 0.85$). Nevertheless, the forward-field result for GRILLIX gives the highest level-of-agreement from amongst the codes and the reversed-field gives a similar result to GBS ($\chi = 0.86$). Therefore, from the qualitative metric, we can safely say that GRILLIX is performing at least as well or better than the other models. Combined with the fact that GRILLIX was also able to perform simulations without relaxed parameters and at a higher poloidal resolution than the other models, this result suggests that the locally-field-aligned method used by GRILLIX is both accurate and computationally efficient.

---

[12] The simulation hierarchies should be updated if validating, say, a gyrofluid model which calculates the heat flux directly.

8.8. Future validations

This validation gives confidence in the predictive capabilities of GRILLIX and shows how the model can be improved further. Since the TCV-X21 validation case has been publicly documented and released, it is much faster to perform repeat validations against this case. This lets us quickly try new features and to see whether they are giving an improved result, using the model testing cycle shown in figure 6.1. We've just performed the first iteration of this cycle for TCV-X21 and are already in a second iteration testing a diffusive neutrals model (discussed in section 9.2). This should help us rapidly improve the fidelity of the model at minimal computational cost (since TCV-X21 is small). Then, we'll need to work towards more challenging, more reactor-relevant validations. For this, we need well-diagnosed experimental cases, in challenging scenarios like advanced divertor configurations, high-recycling conditions or in H-mode, and on larger machines like full-size TCV, ASDEX Upgrade and JET. With a combination of luck and hard work we'll be able to quantitatively match the divertor measurements in TCV-X21 in the near future, and so should already start to work with experimentalists to build the stepping-stones to reactor-relevant simulations.

Part IV.

Summary and Outlook

> I may not have gone where I intended to go, but I think I have ended up where I needed to be.
>
> *(Douglas Adams)*

9. Summary and outlook

Realistic turbulence simulations of the edge and divertor will play an important role in the development of fusion as a practical source of energy. These simulations will let us study in extreme detail the dynamics of crucial processes such as detachment or the formation and evolution of edge transport barriers, as well as potentially identifying new effects which could lead to improved reactor performance. For this, we need to develop models which are able to accurately reproduce the complex dynamics of the edge. Realistic simulations need to capture many important interacting physical processes in the edge – such as turbulent plasma flows, sheath effects at the walls, neutral dynamics and the effect of diverted magnetic geometries. At the same time, these simulations need to be computationally feasible, and ideally cheap enough that we can perform repeat simulations over profile relaxation time-scales. This forces us to make simplifying assumptions, which inevitably introduce errors, and so we need to carefully balance the computational performance and accuracy of our models. We can assess the accuracy of our numerical models by using the validation process. By comparing simulations against experimental results, we can quantify the error in our simulations and the uncertainty in predicted results. We can also analyse the results of a validation to guide model development and highlight parts of the model which need additional work [168]. This can help to rapidly improve the accuracy of our simulations while reducing unnecessary computational and development costs. However, for the results of a validation to be meaningful we need to compare against experimental cases which contain similar physics to the cases we want to investigate. As such, to develop realistic turbulence models for the edge and divertor, we need to validate our models in diverted geometry. Here, we develop and validate the GRILLIX turbulence model against a diverted reference case, demonstrating that realistic and affordable turbulence simulations of the edge are now possible.

9.1. Summary

In this thesis, we performed a first-of-a-kind comprehensive validation of a turbulence model against the TCV-X21 diverted reference scenario. To achieve this, we extended the GRILLIX turbulence model to permit simulations in realistic divertor geometries. We extended the grid generation algorithm in GRILLIX to handle arbitrary axisymmetric magnetic geometries, using a bicubic spline interpolator to calculate divergence-free magnetic field components from numerically-defined poloidal flux functions. To handle various magnetic reconstruction formats and to perform pre-processing steps such as identifying limiting flux surfaces, we implemented the `parallax-equilibrium` grid preprocessor to interactively build standardised equilibrium NetCDF files. These equilibrium files are developed to contain all of the information required to automatically generate a simulation grid corresponding to a particular case, including the geometry of the divertor and first-wall. This thesis also investigated the challenges of setting parallel boundary conditions in locally field-aligned codes. To reduce spurious cross-field diffusion, GRILLIX uses adjoint parallel operators which require a toroidally-staggered grid. By using a simple 1D advection model, we demonstrated that when combined with sheath boundary conditions, this toroidal staggering can lead to dramatically different dynamics on neighbouring field-lines, causing poloidal corrugations and numerical instabilities. To circumvent this issue, we implemented an immersed boundary condition that smoothly applied boundary conditions over a transition region, permitting numerically-stable simulations with the full GRILLIX model in open field-line geometries. Together, these modifications enabled simulations of real diverted fusion devices.

The extended model was used to perform a first-of-a-kind validation of the GRILLIX model against the TCV-X21 diverted validation case. The simulations were performed with minimal manual tuning, with the only free physics parameter being the density source rate. A remarkably good agreement between simulation and experiment was found at the outboard midplane and divertor entrance, with the simulations matching most of the mean and fluctuation profiles within uncertainty. The positive match indicated that GRILLIX was accurately modelling the dynamics of the edge and upstream scrape-off-layer, and so we implemented additional numerical diagnostics to further investigate the dynamics. As a demonstration, we performed an analysis of the simulated phase-shift and skewness to show that scrape-off-layer filaments in TCV-X21 are being driven ballistically by a region of drift-wave turbulence in the outer confined region. A further blob tracking algorithm and comparison against gas-puff-imaging data is planned, to check that the model is accurately describing these coherent transport events. Shifting our focus to the divertor targets, we found good agreement for the electron temperature, for the parallel current density and its standard deviation, and for the forward-field electrostatic potential. By contrast, the target density and the floating potential showed poor agreement. To improve our match of the target profiles, we should develop a consistent set of conducting-sheath boundary conditions and eliminate the finite-width boundary transition region. Since the edge is a tightly-coupled system, this could also improve our description of the main plasma dynamics. In particular, a more realistic potential boundary condition will improve our description of divertor drifts (affecting cross-field transport) and modify the radial electric field across the separatrix (affecting poloidal rotation and turbulence suppression in the edge).

In parallel to the GRILLIX validation, other edge turbulence models were also validated against the experimental reference case within the TCV-X21 study [2]. This allowed for the direct comparison of different models, which indicated that realistic resistivity and heat conductivities are required to accurately describe the divertor plasma. In contrast to the other codes, GRILLIX was able to perform multiple simulations using realistic physical parameters and at a higher poloidal resolution, which suggests that it had a lower computational cost. Despite a lower cost, GRILLIX also achieved an equal-or-better overall match according to a quantitative validation metric used in the study [2]. This demonstrates that local field-alignment enables accurate and cost-effective edge turbulence simulations of existing devices, while still flexibly handling diverted geometries.

In addition to the TCV-X21 validation, a validation against an 'X-point' scenario in TORPEX was performed [126]. Here, GRILLIX was able to reproduce the density profile reasonably well, capturing an up-down asymmetry observed in the experiment. However, the electron temperature was not matched and the power used in the simulations was significantly less than in the experiment, suggesting that self-consistent neutral dynamics are required to model the weakly-ionised plasma. Other participating codes (which also omitted neutrals) found similar results – and so, despite a poor overall match, GRILLIX again achieved a slightly better result according to the validation metric [126].

Despite focusing on the GRILLIX code, this thesis also contributed to other edge simulation projects. The grid generation procedure was ported to the `parallax` library and is now as standard by both GRILLIX and GENE-X users, requiring little to no user intervention once the equilibrium files are developed. This has been used to perform GRILLIX and GENE-X simulations in TCV and AUG [180, 2], as well as in alternative divertor configurations [62] and negative triangularity cases. By flexibly handling arbitrary geometries, the procedure developed in this thesis lets us study the interaction of turbulence & magnetic geometry and contribute to active research topics aiming to improve our control of the edge. As well as helping to set up GRILLIX and GENE-X simulations, this project has also helped to post-process them. The routines developed for validation were developed into the general-purpose `TorX` library. This library has a long and growing list of functionality – including efficient routines for plotting data, converting to SI units, mapping data to measurement locations, lazy evaluation of large datasets, Fourier analyses along straight field-line coordinates and vector operations and projections in cylindrical coordinates. This makes it significantly easier to perform basic post-processing and comparisons to experiments, while also enabling advanced analyses which help us to further study the dynamics of the simulations.

Beyond GRILLIX and GENE-X, a subset of the `TorX` functionality was also released alongside the TCV-X21 experimental and simulation data in a FAIR public repository, developed in collaboration with SPC and Fair4Fusion. This repository is intended to make it easier for other turbulence models to compare against the TCV-X21 dataset, which is in many ways in-and-of-itself an experiment. By publicly sharing the dataset, we hope to encourage the rigorous validation and open benchmarking of edge turbulence models, as well as encouraging the development and public release of other validation datasets. Although it is too early to see the impact of this work, a culture of collaboration and careful testing could dramatically accelerate the development of edge turbulence modelling.

9.2. Outlook

The results of this landmark study demonstrate that GRILLIX can now perform realistic simulations of real devices. We should now validate the model against cases with more reactor-relevant physics and should use GRILLIX to help interpret experimental results. We will continue to validate GRILLIX against TCV-X21 since – due to its low cost to simulate and

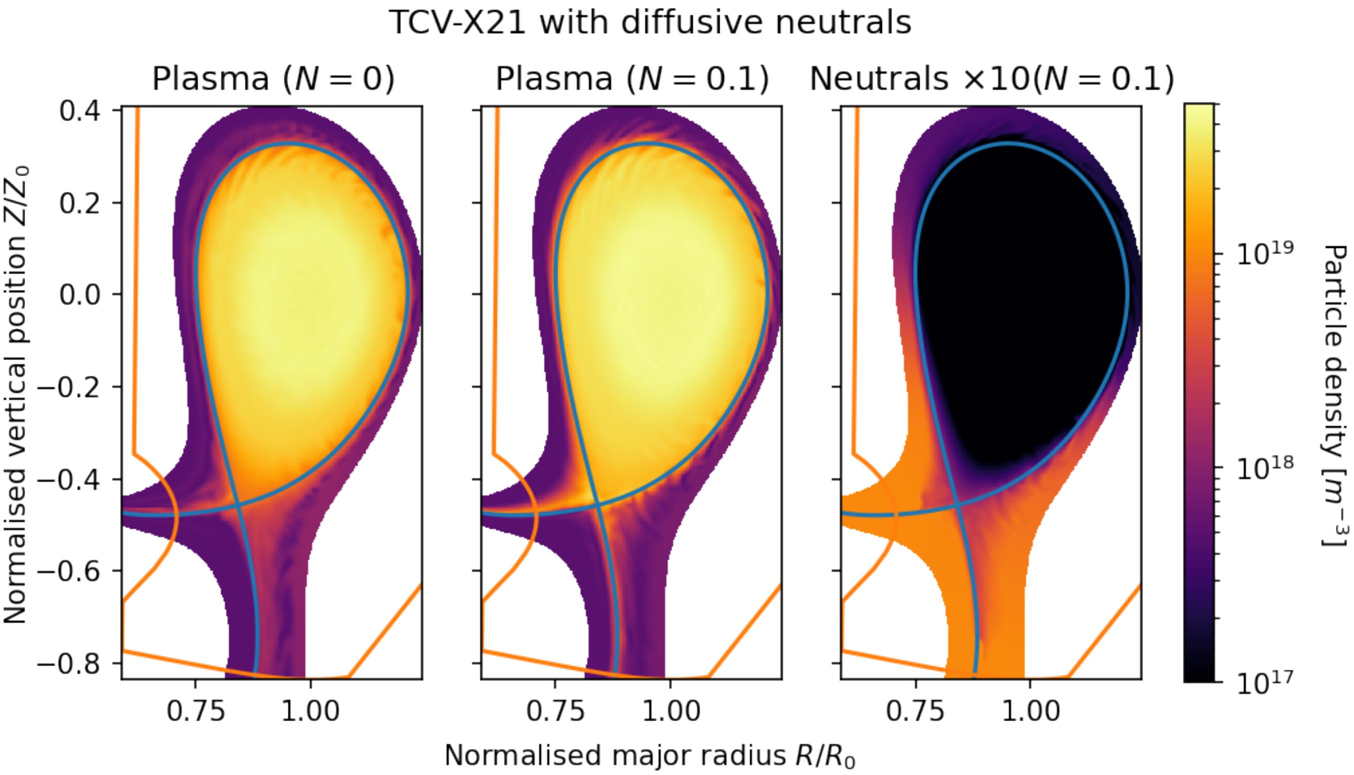

Figure 9.1.: A comparison of the plasma and neutral density with and without neutrals (*left and centre plots*), and the neutral density in the case with neutrals (*right plot*), from simulations performed by Konrad Eder. The neutral density has been multiplied by a factor of 10 to bring its values closer to the plasma density for plotting. In the simulations with neutrals, the neutral density at the divertor targets has been fixed at $1 \times 10^{18}\,\mathrm{m}^{-3}$ (10% of the plasma density reference value).

excellent diagnostic coverage – we can rapidly test new features. Repeat validations have already begun – testing a new version of GRILLIX which was heavily refactored for performance, which also includes the diffusive neutrals model developed in reference [180]. An initial comparison of the plasma density in simulations performed with and without neutrals is shown in figure 9.1, where we see that the neutrals increase the target density (towards the experimental values). Interestingly, the simulations with neutrals also have much more prominent scrape-off-layer filaments, larger in-out asymmetries and a larger difference between forward- and reversed-field simulations – indicating that the neutrals affect much more than just the density source. We will also use TCV-X21 to explore new sets of sheath boundary conditions. From the validation performed in this work, we have identified the need for consistent conducting-sheath boundary conditions. Additionally, to avoid a feedback loop in the drift-corrected velocity boundary conditions and to enable consistent recycling boundary conditions, we will extend the single field-line model developed in section 4.5 to identify sets of boundary conditions which do not require a finite-width transition region. These will then be tested in TCV-X21, before being applied to other validations and interpretive simulations.

Then, to continue developing GRILLIX towards reactor-relevant conditions, we need to validate against cases at more challenging conditions. The first such step has already been taken – GRILLIX was recently validated against an attached ASDEX Upgrade discharge in reference [180], showing remarkably good agreement especially at the outboard midplane. Beyond this, we should test the model under more challenging conditions, aiming to simulate detached cases, in H-mode or ELM-free improved confinement regimes, and in large devices such as JET. For this, the turbulence modelling community should work closely with experimental teams to develop well-diagnosed common validation cases across a broad range of parameters, building a series of 'stepping-stone' cases towards reactor-relevant conditions. To simulate these more challenging cases, we will need to continue to develop our physical and numerical models. We are exploring a Landau-fluid closure [115] to calculate realistic heat fluxes at low collisionality, ion-orbit-losses [190] to improve our description of the radial electric field, a Grad-Zhdanov closure [191] able to model multiple ion species (including impurity ions which are important for radiative cooling [192]) and an extension to 3D geometries including stellarators. Beyond this, we will need to consider how to include kinetic effects for the plasma and neutrals, by coupling to another code or by trying to capture these effects via effective models. Within this context, we will continue to closely collaborate with GENE-X to develop a multi-fidelity approach and will use validations to assess at which point the additional computational cost of a high-fidelity model is justified. To simulate devices with larger magnetic fields and plasma volumes, we will also need to improve the computational weak-scaling of GRILLIX. For this, the model has recently been significantly refactored to reduce thread-branching, and we are currently developing a GPU version for modern supercomputer architectures.

As well as developing and validating the model, we should apply GRILLIX to interpret and predict fusion experiments. An obvious candidate would be a prediction of the ITER heat flux, which could help to confirm or contradict existing predictions from turbulence models. We could also use the flexible magnetic geometry handling to investigate the performance of advanced divertors, predicting power-sharing in the SPARC double-null divertor [193] or – once the model is extended to 3D – investigating detachment in the W7X island divertor [194, 39], for example. At the same time, there is an abundance of unexplained and underexplained edge phenomena already present in devices such as TCV and AUG. Already, we could use GRILLIX to help interpret and augment experimental measurements – such as by providing T_e/T_i for Langmuir probe analyses, or calculating edge fluctuation levels for ECRH power deposition models. Once the neutral model is extended, we will also be able to investigate the dynamics of the detachment front and X-point radiator. The model could also be extended to reproduce the L-H transition and ELMs, which would let us directly observe the evolution of the edge transport barrier and pedestal, study the effects of ELM mitigation, and investigate ELM-free improved-confinement regimes. The positive results in this thesis and the accelerating rate at which the model is being developed suggest that such studies will soon be possible, promising to significantly improve our understanding and control of the edge.

9.3. Conclusion

This thesis extended the GRILLIX fluid-turbulence model to enable realistic and efficient simulations in real divertor geometries. By validating the extended model against experiment, we demonstrated that efficient simulations of the divertor & scrape-off-layer are now possible and already remarkably realistic. The results of this and future validations will be used to accelerate the development of GRILLIX, further improving the accuracy of the model. This will establish GRILLIX as a tool for studying and exploring edge phenomena in existing devices and bring validated reactor-relevant simulations within reach. Accurate, validated and computationally-efficient simulations of the edge will lead to breakthroughs in our understanding and control of the edge, which will in turn help to develop fusion as a practical source of energy.

Part V.

Appendices

A. Normalised equations

In GRILLIX, the equations are normalised by selecting a number of reference parameters, and then dividing the equations to arrive at a dimensionless form. The symbol $\circledast$ (`\circledast`) is used to indicate a reference value, and $\varnothing$ (`\varnothing`) is used to indicate a dimensionless value. The `normalisation` module in the `TorX` library can help with calculating dimensionless values from reference parameters. Note that we always use SI units, except for the temperatures which are expressed as an equivalent energy in electron-volts. Wherever we write T, we implicitly mean $k_B T$ where $k_B = 11\,605\,\mathrm{K\,eV^{-1}}$ is the Boltzmann constant. Note that several plasma physics texts use c.g.s. + eV units. See the NRL plasma formulary for converting between different systems of units. The reference and/or normalisation parameters are:

$R_\circledast$	[m]	major radius of the magnetic axis, used to normalise the length-scale parallel to the magnetic field
$\rho_{s\circledast} = \frac{1}{eB_\circledast}\sqrt{\frac{T_\circledast}{m_i}}$	[m]	reference sound Larmor radius, used to normalise the length-scale perpendicular to the magnetic field
$t_\circledast = R_\circledast / c_{s\circledast}$	[s]	reference time-scale, used to normalise time-scales
$B_\circledast$	[T]	on-axis magnetic field strength
$n_\circledast$	$\left[\mathrm{m^{-3}}\right]$	reference density, usually taken at the outboard-midplane separatrix
$T_\circledast$	[eV]	reference temperature, usually taken at the outboard-midplane separatrix
$\phi_\circledast = T_\circledast / e$	[V]	reference electrostatic potential
$c_{s\circledast} = \sqrt{T_\circledast / m_i}$	$\left[\mathrm{m\,s^{-1}}\right]$	reference velocity, defined as the ion sound speed at the reference temperature
$e n_\circledast c_{s\circledast}$	$\left[\mathrm{A\,m^{-2}}\right]$	reference current density
$\beta_{e\varnothing} B_\circledast \rho_{s\circledast}$	[T m]	reference vector potential, with $\beta_{e\varnothing}$ defined below
$\ln \Lambda_\circledast$	[−]	reference Coulomb logarithm, defined as $6.6 - 0.5 \ln\left(\frac{n_\circledast}{10^{20}\mathrm{m^{-3}}}\right) + 1.5 \ln\left(\frac{T_{e\circledast}}{1\mathrm{eV}}\right)$. Note that we always use $\ln \Lambda_\circledast$ instead of $\ln \Lambda$, since it changes slowly.
$\tau_{e\circledast} = \tilde{\tau}_e \frac{m_e^{0.5} T_\circledast^{1.5}}{\ln \Lambda n_\circledast}$	[s]	reference electron collision time, defined such that $\tau_e = \tau_{e\circledast} \frac{(T_e/T_\circledast)^{1.5}}{(n/n_\circledast)}$, with $\tilde{\tau}_e = 3.605 \times 10^{26}\,\mathrm{s}/\left(\mathrm{kg^{0.5}\,eV^{1.5}\,m^3}\right)$.
$\tau_{i\circledast} = \tilde{\tau}_i \frac{m_i^{0.5} T_\circledast^{1.5}}{\ln \Lambda n_\circledast}$	[s]	reference ion collision time, defined such that $\tau_i = \tau_{i\circledast} \frac{(T_i/T_\circledast)^{1.5}}{(n/n_\circledast)}$, with $\tilde{\tau}_i = \sqrt{2}\tilde{\tau}_e$.

The dimensionless parameters are:

$\delta = R_0/\rho_{s\circledast}$	ratio of parallel to perpendicular length scales
$\beta_{e\varnothing} = v_{A\circledast}^2/c_{s\circledast}^2$	electron dynamical beta, using the reference sound speed and reference Alfvén velocity $v_{A\circledast} = B_\circledast/(\mu_0 n_\circledast m_i)$
m_e/m_i	electron-to-ion mass ratio
$\tau_{e\varnothing} = \sqrt{\frac{m_i}{m_e}}\frac{\tau_{e\circledast}}{t_\circledast}$	normalised reference electron collision time, with an additional factor $\sqrt{\frac{m_i}{m_e}}$ so that both τ_e and τ_i depend on the ion mass
$\tau_{i\varnothing} = \frac{\tau_{i\circledast}}{t_\circledast}$	normalised reference ion collision time
$\eta_{\parallel\varnothing} = 0.51/\tau_{e\varnothing}$	normalised Spitzer resistivity
$\chi_{\parallel e\varnothing} = 3.16\tau_{e\varnothing}$	normalised parallel electron heat conductivity
$\chi_{\parallel i\varnothing} = 3.9\tau_{i\varnothing}$	normalised parallel ion heat conductivity
$\eta_{i\varnothing} = 0.96\tau_{i\varnothing}$	normalised ion viscosity, which scales the ion stress function G

We write the component of the ion viscosity which remains after diamagnetic cancellation in terms of the ion viscous stress function [129]

$$G = -\eta_0^i \left[\frac{2}{B^{3/2}} \nabla \cdot \left(u_\parallel B^{3/2} \hat{\mathbf{b}} \right) - \frac{1}{2} \left(C(\phi) + \frac{1}{en} C\left(p_i\right) \right) \right] \tag{A.1}$$

where $\eta_0^i = 0.96 n T_i \tau_i$.

This lets us write the final equation set in terms of normalised values.
Continuity equation

$$\left[\frac{\partial}{\partial t} + \boldsymbol{u}_{E\times B}\cdot\nabla\right] n = -n\left(\frac{\nabla\times\hat{\mathbf{b}}}{B}\right)\cdot\nabla\phi - \left(\frac{\nabla\times\hat{\mathbf{b}}}{B}\right)\cdot\nabla p_e + \nabla\cdot\left(j_\parallel - n u_\parallel\right)\hat{\mathbf{b}} \tag{A.2}$$

Quasineutrality equation

$$\begin{aligned}\nabla\cdot\frac{n}{B^2}\left[\frac{\partial}{\partial t} + u_\parallel\nabla_\parallel + \boldsymbol{u}_{E\times B}\cdot\nabla\right]\left(\nabla_\perp\phi + \frac{\nabla_\perp p_i}{n}\right)& \\ = \nabla\cdot j_\parallel\hat{\mathbf{b}} + \left(\frac{\nabla\times\hat{\mathbf{b}}}{B}\right)\cdot\nabla_\perp\left(p_e + p_i\right) - \frac{1}{6}\left(\frac{\nabla\times\hat{\mathbf{b}}}{B}\right)\cdot\nabla G &\end{aligned} \tag{A.3}$$

Parallel momentum equation

$$\left[\frac{\partial}{\partial t} + \boldsymbol{u}_{E\times B}\cdot\nabla + u_\parallel\nabla_\parallel\right] u_\parallel = -\frac{1}{n}\nabla_\parallel\left(p_e + p_i\right) + T_i\left(\frac{\nabla\times\hat{\mathbf{b}}}{B}\right)\cdot\nabla u_\parallel - \frac{2}{3}\frac{B^{3/2}}{n}\nabla_\parallel\frac{G}{B^{3/2}} \tag{A.4}$$

Ohm's law

$$\frac{m_e}{m_i}\left[\frac{\partial}{\partial t} + \boldsymbol{u}_{E\times B}\cdot\nabla + v_\parallel\nabla_\parallel\right]\frac{j_\parallel}{n} + \beta_{e\circledast}\frac{\partial A_\parallel}{\partial t} = \frac{\nabla_\parallel p_e}{n} - \nabla_\parallel\phi - \frac{\eta_{\parallel\varnothing}}{T_e^{3/2}}j_\parallel + 0.71\nabla_\parallel T_e \tag{A.5}$$

Electron temperature equation

$$\begin{aligned}\frac{3}{2}\left[\frac{\partial}{\partial t} + \boldsymbol{u}_{E\times B}\cdot\nabla + v_\parallel\nabla_\parallel\right]T_e =& - T_e\left(\left(\frac{\nabla\times\hat{\mathbf{b}}}{B}\right)\cdot\nabla\phi + \nabla\cdot v_\parallel\hat{\mathbf{b}} + \frac{1}{n}\left(\frac{\nabla\times\hat{\mathbf{b}}}{B}\right)\cdot\nabla p_e\right) \\ &+ \frac{1}{n}\nabla\cdot\left[\chi_{\parallel e\varnothing}T_e^{5/2}\nabla_\parallel T_e\hat{\mathbf{b}}\right] + \frac{5}{2}T_e\left(\frac{\nabla\times\hat{\mathbf{b}}}{B}\right)\cdot\nabla T_e \\ &+ 0.71\frac{T_e}{n}\nabla\cdot j_\parallel\hat{\mathbf{b}} + \frac{1}{n}\frac{\eta_{\parallel\varnothing}}{T_e^{3/2}}j_\parallel^2 - \frac{3m_e}{m_i}\frac{\left(T_e - T_i\right)}{\tau_{e\varnothing}T_e^{3/2}/n} + \mathcal{S}_{T_e}\end{aligned} \tag{A.6}$$

Ion temperature equation

$$\begin{aligned}\frac{3}{2}\left[\frac{\partial}{\partial t} + \boldsymbol{u}_{E\times B}\cdot\nabla + u_\parallel\nabla_\parallel\right]T_i =& - T_i\left(\left(\frac{\nabla\times\hat{\mathbf{b}}}{B}\right)\cdot\nabla\phi + \nabla\cdot u_\parallel\hat{\mathbf{b}} + \frac{1}{n}\left(\frac{\nabla\times\hat{\mathbf{b}}}{B}\right)\cdot\nabla p_e\right) \\ &+ \frac{1}{n}\nabla\cdot\left[\chi_{\parallel i\varnothing}T_i^{5/2}\nabla_\parallel T_i\hat{\mathbf{b}}\right] + \frac{5}{2}T_i\left(\frac{\nabla\times\hat{\mathbf{b}}}{B}\right)\cdot\nabla T_i \\ &+ \frac{T_i}{n}\nabla\cdot j_\parallel\hat{\mathbf{b}} + \frac{3m_e}{m_i}\frac{\left(T_e - T_i\right)}{\tau_{e\varnothing}T_e^{3/2}/n} + \frac{G^2}{3n\eta_{i\varnothing}} + \mathcal{S}_{T_i}\end{aligned} \tag{A.7}$$

Ampere's law

$$\nabla_\perp^2 A_\parallel = j_\parallel \tag{A.8}$$

B. Useful formulas

General vector identities. f is an arbitrary scalar function, and A and B are arbitrary vector functions.

Scalar triple product
$$(\boldsymbol{a} \times \boldsymbol{b}) \cdot \boldsymbol{c} = (\boldsymbol{b} \times \boldsymbol{c}) \cdot \boldsymbol{a} = (\boldsymbol{c} \times \boldsymbol{a}) \cdot \boldsymbol{b} \tag{B.1}$$

Reversing a cross-product
$$\boldsymbol{a} \times \boldsymbol{b} = -\boldsymbol{b} \times \boldsymbol{a} \tag{B.2}$$

Expanding a cross-product w. $\hat{\mathbf{e}}_1 \times \hat{\mathbf{e}}_2 = \hat{\mathbf{e}}_3$
$$\boldsymbol{a} \times \boldsymbol{b} = \begin{vmatrix} \hat{\mathbf{e}}_1 & \hat{\mathbf{e}}_2 & \hat{\mathbf{e}}_3 \\ a_1 & a_2 & a_3 \\ b_1 & b_2 & b_3 \end{vmatrix} \tag{B.3}$$

Vector triple product
$$(\boldsymbol{a} \times \boldsymbol{b}) \times \boldsymbol{c} = (\boldsymbol{a} \cdot \boldsymbol{c})\boldsymbol{b} - (\boldsymbol{b} \cdot \boldsymbol{c})\boldsymbol{a} \tag{B.4}$$

Divergence of a scalar-vector product
$$\nabla \cdot (f\boldsymbol{A}) = f\nabla \cdot \boldsymbol{A} + \boldsymbol{A} \cdot \nabla f \tag{B.5}$$

Curl of a scalar-vector product
$$\nabla \times (f\boldsymbol{A}) = f\nabla \times \boldsymbol{A} + (\nabla f) \times \boldsymbol{A} \tag{B.6}$$

Divergence of a cross-product
$$\nabla \cdot (\boldsymbol{A} \times \boldsymbol{B}) = \boldsymbol{B} \cdot (\nabla \times \boldsymbol{A}) - \boldsymbol{A} \cdot (\nabla \times \boldsymbol{B}) \tag{B.7}$$

Curl of a cross-product
$$\nabla \times (\boldsymbol{A} \times \boldsymbol{B}) = \boldsymbol{A}(\nabla \cdot \boldsymbol{B}) - \boldsymbol{B}(\nabla \cdot \boldsymbol{A}) \tag{B.8}$$
$$+ (\boldsymbol{B} \cdot \nabla)\boldsymbol{A} - (\boldsymbol{A} \cdot \nabla)\boldsymbol{B} \tag{B.9}$$

Divergence of a gradient
$$\nabla \cdot (\nabla f) = \nabla^2 f \tag{B.10}$$

Curl of a gradient
$$\nabla \times (\nabla f) = 0 \tag{B.11}$$

Divergence of a curl
$$\nabla \cdot (\nabla \times \boldsymbol{A}) = 0 \tag{B.12}$$

Curl of a curl
$$\nabla \times (\nabla \times \boldsymbol{A}) = \nabla(\nabla \cdot \boldsymbol{A}) - \nabla^2 \boldsymbol{A} \tag{B.13}$$

Gauß's theorem
$$\int_{\mathcal{V}} (\nabla \cdot \boldsymbol{A}) d\mathcal{V} = \oint_{\partial\mathcal{V}} \boldsymbol{A} \cdot d\boldsymbol{\mathcal{S}} \tag{B.14}$$

Stoke's theorem
$$\int_{\mathcal{S}} (\nabla \times \boldsymbol{A}) \cdot d\boldsymbol{\mathcal{S}} = \oint_{\partial\mathcal{S}} \boldsymbol{A} \cdot dl \tag{B.15}$$

$$\tag{B.16}$$

GRILLIX-specific formulas. $\boldsymbol{B} = B\hat{\mathbf{b}}$ is the magnetic field vector, which points in the direction $\hat{\mathbf{b}}$ and has a magnitude B.

Drift operator
$$\frac{1}{B}\hat{\mathbf{b}} \times (\boldsymbol{A} \times \boldsymbol{B}) = \boldsymbol{A} - \boldsymbol{A} \cdot \boldsymbol{b} = \boldsymbol{A}_\perp \tag{B.17}$$

Curvature operator
$$\mathcal{K}(f) = -\nabla \cdot \left(\frac{\hat{\mathbf{b}} \times \nabla f}{B} \right) = -\left(\frac{\nabla \times \hat{\mathbf{b}}}{B} \right) \cdot \nabla f \tag{B.18}$$

Coordinate systems

$$|\nabla x| = |\nabla y| = |\nabla z| = 1 \text{ (Cartesian)} \tag{B.19}$$

$$|\nabla R| = 1, |\nabla \phi| = \frac{1}{R}, |\nabla Z| = 1 \text{ (Cylindrical)} \tag{B.20}$$

$$|\nabla R| = 1, |\nabla \theta| = |\nabla \phi| = \frac{1}{R} \text{ (Spherical)} \tag{B.21}$$

In Cylindrical coordinates:

Gradient
$$\nabla f = \frac{\partial f}{\partial R}\hat{\mathbf{R}} + \frac{1}{R}\frac{\partial f}{\partial \phi}\hat{\phi} + \frac{\partial f}{\partial Z}\hat{\mathbf{Z}} \tag{B.22}$$

Divergence
$$\nabla \cdot \boldsymbol{A} = \frac{1}{R}\frac{\partial\left(R\boldsymbol{A}_R\right)}{\partial R} + \frac{1}{R}\frac{\partial \boldsymbol{A}_\phi}{\partial \phi} + \frac{\partial \boldsymbol{A}_Z}{\partial Z} \tag{B.23}$$

Curl
$$\nabla \times \boldsymbol{A} = \frac{1}{R}\begin{vmatrix} \hat{\mathbf{R}} & R\hat{\phi} & \hat{\mathbf{Z}} \\ \frac{\partial}{\partial R} & \frac{\partial}{\partial \phi} & \frac{\partial}{\partial Z} \\ A_R & RA_\phi & A_Z \end{vmatrix} \tag{B.24}$$

$$= \left(\frac{1}{R}\frac{\partial A_Z}{\partial \phi} - \frac{\partial A_\phi}{\partial Z}\right)\hat{R} + \left(\frac{\partial A_R}{\partial Z} - \frac{\partial A_Z}{\partial R}\right)\hat{\phi} + \frac{1}{R}\left(\frac{\partial\left(RA_\phi\right)}{\partial R} - \frac{\partial A_R}{\partial \phi}\right)\hat{Z} \tag{B.25}$$

Laplacian
$$\nabla^2 f = \frac{1}{R}\frac{\partial}{\partial R}\left(R\frac{\partial f}{\partial R}\right) + \frac{1}{R^2}\frac{\partial^2 f}{\partial \phi^2} + \frac{\partial^2 f}{\partial Z^2} \tag{B.26}$$

Differential length
$$d\boldsymbol{l} = dR\hat{\mathbf{R}} + Rd\phi\hat{\phi} + dZ\hat{\mathbf{Z}} \tag{B.27}$$

Differential area
$$d\boldsymbol{S} = Rd\phi dZ\hat{\mathbf{R}} + dRdZ\hat{\phi} + RdRd\phi\hat{\mathbf{Z}} \tag{B.28}$$

Differential volume
$$d\boldsymbol{V} = RdRd\phi dZ \tag{B.29}$$

C. Additional results

C.1. Deriving the electron temperature equation

Starting from the Braginskii T_e equation (2.38)

$$\frac{3}{2}n\left[\frac{\partial}{\partial t}+\boldsymbol{v}\cdot\nabla\right]T_e+p_e\nabla\cdot\boldsymbol{v}=-\nabla\cdot\boldsymbol{q}_e+(Q_e-Q_{ei})+\mathcal{S}_{\varepsilon_e} \tag{C.1}$$

with

$$\boldsymbol{v}=\boldsymbol{u}_{E\times B}+\boldsymbol{v}_{dia}+\left(u_{\|}-\frac{j_{\|}}{en}\right)\hat{\mathbf{b}} \tag{C.2}$$

$$\boldsymbol{u}=\boldsymbol{u}_{E\times B}+\boldsymbol{u}_{dia}+\boldsymbol{u}_{pol}+u_{\|}\hat{\mathbf{b}} \tag{C.3}$$

$$\boldsymbol{q}_e=-\chi_{\|,e}\nabla_{\|}T_e\hat{\mathbf{b}}-\frac{5}{2}\frac{p_e}{eB}\hat{\mathbf{b}}\times\nabla T_e-0.71\frac{1}{e}T_ej_{\|}\hat{\mathbf{b}} \tag{C.4}$$

$$Q_e=(u_{\|}-v_{\|})R_{\|}=\eta_{\|}j_{\|}^2-0.71\frac{1}{e}j_{\|}\nabla T_e \tag{C.5}$$

$$Q_{ei}=\frac{3m_e}{m_i}\frac{n\left(T_e-T_i\right)}{\tau_e} \tag{C.6}$$

The perpendicular heat flux can be rewritten using identify B.7 as

$$\nabla\cdot\left[\frac{5}{2}\frac{p_e}{eB}\hat{\mathbf{b}}\times\nabla T_e\right]=\frac{5}{2}\left[\nabla T_e\cdot\left(\nabla\times\frac{p_e}{eB}\hat{\mathbf{b}}\right)-\frac{p_e}{eB}\cancel{\hat{\mathbf{b}}\cdot(\nabla\times(\nabla T_e))}\right] \tag{C.7}$$

Then, using identity B.5 to expand the $\nabla\times\frac{p_e}{eB}\hat{\mathbf{b}}$ term

$$\nabla\cdot\left[\frac{5}{2}\frac{p_e}{eB}\hat{\mathbf{b}}\times\nabla T_e\right]=\frac{5}{2}\frac{p_e}{e}\left(\frac{\nabla\times\hat{\mathbf{b}}}{B}\right)\cdot\nabla T_e+\frac{5}{2}\nabla\left(\frac{p_e}{eB}\right)\times\hat{\mathbf{b}}\cdot\nabla T_e \tag{C.8}$$

Assuming that we can commute $\frac{1}{B}$ through the derivative and recognising the electron diamagnetic velocity (2.47) we can write this as

$$\nabla\cdot\left[\frac{5}{2}\frac{p_e}{eB}\hat{\mathbf{b}}\times\nabla T_e\right]=\frac{5}{2}\frac{p_e}{e}\left(\frac{\nabla\times\hat{\mathbf{b}}}{B}\right)\cdot\nabla T_e+\frac{5}{2}n\boldsymbol{v}_{dia}\cdot\nabla T_e \tag{C.9}$$

We can also combine the terms related to the thermal force using identity B.5

$$-\nabla\cdot\left[-0.71\frac{1}{e}T_ej_{\|}\hat{\mathbf{b}}\right]-0.71\frac{1}{e}j_{\|}\nabla_{\|}T_e=\frac{0.71}{e}\left(\nabla\cdot\left[T_ej_{\|}\hat{\mathbf{b}}\right]-j_{\|}\nabla_{\|}T_e\right) \tag{C.10}$$

$$=\frac{0.71}{e}\left(T_e\nabla\cdot j_{\|}\hat{\mathbf{b}}+\cancel{j_{\|}\hat{\mathbf{b}}\cdot\nabla T_e-j_{\|}\nabla_{\|}T_e}\right) \tag{C.11}$$

We then combine the $\frac{3}{2}\boldsymbol{v}_{dia} \cdot \nabla T_e$ from the LHS with the $\frac{5}{2}\boldsymbol{v}_{dia} \cdot \nabla T_e$ term from the perpendicular heat flux, giving a $\boldsymbol{v}_{dia} \cdot \nabla T_e$ on the RHS. By using the expression for the electron diamagnetic velocity $\boldsymbol{v}_{dia} = \frac{-\hat{\mathbf{b}}\times\nabla(nT_e)}{enB}$, the chain rule and identities B.1 and B.2, we can rewrite this as

$$\begin{aligned}
\boldsymbol{v}_{dia} \cdot \nabla T_e &= \frac{-1}{enB}\left(\hat{\mathbf{b}} \times (n\nabla T_e + T_e \nabla n)\right) \cdot \nabla T_e && \text{(C.12)}\\
&= \frac{-T_e}{enB}\left(\hat{\mathbf{b}} \times \nabla n\right) \cdot \nabla T_e && \text{(C.13)}\\
&= \frac{-T_e}{enB}\left(\nabla T_e \times \nabla \hat{\mathbf{b}}\right) \cdot \nabla n && \text{(C.14)}\\
&= \frac{T_e}{enB}\left(\nabla \hat{\mathbf{b}} \times \nabla T_e\right) \cdot \nabla n && \text{(C.15)}\\
&= \frac{-T_e}{n}\frac{-1}{enB}\left(\nabla \hat{\mathbf{b}} \times n\nabla T_e\right) \cdot \nabla n && \text{(C.16)}
\end{aligned}$$

We are allowed to add back in a term $T_e\left(\hat{\mathbf{b}} \times \nabla n\right) \cdot \nabla n$, since this will be zero.

$$= \frac{-T_e}{n}\frac{-1}{enB}\left(\nabla \hat{\mathbf{b}} \times n\nabla T_e + T_e \nabla n\right) \cdot \nabla n \tag{C.17}$$

$$\boxed{\boldsymbol{v}_{dia} \cdot \nabla T_e = \frac{-T_e}{n}\boldsymbol{v}_{dia} \cdot \nabla n} \tag{C.18}$$

This is then combined with the $-T_e\nabla \cdot \boldsymbol{v}_{dia}$ term using identity B.5 to give

$$\begin{aligned}
-T_e \nabla \cdot \boldsymbol{v}_{dia} + \boldsymbol{v}_{dia} \cdot \nabla T_e &= \frac{-T_e}{n}\left(n\nabla \cdot \boldsymbol{v}_{dia} + \boldsymbol{v}_{dia} \cdot \nabla n\right) && \text{(C.19)}\\
&= \frac{-T_e}{n}\nabla \cdot (n\boldsymbol{v}_{dia}) && \text{(C.20)}
\end{aligned}$$

This gives the final form of the electron temperature equation (2.67)

$$\begin{aligned}
\frac{3}{2}\left[\frac{\partial}{\partial t} + \boldsymbol{u}_{E\times B} \cdot \nabla + v_{\|}\nabla_{\|}\right] T_e =& - T_e \nabla \cdot \left(\boldsymbol{u}_{E\times B} + v_{\|}\hat{\mathbf{b}}\right) - \frac{T_e}{n}\nabla \cdot (n\boldsymbol{v}_{dia})\\
&+ \frac{1}{n}\nabla \cdot \left[\chi_{\|,e}\nabla_{\|}T_e\hat{\mathbf{b}}\right] + \frac{5}{2}\frac{T_e}{e}\left(\frac{\nabla \times \hat{\mathbf{b}}}{B}\right) \cdot \nabla T_e\\
&+ \frac{0.71}{e}\frac{T_e}{n}\nabla \cdot j_{\|}\hat{\mathbf{b}} + \frac{1}{n}\eta_{\|}j_{\|}^2 - \frac{3m_e}{m_i}\frac{(T_e - T_i)}{\tau_e} + \mathcal{S}_{T_e}
\end{aligned} \tag{C.21}$$

or, using the expressions for the perpendicular velocities

$$\begin{aligned}
\frac{3}{2}\left[\frac{\partial}{\partial t} + \boldsymbol{u}_{E\times B} \cdot \nabla + v_{\|}\nabla_{\|}\right] T_e =& - T_e\left(\left(\frac{\nabla \times \hat{\mathbf{b}}}{B}\right) \cdot \nabla \phi + \nabla \cdot v_{\|}\hat{\mathbf{b}} + \frac{1}{n}\left(\frac{\nabla \times \hat{\mathbf{b}}}{B}\right) \cdot \nabla p_e\right)\\
&+ \frac{1}{n}\nabla \cdot \left[\chi_{\|,e}\nabla_{\|}T_e\hat{\mathbf{b}}\right] + \frac{5}{2}\frac{T_e}{e}\left(\frac{\nabla \times \hat{\mathbf{b}}}{B}\right) \cdot \nabla T_e\\
&+ \frac{0.71}{e}\frac{T_e}{n}\nabla \cdot j_{\|}\hat{\mathbf{b}} + \frac{1}{n}\eta_{\|}j_{\|}^2 - \frac{3m_e}{m_i}\frac{(T_e - T_i)}{\tau_e} + \mathcal{S}_{T_e}
\end{aligned} \tag{C.22}$$

C.2. Deriving the ion temperature equation

Starting from the Braginskii T_i equation (2.39)

$$\frac{3}{2}n\left[\frac{\partial}{\partial t}+\boldsymbol{u}\cdot\nabla\right]T_i+p_i\nabla\cdot\boldsymbol{u}+\underline{\underline{\boldsymbol{\Pi}}}_i:\boldsymbol{u}=-\nabla\cdot\boldsymbol{q}_i+Q_{ei}+\mathcal{S}_{\varepsilon_i} \tag{C.23}$$

with $\boldsymbol{v}$, $\boldsymbol{u}$ and Q_{ei} defined in the previous section and

$$\boldsymbol{q}_i=-\chi_{\|,i}\nabla_{\|}T_i\hat{\mathbf{b}}-\frac{5}{2}\frac{p_i}{eB^2}\boldsymbol{B}\times\nabla T_i \tag{C.24}$$

Following the same procedure as in the previous section, we can write

$$\begin{aligned}\frac{3}{2}\left[\frac{\partial}{\partial t}+\boldsymbol{u}_{E\times B}\cdot\nabla+\cancel{\boldsymbol{u}_{pol}\cdot\nabla}+u_{\|}\nabla_{\|}\right]T_i=&-T_i\nabla\cdot\left(\boldsymbol{u}_{E\times B}+\boldsymbol{u}_{dia}+\boldsymbol{u}_{pol}+u_{\|}\hat{\mathbf{b}}\right)\\&+\frac{1}{n}\nabla\cdot\left[\chi_{\|,i}\nabla_{\|}T_i\right]+\frac{5}{2}\frac{T_i}{e}\left(\frac{\nabla\times\hat{\mathbf{b}}}{B}\right)\cdot\nabla T_i+n\boldsymbol{u}_{dia}\cdot\nabla T_i\\&+\frac{3m_e}{m_i}\frac{(T_e-T_i)}{\tau_e}+\frac{G^2}{3n\eta_i}+\mathcal{S}_{T_i}\end{aligned} \tag{C.25}$$

where the G term comes from the component of the ion viscosity tensor which remains after diamagnetic cancellation. Like always, we drop $\boldsymbol{u}_{pol}$ from the advective derivative, since this term is difficult to deal with numerically. However, we also have a $\nabla\cdot\boldsymbol{u}_{pol}$ term, and since it's under a divergence we should not neglect it. To simplify this term, we can use the fact that due to quasineutrality $\frac{\partial n}{\partial t}+\nabla\cdot(n\boldsymbol{u})=\frac{\partial n}{\partial t}+\nabla\cdot(n\boldsymbol{v})=0$. We can therefore rewrite a divergence of the ion flux in terms of a divergence of the electron flux.

$$\nabla\cdot(n\boldsymbol{u})=\nabla\cdot(n\boldsymbol{v}) \tag{C.26}$$

$$n\nabla\cdot\boldsymbol{u}+\boldsymbol{u}\cdot\nabla n=n\nabla\cdot\boldsymbol{v}+\boldsymbol{v}\cdot\nabla n \tag{C.27}$$

$$\nabla\cdot\boldsymbol{u}=\nabla\cdot\boldsymbol{v}+\frac{1}{n}(\boldsymbol{v}-\boldsymbol{u})\cdot\nabla n \tag{C.28}$$

$$=\nabla\cdot\left(\boldsymbol{u}_{E\times B}+\boldsymbol{v}_{dia}+v_{\|}\hat{\mathbf{b}}\right)+\frac{\boldsymbol{v}_{dia}-\boldsymbol{u}_{dia}}{n}\cdot\nabla n-\frac{u_{\|}-v_{\|}}{n}\nabla_{\|}n \tag{C.29}$$

Using $v_{\|}=u_{\|}-\frac{j_{\|}}{en}$, we can rewrite this in terms of $u_{\|}$ and $j_{\|}$

$$=\nabla\cdot\left(\boldsymbol{u}_{E\times B}+\boldsymbol{v}_{dia}+u_{\|}\hat{\mathbf{b}}\right)+\frac{\boldsymbol{v}_{dia}-\boldsymbol{u}_{dia}}{n}\cdot\nabla n-\nabla\cdot\frac{j_{\|}}{en}\hat{\mathbf{b}}-\frac{1}{n}\frac{j_{\|}}{en}\nabla_{\|}n \tag{C.30}$$

We use identity B.5 to rewrite the terms with $j_{\|}$ as $\frac{1}{n}\left(n\nabla\cdot\frac{j_{\|}}{en}\hat{\mathbf{b}}+\frac{j_{\|}}{en}\nabla_{\|}n\right)=\frac{1}{n}\nabla\cdot\frac{j_{\|}}{e}\hat{\mathbf{b}}$. Then, we combine the terms with the electron and ion diamagnetic velocities, using the form of the ion diamagnetic velocity $\boldsymbol{u}_{dia}=\frac{\hat{\mathbf{b}}\times\nabla(nT_e)}{enB}$ and the electron diamagnetic velocity given in the previous section. We can use equation C.18 (replacing T_e with T_i) to cancel

$$\boldsymbol{u}_{dia}\cdot\nabla T_i+\frac{T_i}{n}\boldsymbol{u}_{dia}\cdot\nabla n=0 \tag{C.31}$$

which simplifies the diamagnetic terms in equation C.25 (using identity B.5) to

$$-T_i\nabla\cdot\boldsymbol{v}_{dia}-\frac{T_i}{n}\boldsymbol{v}_{dia}\cdot\nabla n=\frac{-T_i}{n}\nabla\cdot\left(n\boldsymbol{v}_{dia}\right)\tag{C.32}$$

This gives the final form of the ion temperature equation (2.71)

$$\begin{aligned}\frac{3}{2}\left[\frac{\partial}{\partial t}+\boldsymbol{u}_{E\times B}\cdot\nabla+u_{\|}\nabla_{\|}\right]T_i=&-T_i\nabla\cdot\left(\boldsymbol{u}_{E\times B}+u_{\|}\hat{\mathbf{b}}\right)-\frac{T_i}{n}\nabla\cdot\left(n\boldsymbol{v}_{dia}\right)\\&+\frac{1}{n}\nabla\cdot\left[\chi_{\|,i}\nabla_{\|}T_i\hat{\mathbf{b}}\right]+\frac{5}{2}\frac{T_i}{e}\left(\frac{\nabla\times\hat{\mathbf{b}}}{B}\right)\cdot\nabla T_i\\&+\frac{T_i}{n}\nabla\cdot\frac{j_{\|}}{e}\hat{\mathbf{b}}+\frac{3m_e}{m_i}\frac{\left(T_e-T_i\right)}{\tau_e}+\frac{G^2}{3n\eta_i}+\mathcal{S}_{T_i}\end{aligned}\tag{C.33}$$

which has the *electron* diamagnetic velocity $\boldsymbol{v}_{dia}$ in the first line. We can also write this using the expressions for the perpendicular velocities

$$\begin{aligned}\frac{3}{2}\left[\frac{\partial}{\partial t}+\boldsymbol{u}_{E\times B}\cdot\nabla+u_{\|}\nabla_{\|}\right]T_i=&-T_i\left(\left(\frac{\nabla\times\hat{\mathbf{b}}}{B}\right)\cdot\nabla\phi+\nabla\cdot u_{\|}\hat{\mathbf{b}}+\frac{1}{n}\left(\frac{\nabla\times\hat{\mathbf{b}}}{B}\right)\cdot\nabla p_e\right)\\&+\frac{1}{n}\nabla\cdot\left[\chi_{\|,i}\nabla_{\|}T_i\hat{\mathbf{b}}\right]+\frac{5}{2}\frac{T_i}{e}\left(\frac{\nabla\times\hat{\mathbf{b}}}{B}\right)\cdot\nabla T_i\\&+\frac{T_i}{n}\nabla\cdot\frac{j_{\|}}{e}\hat{\mathbf{b}}+\frac{3m_e}{m_i}\frac{\left(T_e-T_i\right)}{\tau_e}+\frac{G^2}{3n\eta_i}+\mathcal{S}_{T_i}\end{aligned}\tag{C.34}$$

C.3. Testing other boundary conditions with 1D advection

We can use the 1D advection model in section 4.5 to quickly test other boundary conditions. In figure C.1, we show the corresponding scan using Bohm and constant flux boundary conditions. The Bohm condition is implemented taking the maximum of the sonic velocity and the extrapolated velocity (or the minimum, at the opposite boundary). The constant flux boundary condition sets $n_{exterior}=\Gamma_{boundary}/u_{exterior}=n_{boundary}\cdot u_{boundary}/u_{exterior}$. It is seen that the corrugations in figure C.1 are much less pronounced than in figure 4.6, but still visible. As a point of curiosity, we can reduce the corrugations further by applying the velocity boundary condition to any vector-grid-points outside the outermost scalar-grid-point (even if those points are within the boundary), giving figure C.2 – which introduces an error dependent on the grid-spacing, but which eliminates the stencil collapse issue.

In general, this highlights the need to consider the boundary conditions as a coupled system. It also suggests that we might be able to improve the situation by treating points near the boundary exceptionally. In future work, we will extend the simple 1D model to include the parallel components of the other equations. We will then try to set the boundary conditions via Taylor or Padé approximations, aiming to identify a set which gives a continuous solution as we scan the boundary position.

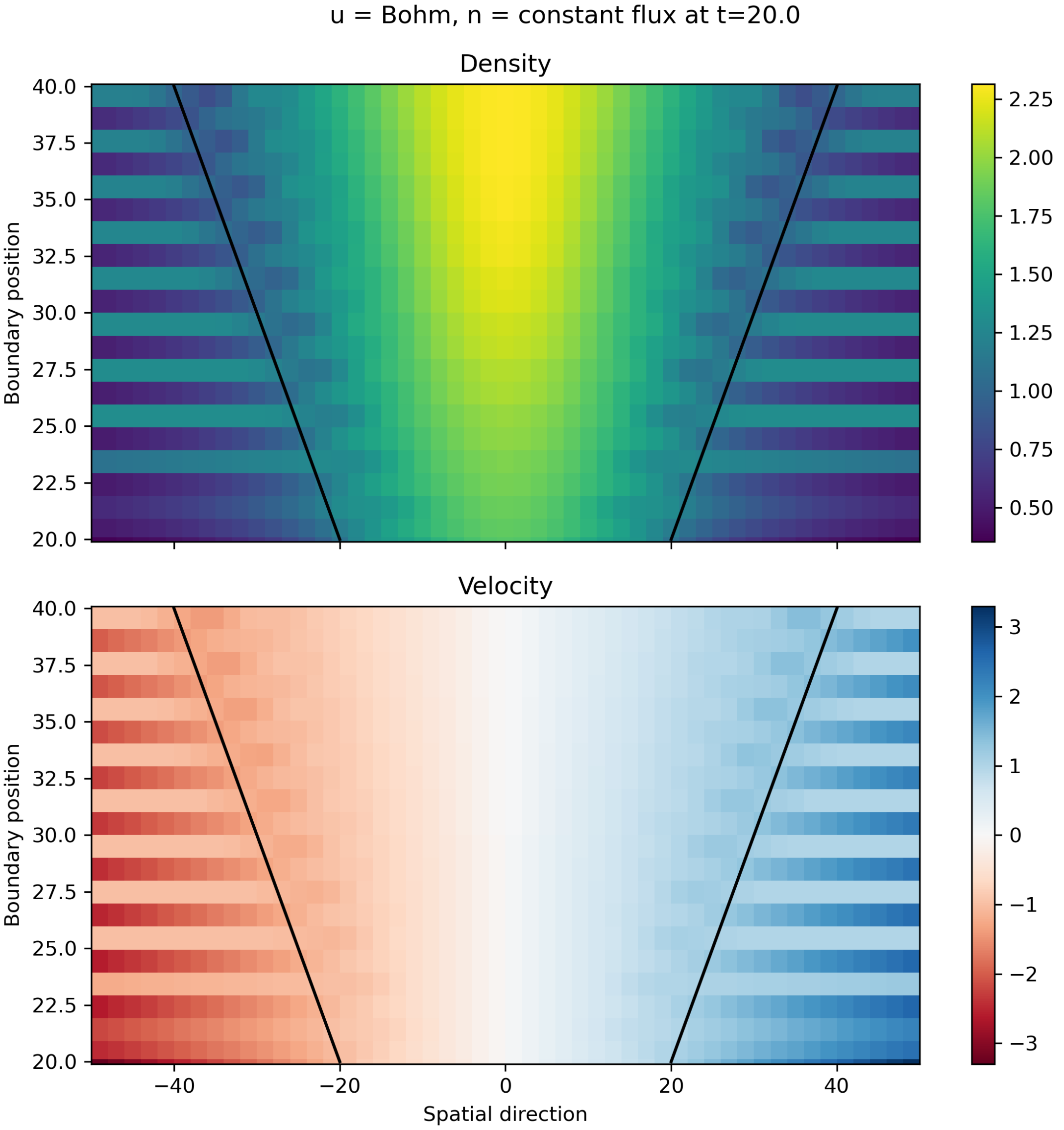

Figure C.1.: Density and velocity profiles after 100 time-steps of the advection equations, using Bohm and constant flux boundary conditions.

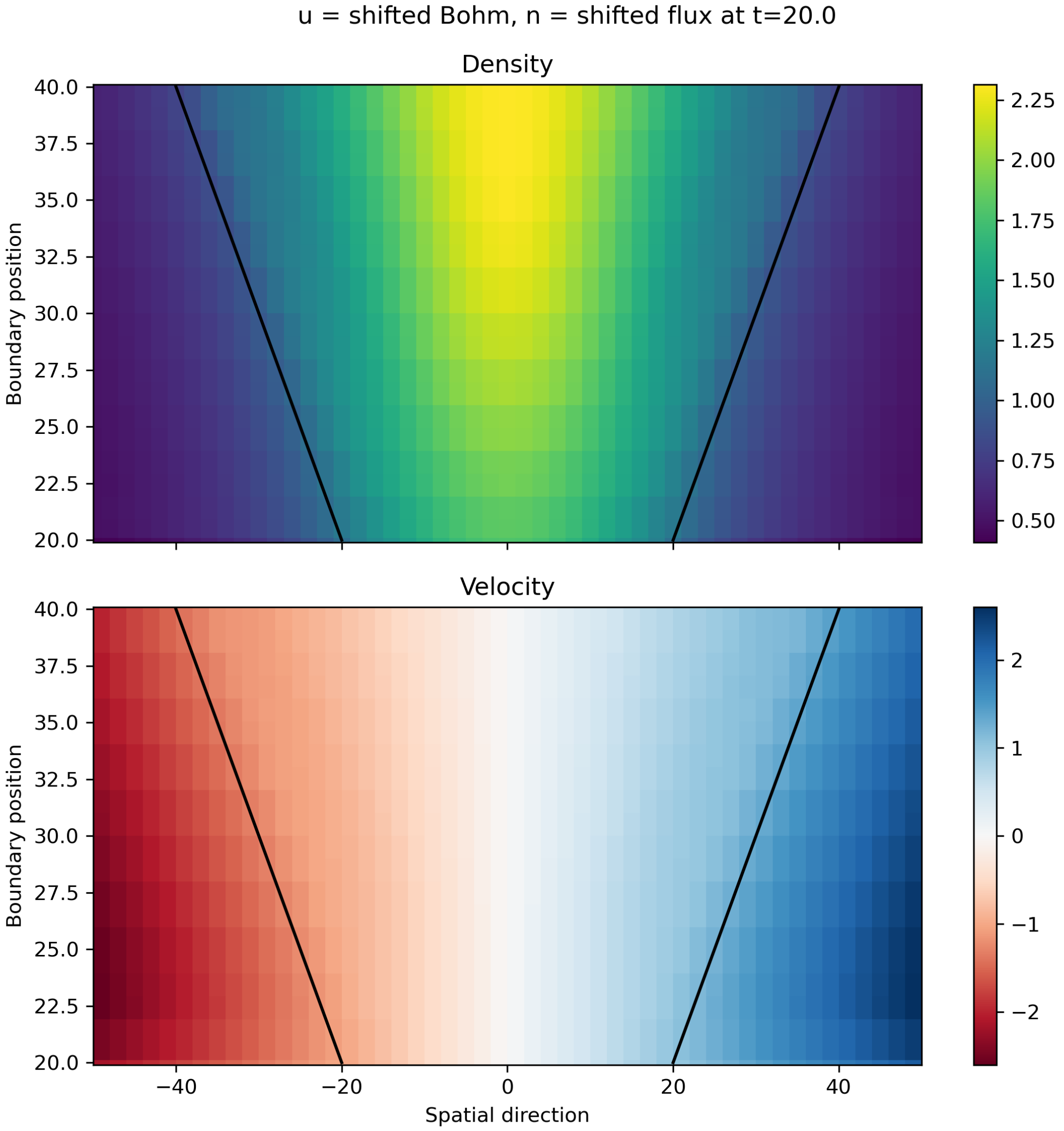

Figure C.2.: Density and velocity profiles after 100 time-steps of the advection equations, using Bohm and constant flux boundary conditions. For this case, if the boundary is vector-grid-adjacent, it is shifted until it is scalar-grid-adjacent. This leads to an error dependent on the grid-spacing, but it ensures that the velocity boundary condition is directly involved in the density evolution stencil.

D. `parallax`-standard equilibrium NetCDF

The `parallax-equilibrium` code writes NetCDF files which have a tightly defined structure, to reduce the amount of work which needs to be done by `parallax`. Each equilibrium file will have the following global attributes

- `description`: a short tag explaining where the equilibrium file came from, the shot number and time, and any other relevant information
- `build_url`: `https://gitlab.mpcdf.mpg.de/phoenix/parallax_equilibrium`
- `build_hash`: the git hash of `pxequi` used to construct this equilibrium
- `history`: date and time of file creation
- `author`: email address of the user who made the equilibrium
- `smoother`: details of the numerical smoother used, if any
- `version`: an optional tag which indicates which version of `parallax` this file is compatible with

The equilibrium data is separated into NetCDF groups. The groups and their contents are

- `Magnetic_geometry`
  - `psi`: The poloidal flux function $\Psi(R, Z)$ in units of Weber, defined over a rectangular (R, Z) grid
  - `btor`: (optional) The toroidal field $B_\phi(R, Z)$ in Tesla, defined over the same rectangular (R, Z) grid as `psi`
  - `R`: normalised radial positions R/R_0 where values of Ψ and B_ϕ are given
  - `Z`: normalised vertical positions R/R_0 where values of Ψ and B_ϕ are given
  - `axis_Btor`: toroidal magnetic field at the magnetic axis $B_\phi(R_0, Z_0)$, in units of Tesla
  - `magnetic_axis_R` and `magnetic_axis_Z`: radial and vertical position of the magnetic axis R_0, Z_0, in units of metres
  - `x_point_R` and `x_point_Z`: radial and vertical position of the X-point(s) R_X, Z_X, in units of metres. Not used by `parallax`, but useful for post-processing. For equilibria with multiple X-points, these can be given as a list.
- `Psi_limits`

  - `psi_axis`: the poloidal magnetic flux at the magnetic axis Ψ_0, in Weber
  - `psi_separatrix`: the poloidal magnetic flux at the separatrix (or equivalently, at the primary X-point) Ψ_X, in Weber
  - `rho_min`: the limiting flux-surface used to exclude the core, usually $\rho_{min} = 0.9$. Given as a value of the normalised poloidal flux ρ.
  - `rho_max`: the limiting flux-surface used to avoid glancing-angle parallel boundary conditions at the first wall, usually approximately the outermost flux surface which intersects only the divertors and not the first-wall. Given as a value of the normalised poloidal flux ρ.
  - sub-groups used for applying additional flux-limits within a polygon. The name of the group is not used by `parallax` and so can be used to identify the purpose of the flux limit – i.e. `privflux` is usually used for the private-flux region in a single-null configuration. The group should contain
    - `R_points` and `Z_points`: arrays defining the R/R_0 and Z/R_0 points of the polygon, normalised to the magnetic axis radius R_0
    - `invert`: whether the flux-limit should be applied for points inside the polygon or outside the polygon
    - `use_local_max` and `use_local_min`: boolean flags used to defined whether the polygon defines a minimum or maximum ρ limiting flux-surface
    - `local_rho_min` or `local_rho_max`: (optional if boolean flag is `false`) float values which give the limiting flux-surface value to be applied within the polygon. Given as values of the normalised poloidal flux ρ.

- `Grid_limits`
  - `grid_rmin`, `grid_rmax`, `grid_zmin` and `grid_zmax`: floats defining the range From which points should be sampled for the numerical grid, normalised to the magnetic axis radius R_0.
  - `spline_rmin`, `spline_rmax`, `spline_zmin` and `spline_zmax`: floats defining the extent of the grid of Ψ values, normalised to the magnetic axis radius R_0. Not used by `parallax`, but useful for documentation.

- `divertor_polygon` and `exclusion_polygon`: Polygons which define the divertor-first-wall polygon and the exclusion polygon (see previous section). Each polygon group contains
  - `R_points` and `Z_points`: arrays defining the R/R_0 and Z/R_0 points of the polygon, normalised to the magnetic axis radius R_0
  - `invert`: whether points inside of the polygon should be considered as the 'interior' or the 'exterior'.

List of Figures

Bibliography

[1] D. Galassi, C. Theiler, T. Body, et al. "Validation of Edge Turbulence Codes in a Magnetic X-point Scenario in TORPEX". In: *Physics of Plasmas* 29.1 (Jan. 1, 2022). DOI: `10.1063/5.0064522`.

[2] D. S. Oliveira, T. Body, D. Galassi, et al. "Validation of Edge Turbulence Codes against the TCV-X21 Diverted L-mode Reference Case". In: *Nuclear Fusion* 62.9 (July 2022). DOI: `10.1088/1741-4326/ac4cde`.

[3] J. Ongena, R. Koch, R. Wolf, and H. Zohm. "Magnetic-Confinement Fusion". In: *Nature Physics* 12.5 (May 2016). DOI: `10.1038/nphys3745`.

[4] M. L. E. Oliphant, P. Harteck, and E. Rutherford. "Transmutation Effects Observed with Heavy Hydrogen". In: *Proceedings of the Royal Society of London. Series A, Containing Papers of a Mathematical and Physical Character* 144.853 (May 1, 1934). DOI: `10.1098/rspa.1934.0077`.

[5] J. P. Freidberg. *Ideal MHD.* New York: Cambridge University Press, 2014. 722 pp. ISBN: 978-1-107-00625-6.

[6] Y. Xu. "A General Comparison between Tokamak and Stellarator Plasmas". In: *Matter and Radiation at Extremes* 1.4 (July 2016). DOI: `10.1016/j.mre.2016.07.001`.

[7] J. Wesson and D. J. Campbell. *Tokamaks.* 3rd ed. Oxford Science Publications 118. Oxford : New York: Clarendon Press ; Oxford University Press, 2004. 749 pp. ISBN: 978-0-19-850922-6.

[8] C. Windsor. "Can the Development of Fusion Energy Be Accelerated? An Introduction to the Proceedings". In: *Philosophical Transactions of the Royal Society A: Mathematical, Physical and Engineering Sciences* 377.2141 (Mar. 25, 2019). DOI: `10.1098/rsta.2017.0446`.

[9] M. Kikuchi and J.-6. Team. "Plasma Physics Found in JT-60 Tokamak over the Last 20 Years". In: *AIP Conference Proceedings* 1150.1 (July 24, 2009). DOI: `10.1063/1.3192231`.

[10] B. Bigot. "Progress toward ITER's First Plasma". In: *Nuclear Fusion* 59.11 (June 2019). DOI: `10.1088/1741-4326/ab0f84`.

[11] Y. Kamada, E. DiPietro, M. Hanada, et al. "Completion of JT-60SA Construction and Contribution to ITER". In: *Nuclear Fusion* (2021). DOI: `10.1088/1741-4326/ac10e7`.

[12] T. S. Pedersen, R. König, M. Krychowiak, et al. "First Results from Divertor Operation in Wendelstein 7-X". In: *Plasma Physics and Controlled Fusion* 61.1 (Jan. 1, 2019). DOI: `10.1088/1361-6587/aaec25`.

[13] R. C. Wolf, A. Alonso, S. Äkäslompolo, et al. "Performance of Wendelstein 7-X Stellarator Plasmas during the First Divertor Operation Phase". In: *Physics of Plasmas* 26.8 (Aug. 2019). DOI: `10.1063/1.5098761`.

[14] D. Whyte. "Small, Modular and Economically Attractive Fusion Enabled by High Temperature Superconductors". In: *Philosophical Transactions of the Royal Society A: Mathematical, Physical and Engineering Sciences* 377.2141 (Mar. 25, 2019). DOI: `10.1098/rsta.2018.0354`.

[15] R. V. Petrescu, R. Aversa, B. Akash, et al. *History of Aviation - A Short Review.* SSRN Scholarly Paper ID 3073974. Rochester, NY: Social Science Research Network, Nov. 19, 2017. URL: `https://papers.ssrn.com/abstract=3073974` (visited on 01/04/2022).

[16] M. Claessens. *ITER: The Giant Fusion Reactor: Bringing a Sun to Earth.* Cham: Springer International Publishing, 2020. ISBN: 978-3-030-27580-8 978-3-030-27581-5. DOI: `10.1007/978-3-030-27581-5`.

[17] N. J. L. Cardozo. "Economic Aspects of the Deployment of Fusion Energy: The Valley of Death and the Innovation Cycle". In: *Philosophical Transactions of the Royal Society A: Mathematical, Physical and Engineering Sciences* 377.2141 (Mar. 25, 2019). DOI: `10.1098/rsta.2017.0444`.

[18] S. Entler, J. Horacek, T. Dlouhy, and V. Dostal. "Approximation of the Economy of Fusion Energy". In: *Energy* 152 (June 1, 2018). DOI: `10.1016/j.energy.2018.03.130`.

[19] G. Janeschitz. "An Economical Viable Tokamak Fusion Reactor Based on the ITER Experience". In: *Philosophical Transactions of the Royal Society A: Mathematical, Physical and Engineering Sciences* 377.2141 (Mar. 25, 2019). DOI: `10.1098/rsta.2017.0433`.

[20] A. J. H. Donné. "The European Roadmap towards Fusion Electricity". In: *Philosophical Transactions of the Royal Society A: Mathematical, Physical and Engineering Sciences* 377.2141 (Mar. 25, 2019). DOI: `10.1098/rsta.2017.0432`.

[21] H. Zohm. "On the Size of Tokamak Fusion Power Plants". In: *Philosophical Transactions of the Royal Society A: Mathematical, Physical and Engineering Sciences* 377.2141 (Mar. 25, 2019). DOI: `10.1098/rsta.2017.0437`.

[22] B. N. Sorbom, J. Ball, T. R. Palmer, et al. "ARC: A Compact, High-Field, Fusion Nuclear Science Facility and Demonstration Power Plant with Demountable Magnets". In: *Fusion Engineering and Design* 100 (Nov. 1, 2015). DOI: `10.1016/j.fusengdes.2015.07.008`.

[23] H. Wilson. "The Impact of Plasma Physics on the Timescale to a Tokamak Fusion Power Plant". In: *Philosophical Transactions of the Royal Society A: Mathematical, Physical and Engineering Sciences* 377.2141 (Mar. 25, 2019). DOI: `10.1098/rsta.2017.0435`.

[24] H. Anand, R. A. Pitts, P. C. D. Vries, et al. "A Framework for the Assessment and Control of ITER Main Chamber Heat Loads". In: *Nuclear Fusion* 60.3 (Feb. 2020). DOI: `10.1088/1741-4326/ab6150`.

[25] P. Lorenzetto, J. Andrade, S. Banetta, et al. "EU Contribution to the Procurement of Blanket First Wall and Divertor Components for ITER". In: *Fusion Engineering and Design*. Special Issue: Proceedings of the 13th International Symposium on Fusion Nuclear Technology (ISFNT-13) 136 (Nov. 1, 2018). DOI: `10.1016/j.fusengdes.2018.04.050`.

[26] R. Dux, A. Loarte, C. Angioni, et al. "The Interplay of Controlling the Power Exhaust and the Tungsten Content in ITER". In: *Nuclear Materials and Energy*. Proceedings of the 22nd International Conference on Plasma Surface Interactions 2016, 22nd PSI 12 (Aug. 1, 2017). DOI: `10.1016/j.nme.2016.10.013`.

[27] R. A. Pitts, X. Bonnin, F. Escourbiac, et al. "Physics Basis for the First ITER Tungsten Divertor". In: *Nuclear Materials and Energy* 20 (Aug. 1, 2019). DOI: `10.1016/j.nme.2019.100696`.

[28] I. E. Alber. "Estimating the Orbiter Reentry Trajectory and the Associated Peak Heating Rates". In: *Aerospace Engineering on the Back of an Envelope*. Ed. by I. E. Alber. Springer Praxis Books. Berlin, Heidelberg: Springer, 2012. ISBN: 978-3-642-22537-6. DOI: `10.1007/978-3-642-22537-6_5`.

[29] D. Terentyev, C.-C. Chang, C. Yin, A. Zinovev, and X.-F. He. "Neutron Irradiation Effects on Mechanical Properties of ITER Specification Tungsten". In: *Tungsten* 3.4 (Dec. 1, 2021). DOI: `10.1007/s42864-021-00105-6`.

[30] A. Rajantie. "Introduction to Magnetic Monopoles". In: *Contemporary Physics* 53.3 (May 1, 2012). DOI: `10.1080/00107514.2012.685693`.

[31] C. S. Pitcher and P. C. Stangeby. "Experimental Divertor Physics". In: *Plasma Physics and Controlled Fusion* 39.6 (June 1, 1997). DOI: `10.1088/0741-3335/39/6/001`.

[32] R. Pitts, S. Bardin, B. Bazylev, et al. "Physics Conclusions in Support of ITER W Divertor Monoblock Shaping". In: *Nuclear Materials and Energy* 12 (Aug. 2017). DOI: `10.1016/j.nme.2017.03.005`.

[33] S. A. Silburn, G. F. Matthews, C. D. Challis, et al. "Mitigation of Divertor Heat Loads by Strike Point Sweeping in High Power JET Discharges". In: *Physica Scripta* T170 (Oct. 2017). DOI: `10.1088/1402-4896/aa8db1`.

[34] H. Reimerdes, R. Ambrosino, P. Innocente, et al. "Assessment of Alternative Divertor Configurations as an Exhaust Solution for DEMO". In: *Nuclear Fusion* 60.6 (June 1, 2020). DOI: `10.1088/1741-4326/ab8a6a`.

[35] R. Neu, K. Asmussen, K. Krieger, et al. "The Tungsten Divertor Experiment at ASDEX Upgrade". In: *Plasma Physics and Controlled Fusion* 38 (12A Dec. 1996). DOI: `10.1088/0741-3335/38/12A/013`.

[36] M. Keilhacker, A. Gibson, C. Gormezano, and P. H. Rebut. "The Scientific Success of JET". In: *Nuclear Fusion* 41.12 (Dec. 2001). DOI: `10.1088/0029-5515/41/12/217`.

[37] S. Coda, M. Agostini, R. Albanese, et al. "Physics Research on the TCV Tokamak Facility: From Conventional to Alternative Scenarios and Beyond". In: *Nuclear Fusion* 59.11 (Aug. 2019). DOI: `10.1088/1741-4326/ab25cb`.

[38] W. Morris, J. R. Harrison, A. Kirk, et al. “MAST Upgrade Divertor Facility: A Test Bed for Novel Divertor Solutions”. In: *IEEE Transactions on Plasma Science* 46.5 (May 2018). DOI: `10.1109/TPS.2018.2815283`.

[39] M. Jakubowski, M. Endler, Y. Feng, et al. “Overview of the Results from Divertor Experiments with Attached and Detached Plasmas at Wendelstein 7-X and Their Implications for Steady-State Operation”. In: *Nuclear Fusion* 61.10 (Aug. 2021). DOI: `10.1088/1741-4326/ac1b68`.

[40] D. Farina, R. Pozzoli, and D. D. Ryutov. “Effect of the Magnetic Field Geometry on the Flute-like Perturbations near the Divertor X Point”. In: *Nuclear Fusion* 33.9 (Sept. 1993). DOI: `10.1088/0029-5515/33/9/I06`.

[41] F. Nespoli, P. Tamain, N. Fedorczak, D. Galassi, and Y. Marandet. “A New Mechanism for Filament Disconnection at the X-point: Poloidal Shear in Radial E × B Velocity”. In: *Nuclear Fusion* 60.4 (Feb. 2020). DOI: `10.1088/1741-4326/ab6f1e`.

[42] A. Kallenbach, M. Bernert, R. Dux, et al. “Impurity Seeding for Tokamak Power Exhaust: From Present Devices via ITER to DEMO”. In: *Plasma Physics and Controlled Fusion* 55.12 (Dec. 1, 2013). DOI: `10.1088/0741-3335/55/12/124041`.

[43] S. I. Krasheninnikov and A. S. Kukushkin. “Physics of Ultimate Detachment of a Tokamak Divertor Plasma”. In: *Journal of Plasma Physics* 83.5 (Oct. 2017). DOI: `10.1017/S0022377817000654`.

[44] S. I. Krasheninnikov, A. S. Kukushkin, and A. A. Pshenov. “Divertor Plasma Detachment”. In: *Physics of Plasmas* 23.5 (May 2016). DOI: `10.1063/1.4948273`.

[45] G. Matthews. “Plasma Detachment from Divertor Targets and Limiters”. In: *Journal of Nuclear Materials* 220–222 (Apr. 1995). DOI: `10.1016/0022-3115(94)00450-1`.

[46] F. Wagner, G. Becker, K. Behringer, et al. “Regime of Improved Confinement and High Beta in Neutral-Beam-Heated Divertor Discharges of the ASDEX Tokamak”. In: *Physical Review Letters* 49.19 (Nov. 8, 1982). DOI: `10.1103/PhysRevLett.49.1408`.

[47] D. Kalupin, M. Z. Tokar, B. Unterberg, et al. “On the Difference of H-mode Power Threshold in Divertor and Limiter Tokamaks”. In: *Plasma Physics and Controlled Fusion* 48 (5A Apr. 2006). DOI: `10.1088/0741-3335/48/5A/S30`.

[48] F. Wagner. “A Quarter-Century of H-mode Studies”. In: *Plasma Physics and Controlled Fusion* 49 (12B Nov. 2007). DOI: `10.1088/0741-3335/49/12B/S01`.

[49] R. J. Groebner, K. H. Burrell, and R. P. Seraydarian. “Role of Edge Electric Field and Poloidal Rotation in the L - H Transition”. In: *Physical Review Letters* 64.25 (June 18, 1990). DOI: `10.1103/PhysRevLett.64.3015`.

[50] J. Hugill. “Edge Turbulence in Tokamaks and the L-mode to H-mode Transition”. In: *Plasma Physics and Controlled Fusion* 42.8 (Aug. 2000). DOI: `10.1088/0741-3335/42/8/201`.

[51] J. W. Connor and H. R. Wilson. “A Review of Theories of the L-H Transition”. In: *Plasma Physics and Controlled Fusion* 42.1 (Jan. 1, 2000). DOI: `10.1088/0741-3335/42/1/201`.

[52] P. Manz, G. S. Xu, B. N. Wan, et al. "Zonal Flow Triggers the L-H Transition in the Experimental Advanced Superconducting Tokamak". In: *Physics of Plasmas* 19.7 (July 1, 2012). DOI: `10.1063/1.4737612`.

[53] T. Estrada, T. Happel, C. Hidalgo, E. Ascasíbar, and E. Blanco. "Experimental Observation of Coupling between Turbulence and Sheared Flows during L-H Transitions in a Toroidal Plasma". In: *EPL (Europhysics Letters)* 92.3 (Nov. 1, 2010). DOI: `10.1209/0295-5075/92/35001`.

[54] T. Eich, A. Leonard, R. Pitts, et al. "Scaling of the Tokamak near the Scrape-off Layer H-mode Power Width and Implications for ITER". In: *Nuclear Fusion* 53.9 (Sept. 1, 2013). DOI: `10.1088/0029-5515/53/9/093031`.

[55] D. Brunner, B. LaBombard, A. Q. Kuang, and J. L. Terry. "High-Resolution Heat Flux Width Measurements at Reactor-Level Magnetic Fields and Observation of a Unified Width Scaling across Confinement Regimes in the Alcator C-Mod Tokamak". In: *Nuclear Fusion* 58.9 (July 2018). DOI: `10.1088/1741-4326/aad0d6`.

[56] C. S. Chang, S. Ku, A. Loarte, et al. "Gyrokinetic Projection of the Divertor Heat-Flux Width from Present Tokamaks to ITER". In: *Nucl. Fusion* (2017).

[57] Z.-Y. Li, X. Q. Xu, N.-M. Li, V. S. Chan, and X.-G. Wang. "Prediction of Divertor Heat Flux Width for ITER Using BOUT$\mathplus$$\mathplus$ Transport and Turbulence Module". In: *Nuclear Fusion* 59.4 (Feb. 2019). DOI: `10.1088/1741-4326/ab0184`.

[58] C. S. Chang, S. Ku, R. Hager, et al. "Constructing a New Predictive Scaling Formula for ITER's Divertor Heat-Load Width Informed by a Simulation-Anchored Machine Learning". In: *Physics of Plasmas* 28.2 (Feb. 2021). DOI: `10.1063/5.0027637`.

[59] V. Rozhansky, E. Kaveeva, I. Senichenkov, and E. Vekshina. "Structure of the Classical Scrape-off Layer of a Tokamak". In: *Plasma Physics and Controlled Fusion* 60.3 (Jan. 2018). DOI: `10.1088/1361-6587/aaa11a`.

[60] R. J. Goldston. "Heuristic Drift-Based Model of the Power Scrape-off Width in Low-Gas-Puff H-mode Tokamaks". In: *Nuclear Fusion* 52.1 (Dec. 2011). DOI: `10.1088/0029-5515/52/1/013009`.

[61] T. Eich, P. Manz, R. J. Goldston, et al. "Turbulence Driven Widening of the Near-SOL Power Width in ASDEX Upgrade H-Mode Discharges". In: *Nuclear Fusion* 60.5 (Apr. 2020). DOI: `10.1088/1741-4326/ab7a66`.

[62] F. Militello, L. Aho-Mantila, R. Ambrosino, et al. "Preliminary Analysis of Alternative Divertors for DEMO". In: *Nuclear Materials and Energy* 26 (Mar. 2021). DOI: `10.1016/j.nme.2021.100908`.

[63] C. Theiler, B. Lipschultz, J. Harrison, et al. "Results from Recent Detachment Experiments in Alternative Divertor Configurations on TCV". In: *Nuclear Fusion* 57.7 (July 1, 2017). DOI: `10.1088/1741-4326/aa5fb7`.

[64] T. Lunt, M. Bernert, D. Brida, et al. “Study of Detachment in Future ASDEX Upgrade Alternative Divertor Configurations by Means of EMC3-EIRENE”. In: *Nuclear Materials and Energy* (Feb. 2021). DOI: `10.1016/j.nme.2021.100950`.

[65] R. Albanese, on behalf of the WPDTT2 Team, and the DTT Project Proposal Contributors. “DTT: A Divertor Tokamak Test Facility for the Study of the Power Exhaust Issues in View of DEMO”. In: *Nuclear Fusion* 57.1 (Jan. 1, 2017). DOI: `10.1088/0029-5515/57/1/016010`.

[66] D. D. Ryutov. “Geometrical Properties of a “Snowflake” Divertor”. In: *Physics of Plasmas* 14.6 (June 2007). DOI: `10.1063/1.2738399`.

[67] M. Kotschenreuther, P. Valanju, B. Covele, and S. Mahajan. “Magnetic Geometry and Physics of Advanced Divertors: The X-divertor and the Snowflake”. In: *Physics of Plasmas* 20.10 (Oct. 2013). DOI: `10.1063/1.4824735`.

[68] P. M. Valanju, M. Kotschenreuther, S. M. Mahajan, and J. Canik. “Super-X Divertors and High Power Density Fusion Devices”. In: *Physics of Plasmas* 16.5 (May 2009). DOI: `10.1063/1.3110984`.

[69] D. Brunner, A. Q. Kuang, B. LaBombard, and J. L. Terry. “The Dependence of Divertor Power Sharing on Magnetic Flux Balance in near Double- Null Configurations on Alcator C-Mod”. In: *Nucl. Fusion* (2018).

[70] P. Rindt, T. W. Morgan, M. A. Jaworski, and N. J. L. Cardozo. “Power Handling Limit of Liquid Lithium Divertor Targets”. In: *Nuclear Fusion* 58.10 (July 2018). DOI: `10.1088/1741-4326/aad290`.

[71] T. W. Morgan, P. Rindt, G. G. van Eden, et al. “Liquid Metals as a Divertor Plasma-Facing Material Explored Using the Pilot-PSI and Magnum-PSI Linear Devices”. In: *Plasma Physics and Controlled Fusion* 60.1 (Jan. 1, 2018). DOI: `10.1088/1361-6587/aa86cd`.

[72] R. Dejarnac, J. Horacek, M. Hron, et al. “Overview of Power Exhaust Experiments in the COMPASS Divertor with Liquid Metals”. In: *Nuclear Materials and Energy* 25 (Dec. 1, 2020). DOI: `10.1016/j.nme.2020.100801`.

[73] M. Greenwald, J. L. Terry, S. M. Wolfe, et al. “A New Look at Density Limits in Tokamaks”. In: *Nuclear Fusion* 28.12 (Dec. 1988). DOI: `10.1088/0029-5515/28/12/009`.

[74] B. Lipschultz, B. LaBombard, E. Marmar, et al. “Marfe: An Edge Plasma Phenomenon”. In: *Nuclear Fusion* 24.8 (Aug. 1, 1984). DOI: `10.1088/0029-5515/24/8/002`.

[75] M. Bernert, M. Wischmeier, A. Huber, et al. “Power Exhaust by SOL and Pedestal Radiation at ASDEX Upgrade and JET”. In: *Nuclear Materials and Energy*. Proceedings of the 22nd International Conference on Plasma Surface Interactions 2016, 22nd PSI 12 (Aug. 1, 2017). DOI: `10.1016/j.nme.2016.12.029`.

[76] M. Bernert, F. Janky, B. Sieglin, et al. “X-Point Radiation, Its Control and an ELM Suppressed Radiating Regime at the ASDEX Upgrade Tokamak”. In: *Nuclear Fusion* 61.2 (Feb. 1, 2021). DOI: `10.1088/1741-4326/abc936`.

[77] A. H. Boozer. “Theory of Tokamak Disruptions”. In: *Physics of Plasmas* 19.5 (May 1, 2012). DOI: `10.1063/1.3703327`.

[78] L. E. Zakharov, S. A. Galkin, S. N. Gerasimov, and J.-E. contributors. “Understanding Disruptions in Tokamaks”. In: *Physics of Plasmas* 19.5 (May 1, 2012). DOI: `10.1063/1.4705694`.

[79] A. Cathey, M. Hoelzl, K. Lackner, et al. “Non-Linear Extended MHD Simulations of Type-I Edge Localised Mode Cycles in ASDEX Upgrade and Their Underlying Triggering Mechanism”. In: *Nuclear Fusion* 60.12 (Nov. 2020). DOI: `10.1088/1741-4326/abbc87`.

[80] J. W. Connor, A. Kirk, and H. R. Wilson. “Edge Localised Modes (ELMs): Experiments and Theory”. In: *AIP Conference Proceedings* 1013.1 (May 14, 2008). DOI: `10.1063/1.2939030`.

[81] T. E. Evans, R. A. Moyer, P. R. Thomas, et al. “Suppression of Large Edge-Localized Modes in High-Confinement DIII-D Plasmas with a Stochastic Magnetic Boundary”. In: *Physical Review Letters* 92.23 (June 10, 2004). DOI: `10.1103/PhysRevLett.92.235003`.

[82] A. Kirk, I. T. Chapman, T. E. Evans, et al. “Understanding the Effect Resonant Magnetic Perturbations Have on ELMs”. In: *Plasma Physics and Controlled Fusion* 55.12 (Nov. 2013). DOI: `10.1088/0741-3335/55/12/124003`.

[83] P. T. Lang, D. Frigione, A. Géraud, et al. “ELM Pacing and Trigger Investigations at JET with the New ITER-like Wall”. In: *Nuclear Fusion* 53.7 (May 2013). DOI: `10.1088/0029-5515/53/7/073010`.

[84] X. Chen, K. H. Burrell, T. H. Osborne, et al. “Expanding the Parameter Space of the Wide-Pedestal QH-mode towards ITER Conditions”. In: *Nuclear Fusion* 60.9 (Aug. 2020). DOI: `10.1088/1741-4326/ab9fa5`.

[85] L. Gil, C. Silva, T. Happel, et al. “Stationary ELM-free H-mode in ASDEX Upgrade”. In: *Nuclear Fusion* 60.5 (May 1, 2020). DOI: `10.1088/1741-4326/ab7d1b`.

[86] P. Manz, T. Happel, U. Stroth, T. Eich, and D. S. and. “Physical Mechanism behind and Access to the I-mode Confinement Regime in Tokamaks”. In: *Nuclear Fusion* 60.9 (Aug. 2020). DOI: `10.1088/1741-4326/ab9e17`.

[87] T. Happel, M. L. Reinke, D. Silvagni, et al. “Approaching Detachment in I-mode—Response of Core Confinement and the Edge Pedestal in the ASDEX Upgrade Tokamak”. In: *Nuclear Fusion* 61.3 (Feb. 2021). DOI: `10.1088/1741-4326/abd7b7`.

[88] P. Manz. “The Microscopic Picture of Plasma Edge Turbulence”. TUM, 2018.

[89] J. Carlson, J. A. Carlson, A. Jaffe, et al. *The Millennium Prize Problems.* American Mathematical Soc., 2006. 192 pp. ISBN: 978-0-8218-3679-8. Google Books: `7wJIPJ80RdUC`.

[90] A. Fasoli, S. Brunner, W. A. Cooper, et al. “Computational Challenges in Magnetic-Confinement Fusion Physics”. In: *Nature Physics* 12.5 (May 2016). DOI: `10.1038/nphys3744`.

[91] H. Bufferand, J. Bucalossi, G. Ciraolo, et al. “Progress in Edge Plasma Turbulence Modelling—Hierarchy of Models from 2D Transport Application to 3D Fluid Simulations in Realistic Tokamak Geometry”. In: *Nuclear Fusion* 61.11 (Oct. 2021). DOI: `10.1088/1741-4326/ac2873`.

[92] S. Wiesen, D. Reiter, V. Kotov, et al. “The New SOLPS-ITER Code Package”. In: *Journal of Nuclear Materials* 463 (Aug. 2015). DOI: `10.1016/j.jnucmat.2014.10.012`.

[93] E. Kaveeva, V. Rozhansky, I. Senichenkov, et al. “SOLPS-ITER Modelling of ITER Edge Plasma with Drifts and Currents”. In: *Nuclear Fusion* 60.4 (Mar. 2020). DOI: `10.1088/1741-4326/ab73c1`.

[94] Y. Feng and J. Kisslinger. “Status and Application of the EMC3/EIRENE Code”. In: *Contributions to Plasma Physics* 40.3-4 (2000). DOI: `10.1002/1521-3986(200006)40:3/4<271::AID-CTPP271>3.0.CO;2-1`.

[95] Y. Feng, H. Frerichs, M. Kobayashi, et al. “Recent Improvements in the EMC3-Eirene Code”. In: *Contributions to Plasma Physics* 54.4-6 (2014). DOI: `10.1002/ctpp.201410092`.

[96] T. D. Rognlien, J. L. Milovich, M. E. Rensink, and G. D. Porter. “A Fully Implicit, Time Dependent 2-D Fluid Code for Modeling Tokamak Edge Plasmas”. In: *Journal of Nuclear Materials*. Plasma-Surface Interactions in Controlled Fusion Devices 196–198 (Dec. 1, 1992). DOI: `10.1016/S0022-3115(06)80058-9`.

[97] E. Serre, H. Bufferand, A. Paredes, et al. “Numerical Modeling of the Impact of Geometry and Wall Components on Transport in the Tokamak Edge”. In: *Contributions to Plasma Physics* 52.5-6 (2012). DOI: `10.1002/ctpp.201210023`.

[98] S. Baschetti, H. Bufferand, G. Ciraolo, et al. “Self-Consistent Cross-Field Transport Model for Core and Edge Plasma Transport”. In: *Nuclear Fusion* 61.10 (Sept. 2021). DOI: `10.1088/1741-4326/ac1e60`.

[99] V. Naulin. “Turbulent Transport and the Plasma Edge”. In: *Journal of Nuclear Materials* (2007).

[100] D. A. D’Ippolito, J. R. Myra, and S. J. Zweben. “Convective Transport by Intermittent Blob-Filaments: Comparison of Theory and Experiment”. In: *Physics of Plasmas* 18.6 (June 2011). DOI: `10.1063/1.3594609`.

[101] D. A. D’Ippolito, J. R. Myra, S. I. Krasheninnikov, G. Q. Yu, and A. Y. Pigarov. “Blob Transport in the Tokamak Scrape-off-Layer”. In: *Contributions to Plasma Physics* 44.13 (Apr. 2004). DOI: `10.1002/ctpp.200410030`.

[102] M. Dorf and M. Dorr. “Continuum Gyrokinetic Simulations of Edge Plasmas in Single-Null Geometries”. In: *Physics of Plasmas* 28.3 (Mar. 2021). DOI: `10.1063/5.0039169`.

[103] D. Michels, A. Stegmeir, P. Ulbl, D. Jarema, and F. Jenko. “GENE-X: A Full-f Gyrokinetic Turbulence Code Based on the Flux-Coordinate Independent Approach”. In: *Computer Physics Communications* 264.107986 (2021). DOI: `10.1016/j.cpc.2021.107986`.

[104] A. H. Hakim, N. R. Mandell, T. N. Bernard, et al. "Continuum Electromagnetic Gyrokinetic Simulations of Turbulence in the Tokamak Scrape-off Layer and Laboratory Devices". In: *Physics of Plasmas* 27.4 (Apr. 1, 2020). DOI: `10.1063/1.5141157`.

[105] M. Boesl, A. Bergmann, A. Bottino, et al. "Gyrokinetic Full-f Particle-in-Cell Simulations on Open Field Lines with PICLS". In: *Physics of Plasmas* 26.12 (Dec. 4, 2019). DOI: `10.1063/1.5121262`.

[106] E. Caschera, G. Dif-Pradalier, P. Ghendrih, et al. "Immersed Boundary Conditions in Global, Flux-Driven, Gyrokinetic Simulations". In: *Journal of Physics: Conference Series* 1125 (Nov. 2018). DOI: `10.1088/1742-6596/1125/1/012006`.

[107] M. Wiesenberger, L. Einkemmer, M. Held, et al. "Reproducibility, Accuracy and Performance of the FELTOR Code and Library on Parallel Computer Architectures". In: *Computer Physics Communications* 238 (May 2019). DOI: `10.1016/j.cpc.2018.12.006`.

[108] A. Stegmeir, D. Coster, A. Ross, et al. "GRILLIX: A 3D Turbulence Code Based on the Flux-Coordinate Independent Approach". In: *Plasma Physics and Controlled Fusion* 60.3 (Mar. 1, 2018). DOI: `10.1088/1361-6587/aaa373`.

[109] A. Stegmeir, A. Ross, T. Body, et al. "Global Turbulence Simulations of the Tokamak Edge Region with GRILLIX". In: *Physics of Plasmas* 26.5 (May 2019). DOI: `10.1063/1.5089864`.

[110] F. Halpern, P. Ricci, S. Jolliet, et al. "The GBS Code for Tokamak Scrape-off Layer Simulations". In: *Journal of Computational Physics* 315 (June 2016). DOI: `10.1016/j.jcp.2016.03.040`.

[111] P. Paruta, P. Ricci, F. Riva, et al. "Simulation of Plasma Turbulence in the Periphery of Diverted Tokamak by Using the GBS Code". In: *Physics of Plasmas* 25.11 (Nov. 1, 2018). DOI: `10.1063/1.5047741`.

[112] B. Dudson, M. Umansky, X. Xu, P. Snyder, and H. Wilson. "BOUT++: A Framework for Parallel Plasma Fluid Simulations". In: *Computer Physics Communications* 180.9 (Sept. 2009). DOI: `10.1016/j.cpc.2009.03.008`.

[113] F. Riva, F. Militello, S. Elmore, et al. "Three-Dimensional Plasma Edge Turbulence Simulations of the Mega Ampere Spherical Tokamak and Comparison with Experimental Measurements". In: *Plasma Physics and Controlled Fusion* 61.9 (Sept. 1, 2019). DOI: `10.1088/1361-6587/ab3561`.

[114] B. D. Dudson and J. Leddy. "Hermes: Global Plasma Edge Fluid Turbulence Simulations". In: *Plasma Physics and Controlled Fusion* 59.5 (May 1, 2017). DOI: `10.1088/1361-6587/aa63d2`.

[115] B. Zhu, M. Francisquez, and B. N. Rogers. "GDB: A Global 3D Two-Fluid Model of Plasma Turbulence and Transport in the Tokamak Edge". In: *Computer Physics Communications* 232 (Nov. 2018). DOI: `10.1016/j.cpc.2018.06.002`.

[116] A. S. Thrysøe, M. Løiten, J. Madsen, et al. "Plasma Particle Sources Due to Interactions with Neutrals in a Turbulent Scrape-off Layer of a Toroidally Confined Plasma". In: *Physics of Plasmas* 25.3 (Mar. 2018). DOI: `10.1063/1.5019662`.

[117] A. Ross, A. Stegmeir, P. Manz, et al. "On the Nature of Blob Propagation and Generation in the Large Plasma Device: Global GRILLIX Studies". In: *Physics of Plasmas* 26.10 (Oct. 2019). DOI: `10.1063/1.5095712`.

[118] P. Ricci, F. Riva, C. Theiler, et al. "Approaching the Investigation of Plasma Turbulence through a Rigorous Verification and Validation Procedure: A Practical Examplea)". In: *Physics of Plasmas* 22.5 (May 2015). DOI: `10.1063/1.4919276`.

[119] F. Riva, C. Colin, J. Denis, et al. "Blob Dynamics in the TORPEX Experiment: A Multi-Code Validation". In: *Plasma Physics and Controlled Fusion* 58.4 (Apr. 1, 2016). DOI: `10.1088/0741-3335/58/4/044005`.

[120] B. D. Dudson, W. A. Gracias, R. Jorge, et al. "Edge Turbulence in ISTTOK: A Multi-Code Fluid Validation". In: *Plasma Physics and Controlled Fusion* (Feb. 1, 2021). DOI: `10.1088/1361-6587/abe21d`.

[121] F. Riva, C. K. Tsui, J. A. Boedo, P. Ricci, and TCV Team. "Shaping Effects on Scrape-off Layer Plasma Turbulence: A Rigorous Validation of Three-Dimensional Simulations against TCV Measurements". In: *Physics of Plasmas* 27.1 (Jan. 2020). DOI: `10.1063/1.5123451`.

[122] A. Stegmeir, D. Coster, O. Maj, K. Hallatschek, and K. Lackner. "The Field Line Map Approach for Simulations of Magnetically Confined Plasmas". In: *Computer Physics Communications* 198 (Jan. 2016). DOI: `10.1016/j.cpc.2015.09.016`.

[123] H. Bufferand, G. Ciraolo, G. Dif-Pradalier, et al. "Magnetic Geometry and Particle Source Drive of Supersonic Divertor Regimes". In: *Plasma Physics and Controlled Fusion* 56.12 (Dec. 1, 2014). DOI: `10.1088/0741-3335/56/12/122001`.

[124] N. Christen, C. Theiler, T. Rognlien, et al. "Exploring Drift Effects in TCV Single-Null Plasmas with the UEDGE Code". In: *Plasma Physics and Controlled Fusion* 59.10 (Oct. 1, 2017). DOI: `10.1088/1361-6587/aa7c8e`.

[125] T. Body, A. Stegmeir, W. Zholobenko, D. Coster, and F. Jenko. "Treatment of Advanced Divertor Configurations in the Flux-coordinate Independent Turbulence Code GRILLIX". In: *Contributions to Plasma Physics* 60.5-6 (June 2020). DOI: `10.1002/ctpp.201900139`.

[126] D. Galassi, C. Theiler, T. Body, et al. "Turbulence Dynamics around the X-point in TORPEX and Comparison with Multi-Code 3D Flux-Driven Simulations". In: *Journal of Plasma Physics* (2021).

[127] P. W. Terry, M. Greenwald, J.-N. Leboeuf, et al. "Validation in Fusion Research: Towards Guidelines and Best Practices". In: *Physics of Plasmas* 15.6 (June 2008). DOI: `10.1063/1.2928909`.

[128] H. Zohm. *Magnetohydrodynamic Stability of Tokamaks.*

[129] W. Zholobenko, T. Body, P. Manz, et al. "Electric Field and Turbulence in Global Braginskii Simulations across the ASDEX Upgrade Edge and Scrape-off Layer". In: *Plasma Physics and Controlled Fusion* 63.3 (Mar. 1, 2021). DOI: `10.1088/1361-6587/abd97e`.

[130] D. Tskhakaya. "One-Dimensional Plasma Sheath Model in Front of the Divertor Plates". In: *Plasma Physics and Controlled Fusion* 59.11 (Sept. 2017). DOI: `10.1088/1361-6587/aa8486`.

[131] R. Chodura. "Limiting Boundary Conditions of a Plasma Fluid at an Absorbing Target". In: *Physics of Plasmas* 12.1 (Jan. 2005). DOI: `10.1063/1.1796711`.

[132] J. P. Gunn. "Evidence for Strong Secondary Electron Emission in the Tokamak Scrape-off Layer". In: *Plasma Physics and Controlled Fusion* 54.8 (June 2012). DOI: `10.1088/0741-3335/54/8/085007`.

[133] R. L. Merlino. "Understanding Langmuir Probe Current-Voltage Characteristics". In: *American Journal of Physics* 75.12 (Dec. 1, 2007). DOI: `10.1119/1.2772282`.

[134] R. Tatali, E. Serre, P. Tamain, et al. "Impact of Collisionality on Turbulence in the Edge of Tokamak Plasma Using 3D Global Simulations". In: *Nuclear Fusion* (Feb. 24, 2021). DOI: `10.1088/1741-4326/abe98b`.

[135] P. C. Stangeby. *The Plasma Boundary of Magnetic Confinement Fusion Devices*. 2000.

[136] R. Chodura. "Plasma–Wall Transition in an Oblique Magnetic Field". In: *Physics of Fluids* 25.9 (1982). DOI: `10.1063/1.863955`.

[137] A. Geraldini, F. I. Parra, and F. Militello. "Solution to a Collisionless Shallow-Angle Magnetic Presheath with Kinetic Ions". In: *Plasma Physics and Controlled Fusion* 60.12 (Dec. 1, 2018). DOI: `10.1088/1361-6587/aae29f`.

[138] J. Moritz, E. Faudot, S. Devaux, and S. Heuraux. "Plasma Sheath Properties in a Magnetic Field Parallel to the Wall". In: *Physics of Plasmas* 23.6 (June 2016). DOI: `10.1063/1.4953897`.

[139] P. C. Stangeby. "The Bohm–Chodura Plasma Sheath Criterion". In: *Physics of Plasmas* 2.3 (Mar. 1995). DOI: `10.1063/1.871483`.

[140] P. C. Stangeby and A. V. Chankin. "The Ion Velocity (Bohm–Chodura) Boundary Condition at the Entrance to the Magnetic Presheath in the Presence of Diamagnetic and $\mathbf{E}\times\mathbf{B}$ Drifts in the Scrape-off Layer". In: *Physics of Plasmas* 2.3 (Mar. 1995). DOI: `10.1063/1.871421`.

[141] A. V. Chankin and P. C. Stangeby. "The Effect of Diamagnetic Drift on the Boundary Conditions in Tokamak Scrape-off Layers and the Distribution of Plasma Fluxes near the Target". In: 36.9 (Sept. 1994). DOI: `10.1088/0741-3335/36/9/008`.

[142] D. Tskhakaya and S. Kuhn. "Effect of $\mathrm{E} \times \mathrm{B}$ Drift on the Plasma Flow at the Magnetic Presheath Entrance". In: *Contributions to Plasma Physics* 42.2-4 (2002). DOI: `10.1002/1521-3986(200204)42:2/4<302::AID-CTPP302>3.0.CO;2-K`.

[143] X.-Z. Tang and Z. Guo. “Bohm Criterion and Plasma Particle/Power Exhaust to and Recycling at the Wall”. In: *Nuclear Materials and Energy* 12 (Aug. 2017). DOI: `10.1016/j.nme.2017.05.011`.

[144] T. M. G. Zimmermann, M. Coppins, and J. E. Allen. “Fluid Model of the Boundary of a One-Dimensional Plasma under the Influence of an Oblique Magnetic Field for a Wide Range of Collisionality”. In: *Physics of Plasmas* 15.7 (July 2008). DOI: `10.1063/1.2946436`.

[145] P. Cagas, A. Hakim, J. Juno, and B. Srinivasan. “Continuum Kinetic and Multi-Fluid Simulations of Classical Sheaths”. In: *Physics of Plasmas* 24.2 (Feb. 2017). DOI: `10.1063/1.4976544`.

[146] S. C. Cowley, R. M. Kulsrud, and R. Sudan. “Considerations of Ion-temperature-gradient-driven Turbulence”. In: *Physics of Fluids B: Plasma Physics* 3.10 (Oct. 1, 1991). DOI: `10.1063/1.859913`.

[147] M. A. Beer, S. C. Cowley, and G. W. Hammett. “Field-aligned Coordinates for Nonlinear Simulations of Tokamak Turbulence”. In: *Physics of Plasmas* 2.7 (Aug. 1, 1995). DOI: `10.1063/1.871232`.

[148] A. H. Boozer. “Establishment of Magnetic Coordinates for a given Magnetic Field”. In: *The Physics of Fluids* 25.3 (Mar. 1, 1982). DOI: `10.1063/1.863765`.

[149] M. Ottaviani. “An Alternative Approach to Field-Aligned Coordinates for Plasma Turbulence Simulations”. In: *Physics Letters A* 375.15 (Apr. 2011). DOI: `10.1016/j.physleta.2011.02.069`.

[150] F. Hariri and M. Ottaviani. “A Flux-Coordinate Independent Field-Aligned Approach to Plasma Turbulence Simulations”. In: *Computer Physics Communications* 184.11 (Nov. 2013). DOI: `10.1016/j.cpc.2013.06.005`.

[151] F. Hariri, P. Hill, M. Ottaviani, and Y. Sarazin. “The Flux-Coordinate Independent Approach Applied to X-point Geometries”. In: *Physics of Plasmas* 21.8 (Aug. 1, 2014). DOI: `10.1063/1.4892405`.

[152] A. Stegmeir, O. Maj, D. Coster, et al. “Advances in the Flux-Coordinate Independent Approach”. In: *Computer Physics Communications* 213 (Apr. 2017). DOI: `10.1016/j.cpc.2016.12.014`.

[153] B. Shanahan, B. Dudson, and P. Hill. “Fluid Simulations of Plasma Filaments in Stellarator Geometries with BSTING”. In: *Plasma Physics and Controlled Fusion* 61.2 (Feb. 1, 2019). DOI: `10.1088/1361-6587/aaed7d`.

[154] B. Shanahan, P. Hill, and B. Dudson. “Towards Nonaxisymmetry; Initial Results Using the Flux Coordinate Independent Method in BOUT++”. In: *Journal of Physics: Conference Series* 775 (Nov. 2016). DOI: `10.1088/1742-6596/775/1/012012`. arXiv: `1609.06603`.

[155] M. Shashkov and S. Steinberg. *Conservative Finite-Difference Methods on General Grids*. Second. Boca Raton: CRC Press, June 2020. ISBN: 978-1-315-14020-9. DOI: `10.1201/9781315140209`.

[156] L. Isoardi, G. Chiavassa, G. Ciraolo, et al. “Penalization Modeling of a Limiter in the Tokamak Edge Plasma”. In: *Journal of Computational Physics* 229.6 (Mar. 2010). DOI: `10.1016/j.jcp.2009.11.031`.

[157] P. J. Roache. “The Method of Manufactured Solutions for Code Verification”. In: *Computer Simulation Validation: Fundamental Concepts, Methodological Frameworks, and Philosophical Perspectives.* Ed. by C. Beisbart and N. J. Saam. Simulation Foundations, Methods and Applications. Cham: Springer International Publishing, 2019. ISBN: 978-3-319-70766-2. DOI: `10.1007/978-3-319-70766-2_12`.

[158] D. P. O’Brien, L. L. Lao, E. R. Solano, et al. “Equilibrium Analysis of Iron Core Tokamaks Using a Full Domain Method”. In: 32.8 (Aug. 1992). DOI: `10.1088/0029-5515/32/8/I05`.

[159] P. J. McCarthy, P. Martin, and W. Schneider. *The CLISTE Interpretive Equilibrium Code.* 1999.

[160] J. .-M. Moret, B. P. Duval, H. B. Le, et al. “Tokamak Equilibrium Reconstruction Code LIUQE and Its Real Time Implementation”. In: *Fusion Engineering and Design* 91 (Feb. 1, 2015). DOI: `10.1016/j.fusengdes.2014.09.019`.

[161] R. Fischer, A. Bock, M. Dunne, et al. “Coupling of the Flux Diffusion Equation with the Equilibrium Reconstruction at ASDEX Upgrade”. In: *Fusion Science and Technology* 69.2 (Apr. 2016). DOI: `10.13182/FST15-185`.

[162] M. Brix, N. C. Hawkes, A. Boboc, et al. “Accuracy of EFIT Equilibrium Reconstruction with Internal Diagnostic Information at JETa)”. In: *Review of Scientific Instruments* 79.10 (Oct. 31, 2008). DOI: `10.1063/1.2964180`.

[163] R. Fischer, L. Giannone, J. Illerhaus, et al. “Estimation and Uncertainties of Profiles and Equilibria for Fusion Modeling Codes”. In: *Fusion Science and Technology* 76.8 (Nov. 16, 2020). DOI: `10.1080/15361055.2020.1820794`.

[164] H. Akima. *A Method of Bivariate Interpolation and Smooth Surface Fitting Based on Local Procedures.* U.S. Office of Telecommunications, 1973. 52 pp.

[165] D. Alciatore and R. Miranda. “A Winding Number and Point-in-Polygon Algorithm”. In: (1995).

[166] G. N. Kumar and M. Bangi. “An Extension to Winding Number and Point-in-Polygon Algorithm”. In: *IFAC-PapersOnLine.* 5th IFAC Conference on Advances in Control and Optimization of Dynamical Systems ACODS 2018 51.1 (Jan. 1, 2018). DOI: `10.1016/j.ifacol.2018.05.092`.

[167] T. Lunt, H. Zohm, A. Herrmann, et al. “Proposal of an Alternative Upper Divertor in ASDEX Upgrade Supported by EMC3-EIRENE Simulations”. In: *Nuclear Materials and Energy* 12 (Aug. 2017). DOI: `10.1016/j.nme.2016.12.035`.

[168] M. Greenwald. “Verification and Validation for Magnetic Fusion”. In: *Physics of Plasmas* 17.5 (May 2010). DOI: `10.1063/1.3298884`.

[169] W. L. Oberkampf and T. G. Trucano. “Verification and Validation in Computational Fluid Dynamics”. In: *Progress in Aerospace Sciences* (2002).

[170] A. Ho, J. Citrin, F. Auriemma, et al. "Application of Gaussian Process Regression to Plasma Turbulent Transport Model Validation via Integrated Modelling". In: *Nuclear Fusion* 59.5 (May 1, 2019). DOI: `10.1088/1741-4326/ab065a`.

[171] A. E. White. "Validation of Nonlinear Gyrokinetic Transport Models Using Turbulence Measurements". In: *Journal of Plasma Physics* 85.1 (Feb. 2019). DOI: `10.1017/S0022377818001253`.

[172] I. Furno, F. Avino, A. Bovet, et al. "Plasma Turbulence, Suprathermal Ion Dynamics and Code Validation on the Basic Plasma Physics Device TORPEX". In: *Journal of Plasma Physics* 81.3 (June 2015). DOI: `10.1017/S0022377815000161`.

[173] A. Fasoli. "The Role of Basic Plasmas Studies in the Quest for Fusion Power". In: *Nature Physics* 15 (2019).

[174] M. Podestà, A. Fasoli, B. Labit, et al. "Plasma Production by Low-Field Side Injection of Electron Cyclotron Waves in a Simple Magnetized Torus". In: 47.11 (Oct. 2005). DOI: `10.1088/0741-3335/47/11/008`.

[175] R. H. Cohen and D. D. Ryutov. "Plasma Sheath in a Tilted Magnetic Field: Closing of the Diamagnetic Currents; Effect on Plasma Convection". In: *Physics of Plasmas* 2.6 (June 1995). DOI: `10.1063/1.871288`.

[176] R. H. Cohen and D. Ryutov. "Drifts, Boundary Conditions and Convection on Open Field Lines". In: *Physics of Plasmas* 6.5 (May 1999). DOI: `10.1063/1.873455`.

[177] P. Ricci, C. Theiler, A. Fasoli, et al. "Methodology for Turbulence Code Validation: Quantification of Simulation-Experiment Agreement and Application to the TORPEX Experiment". In: *Physics of Plasmas* 18.3 (Mar. 2011). DOI: `10.1063/1.3559436`.

[178] B. Efron. "Bootstrap Methods: Another Look at the Jackknife". In: *The Annals of Statistics* 7.1 (Jan. 1979). DOI: `10.1214/aos/1176344552`.

[179] C. J. Roy. "Errors and Uncertainties: Their Sources and Treatment". In: *Computer Simulation Validation: Fundamental Concepts, Methodological Frameworks, and Philosophical Perspectives.* Ed. by C. Beisbart and N. J. Saam. Simulation Foundations, Methods and Applications. Cham: Springer International Publishing, 2019. ISBN: 978-3-319-70766-2. DOI: `10.1007/978-3-319-70766-2_5`.

[180] W. Zholobenko, A. Stegmeir, M. Griener, et al. "The Role of Neutral Gas in Validated Global Edge Turbulence Simulations". In: *Nuclear Fusion* (2021). DOI: `10.1088/1741-4326/ac1e61`.

[181] C. Angioni, E. Fable, M. Greenwald, et al. "Particle Transport in Tokamak Plasmas, Theory and Experiment". In: *Plasma Physics and Controlled Fusion* 51.12 (Dec. 1, 2009). DOI: `10.1088/0741-3335/51/12/124017`.

[182] C. K. Tsui, J. A. Boedo, and P. C. Stangeby. "Accounting for Debye Sheath Expansion for Proud Langmuir Probes in Magnetic Confinement Fusion Plasmas". In: *Review of Scientific Instruments* 89.1 (Jan. 1, 2018). DOI: `10.1063/1.4995353`.

[183] S. Kokoska and D. Zwillinger. “CRC Standard Probability and Statistics Tables and Formulae, Student Edition”. In: 1999. DOI: `10.1201/b16923`.

[184] P. Virtanen, R. Gommers, T. E. Oliphant, et al. “SciPy 1.0: Fundamental Algorithms for Scientific Computing in Python”. In: *Nature Methods* 17.3 (3 Mar. 2020). DOI: `10.1038/s41592-019-0686-2`.

[185] W. D. D’haeseleer, W. N. G. Hitchon, J. D. Callen, and J. L. Shohet. *Flux Coordinates and Magnetic Field Structure.* Berlin, Heidelberg: Springer Berlin Heidelberg, 1991. ISBN: 978-3-642-75597-2 978-3-642-75595-8. DOI: `10.1007/978-3-642-75595-8`.

[186] B. D. Scott. “Low Frequency Fluid Drift Turbulence in Magnetised Plasmas”. Habilitation. Max Planck Institute for Plasma Physics, 2000.

[187] L. Wu, K. John Wu, A. Sim, et al. “Towards Real-Time Detection and Tracking of Spatio-Temporal Features: Blob-Filaments in Fusion Plasma”. In: *IEEE Transactions on Big Data* 2.3 (Sept. 1, 2016). DOI: `10.1109/TBDATA.2016.2599929`.

[188] J. Loizu, P. Ricci, F. D. Halpern, and S. Jolliet. “Boundary Conditions for Plasma Fluid Models at the Magnetic Presheath Entrance”. In: *Physics of Plasmas* 19.12 (Dec. 2012). DOI: `10.1063/1.4771573`.

[189] B. D. Dudson, S. L. Newton, J. T. Omotani, and J. Birch. “On Ohm’s Law in Reduced Plasma Fluid Models”. In: 63.12 (Oct. 2021). DOI: `10.1088/1361-6587/ac2af9`.

[190] R. W. Brzozowski, F. Jenko, R. Bilato, M. Cavedon, and the ASDEX Upgrade Team. “A Geometric Model of Ion Orbit Loss under the Influence of a Radial Electric Field”. In: *Physics of Plasmas* 26.4 (Apr. 2019). DOI: `10.1063/1.5075613`.

[191] S. O. Makarov, D. P. Coster, V. A. Rozhansky, et al. “Equations and Improved Coefficients for Parallel Transport in Multicomponent Collisional Plasmas: Method and Application for Tokamak Modeling”. In: *Physics of Plasmas* 28.6 (June 2021). DOI: `10.1063/5.0047618`.

[192] B. D. Dudson, J. Allen, T. Body, et al. “The Role of Particle, Energy and Momentum Losses in 1D Simulations of Divertor Detachment”. In: *Plasma Physics and Controlled Fusion* 61.6 (June 1, 2019). DOI: `10.1088/1361-6587/ab1321`.

[193] A. Q. Kuang, S. Ballinger, D. Brunner, et al. “Divertor Heat Flux Challenge and Mitigation in SPARC”. In: *Journal of Plasma Physics* 86.5 (Oct. 2020). DOI: `10.1017/S0022377820001117`.

[194] O. Schmitz, Y. Feng, M. Jakubowski, et al. “Stable Heat and Particle Flux Detachment with Efficient Particle Exhaust in the Island Divertor of Wendelstein 7-X”. In: *Nuclear Fusion* (Sept. 2020). DOI: `10.1088/1741-4326/abb51e`.